

SIMULATION AND MODELING OF HOMOGENEOUS, COMPRESSED TURBULENCE

by
C-T. Wu,
J. H. Ferziger
and
D. R. Chapman

Computational facilities and financial support were supplied by
Control Data Corporation

Supported in part by NASA-Ames Research Center under Grant
NASA-NCC-2-15

(NASA-CR-176939) SIMULATION AND MODELING OF
HOMOGENEOUS, COMPRESSED TURBULENCE (Stanford
Univ.) 206 p CSCL 20D

N86-30958

Unclas
G3/34 43030

Report No. TF-21



Thermosciences Division
Department of Mechanical Engineering
Stanford University
Stanford, California 94305

May 1985

SIMULATION AND MODELING OF HOMOGENEOUS COMPRESSED TURBULENCE

by

C-T. Wu, J. H. Ferziger, and D. R. Chapman

Computational facilities and financial support were supplied by
Control Data Corporation

Supported in part by NASA-Ames Research Center under Grant
NASA-NCC-2-15

Technical Report TF-21

Thermosciences Division
Department of Mechanical Engineering
Stanford University
Stanford, California 94305

May 1985

Acknowledgments

The authors thank Professor W. C. Reynolds for many helpful discussions and useful ideas and for his critical reading of this manuscript. We also gratefully acknowledge Drs. R. Rogallo, P. Moin, N. Mansour, A. Wray, J. Kim, and A. Leonard for their help during the course of this work. We also appreciate the help of Messrs. A. Lazanoff and H. Rothmund of Control Data Corporation and the liaison staff of the Institute for Computational Studies at Colorado State University in unraveling the mysteries of the CYBER 205 computer.

Ms. Ruth Korb has done an excellent job in preparing the final form of this report. Her typing and editorial efforts are very much appreciated.

Special thanks go to Control Data Corporation for support under Grant 82CSU19, and to the National Aeronautics and Space Administration, which under Grant NASA-NCC-2-15, provided financial support for the last two years.

PRECEDING PAGE BLANK NOT FILMED

Abstract

Low Reynolds number homogeneous turbulence undergoing low Mach number isotropic and one-dimensional compression has been simulated by numerically solving the Navier-Stokes equations. The numerical simulations were carried out on a CYBER 205 computer using a $64 \times 64 \times 64$ mesh. A spectral method was used for spatial differencing and the second-order Runge-Kutta method for time advancement. A variety of statistical information was extracted from the computed flow fields. These include three-dimensional energy and dissipation spectra, two-point velocity correlations, one-dimensional energy spectra, turbulent kinetic energy and its dissipation rate, integral length scales, Taylor microscales, and Kolmogorov length scale.

It was found that the ratio of the turbulence time scale to the mean-flow time scale is an important parameter in these flows. When this ratio is large, the flow is immediately affected by the mean strain in a manner similar to that predicted by rapid distortion theory. When this ratio is small, the flow retains the character of decaying isotropic turbulence initially; only after the strain has been applied for a long period does the flow accumulate a significant reflection of the effect of mean strain. In these flows, the Kolmogorov length scale decreases rapidly with increasing total strain, due to the density increase that accompanies compression.

Results from the simulated flow fields were used to test one-point-closure, two-equation turbulence models. The two-equation models perform well only when the compression rate is small compared to the eddy turn-over rate. A new one-point-closure, three-equation turbulence model which accounts for the effect of compression is proposed. The new model accurately calculates four types of flows (isotropic decay, isotropic compression, one-dimensional compression, and axisymmetric expansion flows) for a wide range of strain rates.

Table of Contents

	Page
Acknowledgments	iii
Abstract	iv
List of Tables	vii
List of Figures	viii
Nomenclature	xvi
 Chapter	
I. INTRODUCTION	1
1.1 Compression Effects on Turbulence in Engines	1
1.2 Turbulent Flow Simulation	5
1.3 Motivation and Objectives	7
II. MATHEMATICAL FORMULATION	9
2.1 Problem Statement	9
2.2 Mathematical Formulation	10
2.3 Mean Flow	11
2.4 Coordinate Transformations	14
2.5 Isotropically Compressed Turbulence	17
2.6 One-Dimensionally Compressed Turbulence	18
III. NUMERICAL METHOD	23
3.1 Introduction	23
3.2 Approximation of Spatial Derivatives	24
A. Spectral Method	24
B. Alias Removal by Truncation	26
C. Alias Removal by Phase Shifting	27
3.3 Time Advancement	28
3.4 Initial Conditions	29
IV. COMPUTER PROGRAM DEVELOPMENT ON THE CYBER 205	31
4.1 The CYBER 205 Computer	31
4.2 Data Management	31
4.3 Computer Performance	32
4.4 Tests of the Code	36
A. Decay of Isotropic Turbulence	36
B. Plane Strain	37
4.5 General Description of the Simulations	38
V. HOMOGENEOUS ISOTROPIC TURBULENCE UNDERGOING ISOTROPIC COMPRESSION	45
5.1 Rapid Distortion Theory	45
5.2 Simulation Results	50
A. Description of the Rapid Distortion Run	50
B. Summary of Isotropic Compression Simulations	53

VI.	RESULTS FOR HOMOGENEOUS TURBULENCE UNDERGOING ONE-DIMENSIONAL COMPRESSION	67
6.1	Description of The Flows	67
6.2	Simulation Results	69
	A. Summary of One-Dimensional Compression Simulations	69
	B. Summary of Incompressible Axisymmetric Expansion Simulations	71
VII.	$k-\epsilon$ TURBULENCE MODEL TESTING AND MODIFICATIONS	89
7.1	Introduction	89
7.2	Testing $k-\epsilon$ Turbulence Models	90
	A. Background	90
	B. Isotropic Compression Flow	92
	C. Incompressible Axisymmetric Expansion Flow	94
	D. One-Dimensional Compression Flow	94
	E. Comments on Turbulence Length Scale Model	95
	F. Testing Model Constants in Modeled Dissipation Equation	96
	G. Summary of $k-\epsilon$ Model Testing	97
7.3	A One-Point-Closure Three-Equation Turbulence Model	98
	A. Motivation	98
	B. Homogeneous Isotropic Decay Flow	98
	C. Return to Equilibrium	99
	D. Isotropic Compression Flow	100
	E. Incompressible Axisymmetric Expansion Flow	101
	F. Reynolds Stress Model	103
	G. One-Dimensional Compression Flow	108
	H. Summary	109
VIII.	CONCLUSIONS AND RECOMMENDATIONS	151
8.1	Conclusions	151
8.2	Recommendations	152
Appendix	TABULATED DATA	155
References	183

List of Tables

Table	Page
4.1 Performance of CYBER 205 at CSU (Two pipes with 2M 64-Bit Word)	33
4.2 Performance of CYBER 205 at CDC (Four Pipes with 4M 64-Bit Word)	35
5.1. Some Details of the Initial Condition of the Isotropically Compressed Turbulence Simulations	51
5.2. Description of Simulations of Isotropically Compressed Turbulence	52
6.1. Description of Simulations of One-Dimensionally Compressed Turbulence	74
6.2. Description of Simulations of Axisymmetric Expansion Flow .	75
6.3. Some Details of the Initial Condition of the One- Dimensionally Compressed Turbulence Simulations	76
6.4. Some Details of the Initial Condition of the Axisymmetric Expansion Flow Simulations	76
7.1. The Values of the Model Constants in the $k-\epsilon$ Models . . .	92
7.2. The Values of the Model Constants in the $k-\epsilon-\tau$ Model . .	109

List of Figures

Figure		Page
2-1	Schematic description of homogeneous, isotropic compression flow.	20
2-2	Schematic description of homogeneous, one-dimensional compression flow	20
2-3	The mean velocity profile for one-dimensional compression flow	21
2-4	Lagrangian coordinate system for one-dimensional compression simulations	21
3-1	The stability diagram for second-order Runge-Kutta method .	30
4-1	The performance of a two-pipe CYBER 205 for addition and multiplication	39
4-2	Sketch of the computational box	39
4-3	Three-dimensional energy spectra for isotropic-decay turbulence	40
4-4	Three-dimensional dissipation spectra for isotropic-decay turbulence	40
4-5	One-dimensional energy spectra for isotropic-decay turbulence	41
4-6	Two-point velocity correlations for isotropic-decay turbulence	41
4-7	The evolution of the component energy ratio for present and Rogallo's simulations	42
4-8	The evolution of the structure parameter K_1 ($K_1 = R_{22} - R_{33} / R_{22} + R_{33}$) for present and Rogallo's simulations . .	42
4-9	The evolution of the component energy ratio for two different choices of strain axes	43
5-1	The initial lateral one-dimensional energy spectrum of run SQF	56
5-2	The lateral one-dimensional energy spectra of run SQF and RDT analysis at total strain 0.552	56
5-3	The initial longitudinal one-dimensional energy spectrum of run SQF	57

5-4	The longitudinal one-dimensional energy spectra of run SQF and RDT analysis at total strain 0.552	57
5-5	The longitudinal two-point velocity correlations of run SQF AT total strain 1, 0.779, and 0.552	58
5-6	The lateral two-point velocity correlations of run SQF at total strain 1, 0.779, and 0.552	58
5-7	The evolution of twice the turbulent kinetic energy of run SQF and RDT analysis	59
5-8	The evolution of the dissipation rate of run SQF and RDT analysis	59
5-9	The evolution of a longitudinal integral length scale of run SQF and RDT analysis	60
5-10	The evolution of a Taylor microscale of run SQF and RDT analysis	60
5-11	The evolution of the Kolmogorov length scale of run SQF and RDT analysis	61
5-12	The evolution of the turbulent Reynolds number for four isotropic compression simulations	61
5-13	The range of $ S q^2/\epsilon$ covered in four isotropic compression simulations	62
5-14	The three-dimensional energy spectra of runs SQF and SQH at total strain 0.785	62
5-15	The three-dimensional dissipation spectra of runs SQF and SQH at total strain 0.785	63
5-16	The lateral two-point velocity correlations of runs SQF and SQH at total strain 0.785	63
5-17	The longitudinal two-point velocity correlations of runs SQF and SQH at total strain 0.785	64
5-18	The evolution of the turbulent kinetic energy for four isotropic compression simulations	64
5-19	The evolution of the dissipation rate for four isotropic compression simulations	65
5-20	The evolution of a longitudinal integral length scale for four isotropic compression simulations	65
5-21	The evolution of a Taylor microscale for four isotropic compression simulations	66

5-22	The evolution of the Kolmogorov length scale for four isotropic compression simulations	66
6-1	Schematic description of homogeneous, incompressible, axisymmetric expansion flow	77
6-2	The evolution of the turbulent Reynolds number for four one-dimensional compression simulations	78
6-3	The range of $ S q^2/\epsilon$ covered in four one-dimensional compression simulations	78
6-4	The three-dimensional energy spectra of run ODD at total strain 1 and 0.494	79
6-5	The three-dimensional dissipation spectra of run ODD at total strain 1 and 0.494	79
6-6	The three-dimensional spectra of the three normal energy components of run ODD at total strain 0.494	80
6-7	The three-dimensional energy spectra of runs ODB and ODD at total strain 0.847	80
6-8	The longitudinal two-point velocity correlations in the compression direction of runs ODB and ODD at total strain 0.847	81
6-9	The longitudinal two-point velocity correlations in the non-compression direction of runs ODB and ODD at total strain 0.847	81
6-10	The evolution of twice the turbulent kinetic energy for four one-dimensional compression simulations	82
6-11	The evolution of the dissipation rate for four one-dimensional compression simulations	82
6-12	The evolution of b_{11} for four one-dimensional compression simulations	83
6-13	The evolution of the longitudinal integral length scale in the compression direction for four one-dimensional compression simulations	83
6-14	The evolution of a Taylor microscale for four one-dimensional compression simulations	84
6-15	The evolution of the Kolmogorov length scale for four one-dimensional compression simulations	84
6-16	The evolution of the turbulent Reynolds number for three axisymmetric expansional strain simulations	85

6-17	The range of $ S q^2/\epsilon$ covered in three axisymmetric expansional strain simulations	85
6-18	The evolution of twice the turbulent kinetic energy for three axisymmetric expansional strain simulations	86
6-19	The evolution of the dissipation rate for three axisymmetric expansional strain simulations	86
6-20	The evolution of b_{11} for three axisymmetric expansional strain simulations	87
6-21	The evolution of the longitudinal integral length scale in the compression direction for three axisymmetric expansional strain simulations	87
6-22	The evolution of a Taylor microscale for three axisymmetric expansional strain simulations	88
6-23	The evolution of the Kolmogorov length scale for three axisymmetric expansional strain simulations	88
7-1(a)	The prediction of the turbulent kinetic energy by $k-\epsilon$ models for run SQF	112
7-1(b)	The prediction of the dissipation rate by $k-\epsilon$ models for run SQF	112
7-2(a)	The prediction of the turbulent kinetic energy by $k-\epsilon$ models for run SQG	113
7-2(b)	The prediction of the dissipation rate by $k-\epsilon$ models for run SQG	113
7-3(a)	The prediction of the turbulent kinetic energy by $k-\epsilon$ models for run SQH	114
7-3(b)	The prediction of the dissipation rate by $k-\epsilon$ models for run SQH	114
7-4(a)	The prediction of the turbulent kinetic energy by $k-\epsilon$ models for run SQI	115
7-4(b)	The prediction of the dissipation rate by $k-\epsilon$ models for run SQI	115
7-5	The prediction of the turbulence length scale by the LSW model for isotropic compression simulations	116
7-6	The prediction of the turbulence length scale by Reynolds' model for isotropic compression simulations	116
7-7(a)	The prediction of the turbulent kinetic energy by $k-\epsilon$ models for run EXQ	117

7-7(b)	The prediction of the dissipation rate by $k-\epsilon$ models for run EXQ	117
7-7(c)	The prediction of R_{11} by $k-\epsilon$ models for run EXQ	118
7-8(a)	The prediction of the turbulent kinetic energy by $k-\epsilon$ models for run EXP	118
7-8(b)	The prediction of the dissipation rate by $k-\epsilon$ models for run EXP	119
7-8(c)	The prediction of R_{11} by $k-\epsilon$ models for run EXP	119
7-9(a)	The prediction of the turbulent kinetic energy by $k-\epsilon$ models for run EXO	120
7-9(b)	The prediction of the dissipation rate by $k-\epsilon$ models for run EXO	120
7-9(c)	The prediction of R_{11} by $k-\epsilon$ models for run EXO	121
7-10	The prediction of the turbulence length scale by the LSW model for three axisymmetric expansional strain simulations	121
7-11	The prediction of the turbulence length scale by Reynolds' model for three axisymmetric expansional strain simulations	122
7-12(a)	The prediction of the turbulent kinetic energy by $k-\epsilon$ models for run ODB	122
7-12(b)	The prediction of the dissipation rate by $k-\epsilon$ models for run ODB	123
7-12(c)	The prediction of R_{11} by $k-\epsilon$ models for run ODB	123
7-13(a)	The prediction of the turbulent kinetic energy by $k-\epsilon$ models for run ODC	124
7-13(b)	The prediction of the dissipation rate by $k-\epsilon$ models for run ODC	124
7-13(c)	The prediction of R_{11} by $k-\epsilon$ models for run ODC	125
7-14(a)	The prediction of the turbulent kinetic energy by $k-\epsilon$ models for run ODD	125
7-14(b)	The prediction of the dissipation rate by $k-\epsilon$ models for run ODD	126
7-14(c)	The prediction of R_{11} by $k-\epsilon$ models for run ODD	126

7-15(a)	The prediction of the turbulent kinetic energy by $k-\epsilon$ models for run ODE	127
7-15(b)	The prediction of the dissipation rate by $k-\epsilon$ models for run ODE	127
7-15(c)	The prediction of R_{11} by $k-\epsilon$ models for run ODE	128
7-16	The prediction of the turbulence length scale by the LSW model for one-dimensional compression simulations	128
7-17	The prediction of the turbulence length scale by Reynolds' model for one-dimensional compression simulations	129
7-18(a)	The evolution of q^3/ϵ in isotropic compression simulations	129
7-18(b)	The evolution of a longitudinal integral length scale in isotropic compression simulations	130
7-19(a)	The evolution of q^3/ϵ in incompressible, axisymmetric expansional strain simulations	130
7-19(b)	The evolution of the longitudinal integral length scale in the compression direction for incompressible, axisymmetric expansional strain simulations	131
7-20(a)	The evolution of q^3/ϵ in one-dimensional compression simulations	131
7-20(b)	The evolution of the longitudinal integral length scale in the compression direction for one-dimensional compression simulations	132
7-21	A plot of $-(k/\epsilon^2)(d\epsilon/dt)$ against P/ϵ for isotropic compression simulations	132
7-22	A plot of $-(k/\epsilon^2)(d\epsilon/dt)$ against P/ϵ for incompressible, axisymmetric expansional strain simulations	133
7-23(a)	The prediction of the turbulent kinetic energy by $k-\epsilon-\tau$ and $k-\epsilon$ models for run SQF	133
7-23(b)	The prediction of the dissipation rate by $k-\epsilon-\tau$ and $k-\epsilon$ models for run SQF	134
7-24(a)	The prediction of the turbulent kinetic energy by $k-\epsilon-\tau$ and $k-\epsilon$ models for run SQG	134
7-24(b)	The prediction of the dissipation rate by $k-\epsilon-\tau$ and $k-\epsilon$ models for run SQG	135
7-25(a)	The prediction of the turbulent kinetic energy by $k-\epsilon-\tau$ and $k-\epsilon$ models for run SQH	135

7-25(b)	The prediction of the dissipation rate by $k-\epsilon-\tau$ and $k-\epsilon$ models for run SQH	136
7-26(a)	The prediction of the turbulent kinetic energy by $k-\epsilon-\tau$ and $k-\epsilon$ models for run SQI	136
7-26(b)	The prediction of the dissipation rate by $k-\epsilon-\tau$ and $k-\epsilon$ models for run SQI	137
7-27	The evolution of the modeled turbulence time scale in isotropic compression simulations	137
7-28	A plot of the model coefficient A_1 as a function of P/ϵ and its fitting in incompressible, axisymmetric expansional strain flow	138
7-29	The evolution of the model coefficient A_0 in incompressible, axisymmetric expansional strain flow	138
7-30(a)	The prediction of the turbulent kinetic energy by $k-\epsilon-\tau$ and $k-\epsilon$ models for run EXQ	139
7-30(b)	The prediction of the dissipation rate by $k-\epsilon-\tau$ and $k-\epsilon$ models for run EXQ	139
7-30(c)	The prediction of R_{11} by $k-\epsilon-\tau$ and $k-\epsilon$ models for run EXQ	140
7-31(a)	The prediction of the turbulent kinetic energy by $k-\epsilon-\tau$ and $k-\epsilon$ models for run EXP	140
7-31(b)	The prediction of the dissipation rate by $k-\epsilon-\tau$ and $k-\epsilon$ models for run EXP	141
7-31(c)	The prediction of R_{11} by $k-\epsilon-\tau$ and $k-\epsilon$ models for run EXP	141
7-32(a)	The prediction of the turbulent kinetic energy by $k-\epsilon-\tau$ and $k-\epsilon$ models for run EXO	142
7-32(b)	The prediction of the dissipation rate by $k-\epsilon-\tau$ and $k-\epsilon$ models for run EXO	142
7-32(c)	The prediction of R_{11} by $k-\epsilon-\tau$ and $k-\epsilon$ models for run EXO	143
7-33	The evolution of the modeled turbulence time scale in incompressible, axisymmetric expansional strain flow	143
7-34(a)	The prediction of the turbulent kinetic energy by $k-\epsilon-\tau$ and $k-\epsilon$ models for run ODB	144
7-34(b)	The prediction of the dissipation rate by $k-\epsilon-\tau$ and $k-\epsilon$ models for run ODB	144

7-34(c)	The prediction of R_{11} by $k-\epsilon-\tau$ and $k-\epsilon$ models for run ODB	145
7-35(a)	The prediction of the turbulent kinetic energy by $k-\epsilon-\tau$ and $k-\epsilon$ models for run ODC	145
7-35(b)	The prediction of the dissipation rate by $k-\epsilon-\tau$ and $k-\epsilon$ models for run ODC	146
7-35(c)	The prediction of R_{11} by $k-\epsilon-\tau$ and $k-\epsilon$ models for run ODC	146
7-36(a)	The prediction of the turbulent kinetic energy by $k-\epsilon-\tau$ and $k-\epsilon$ models for run ODD	147
7-36(b)	The prediction of the dissipation rate by $k-\epsilon-\tau$ and $k-\epsilon$ models for run ODD	147
7-36(c)	The prediction of R_{11} by $k-\epsilon-\tau$ and $k-\epsilon$ models for run ODD	148
7-37(a)	The prediction of the turbulent kinetic energy by $k-\epsilon-\tau$ and $k-\epsilon$ models for run ODE	148
7-37(b)	The prediction of the dissipation rate by $k-\epsilon-\tau$ and $k-\epsilon$ models for run ODE	149
7-37(c)	The prediction of R_{11} by $k-\epsilon-\tau$ and $k-\epsilon$ models for run ODE	149
7-38	The evolution of the modeled turbulence time scale in one-dimensional compression flow	150

Nomenclature

A_0, A_1	Model constants.
\tilde{a}	Function, Eq. (3-11).
B_{ij}	Coordinate transformation tensor, Eq. (2-23).
\tilde{b}	Function, Eq. (3-11).
b_{ij}	The Reynolds stress anisotropic tensor.
C	Function, Eq. (3-8).
\hat{C}', \hat{C}''	Shifted Fourier coefficients of function C , Eqs. (3-12) and (3-13).
C_1, C_5	Model constants.
C_2, C_6, AXI	" "
C_3, C_6, ISO	" "
C_4, C_μ	" "
$D(k)$	Three-dimensional dissipation spectrum.
D_{ij}	Dissipation tensor, Eq. (7-31).
$E(k)$	Three-dimensional energy spectrum.
$E_{ij}(k_1)$	One-dimensional spectrum of velocity field in the k_1 direction, Eq. (4-2).
$E_{ij}(\underline{k}', t)$	The spectra of $\overline{u'_i u'_j}$, Eq. (5-12).
F	Function, Eq. (3-4).
h	Mesh size.
h'	Shifted mesh size, Eq. (3-13).
J_{ijk}	Diffusive flux tensor, Eq. (7-32).
k	Turbulent kinetic energy.
k	Scalar wavenumber, Eq. (4-1).
k'_1, \underline{k}'	Fourier wave vector correspondint to \underline{x}' .
k_n	Wave number.
L	Period.
L_0	Initial box length.

$L_{ij,m}$ Integral length scales.
 l Length scale of energy-containing eddies, Eq. (3-2).
 M_{ijpq} See Eq. (7-38).
 MY, MZ Pencil sizes in y and z directions.
 N Number of mesh points, Eq. (3-4).
 NX, NY, NZ Number of mesh points of the computational box in the x, y, and z directions, respectively.
 n Time step n.
 n Decay exponent, Eq. (7-14).
 P_{ij} Production tensor, Eq. (7-29).
 p Total pressure.
 p Production of the turbulent kinetic energy by the mean flow.
 P_{DIL} Production of the turbulent kinetic energy by the dilatation part of the mean flow.
 P_{INC} Production of the turbulent kinetic energy by the incompressible part of the mean flow.
 \bar{p} Mean pressure.
 p' Fluctuating pressure.
 $p^{(1)}$ Rapid part of the fluctuating pressure, Eq. (7-35).
 $p^{(2)}$ Slow part of the fluctuating pressure, Eq. (7-36).
 $Q_{ij}(\underline{y})$ Two-point velocity correlation tensor with separation vector \underline{y} .
 q Turbulent velocity.
 R Gas constant.
 Re_l Turbulent Reynolds number, Eq. (3-3).
 R_{ij} The Reynolds stress tensor.
 S Mean strain rate.
 S_{AXI} Mean strain rate for axisymmetric expansion flow.
 S_{ISO} Mean strain rate for isotropic compression flow.
 S_{ij} Mean strain-rate tensor.

\bar{T}	Mean temperature.
T_{ij}	Transfer tensor, Eq. (7-30).
$T_{ij}^{(1)}$	Rapid part of the pressure-strain tensor.
t	Time (in laboratory coordinates).
t_0	An effective origin of time for isotropic decay turbulence, Eq. (7-14).
t'	Time (in Lagrangian coordinate).
\bar{U}_i	Mean velocity in the i -direction.
u_i	Total velocity in the i -direction.
u_i'	Fluctuating velocity in the i -direction.
$u^{(n)}$	Value of u at time step n , Eq. (3-15).
u^*	Value of u at intermediate step, Eq. (3-15).
\hat{u}_i^*	Complex conjugate of \hat{u}_i , Eq. (4-2).
V_p	Compression speed.
W_i	Mean vorticity in the i -direction.
w_i'	Fluctuating vorticity in the i -direction.
X_p	Box length.
x	Independent variable, Eq. (3-4).
x, y, z	Spatial directions.
x_i, \underline{x}	Laboratory coordinate.
x_i', \underline{x}'	Lagrangian coordinate.
z	$\epsilon\tau/k$, Eq. (7-19).

Greek Symbols

γ	Ratio of specific heats.
$\underline{\gamma}$	Separation vector, Eq. (4-3).
Δk	The difference between the magnitudes of the two nearest neighbor wavenumbers
Δt	Time step.
Δx_i	The computational mesh size in the i -direction

δ_{ij}	Kronecker delta \equiv	$1, j = i,$ $0, i \neq j.$
ϵ	Dissipation rate of turbulent kinetic energy.	
ϵ_{ijk}	The Levi-Civita symbol.	
η	Kolmogorov length scale.	
θ	See Eq. (3-18).	
λ	See Eq. (3-17).	
λ_{ii}	Taylor microscales.	
μ	Absolute viscosity.	
ν	Kinematic viscosity.	
ν_t	Turbulent eddy viscosity, Eq. (7-5).	
ρ	Total density.	
$\bar{\rho}$	Mean density.	
σ_{ij}	Stress tensor.	
τ	Turbulent time scale.	
$\phi_{ij}(\underline{k}', t)$	The spectra of $\overline{w_i' w_j'}$, Eq. (5-13).	
ϕ_{ij}	See Eq. (7-43).	
Ω_{ij}	Mean rotation tensor, Eq. (7-29).	
ω_i	Total vorticity in the i -direction.	

Other Symbols

$(\hat{\quad})$	Fourier transform.
I	The first invariant of tensor b_{ij} , Eq. (6-3).
II	The second invariant of tensor b_{ij} , Eq. (6-4).
III	The third invariant of tensor b_{ij} , Eq. (6-5).

Chapter I

INTRODUCTION

Turbulent flow undergoing compression is of great technological interest; understanding it is therefore of considerable importance. For example, the compression stroke in an internal combustion engine modifies the turbulence in the cylinder in important ways and thereby influences the nature of the combustion process and overall engine performance. Compression of turbulence is also important in shock wave-turbulent boundary layer interaction and other applications. However, current turbulence models, including the popular $k-\epsilon$ model, do not predict compression effects accurately. This is evidenced by their poor performance in piston-engine flow calculations. Reynolds (1980) and Morel and Mansour (1982) pointed out defects in the existing model and proposed new model constants. Although the predictions of the modified model look reasonable, they have not been tested against experimental data, thus leaving the model user in an uncomfortable position.

1.1 Compression Effects on Turbulence in Engines

The effects of compression on turbulence have been investigated both theoretically and experimentally. Rapid distortion theory (RDT) predicts the evolution of turbulence undergoing extremely rapid compression. Under the assumption that the strain is applied rapidly, nonlinear turbulence interactions are unimportant and the dissipation process is too slow to be significant. Thus, RDT is a linear, inviscid analysis of turbulence. It was originated by Taylor (1935) and was extensively developed by Batchelor and Proudman (1954).

Hoult and Wong (1980) applied RDT to the prediction of the evolution of the turbulence undergoing rapid compression. Computations based on this theory were compared with the available hot-wire measurements (Witze, 1977; and Lancaster, 1976), and reasonably good agreement was obtained.

Hunt (1978) reviewed RDT and applied it to various types of flows. He found that in rapid, one-dimensional compression the vorticity that

is aligned with the compression axis does not change, while the vorticity in the other two directions increases. He also worked out the evolution of the components of the turbulence kinetic energy for the rapid-compression case. RDT describes a limiting case; the conditions for its validity are not often met in practice. However, it does provide a useful analytical solution against which models and simulations can be tested.

Semenov (1958) measured turbulence in a motored, single-cylinder engine with a hot-wire anemometer. He found that the turbulence intensity at top dead center (TDC) was affected primarily by engine speed. Winsor and Patterson (1973) used a hot-wire anemometer to measure velocity fluctuations in a motored engine and found that the turbulence decayed during compression. Lancaster (1976) used a tri-axial, hot-wire anemometer to study turbulence in a motored single-cylinder engine; the measured turbulence intensity was found to decrease quite rapidly, reaching a minimum near TDC. He attributed this result to changes in flow orientation or pattern and viscous dissipation. He also found that the spectrum of the turbulence energy shifted to lower frequencies during compression. These results supported his argument that turbulence decays during compression. The hot-wire experiments of Witze (1977) were performed on a motored, single-cylinder engine. He found that turbulence intensity increases during the compression stroke, but later (1980) admitted that his data-reduction techniques overestimated the turbulence intensity. The problem stems from the fact that a hot wire does not measure the velocity directly, but responds to mass flux. As a consequence, it is necessary to account for the thermodynamic state of the gas when reducing the anemometer signal. There is reason to suspect that this problem is present in much of the published data taken with hot wires in engines.

More recently, investigators have used laser-Doppler anemometers (LDAs) to study in-cylinder fluid mechanics in internal-combustion engines. The group at Imperial College did a series of investigations on this subject. Morse, Whitelaw, and Yianneskis (1979, 1980) made LDA turbulence measurements in motored, piston-cylinder assemblies without compression; only the intake and exhaust strokes were allowed in their

apparatus. Arcoumanis, Bicen, and Whitelaw (1982) studied turbulence in a model four-stroke motored engine with a compression ratio of 3.5. They concluded that the turbulence level decays considerably in the early part of the compression stroke, while in the second half of the stroke the piston configuration becomes increasingly important. A flat piston produces an almost constant turbulence level. A cylindrical bowl has no significant effect on the flow, independent of the bowl depth within the practical range. However, the addition of a lip causes a substantial inward motion of the air toward the bowl but no apparent effect on the turbulence levels outside the bowl. The same authors (1983) also studied the squish effect on turbulence near TDC of compression in a motored model internal-combustion engine with compression ratio 6.7. They found that the squish did not alter the overall turbulence levels, which were comparable to those obtained with the flat piston. They claimed that squish is an important contributor to the mean motion rather than to the turbulence.

At Stanford, Richman (1982) developed a Flow Diagnostics Engine (FDE) which is a single-cylinder engine with a transparent cylinder made from single-crystal sapphire. The valve motion can be completely controlled by a minicomputer. A special Schlieren system was developed to visualize flows within the engine cylinder. His visualizations suggested that the scale of the turbulent motions decreases as the flow is compressed.

To model the effect of compression on turbulence, Watkins (1977) extended the $k-\epsilon$ model for incompressible flows developed by Launder and Spalding (1974), by adding a dilatation term to the modeled dissipation equation. The new term had a constant equal to unity, a natural outcome of the derivation. Gosman and Watkins (1977), Gosman and Johns (1978, 1980), Gosman, Johns, and Watkins (1980) all employed this extended $k-\epsilon$ turbulence model to predict the flow in reciprocating engines. Grasso and Bracco (1983) also introduced this $k-\epsilon$ model into a modified version of a code developed at Los Alamos by Butler et al. (1979), and used it to study the squish effect. Ahmadi-Befrui, Gosman, Lockwood, and Watkins (1981) made calculations with three different values of the model constant: 0, 1.0, and -0.373. Gosman and Harvey

(1982) used these constants to predict the behavior of a Diesel engine. Gosman and Jahanbakhsh (1981) reported that the predictions of turbulence intensity using -0.373 as the model constant are marginally better than those found using the alternative values. Ramos, Humphrey, and Sirignano (1979) used a purely "ad-hoc" turbulence model.

Reynolds (1980) pointed out that Watkins' model predicts growth of the length scale during compression independent of the rate of compression. Morel and Mansour (1982) found that, in an engine simulation, the length scale predicted by the Watkins model reached values several times the cylinder height near TDC; this is clearly incorrect. Reynolds (1980) applied rapid-distortion analysis to the isotropic compression case and suggested that the model constant in the dilatation term be $-2/3$. Borgnakke, Arpacı, and Tabaczynski (1980) independently found the same value. Morel and Mansour (1982) extended Reynolds' work to encompass three different "modes" of compression, i.e., isotropic, one-dimensional, and two-dimensional compressions. This led to a different model constant for each case. Mansour (1982) employed this modified $k-\epsilon$ model to study dispersion in stratified-charge engine cylinders during the compression stroke. His results are model-dependent and, in the absence of accurate data, they cannot be relied upon.

El Tahry (1983) derived exact transport equations for turbulence kinetic energy and its dissipation rate. An order-of-magnitude analysis was applied to the terms in these equations, and the small terms were neglected. It turned out that the k -equation retains its usual form, while four new terms are added to the dissipation equation; the constant in the dilatation term was found to be $-1/3$. Results of calculations using this modified dissipation equation are more physically plausible than those obtained with Watkins' version of the model. However, this does not answer the question of whether the present version of the $k-\epsilon$ model is adequate for use in engine flow computations.

Dussauge, Gaviglio, and Favre (1978) suggested that production of turbulence can be broken into two parts: (i) a "dilatation" production and (ii) an "isovolumetric" production related to the incompressible component of the strain. This suggestion will be used in the present work.

In summary, RDT provides a limiting solution demonstrating how compression affects turbulence. In attempts to understand the effects of compression on turbulence for the range of parameters encountered in engineering flows, people have looked to experiments. Due to the complexity of the flows studied and the difficulties associated with measurements in complex flows, only qualitative results have been obtained. Model builders have suggested various turbulence models aimed at representing the effects of compression; these models differ, especially with respect to the constant associated with the dilatation term. Users have employed these models in codes aimed at predicting fluid motion inside internal-combustion engines with only moderate success. It is difficult to identify the source of the discrepancy between the numerical predictions and the experimental results. A common conclusion by model-users is that the turbulence models appear to predict the general behavior of the turbulence field. However, the quality of experimental data does not allow accurate evaluation of the models.

1.2 Turbulent Flow Simulation

Newtonian fluid motion is governed by the Navier-Stokes equations. However, the wide range of length scales present in turbulent flows makes simulation of them via solution of the Navier-Stokes equations impossible at the Reynolds numbers of interest in engineering flows. However, full numerical simulation of turbulent flows at low Reynolds number in simple geometries has recently become feasible. In this approach, the only errors made are numerical ones which can be controlled. These simulations can be regarded as numerical experiments, and the results complement laboratory measurements. Such simulations can provide understanding of turbulence phenomena. A unique advantage of numerical simulation is that, with it, one can single out a particular effect and study its influence on turbulence. Full simulations are currently limited to simple, low-Reynolds-number turbulent flows and require supercomputers; they are impractical for direct engineering applications. However, they can be used as a research tool for investigating both the physics of turbulence and the models used to represent it.

We limit our discussion of full simulation to homogeneous flows. In these flows, the statistical turbulence quantities are independent of spatial position; they develop in time. In homogeneous flows without mean strain or shear, the turbulence decays with time; when mean strain or shear are applied, the kinetic energy of the turbulence may increase with time.

Homogeneous isotropic turbulence has been simulated by Orszag and Patterson (1972), Schumann and Patterson (1978), Clark, Ferziger, and Reynolds (1979), and many other people. The results have been used to determine turbulence model constants associated with dissipation, and it is usually the first flow simulated by people doing full simulations.

The next group of flows contains those in which there is energy exchange between the various components of the Reynolds stress (redistribution) in addition to dissipation, but no direct production of turbulence energy. There are two such flows: homogeneous turbulence with rotation (which has been simulated by Rogallo, 1981, and Bardina, Ferziger, and Rogallo, 1985) and homogeneous flow relaxing from the effects of strain or shear. Schumann and Herring (1976), Schumann and Patterson (1978), and Rogallo (1981) simulated turbulence undergoing relaxation from axisymmetric contraction strain. Lee and Reynolds (1985) studied the relaxation of turbulence after various types of strain; some details of their simulations will be given later.

The final group of homogeneous flows contains flows in which all of the phenomena that are possible in homogeneous flows actually occur: production, dissipation, and redistribution. There include homogeneous sheared turbulence and various types of homogeneous strained turbulence.

Full simulation of homogeneous sheared turbulence was performed by Rogallo (1981). Shirani, Ferziger, and Reynolds (1981) added a passive scalar to homogeneous shear flow, and Feiereisen, Reynolds, and Ferziger (1981) studied the effects of compressibility on homogeneous sheared turbulence.

Full simulation of homogeneous strained turbulence was performed by Rogallo (1981). He considered the axisymmetric contraction and plane strain cases. Dang (1985) simulated homogeneous turbulence subjected to

two successive plane strains. Lee and Reynolds (1985) did the most comprehensive study of homogeneous turbulence subjected to plane, axisymmetric contraction, axisymmetric expansion strains, and combinations of them.

1.3 Motivation and Objectives

Turbulence undergoing compression is of considerable technological interest, but the effects of compression on turbulence are not well understood. RDT provides solutions for cases which are far from those that arise in engineering applications. Due to the limitations of measurement techniques, experiments have provided only a qualitative picture of the effects of compression. As the state-of-art of experimental techniques advances, it will shed more light on this subject. On the other hand, model-builders have developed various turbulence models intended to represent the effects of compression but have insufficient data with which to validate the models.

Full simulation of turbulent flows is a research tool which allows one to better understand the physics of turbulence and is a valuable supplement to laboratory measurements. In particular, full simulation of turbulence undergoing compression is a unique tool that can be applied to answer some of the questions raised above. In this work, we perform full simulations of homogeneous turbulence undergoing isotropic and one-dimensional compression and use the resulting flow fields as a data base for turbulence model development. The simulations were performed on a CYBER 205 computer.

Our objectives are:

1. To simulate homogeneous turbulence subjected to isotropic and one-dimensional compression at low Reynolds number by solving the Navier-Stokes equations numerically.
2. To study the effects of compression on turbulence using the data generated by full simulations.
3. To test various turbulence models for compressed flow by comparing them with results of the full simulations.

4. To construct a turbulence model which accurately predicts compression effects on turbulence.

In Chapter II we present the mathematical foundations of these simulations. The numerical methods employed are discussed in Chapter III. In Chapter IV we describe the data management and the performance of the code on a CYBER 205 computer. In Chapters V and VI we present the results of isotropic and one-dimensional compression simulations, respectively. Turbulence model testing and a new model are presented in Chapter VII. Chapter VIII contains the conclusions.

Chapter II

MATHEMATICAL FORMULATION

This chapter describes the flows simulated and presents the mathematical formulation including the governing system of equations, the solution for the inviscid flow, and the coordinate transformation used to transform the governing equations from a Cartesian coordinate system to the Lagrangian coordinate system in which the simulations were performed.

2.1 Problem Statement

In this section we describe the flows to be simulated numerically. Since the principal objective is to understand the effects of compression on turbulence, we choose a flow to study which is not affected by the presence of solid boundaries. Homogeneous turbulence offers this possibility. In particular, we shall consider the case of a fixed mass of turbulent fluid contained within a rectangular parallelepiped, the opposing sides of which can move inward or outward with time. The turbulence may undergo uniform isotropic compression if all three pairs of sides move inward at same rate; this case is illustrated in Figure 2-1. This case simulates the squish effect of an engine which has a cup-in-piston design. If only one pair of sides moves inward as shown in Figure 2-2, the turbulence undergoes one-dimensional compression. This case simulates the compression stroke in an internal combustion engine with a flat piston and is also related to the compression of turbulence passing through a shock wave.

There are several important assumptions on which the simulations are based. These are stated below.

- The fluid is Newtonian and obeys the ideal gas law.
- Body forces are negligible.
- The compression is adiabatic.
- The Mach number is sufficiently small that sound waves play no significant role. Under this assumption, the fluid is compressed so that the fluid density depends only on time, not on space.

- Since there is no heat release and the Mach number is small, the fluctuations of temperature can be neglected which means that we can assume the fluid properties to be functions of time alone.

2.2 Mathematical Formulation

The basic equations of motion for a Newtonian fluid are the Navier-Stokes equations:

$$\frac{\partial \rho}{\partial t} + (\rho u_1)_{,1} = 0 \quad (2-1)$$

$$\frac{\partial(\rho u_1)}{\partial t} + (\rho u_1 u_j)_{,j} = \sigma_{1j,j} \quad (2-2)$$

$$\sigma_{1j} = -p\delta_{1j} + \mu(u_{1,j} + u_{j,1} - \frac{2}{3}u_{k,k}\delta_{1j}) \quad (2-3)$$

where t , ρ , u , σ , p , and μ are time, density, velocity, stress, pressure, and absolute viscosity, respectively. Indices run from 1 to 3, and a repeated index in any term implies summation. Subscripts after commas denote partial differentiation, e.g., $u_{1,j} = \partial u_1 / \partial x_j$.

All flow quantities may be decomposed into mean and turbulence components:

$$u_1(\underline{x}, t) = \bar{U}_1(\underline{x}, t) + u'_1(\underline{x}, t) \quad (2-4)$$

$$p(\underline{x}, t) = \bar{p}(t) + p'(\underline{x}, t) \quad (2-5)$$

$$\rho(t) = \bar{\rho}(t) \quad (2-6)$$

Substituting these into the equations of motion, (2-1), (2-2), and (2-3), taking the ensemble average and applying the assumption of homogeneity of the turbulence so that $\overline{(u'_1 u'_j)}_{,j} = 0$, we obtain the following equations for the mean components:

$$\frac{\partial \bar{\rho}}{\partial t} + (\bar{\rho} \bar{U}_1)_{,1} = 0 \quad (2-7)$$

$$\frac{\partial(\bar{\rho} \bar{U}_1)}{\partial t} + (\bar{\rho} \bar{U}_1 \bar{U}_j)_{,j} = 0 \quad (2-8)$$

Subtracting the mean equations from the total equations, we obtain the basic equations of motion for the turbulent component of the flow field.

$$u'_{i,i} = 0 \quad (2-9)$$

$$\frac{\partial(\bar{\rho}u'_i)}{\partial t} + \bar{\rho}(\bar{U}_i u'_{i,j} + \bar{U}_j u'_{i,j} + u'_{i,j}u'_{i,j})_{,j} = -p'_{,i} + \mu u'_{i,jj} \quad (2-10)$$

2.3 Mean Flow

The governing equations of the mean flow are Eqs. (2-7) and (2-8). The mean flow provides the driving force for the turbulence. Eq. (2-8) shows the mean flow is driven by its inertial force because the right- and side of the equation which represents the surface forces effect is zero.

Due to the assumption of homogeneity of the turbulence, the mean velocity field \bar{U}_i must be linear in the spatial coordinates

$$\bar{U}_i = \bar{U}_{i,j} X_j \quad (2-11)$$

where $\bar{U}_{i,j}$ depends only on time. The mean-deformation tensor $\bar{U}_{i,j}$ has the form

$$\bar{U}_{i,j} = \begin{pmatrix} S_1(t) & 0 & 0 \\ 0 & S_2(t) & 0 \\ 0 & 0 & S_3(t) \end{pmatrix} \quad (2-12)$$

In isotropic compression, $S_1(t) = S_2(t) = S_3(t)$; $S_2(t) = S_3(t) = 0$ in the one-dimensional compression case. $S_1(t)$ is $V_p/X_p(t)$, where V_p is the compression speed (assumed to be constant in all runs herein) and $X_p(t)$ is the box length at time t . The mean velocity vanishes at one end of the box while at the other end of the box it is equal to the compression speed V_p . The mean velocity profile for one-dimensional compression case is illustrated in Figure 2-3.

The density of the fluid can be obtained by applying the mass conservation law. For isotropic compression cases

$$\bar{\rho}(t) x_p^3(t) = \bar{\rho}(0) L_o^3 \quad (2-13)$$

while, for the one-dimensional compression cases:

$$\bar{\rho}(t) x_p(t) = \bar{\rho}(0) L_o \quad (2-14)$$

where L_o denotes the initial box length.

Due to the assumptions of adiabatic compression of the mean flow and the ratio of specific heats, γ , of the fluid being constant, the mean temperature can be obtained from thermodynamics:

$$\frac{\bar{T}(t)}{\bar{T}(0)} = \left(\frac{\bar{\rho}(t)}{\bar{\rho}(0)} \right)^{\gamma-1} \quad (2-15)$$

The mean pressure can be obtained from the assumption of ideal gas behavior of the fluid, i.e.,

$$\bar{P}(t) = \bar{\rho}(t) R \bar{T}(t) \quad (2-16)$$

where R is the gas constant.

The absolute viscosity of the fluid $\mu(\bar{T})$ is assumed to have the following functional form in the range of the mean temperature we consider (Touloukian et al., 1975):

$$\mu(\bar{T}) = \frac{145.8 \bar{T}^{1.5}}{110.4 + \bar{T}} \times 10^{-8} \text{ kg/(m-sec)} \quad \text{for } 250\text{K} \leq \bar{T} \leq 850\text{K} \quad (2-17)$$

Since the mean temperature is a function of time only, we can rewrite Eq. (2-17) as

$$\frac{\mu(t)}{\mu(0)} = \left(\frac{\bar{T}(t)}{\bar{T}(0)} \right)^{1.5} \left(\frac{110.4 + \bar{T}(0)}{110.4 + \bar{T}(t)} \right) \quad (2-18)$$

The second term on the right hand side of Eq. (2-18) can be approximated by:

$$\left(\frac{110.4 + \bar{T}(0)}{110.4 + \bar{T}(t)} \right) \approx \left(\frac{\bar{T}(t)}{\bar{T}(0)} \right)^{-0.75} \quad (2-19)$$

Substituting Eq.(2-19) into (2-18), we get the absolute viscosity as a function of time

$$\frac{\mu(t)}{\mu(0)} = \left(\frac{\bar{T}(t)}{\bar{T}(0)} \right)^{0.75} \quad (2-20)$$

We summarize the mean flow for each type of compression as follows:

Isotropic compression:

$$\begin{aligned} \bar{U}_1(\underline{x}, t) &= \frac{v_p}{x_p(t)} x_1 \\ \bar{U}_2(\underline{x}, t) &= \frac{v_p}{x_p(t)} x_2 \\ \bar{U}_3(\underline{x}, t) &= \frac{v_p}{x_p(t)} x_3 \\ \bar{\rho}(t) &= \bar{\rho}(0) \left(\frac{L_o}{x_p(t)} \right)^3 \\ \bar{T}(t) &= \bar{T}(0) \left(\frac{L_o}{x_p(t)} \right)^{1.2} \\ \bar{p}(t) &= \bar{p}(0) \left(\frac{L_o}{x_p(t)} \right)^{4.2} \\ \mu(t) &= \mu(0) \left(\frac{L_o}{x_p(t)} \right)^{0.9} \end{aligned} \quad (2-21)$$

One-dimensional compression:

$$\bar{U}_1(\underline{x}, t) = \frac{v_p}{x_p(t)} x_1$$

$$\bar{U}_2(\underline{x}, t) = 0$$

$$\bar{U}_3(\underline{x}, t) = 0$$

$$\bar{\rho}(t) = \bar{\rho}(0) \frac{L_o}{x_p(t)} \quad (2-22)$$

$$\bar{T}(t) = \bar{T}(0) \left(\frac{L_o}{x_p(t)} \right)^{0.4}$$

$$\bar{p}(t) = \bar{p}(0) \left(\frac{L_o}{x_p(t)} \right)^{1.4}$$

$$\mu(t) = \mu(0) \left(\frac{L_o}{x_p(t)} \right)^{0.3}$$

These mean properties will be used in the simulations.

2.4 Coordinate Transformations

The equations of motion for the turbulence field in the inertial laboratory frame are Eqs. (2-9) and (2-10). Periodic boundary conditions will be imposed in this coordinate system. Although these boundary conditions are not exact, they are the best that one can do in simulating homogeneous flows and allow the turbulence to develop with a minimum of external interference. Previous simulations (Rogallo, 1981; Feiereisen et al., 1981; Shirani et al., 1981) showed the usefulness of periodic boundary conditions for simulating homogeneous turbulence.

The presence of \bar{U}_1 in the convective term in Eq. (2-10) makes this term aperiodic in space and prohibits the application of periodic

boundary conditions to the equation as a whole. To overcome this problem, we need to introduce a coordinate transformation which eliminates the non-periodic terms. This new spatial coordinate system moves with the mean flow; it is essentially a Lagrangian coordinate system i.e. we are riding on the mean flow watching the evolution of turbulence.

We define this transformation for the general case by

$$x'_i = B_{ij} x_j, \quad t' = t \quad (2-23)$$

where B_{ij} is a tensor relating the transformed coordinates to the Cartesian coordinates, x'_i and t' are the transformed coordinates, and x_i and t are the Cartesian coordinates. Following Rogallo (1981), the transformation tensor B_{ij} is the solution of the following set of ordinary differential equations:

$$\frac{dB_{ij}}{dt} + B_{ik} \bar{U}_{k,j} = 0 \quad (2-24)$$

subject to the initial conditions:

$$B_{ij} = \delta_{ij}, \quad \text{at } t = 0 \quad (2-25)$$

For the isotropic compression case, the mean-deformation tensor $\bar{U}_{i,j}$ is

$$\bar{U}_{i,j} = \begin{pmatrix} V_p/X_p & 0 & 0 \\ 0 & V_p/X_p & 0 \\ 0 & 0 & V_p/X_p \end{pmatrix} \quad (2-26)$$

and

$$B_{11}(t) = \exp \left[- \int_0^t \frac{V_p}{X_p(t)} dt \right] = \frac{L_0}{X_p(t)} \quad (2-27)$$

where V_p is a constant and X_p is equal to $L_0 + V_p t$.

$$B_{22}(t) = B_{33}(t) = B_{11}(t) \quad (2-28)$$

Eq.(2-23) then becomes

$$\begin{aligned}x_1' &= \frac{L_o}{x_p(t)} x_1 \\x_2' &= \frac{L_o}{x_p(t)} x_2 \\x_3' &= \frac{L_o}{x_p(t)} x_3\end{aligned}\tag{2-29}$$

$$t' = t$$

For the one-dimensional compression case, the mean-deformation tensor $\bar{U}_{i,j}$ is

$$\bar{U}_{i,j} = \begin{pmatrix} v_p/x_p & 0 & 0 \\ 0 & 0 & 0 \\ 0 & 0 & 0 \end{pmatrix}\tag{2-30}$$

so

$$B_{11}(t) = \frac{L_o}{x_p(t)}\tag{2-31}$$

$$B_{22}(t) = B_{33}(t) = 1\tag{2-32}$$

Equation (2-23) then becomes

$$\begin{aligned}x_1' &= \frac{L_o}{x_p(t)} x_1 \\x_1' &= x_2 \\x_3' &= x_3 \\t' &= t\end{aligned}\tag{2-33}$$

Figure 2-4 shows how the new coordinate system moves with the mean flow. Transformation of the equations from the Cartesian coordinate system to the new coordinate system is done by using the chain rule. The resulting equations will be given below.

2.5 Isotropically Compressed Turbulence

The governing equations for the isotropic compression cases in the Lagrangian coordinate system are obtained using Eq. (2-29) and chain rule. We get

$$\frac{\partial}{\partial x_1} = \frac{L_o}{x_p(t)} \frac{\partial}{\partial x'_1}$$

$$\frac{\partial}{\partial x_2} = \frac{L_o}{x_p(t)} \frac{\partial}{\partial x'_2}$$

$$\frac{\partial}{\partial x_3} = \frac{L_o}{x_p(t)} \frac{\partial}{\partial x'_3}$$

$$\frac{\partial}{\partial t} = -\frac{v_p x'_1}{x_p(t)} \frac{\partial}{\partial x'_1} - \frac{v_p x'_2}{x_p(t)} \frac{\partial}{\partial x'_2} - \frac{v_p x'_3}{x_p(t)} \frac{\partial}{\partial x'_3} + \frac{\partial}{\partial t'} \quad (2-34)$$

$$\frac{\partial^2}{\partial x_1 \partial x_1} = \frac{L_o^2}{x_p^2(t)} \frac{\partial^2}{\partial x'_1 \partial x'_1}$$

$$\frac{\partial^2}{\partial x_2 \partial x_2} = \frac{L_o^2}{x_p^2(t)} \frac{\partial^2}{\partial x'_2 \partial x'_2}$$

$$\frac{\partial^2}{\partial x_3 \partial x_3} = \frac{L_o^2}{x_p^2(t)} \frac{\partial^2}{\partial x'_3 \partial x'_3}$$

Substituting Eqs. (2-34) and (2-21) into (2-9) and (2-10), we get the transformed continuity equation

$$\frac{\partial u'_1}{\partial x'_1} = 0 \quad (2-35)$$

The momentum equations become

$$\frac{\partial u'_i}{\partial t} + \frac{v_p}{x_p} u'_i + \frac{L_o}{x_p} u'_j \frac{\partial u'_i}{\partial x'_j} = - \frac{L_o}{x_p \rho} \frac{\partial p'}{\partial x'_i} + \frac{\mu}{\rho} \frac{L_o^2}{x_p^2} \frac{\partial^2 u'_i}{\partial x'_j \partial x'_j} \quad (2-36)$$

where V_p , L_o , and x_p are the compression speed, initial box length, and the box length at time t respectively.

Density and absolute viscosity can be related to the instantaneous box length by:

$$\bar{\rho}(t) = \bar{\rho}(0) \left(\frac{L_o}{x_p} \right)^3$$

$$\mu(t) = \mu(0) \left(\frac{L_o}{x_p} \right)^{0.9}$$

Since the troublesome convection terms has been transformed away, the transformed equations admit periodic boundary conditions.

2.6 One-Dimensionally Compressed Turbulence

The governing equations for one-dimensional compression cases in the Lagrangian coordinate system are obtained in much the same way as for the isotropic compression case. However, because the mean flow in these two cases are different, the transformed governing equations are not the same. We get:

$$\frac{\partial}{\partial x_1} = \frac{L_o}{x_p(t)} \frac{\partial}{\partial x'_1}$$

$$\frac{\partial}{\partial x_2} = \frac{\partial}{\partial x'_2}$$

$$\frac{\partial}{\partial x_3} = \frac{\partial}{\partial x'_3}$$

$$\frac{\partial}{\partial t} = - \frac{v_p x'_1}{x_p} \frac{\partial}{\partial x'_1} + \frac{\partial}{\partial t'} \quad (2-37)$$

$$\frac{\partial^2}{\partial x_1 \partial x_1} = \frac{L_o^2}{x_p^2} \frac{\partial^2}{\partial x'_1 \partial x'_1}$$

$$\frac{\partial^2}{\partial x_2 \partial x_2} = \frac{\partial^2}{\partial x'_2 \partial x'_2}$$

$$\frac{\partial^2}{\partial x_3 \partial x_3} = \frac{\partial^2}{\partial x'_3 \partial x'_3}$$

Substituting Eqs.(2-37) and (2-22) into (2-9) and (2-10), we get the transformed continuity equation

$$\frac{\partial u'_i}{\partial x'_i} + \left(\frac{L_o}{x_p} - 1 \right) \frac{\partial u'_1}{\partial x'_1} = 0 \quad (2-38)$$

The momentum equations become

$$\begin{aligned} \frac{\partial u'_i}{\partial t} + \frac{v_p}{x_p} u'_1 \delta_{i1} + u'_j \frac{\partial u'_i}{\partial x'_j} + \left(\frac{L_o}{x_p} - 1 \right) u'_1 \frac{\partial u'_i}{\partial x'_1} \\ = - \frac{1}{\rho} \left[\frac{\partial p'}{\partial x'_i} + \left(\frac{L_o}{x_p} - 1 \right) \frac{\partial p'}{\partial x'_1} \delta_{i1} \right] + \frac{\mu}{\rho} \left[\frac{\partial^2 u'_i}{\partial x'_j \partial x'_j} + \left(\frac{L_o^2}{x_p^2} - 1 \right) \frac{\partial^2 u'_i}{\partial x'_1 \partial x'_1} \right] \end{aligned} \quad (2.39)$$

where V_p , L_o , and x_p are the compression speed, initial box length, and the box length at time t respectively.

Density and absolute viscosity can be related to the instantaneous box length by:

$$\bar{\rho}(t) = \bar{\rho}(0) \left(\frac{L_o}{x_p} \right)$$

$$\mu(t) = \mu(0) \left(\frac{L_o}{x_p} \right)^{0.3}$$

There are no known analytical solutions of the equations of motion for the turbulence field, Eqs. (2-35), (2-36), (2-38), and (2-39). Numerical approximations are needed to solve these equations. The simulations will be carried out in a finite domain with specified boundary and initial conditions. These are described in the next chapter.

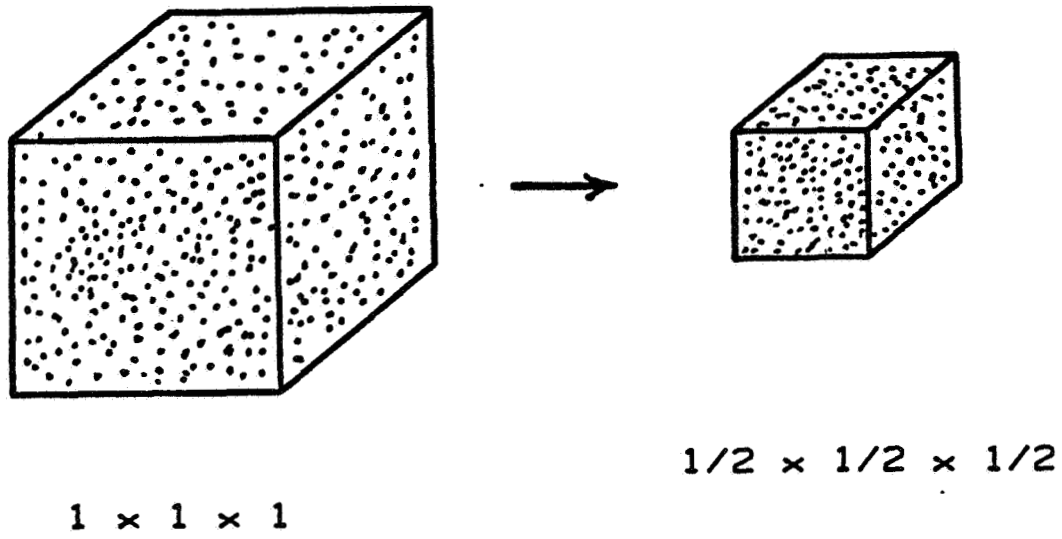


Fig. 2-1. Schematic description of homogeneous, isotropic compression flow.

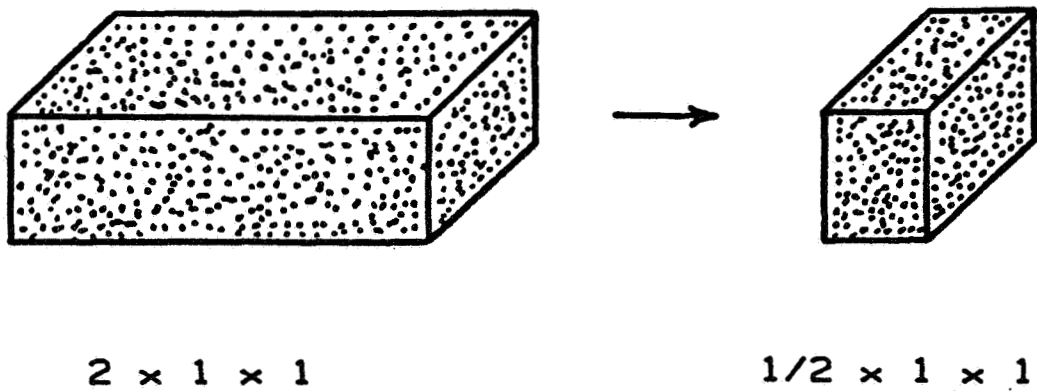


Fig. 2-2. Schematic description of homogeneous, one-dimensional compression flow.

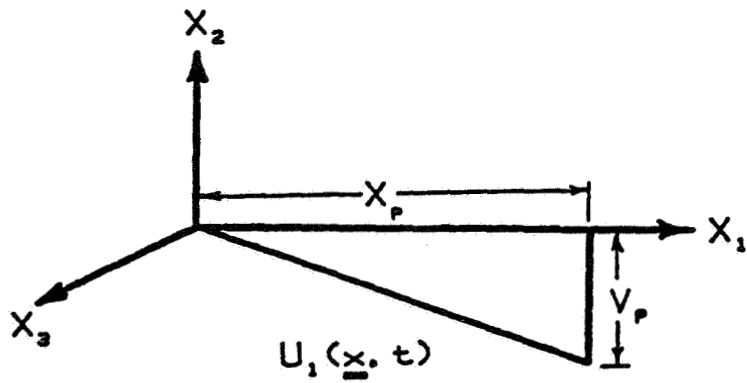


Fig. 2-3. The mean velocity profile for one-dimensional compression flow.

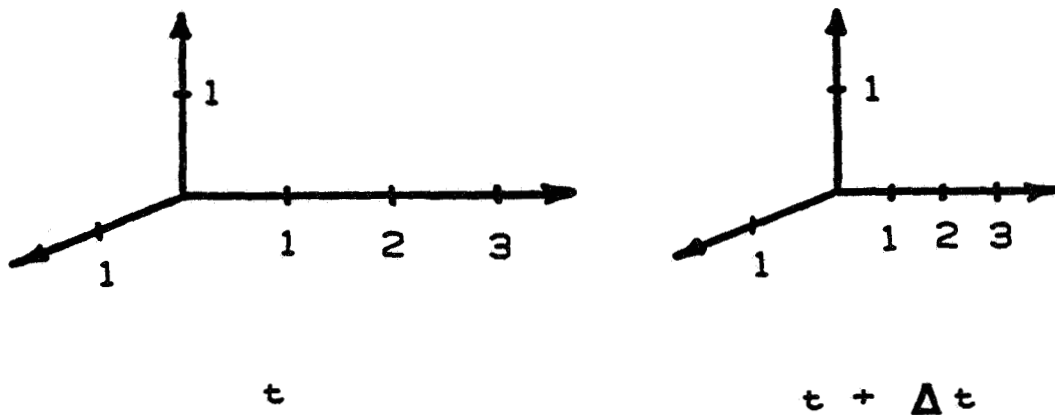


Fig. 2-4. Lagrangian coordinate system for one-dimensional compression simulations.

Chapter III
NUMERICAL METHOD

In this chapter full simulation of turbulent flow is introduced, numerical methods used to perform the simulations are presented and techniques for removing aliasing error and method to generate initial velocity field are described.

3.1 Introduction

Since the equations of motion for the turbulence are highly non-linear, they are not amenable to classical analytical approaches. Numerical approximations are needed to solve these equations. Detailed simulations of turbulent flows can be used to both generate physical understanding and to improve the models. Full-turbulence simulation is the numerical solution of the exact Navier-Stokes equations. The only errors made are numerical ones which can be kept within a desired tolerance.

In full-turbulence simulations, the number of spatial grid points is determined by two constraints: the computational box has to be bigger than the size of the large eddies if the simulation is to capture them. On the other hand, the mesh size has to be smaller than the smallest eddies in order to resolve them.

The smallest scale of importance is the Kolmogorov length scale which is defined as:

$$\eta = (\nu^3/\epsilon)^{1/4} \quad (3-1)$$

where ν is the kinematic viscosity and ϵ is the dissipation rate. Physically η is the size of the eddies for which viscosity is important.

The scale of the energy-containing eddies is usually defined by

$$l = q^3/\epsilon \quad (3-2)$$

PRECEDING PAGE BLANK NOT FILMED

where q is turbulent velocity. Therefore, the number of mesh points required to resolve both the large and small scales along one direction has to be roughly

$$\frac{\ell}{\eta} = \left(\frac{q\ell}{\nu}\right)^{3/4} = Re_{\ell}^{3/4} \quad (3-3)$$

At a Reynolds number based on turbulence quantities of 10,000, a mesh 1000 points on a side is required. Clearly, this is beyond the capacity of any existing computer. Full-turbulence simulations are currently limited by computer resource availability to low turbulent Reynolds numbers. In our case, with $64 \times 64 \times 64$ mesh points, the Reynolds number based on q and ℓ has to be less than about 250.

3.2 Approximation of Spatial Derivatives

Spectral methods are often used in turbulent flow simulations, because, for sufficiently smooth fields, they are very accurate. In addition, the periodic boundary conditions used in homogeneous turbulence simulation make spectral methods based on Fourier expansions quite natural and easy to apply. We shall use the pseudo-spectral method to compute the spatial derivatives in terms of the data at mesh points. Use of this method in the simulation of turbulence was pioneered by Orszag and Patterson (1972) and used by many others since then. This method is made efficient by the Fast Fourier Transform (FFT) algorithm developed by Cooley and Tukey (1965) which is most efficient when the number of mesh points in each direction is a power of 2. Since this method treats each direction independently, we shall consider only the one-dimensional case here.

A. Spectral Method

To see how the method works, consider any function $F(x)$ periodic with period L . The values of such functions at equally spaced mesh points can be represented in terms of a discrete Fourier series as follows:

$$F(x_j) = \sum_{n=-N/2}^{N/2-1} \hat{F}(k_n) e^{ik_n x_j} \quad (3-4)$$

where N is the number of mesh points and

$$x_j = hj, \quad j = 0, 1, 2, 3, \dots, N-1$$

$$h = L/N \quad \text{is the mesh size}$$

$$k_n = 2\pi n/L, \quad n = -N/2, \dots, 0, \dots, N/2 - 1$$

The coefficients of the Fourier series can be obtained from the inverse of Eq. (3-4):

$$\hat{F}(k_n) = \frac{1}{N} \sum_{j=0}^{N-1} F(x_j) e^{-ik_n x_j} \quad (3-5)$$

Equation (3-4) can be rendered an interpolation scheme by replacing x_j with a continuous variable x . Then the derivatives of $F(x)$ with respect to x at x_j can be approximated by differentiating the interpolant:

$$\frac{dF(x_j)}{dx} = \sum_{n=-N/2}^{N/2-1} ik_n \hat{F}(k_n) e^{ik_n x_j} \quad (3-6)$$

$$\frac{d^2 F(x_j)}{dx^2} = \sum_{n=-N/2}^{N/2-1} -k_n^2 \hat{F}(k_n) e^{ik_n x_j} \quad (3-7)$$

The results are an extremely accurate estimates of the derivatives.

The nonlinear terms in the equations of motion (2-36) and (2-39) introduce the possibility of aliasing errors into the numerical simulations. To understand the problem, let us consider the one-dimensional case with period $L = 2\pi = Nh$. If two functions represented as discrete Fourier series of the form (3-4) are multiplied, we obtain:

$$\begin{aligned} C(x_j) = a(x_j)b(x_j) &= \sum_{n=-N/2}^{N/2-1} \sum_{m=-N/2}^{N/2-1} \hat{a}(n)\hat{b}(m) e^{i(n+m)x_j} = \sum_{s=-N}^{N-2} \hat{C}(s) e^{isx_j} \\ &= \sum_{s=-N/2}^{N/2-1} \hat{C}(s) e^{isx_j} + \underbrace{\sum_{s=-N+1}^{-N/2-1+N} \hat{C}(s) e^{isx_j}}_{\text{Aliasing Error}} + \sum_{s=N/2-N}^{N-2-N} \hat{C}(s) e^{isx_j} \end{aligned} \quad (3-8)$$

The product series contains wave-numbers in the range $-N \leq s \leq N-2$, which includes wavenumbers outside the range supported by the grid we are using. Fourier functions with wave-numbers outside the domain $-N/2 \leq s \leq N/2 - 1$ are interpreted as waves that belong to the computational domain. On the grid, the functions are identical, but their derivatives are not identical. This introduces an error called aliasing. The alias error resulting from nonlinear terms can be removed by two different methods (Patterson and Orszag, 1971) which will be explained below.

B. Alias Removal By Truncation

One alias-removal method is the "2/3 rule". It consists of the following:

(1) Given $\hat{a}(n)$ and $\hat{b}(m)$, where $-N/2 \leq n, m \leq N/2 - 1$. Truncate these Fourier representations, keeping only the central two-thirds of the spectrum.

$$\begin{aligned} \hat{\tilde{a}}(n) &= \begin{cases} \hat{a}(n) & , \quad |n| \leq N/3 \\ 0 & , \quad |n| > N/3 \end{cases} \\ \hat{\tilde{b}}(m) &= \begin{cases} \hat{b}(m) & , \quad |m| \leq N/3 \\ 0 & , \quad |m| > N/3 \end{cases} \end{aligned} \quad (3-9)$$

(2) Compute $\tilde{a}(x_j)$ and $\tilde{b}(x_j)$ from the truncated Fourier representation.

(3) Form the product $\tilde{a}(x_j) \tilde{b}(x_j)$ in physical space.

(4) Take the Fourier transform of the result, keeping only the central two-thirds of the spectrum.

With this method of removing alias error, one-third of the mesh points in each direction are wasted in the one-dimensional case. In the three-dimensional case, 19/27 of the total mesh points are wasted. Consequently, this method is costly to use, and an alternative method of removing alias error will be described next.

C. Alias Removal By Phase Shifting

We can rewrite equation (3-8) as

$$\hat{C}(s) = \sum_{n+m=s} \hat{a}(n) \hat{b}(m) + \sum_{n+m=s \pm N} \hat{a}(n) \hat{b}(m) \quad (3-10)$$

The first term on the right-hand side is the alias-free part of the result, while the second term on the right-hand side contains the terms that are aliased to wave-number s .

The shift theorem tells us that if $F(x)$ has the Fourier transform $\hat{F}(k)$, then $F(x-h)$ has the Fourier transform $e^{ikh} \hat{F}(k)$. This can be used as the basis of a method of removing aliasing error. The basic steps of phase shifting method are:

(1) Given $\hat{a}(n)$ and $\hat{b}(m)$, form $\tilde{a}(x_j)$ and $\tilde{b}(x_j)$ on the shifted mesh.

$$\tilde{a}(x_j) = \sum_{n=-N/2}^{N/2-1} \hat{a}(n) e^{inh(j+1)}, \quad \tilde{b}(x_j) = \sum_{m=-N/2}^{N/2-1} \hat{b}(m) e^{imh(j+1)} \quad (3-11)$$

where h is the mesh size.

(2) Form the product $\tilde{c}(x_j) = \tilde{a}(x_j) \tilde{b}(x_j)$ in physical space.

(3) Shift the result back to the original mesh. The Fourier transform of resulting function is:

$$\begin{aligned} \hat{C}'(s) &= e^{-ish} \left\{ \sum_{n+m=s} \hat{a}(n) e^{inh} \times \hat{b}(m) e^{imh} + \sum_{n+m=s \pm N} \hat{a}(n) e^{inh} \times \hat{b}(m) e^{imh} \right\} \\ &= \sum_{n+m=s} \hat{a}(n) \hat{b}(m) + e^{\pm iNh} \sum_{n+m=s \pm N} \hat{a}(n) \hat{b}(m) \end{aligned} \quad (3-12)$$

(4) Repeat steps (1), (2), and (3) with h replaced by $h' = h + \pi/N$. Equation (3-12) becomes

$$\begin{aligned} \hat{C}''(s) &= \sum_{n+m=s} \hat{a}(n) \hat{b}(m) + e^{\pm iN(h+\pi/N)} \sum_{n+m=s \pm N} \hat{a}(n) \hat{b}(m) \\ &= \sum_{n+m=s} \hat{a}(n) \hat{b}(m) - e^{\pm iNh} \sum_{n+m=s \pm N} \hat{a}(n) \hat{b}(m) \end{aligned} \quad (3-13)$$

(5) The alias-free result is obtained by combining (3-12) and (3-13)

$$\sum_{n+m=s} \hat{a}(n)\hat{b}(m) = \frac{1}{2} (\hat{C}'(s) + \hat{C}''(s)) \quad (3-14)$$

The advantage of this method is that it does not waste any mesh points as in the "2/3 rule". It doubles the computation but is far more efficient.

3.3 Time Advancement

In full-turbulence simulations we are looking for time-accurate solutions to the equations of motion. An explicit method of advancing the solution in time is a natural choice. In particular, we used a second-order Runge-Kutta method to advance the solution in time. The algorithm to advance the solution of $du/dt = f(u)$ from the time step n to step $n + 1$ is

$$u^* = u^{(n)} + \Delta t f(u^{(n)}) \quad (3-15)$$

$$u^{(n+1)} = u^{(n)} + \frac{\Delta t}{2} [f(u^{(n)}) + f(u^*)] \quad (3-16)$$

where Δt is the time step and $*$ denotes the intermediate step.

The accuracy of this method can be found by introducing the representative equation $du/dt = \lambda u$. Replacing $f(u)$ by λu in (3-15) and (3-16) and substituting (3-15) into (3-16), we obtain

$$u^{(n+1)} = \left[1 + \lambda \Delta t + \frac{1}{2} (\lambda \Delta t)^2 \right] u^{(n)} \quad (3-17)$$

Equation (3-17) shows this algorithm is indeed second order accurate.

The stability limit of this method is the locus of all λ satisfying the following relationship

$$\left| \frac{1}{2} (\lambda \Delta t)^2 + (\lambda \Delta t) + 1 \right| = \left| e^{1\theta} \right| \quad (3-18)$$

where

$$0 \leq \theta \leq 2\pi$$

Rewriting (3-18)

$$\frac{1}{2} (\lambda\Delta t)^2 + (\lambda\Delta t) + (1 - e^{i\theta}) = 0, \quad 0 \leq \theta \leq 2\pi \quad (3-19)$$

The stability diagram for this method is shown on Figure 3-1. The time step is variable and is determined by setting the Courant number to be 0.05.

3.4 Initial Conditions

There are several ways to generate the initial velocity field (Bardina et al., 1983; Shirani et al., 1981; and Rogallo, 1981). We follow Rogallo's method to produce an initial velocity field which is nearly isotropic in wave space, divergence-free, and has the desired spectrum.

None of the initialization processes mentioned above produces the higher-order velocity statistics of real turbulence. We therefore let the initial field decay until the higher order statistics and the proper energy cascade were developed before introducing compression.

The isotropic fields produced after the initial development period were used as the starting conditions for various straining runs.

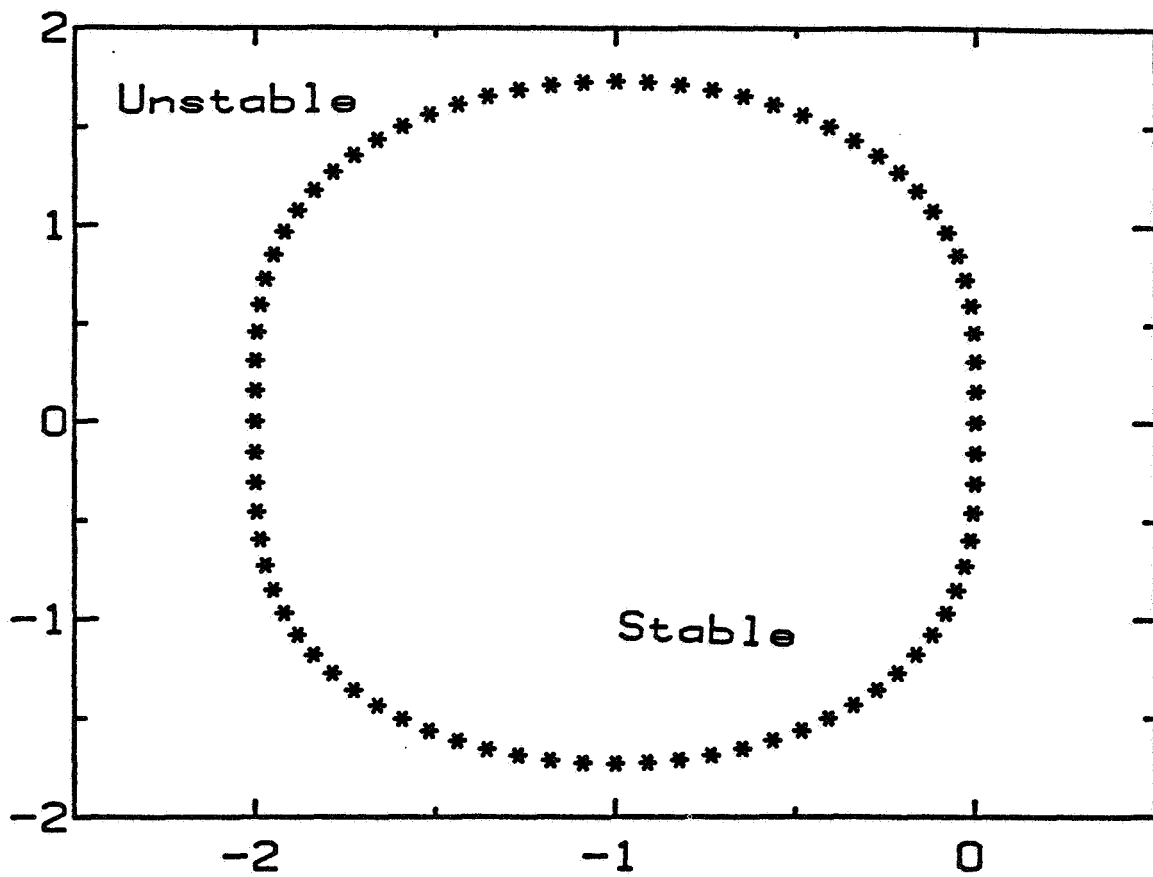


Fig. 3-1. The stability diagram for second-order Runge-Kutta method.

Chapter IV

COMPUTER PROGRAM DEVELOPMENT ON THE CYBER 205

In this chapter, the CYBER 205 computer and the program used to do the simulations are briefly described. The data-management strategy chosen, which takes full advantage of this computer, is presented. The performance of the computer code and the validation checks made are described.

4.1 The CYBER 205 Computer

The simulations were done on two different Control Data Corporation CYBER 205 computers, one at Colorado State University and a larger one with twice the memory and number of processor units at Control Data Corporation, Minneapolis. The CSU computer has two million 64-bit words of central memory. Its central processor unit (CPU) contains a scalar processor and a vector processor with two pipelines.

Figure 4-1 shows the performance of a two-pipe machine for addition and multiplication as a function of vector length. The asymptotic performance, which requires a vector length of 65535, is 100 million floating-point operations per second (Mflops) for 64-bit arithmetic and 200 Mflops for 32-bit arithmetic.

It is obvious that the performance improves with vector length. Vector length 1000 (64-bit case) or 2000 (32-bit case) is required to reach 90% of the asymptotic performance. Constructing a code which uses long vectors is therefore important if maximum performance is to be obtained from the machine.

4.2 Data Management

Based on the "longer vector gives better performance" philosophy, we chose to do the discrete Fourier transforms in parallel. This will be explained in detail later (also see Wu et al. 1983).

In Figure 4-2, N_X , N_Y , and N_Z are the number of mesh points of the computational box in the x , y , and z directions, respectively; M_Y and M_Z are called "pencil size".

On the first sweep, MZ x-y planes of data are Fourier transformed in the y direction; these are done in parallel. The transform length is NY, but by doing them in parallel, a vector length of $3 \times NX/2 \times MZ$ is achieved; the factor 3 is due to the simultaneous processing of three velocity components, while the factor 1/2 arises because only half of the wave space modes are needed in order to represent a real function. To accomplish the vectorization, it is useful to lump every dependent variable into a single big array. The main array is called DATA (NX/2, NY, NZ, 4, 2); the dimensions represent x, y, z, a dependent variable index, and real and imaginary parts of a complex number.

On the second sweep, MY x-z planes are processed. Fourier transforms in the z and x directions are done on this sweep. The vector lengths are $NX/2 \times MY \times 3$ and $NZ \times MY \times 3$, respectively.

A CYBER 205 vector is defined as a contiguous set of memory locations. Since the two sweeps are in different directions, an array transpose has to be done between sweeps and within the second sweep in order to keep processed data in a contiguous set of memory locations. The transpose is done by using gather instructions. The gather instruction puts array elements which are at various locations into a contiguous set of memory locations. An index vector is needed to pick up the desired elements. The Q8VGATHR function (64-bit) or the Q8VXTOV subroutine (32-bit), provided by the manufacturer, is used to do the transposing. As the array gets bigger, so does the index vector length, and an appreciable amount of overhead working space is needed. In the $64 \times 64 \times 64$ run with pencil size 32×16 , the index vector has 17,408 elements.

4.3 Computer Performance

The performance data based on a count of the number of operations per time step are presented in Table 4.1. The mesh size is given in column 2 (each node requires seven words of data storage). The pencil size is given in column 3; this, together with mesh size, determines the vector length shown in column 4. The computational precision is given in column 5, the CPU time in column 6, and the CPU computation rate in column 7. The I/O time per time step in seconds is meaningful only for

Table 4.1

Performance of CYBER 205 at CSU
(Two Pipes with 2M 64-Bit Word)

Run	Mesh Size (nodes)	Pencil Size (nodes)	Vector Length (in FFT)	Prec. (bits)	CPU Time per Step (Sec.)	MFLOPS	I/O Time per Step (sec.)	Memory (M Words)	Comments
1	8x8x8	8x8	192	64	0.014	23.5	-	0.02	in core
2	32x32x32	4x4	384	64	0.690	31.0	-	0.30	in core
3	32x32x32	32x32	3,072	64	0.399	53.6	-	0.69	in core
4	32x32x32	32x32	3,072	32	0.240	89.2	-	0.69	in core
5	64x64x64	16x16	3,072	64	3.378	59.6	56.6	2.70	paging
6	64x64x64	16x16	3,072	32	2.022	99.6	-	2.70	in core
7	64x64x64	32x16	4,608	32	1.980	101.7	-	3.47	in core
8	64x64x64	32x32	6,144	32	1.914	105.2	8.7	3.52	paging

runs with virtual memory paging. Explicit I/O would reduce I/O time considerably, but we did not use it.

Comparing Runs 3 and 4, and Runs 5 and 6 in Table 4.1, it is found that the CPU time for a 32-bit (half) precision run is 60% of that for the corresponding 64-bit (full) precision run. We kept track of the timing in the transpose part of the code and found an interesting fact. In full-precision runs, the transpose takes 15% of the CPU time; 85% of the CPU time is spent in floating point operations. In half-precision runs, due to the lack of a half-precision gather utility, the transpose takes the same time as in full-precision runs, while the floating-point operations require only half of the full-precision CPU time. Consequently, for the half-precision run, the transpose takes 25% of the total time.

Detailed timing from Run 8 shows that 51% of the CPU time is spent in the FFT subroutine, which contains 78% of the floating point operations. In other words, the FFT operates at 157.6 Mflops. The remaining 22% of the floating-point operations are executed at 95 Mflops, due mainly to shorter vector lengths and the occurrence of IF statements.

Table 4.2 shows the performance data obtained from a CYBER 205 with four vector pipelines. The computation rate of a four-pipe machine is twice as fast as that of a two-pipe machine. Note that Run 13 is only 1.7 times faster than Run 8. This is again due to the transpose taking the same amount of time on both machines.

In summary, the present code is fully vectorized to take maximum advantage of the capabilities of the CYBER 205 computer. It can handle up to $64 \times 64 \times 64$ mesh points in core while running at 100 Mflops on a two-pipe machine and 190 Mflops on a four-pipe machine. This computation rate is among the fastest that can be obtained from present supercomputers. To obtain it, the vector length must be long enough and half-precision computation must be used. The slowness of taking the transpose is the key factor in preventing one from getting better performance from the computer. The slow I/O transfer rate prevented us from using a $128 \times 128 \times 128$ mesh.

Table 4.2
Performance of CYBER 205 at CDC
(Four pipes with 4M 64-Bit Word)

Run	Mesh Size (nodes)	Pencil Size (nodes)	Vector Length (in FFT)	Prec. (bits)	CPU Time per Step (sec)	MFLOPS
13	64x64x64	32x32	6,144	32	1.116	180.4
14	64x64x64	64x32	9,216	32	1.088	185.1
15	64x64x64	64x64	12,288	32	1.051	191.6

4.4 Tests of the Code

Several tests were performed in order to qualify the code. Two important checks are described below:

A. Decay of Isotropic Turbulence

A $64 \times 64 \times 64$ run was performed with the mean strain rate tensor $\bar{U}_{1,j}$ set equal to zero. The three-dimensional energy spectrum was obtained by summing the energy in spherical shells of inner radius k and outer radius $k + \Delta k$, where k is the magnitude of the wavevector and Δk is the difference between the magnitudes of the two nearest neighbor wavenumbers. The initial energy spectrum was a top-hat spectrum. The flow evolved from the artificial initial spectrum to a realistic low Reynolds number spectrum as the simulation proceeded. As can be seen from Figure 4-3, the normal Reynolds stresses are slightly anisotropic at low wavenumbers and isotropic at high wavenumbers. This is due to the small number of modes at low wavenumbers. The 3-D dissipation spectrum $D(k)$ is defined as

$$D(k) = \frac{\mu}{\rho} k^2 E(k) \quad (4-1)$$

and its components $D_{\alpha\alpha}(k) = \frac{\mu}{\rho} k^2 E(k)$ are shown in Figure 4-4. The peak of the dissipation spectrum is located well inside the resolvable wavenumber range. This means that the dissipation scale of the flow is resolved.

The longitudinal and lateral one-dimensional spectra of the velocity field are shown in Figure 4-5. The one-dimensional spectrum of the velocity field in the k_1 direction is defined as

$$E_{1j}(k_1) = \iint \hat{u}_1'(\underline{k}) \hat{u}_j'^*(\underline{k}) dk_2 dk_3 \quad (4-2)$$

As shown, the spectra drop several orders of magnitude from low wavenumber to high wavenumber. This again demonstrates that the dissipation scales are well resolved. That $E_{22}(k_1) = E_{33}(k_1)$ shows that the velocity field is isotropic.

The two-point correlations and the one-dimensional spectra are Fourier transform pairs. They are defined as

$$Q_{ij}(\underline{\gamma}) = \frac{\langle u'_i(\underline{x}) u'_j(\underline{x} + \underline{\gamma}) \rangle}{\langle u'_i(\underline{x}) u'_j(\underline{x}) \rangle} \quad (4-3)$$

The close agreement between the two lateral correlations, $Q_{22}(x_1, 0, 0)$ and $Q_{33}(x_1, 0, 0)$, in Figure 4-6, shows that the flow is isotropic.

The time evolution of the turbulent kinetic energy, dissipation rate, integral length scales, and Taylor micro-scales are all in good agreement with both experiments (Comte-Bellot and Corrsin, 1971) and previous simulations (Shirani et al., 1981). These results gave confidence that the code is capable of simulating homogeneous isotropic turbulence. The particular flow field shown in this section was also used as the initial condition for the three-dimensional straining runs.

B. Plane Strain

The second test of the code is isotropic turbulence subjected to uniform two-dimensional strain; one pair of sides of the computational box moves inward at the same rate a second pair moves outward, while the third pair remains stationary. This type of flow has been investigated experimentally by Townsend (1954) and by Tucker and Reynolds (1968); and numerically by Rogallo (1981).

Three different strain rates and two different choices of strain axes were tested, namely: compression in the x_2 direction and stretch in the x_3 direction, and compression in the x_1 direction and stretch in the x_2 direction. The time development of the components of the turbulent kinetic energy and structure parameters of a typical run are shown in Figures 4-7 and 4-8. Figure 4-9 shows the time development of the components of the turbulent kinetic energy for two different choices of strain axes.

The simulated results are in good agreement with Rogallo's results. The differences can be attributed to different turbulence Reynolds numbers. The close agreement between two different choices of strain axes shown in Fig. 4-9 demonstrates that the computer code does not have any direction preference.

From the results of the two tests described in this section, we have confidence that the computer code is operating properly and ready to use to simulate compressed turbulence.

4.5 General Description of the Simulations

As described in Section 3.4, the simulation starts with an artificial initial field. Therefore, there is an initial period in which the simulated flow fields cannot be treated as true turbulence. During this period, an energy cascade is gradually developed; the spectra become realistic, and higher velocity statistics reach asymptotic values.

After the initial "relaxation" period, the velocity field is stored for later use as the initial condition for straining runs. During the straining process, the simulated flow fields can be regarded as true turbulent flows. Statistics are extracted from these flow fields. These will be discussed extensively in Chapters V and VI. This simulation is stopped when the scales of motion grow too large for the computational box.

Beyond this point, the flow fields do not accurately represent true turbulence, because the eddies are influenced by the imposed periodic boundary conditions. The region of validity of the simulation can also be monitored by examining the dissipation spectra. If the peak of the spectra moves beyond the resolvable wavenumber range or energy accumulates at high wavenumbers, the small scales are no longer being accurately resolved. When resolution of either the large or small scales is lost, the simulation is stopped.

In the next chapter we discuss the simulated results for isotropically compressed turbulence.

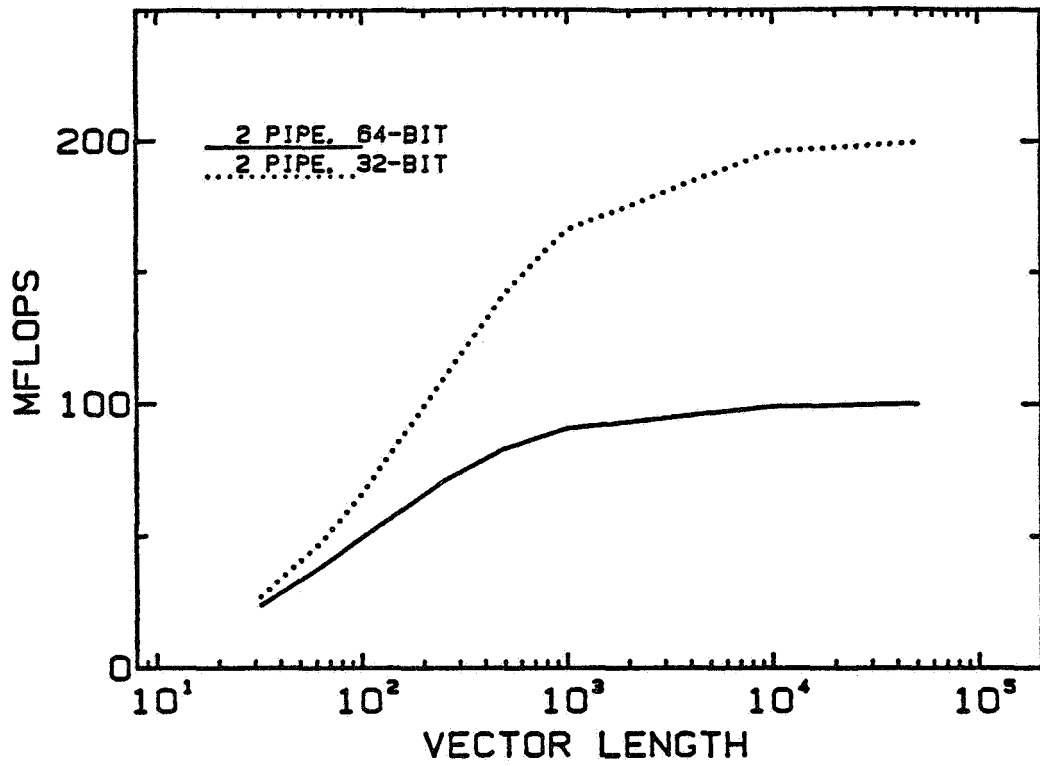


Fig. 4-1. The performance of a two-pipe CYBER 205 for addition and multiplication.

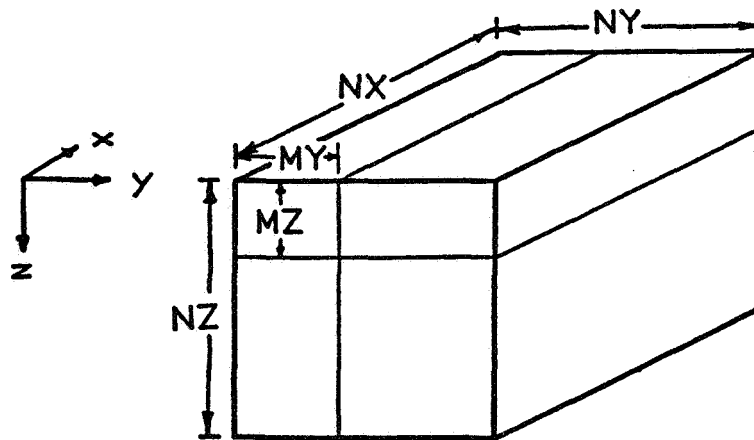


Fig. 4-2. Sketch of the computational box.

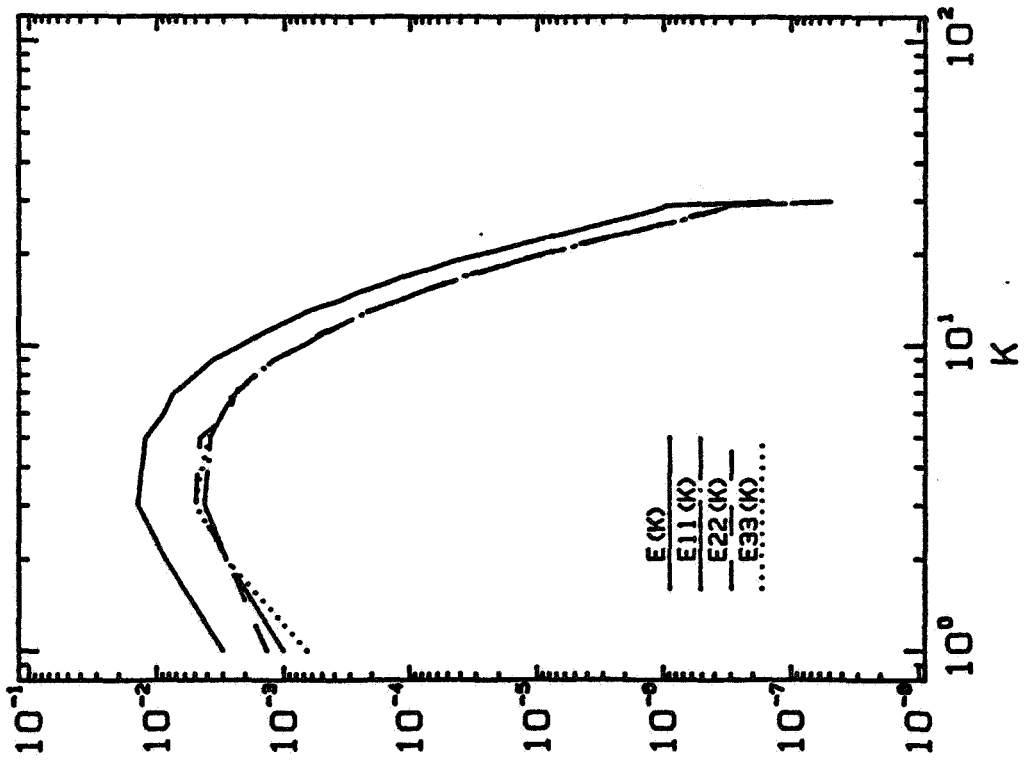


Fig. 4-3. Three-dimensional energy spectra for isotropic-decay turbulence.

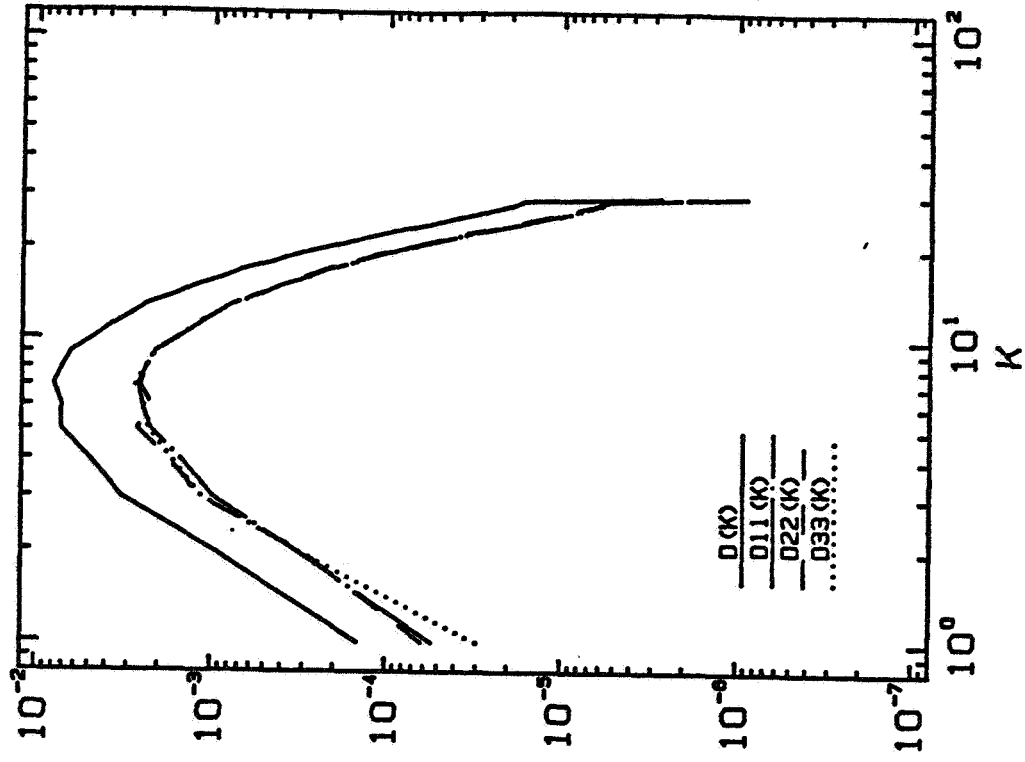


Fig. 4-4. Three-dimensional dissipation spectra for isotropic-decay turbulence.

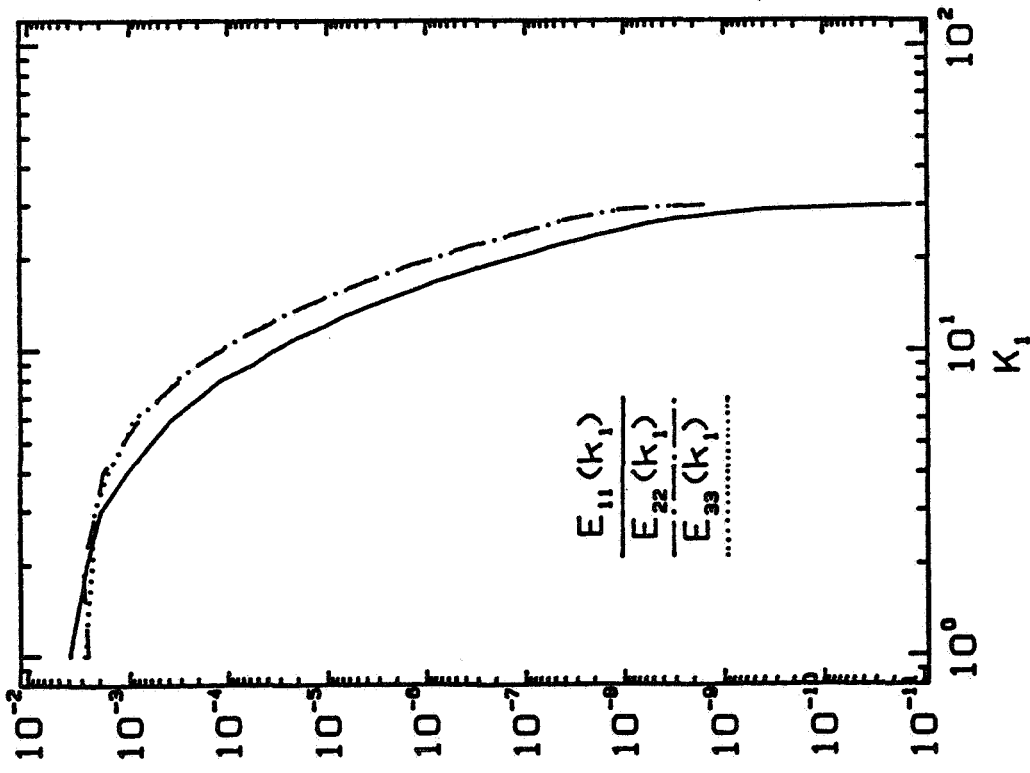


Fig. 4-5. One-dimensional energy spectra for isotropic-decay turbulence.

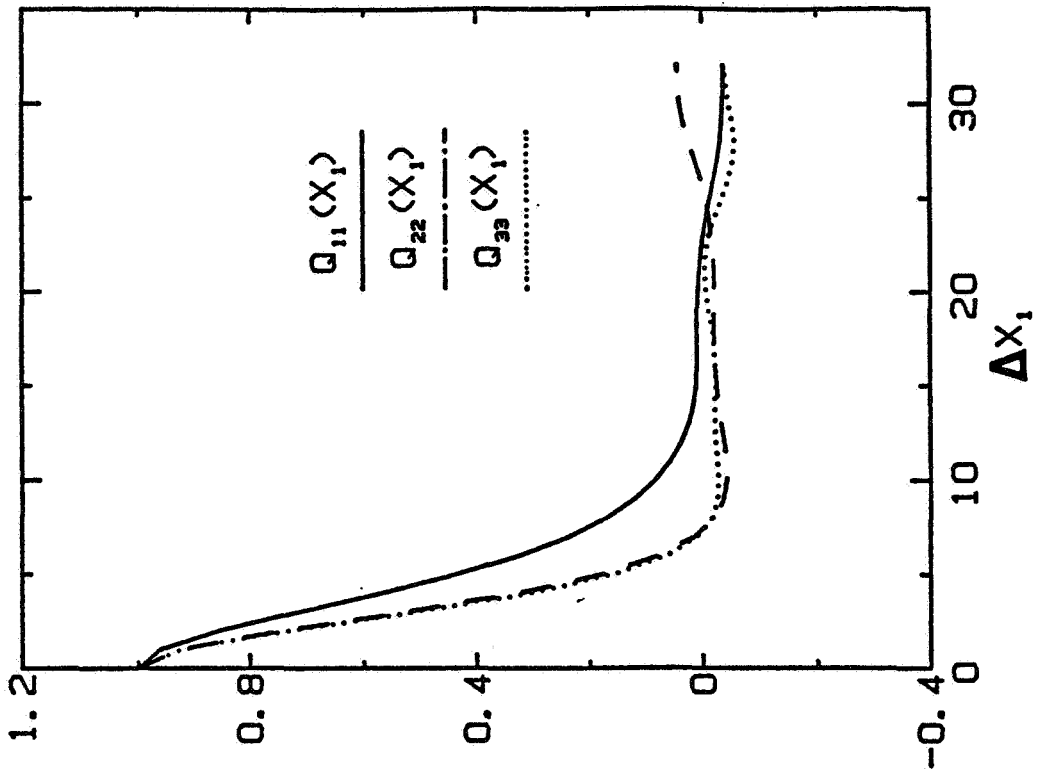


Fig. 4-6. Two-point velocity correlations for isotropic-decay turbulence.

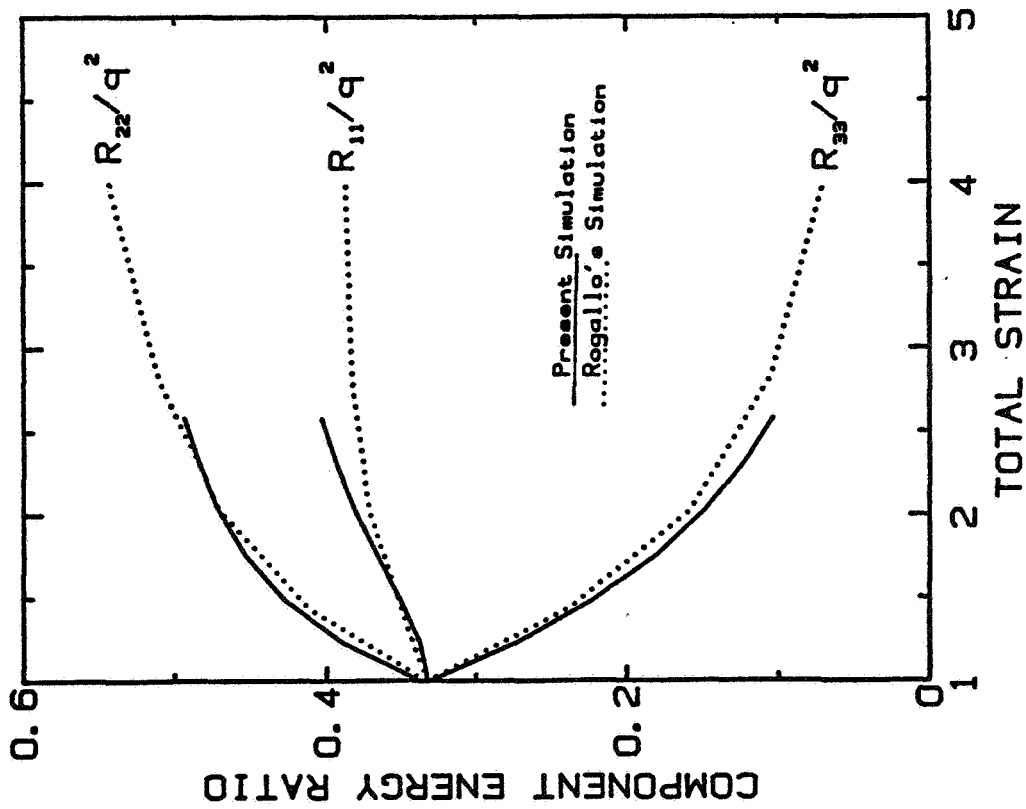


Fig. 4-7. The evolution of the component energy ratio for present and Rogallo's simulations.

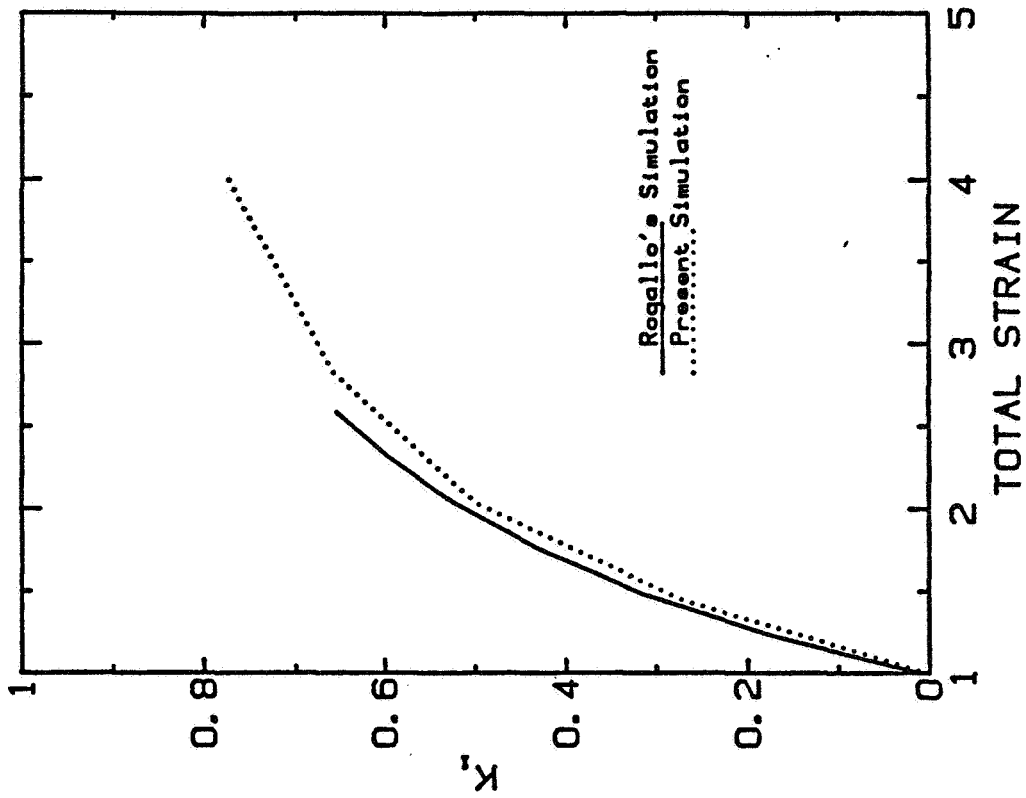


Fig. 4-8. The evolution of the structure parameter K_1 ($K_1 = R_{22}^{-1}R_{33}/R_{22}+R_{33}$) for present and Rogallo's simulations.

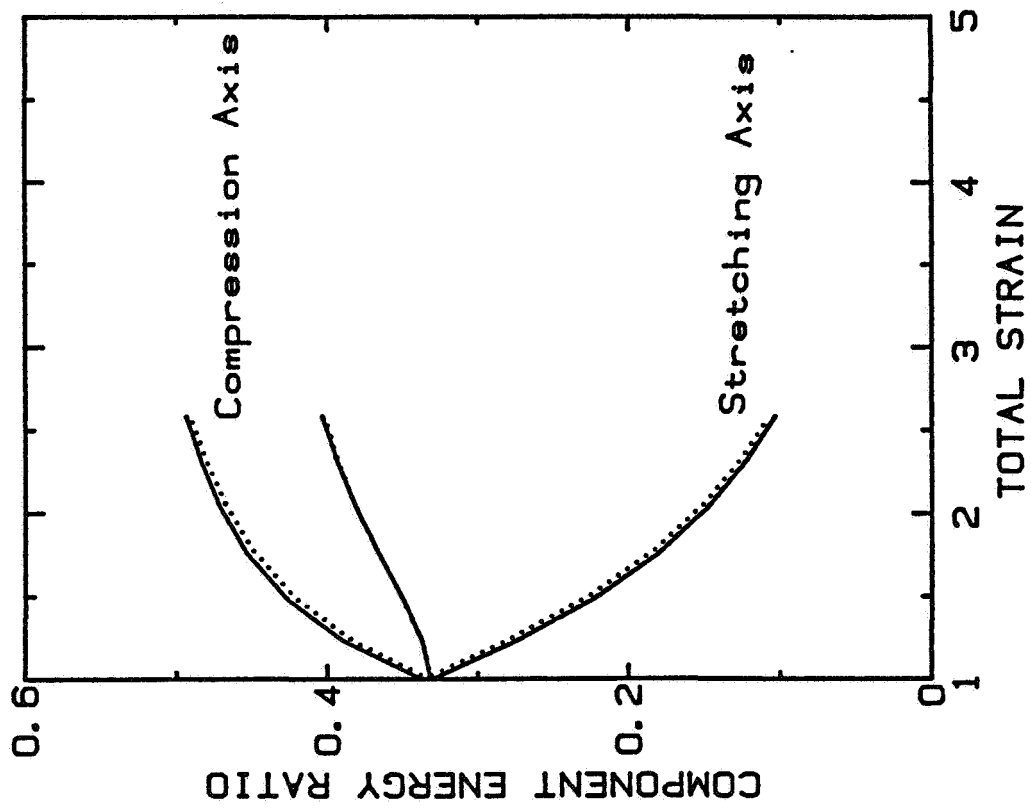


Fig. 4-9. The evolution of the component energy ratio for two different choices of strain axes.

Chapter V

HOMOGENEOUS ISOTROPIC TURBULENCE UNDERGOING ISOTROPIC COMPRESSION

In this chapter we present results for homogeneous isotropic turbulence undergoing isotropic compression. Numerical simulation results are compared with the predictions of rapid distortion theory. Results for four different compression rates are presented and discussed.

5.1 Rapid Distortion Theory

Rapid distortion theory (RDT) is a linear theory which describes the response of turbulence to a rapidly applied mean field. This theory was originated by Taylor (1935) and was extensively developed by Batchelor and Proudman (1954). It is valid only in the limit of extremely rapid distortions. A measure of rapidity is the ratio of the turbulence time scale (q^2/ϵ) to the mean flow time scale ($1/S$). RDT is valid when

$$Sq^2/\epsilon \gg 1$$

where S , q , and ϵ are the mean strain rate, turbulent velocity, and dissipation rate respectively.

When turbulence is distorted by a rapidly applied mean flow, i.e., the time scale of the applied strain is much shorter than the turbulence time scale, nonlinear turbulence interactions are unimportant, so the turbulence energy cascade cannot come to equilibrium with the applied strain. Also, the dissipation process is too slow to be important during the straining. Under these conditions the nonlinear interaction and viscous dissipation terms in the momentum equations may be neglected. Thus, RDT is a linear inviscid analysis of turbulence.

RDT analysis discussed in this section follows Reynolds' work (1984); we are grateful for permission to use his results. In RDT, it is more convenient to work with vorticity field than the velocity field. The vorticity is defined as

$$\omega_i \equiv \epsilon_{ijk} u_{k,j} \quad (5-1)$$

where ω_i , ϵ_{ijk} , and u_k are the vorticity vector, the completely antisymmetric tensor of rank three (the Levi-Civita symbol), and the velocity vector, respectively. We can relate the velocity field to the vorticity field by taking the curl of Eq. (5-1).

$$\epsilon_{pqi}\omega_{i,q} = u_{q,pq} - u_{p,qq} \quad (5-2)$$

The dynamic equations for the vorticity can be derived by taking the curl of the momentum equations:

$$\frac{\partial \omega_i}{\partial t} + u_j \omega_{i,j} = \omega_j S_{ij} - \omega_i S_{kk} + \frac{\mu}{\rho} \omega_{i,jj} \quad (5-3)$$

where $S_{ij} = \frac{1}{2}(u_{i,j} + u_{j,i})$ and ρ and μ are functions of time only. The first two terms on the right-hand side of Eq. (5-3) are the vortex stretching terms and the last term accounts for viscous diffusion.

All flow quantities in Eq. (5-3) can be decomposed into mean and fluctuating parts, that is

$$\omega_i = \bar{W}_i + w'_i \quad (5-4)$$

$$u_i = \bar{U}_i + u'_i$$

Substituting Eq.(5-4) into (5-3) and taking the ensemble average, we get

$$\frac{\partial \bar{W}_i}{\partial t} + \bar{U}_j \bar{W}_{i,j} = \bar{W}_j \bar{S}_{ij} - \bar{W}_i \bar{S}_{kk} + \nu \bar{W}_{i,jj} \quad (5-5)$$

The equations for the fluctuating vorticity (Eq. (5-6)) are obtained by subtracting Eq. (5-5) from (5-3). Note that, in deriving Eq. (5-6), we have assumed (1) that nonlinear interactions and viscous dissipation may be neglected, (2) that the mean strain is irrotational and (3) that the turbulence is homogeneous. These assumptions are applicable in the isotropic compression case.

$$\frac{\partial w'_i}{\partial t} + \bar{U}_j w'_{i,j} = w'_j \bar{S}_{ij} - w'_i \bar{S}_{kk} \quad (5-6)$$

Eq. (5-6) can be transformed to Lagrangian coordinates using the transformation of Chapter II. In the isotropic compression case, Eqs. (2-21) and (2-34) are used to reduce Eq. (5-6) to:

$$\frac{\partial w'_1}{\partial t} = -\frac{2V_p}{x_p(t)} w'_1 \quad (5-7)$$

where V_p is the compression speed and $x_p(t)$ is the box length at time t . The solution of Eq. (5-7) is

$$w'_1(\underline{x}', t) = w'_1(\underline{x}', 0) \left(\frac{x_p(t)}{L_0} \right)^{-2} \quad (5-8)$$

where L_0 is the initial box length, and $x_p(t)/L_0$ is the instantaneous total strain ratio.

The turbulent velocity field is found from the turbulent vorticity field via Eq.(5-2).

$$u'_{i, kk} = -\epsilon_{ikj} w'_{j, k} \quad (5-9)$$

where continuity constraint $u'_{1,1} = 0$ is applied. Transforming Eq.(5-9) to Lagrangian coordinates, we get

$$\frac{L_0^2}{x_p^2} \left(\frac{\partial^2}{\partial x_1'^2} + \frac{\partial^2}{\partial x_2'^2} + \frac{\partial^2}{\partial x_3'^2} \right) \begin{Bmatrix} u'_1 \\ u'_2 \\ u'_3 \end{Bmatrix} = \frac{L_0}{x_p} \begin{Bmatrix} \frac{\partial w'_2}{\partial x_3'} - \frac{\partial w'_3}{\partial x_2'} \\ \frac{\partial w'_3}{\partial x_1'} - \frac{\partial w'_1}{\partial x_3'} \\ \frac{\partial w'_1}{\partial x_2'} - \frac{\partial w'_2}{\partial x_1'} \end{Bmatrix} \quad (5-10)$$

Equations (5-10) are solved by using Fourier transforms. Taking the Fourier transform of Eq.(5-10), we get,

$$\begin{pmatrix} \hat{u}'_1(\underline{k}', t) \\ \hat{u}'_2(\underline{k}', t) \\ \hat{u}'_3(\underline{k}', t) \end{pmatrix} = \frac{-i(x_p/L_0)}{(k_1'^2 + k_2'^2 + k_3'^2)} \begin{pmatrix} k_3' \hat{w}'_2(\underline{k}', t) - k_2' \hat{w}'_3(\underline{k}', t) \\ k_1' \hat{w}'_3(\underline{k}', t) - k_3' \hat{w}'_1(\underline{k}', t) \\ k_2' \hat{w}'_1(\underline{k}', t) - k_1' \hat{w}'_2(\underline{k}', t) \end{pmatrix} \quad (5-11)$$

where \underline{k}' is the Fourier wave vector corresponding to \underline{x}' . We define $E_{ij}(\underline{k}', t)$ and $\phi_{ij}(\underline{k}', t)$ as the spectra of $\overline{u'_i u'_j}$ and $\overline{w'_i w'_j}$, respectively.

$$E_{ij}(\underline{k}', t) \equiv \overline{\hat{u}'_i(\underline{k}', t) \hat{u}'_j{}^*(\underline{k}', t)} \quad (5-12)$$

$$\phi_{ij}(\underline{k}', t) \equiv \overline{\hat{w}'_i(\underline{k}', t) \hat{w}'_j{}^*(\underline{k}', t)} \quad (5-13)$$

where * denotes the complex conjugate. From Eqs.(5-11), (5-12), and (5-13), $E_{11}(\underline{k}', t)$ can be expressed as

$$E_{11}(\underline{k}', t) = \frac{(\pi_p/L_o)^2}{(k'_1{}^2 + k'_2{}^2 + k'_3{}^2)^2} (k'_3{}^2 \phi_{22} + k'_2{}^2 \phi_{33} - 2k'_2 k'_3 \phi_{23}) \quad (5-14)$$

and from Eqs.(5-8) and (5-13) $\phi_{ij}(\underline{k}', t)$ can be expressed as

$$\phi_{ij}(\underline{k}', t) = \left(\frac{\pi_p}{L_o}\right)^{-4} \phi_{ij}(\underline{k}', 0) \quad (5-15)$$

$\phi_{22}(\underline{k}', 0)$ is obtained from Eqs.(5-13), and (5-12)

$$\phi_{22}(\underline{k}', 0) = k'_3{}^2 E_{11}(\underline{k}', 0) + k'_1{}^2 E_{33}(\underline{k}', 0) - 2k'_1 k'_3 E_{13}(\underline{k}', 0) \quad (5-16)$$

If the initial turbulence is isotropic, then

$$E_{ij}(\underline{k}', 0) = -\frac{E(k', 0)}{4\pi k'^2} \left(\frac{k'_i k'_j}{k'^2} - \delta_{ij} \right) \quad (5-17)$$

Combining Eqs.(5-14), (5-15), (5-16), and (5-17) we obtain

$$E_{11}(\underline{k}', t) = \frac{E(k', 0)}{4\pi k'^2} \left(\frac{\pi_p(t)}{L_o} \right)^{-2} \frac{\left[k'_3{}^2 (k'^2 - k'_2{}^2) + k'_2{}^2 (k'^2 - k'_3{}^2) + 2k'_2{}^2 k'_3{}^2 \right]}{(k'_1{}^2 + k'_2{}^2 + k'_3{}^2)^2} \quad (5-18)$$

The spectra of E_{22} and E_{33} can be found by permuting the indices.

Equation (5-18) is the most important result of RDT analysis for isotropically compressed turbulence. It provides the spectrum of the turbulence in terms of the initial spectrum and the instantaneous total strain ratio. Any other quantity dependent upon the spectrum can be

deduced from Eq.(5-18). For example, the evolution of the three-dimensional dissipation spectrum $D(k',t)$ is derived as follows:

$D(k',t)$ is defined as in Equation (4-1).

$$D(k',t) = \frac{\mu(t)}{\rho(t)} k'^2(t) E(k',t)$$

Substituting Eqs. (2-21), (5-19) and $k'(t) = \left(\frac{x_p}{L_o}\right)^{-1} k'(0)$ into Eq. (4-1), we get

$$\begin{aligned} D(k',t) &= \left(\frac{x_p}{L_o}\right)^{-0.9-(-3)+(-2)+(-2)} \frac{\mu(0)}{\rho(0)} k'^2(0) E(k',0) \\ &= \left(\frac{x_p}{L_o}\right)^{-1.9} D(k',0) \end{aligned}$$

Other important results from RDT analysis for isotropic compressed turbulence are summarized below:

$$\text{Three-dimensional energy spectrum: } E(k',t) = \left(\frac{x_p}{L_o}\right)^{-2} E(k',0)$$

$$\text{Three-dimensional dissipation spectrum: } D(k',t) = \left(\frac{x_p}{L_o}\right)^{-1.9} D(k',0)$$

$$\text{One-dimensional energy spectrum: } E_{jj}(k'_i,t) = \left(\frac{x_p}{L_o}\right)^{-2} E_{jj}(k'_i,0)$$

$$\text{Two-point auto-correlation: } Q_{ij}(x'_m,t) = Q_{ij}(x'_m,0)$$

$$\text{Turbulent kinetic energy: } k(t) = \left(\frac{x_p}{L_o}\right)^{-2} k(0) \quad (5-19)$$

$$\text{Dissipation rate: } \varepsilon(t) = \left(\frac{x_p}{L_o}\right)^{-1.9} \varepsilon(0)$$

$$\text{Kolmogorov length scale: } \eta(t) = \left(\frac{x_p}{L_o}\right)^{2.05} \eta(0)$$

$$\text{Taylor microscales: } \lambda_{ii}(t) = \frac{x_p}{L_o} \lambda_{ii}(0)$$

Integral length scales: $L_{ij,m}(t) = \frac{x_p}{L_0} L_{ij,m}(0)$

Turbulent Reynolds number: $Re_\ell(t) = \left(\frac{x_p}{L_0}\right)^{-4.2} Re_\ell(0)$

5.2 Simulation Results

Four simulations of isotropically compressed turbulence were performed. All started with the same isotropic turbulence initial condition, but the compression rate differed in each case. Some details of the isotropic turbulence initial condition are shown in Table 5.1. Three independent dimensionless parameters can be formed from the time t , the strain rate $S(t)$, and the turbulence velocity and time scales, q and q^2/ϵ , respectively. These are taken to be

$$\exp\left(\int_0^t S(t') dt'\right), \quad Sq^2/\epsilon, \quad q^4/\epsilon v,$$

which are the total strain ratio, the ratio of the turbulence and strain time scales, and a turbulence Reynolds number, respectively. Since homogeneous turbulence is a time-developing flow, these dimensionless parameters change during a simulation. Table 5.2 shows the range of these parameters covered in each simulation.

Run SQF had the fastest compression rate among these four cases. The ratio of turbulence and strain time scales is sufficiently high that the rapid distortion limit is applicable. The results of run SQF agree with RDT analysis (Eq.(5-19)); this is demonstrated below.

A. Description of the Rapid Distortion Run

In this section, we present results obtained from the rapid distortion run (SQF). The mean strain-rate tensor is

$$S_{ij} = \begin{pmatrix} S(t) & 0 & 0 \\ 0 & S(t) & 0 \\ 0 & 0 & S(t) \end{pmatrix}$$

where $S(t) = v_p/X_p(t)$. The results are shown in Figures 5-1 through 5-11 and discussed below.

Table 5.1

Some Details of the Initial Condition
of the Isotropically Compressed Turbulence Simulations
(consistent units)

Turbulence Velocity q	0.2856
Dissipation Rate ϵ	0.0324
Integral Length Scale $L_{11,1}$	0.9791
Taylor Microscale λ_{11}	0.3444
Kolmogorov Length Scale η	0.07454
Kinematic Viscosity ν	0.01

Table 5.2
Description of Simulations of Isotropically Compressed Turbulence

Run ID	$ S q^2/\epsilon$ (Initial)	$ S q^2/\epsilon$ (Final)	$q^4/\epsilon\nu$ (Initial)	$q^4/\epsilon\nu$ (Final)	Total Strain Ratio (Final)
SQF	47.04	88.54	20.56	224.58	0.552
SQG	2.52	4.64	20.56	123.95	0.625
SQH	0.50	1.86	20.56	163.85	0.511
SQI	0.10	1.11	20.56	71.86	0.523

Figures 5-1 through 5-4 show the evolution of the lateral and longitudinal one-dimensional spectra of the velocity field; these are defined by Eq.(4-2). The initial lateral and longitudinal spectra are shown in Figures 5-1 and 5-3, respectively. The spectra obtained from the simulation and RDT analysis when the total strain ratio is 0.552, are shown in Figures 5-2 and 5-4, respectively. The agreement is excellent.

Figures 5-5 and 5-6 show the longitudinal and lateral two-point auto-correlations at the initial time, and when the total strain ratio is 0.779 and 0.552. They are given in the Lagrangian coordinates. These figures show that, in accord with RDT analysis (Eq.(5-19)), the two-point auto-correlation in Lagrangian coordinates does not change during the simulation.

Figures 5-7 and 5-8 show the time evolution of twice the turbulent kinetic energy (q^2) and the dissipation rate (ϵ) from the simulation and RDT analysis. Again, the agreement is excellent.

The time evolution of the integral length scale, Taylor microscale, and Kolmogorov length scale from the simulation and RDT analysis are shown in Figs. 5-9, 5-10, and 5-11. The integral length scale, which is the integral of the two-point velocity auto-correlation, shrinks linearly with time in Cartesian coordinates. So does the Taylor microscale. However, the Kolmogorov length scale decreases much faster than the integral length scale. This is due to the rapid decay of the kinematic viscosity, which is, in turn, due to the increasing density and temperature during compression. This results in the small length scale decreasing very rapidly during the compression and is important in understanding some of the results presented later.

In summary, the agreement between the results of RDT analysis and computer run SQF is excellent. This demonstrates that run SQF indeed is a simulation of rapid distortion and, taken together with the results of the isotropic decay run, that the code is performing correctly.

B. Summary of Isotropic Compression Simulations

Important data from all four isotropic compression simulations are compiled in Table 5.2 and discussed in this section. These simulations cover a wide range of initial values of $|S|q^2/\epsilon$, from 0.1 to 47.04. As shown above, the fastest compression simulation agrees with rapid distortion analysis. On the other hand, for extremely slow compression ($|S|q^2/\epsilon \rightarrow 0$), the effect of strain becomes negligible and the flow behaves like the isotropic turbulence decay of Chapter IV.

In the region between these two extremes, there are no known analytical solutions. The effect of $|S|q^2/\epsilon$ on the various turbulence statistics in this region is discussed below. During the compression stroke of an internal combustion engine, the value of $|S|q^2/\epsilon$ is in the range 0.05-0.5. So, runs SQH and SQI are in a range applicable to engines.

Figures 5-12 and 5-13 show the behavior of the Reynolds number and time scale ratio as functions of the total strain, which is an appropriate nondimensional time for this flow, for the four simulations. The four simulations have the same initial condition shown in Table 5.1 but different compression speeds. Both the Reynolds number and time scale ratio increase with time. For cases with small initial $|S|q^2/\epsilon$, the rate of increase of the Reynolds number is less than for cases with larger initial time scale ratio. As can be seen from Fig. 5-13, a wide range of $|S|q^2/\epsilon$ has been covered by these four simulations.

Figure 5-14 shows the three-dimensional energy spectrum at total strain ratio 0.785 in run SQH. The 3-D energy spectrum evolves as the simulation proceeds. No inertial subrange (a region of the spectrum with slope $-5/3$) appears in the 3-D energy spectrum because the Reynolds number is low. The flow field remains isotropic throughout the simulation. The corresponding spectrum from the rapid distortion simulation is plotted for comparison. The difference between these two spectra can be attributed to the effects of viscous dissipation and nonlinear interactions.

Three-dimensional dissipation spectra for runs SQH and SQF at total strain ratio 0.785 are shown in Fig. 5-15. The peaks of the spectra are

located well inside the resolvable wavenumber range. This means that the dissipation scale of the flow is resolved. The difference between these two spectra can be attributed to the fact that run SQH is far from rapid distortion limit.

The lateral and longitudinal two-point correlations of runs SQH and SQF at total strain ratio 0.785 are shown in Lagrangian coordinates, in Figs. 5-16 and 5-17. As can be seen, curves from run SQH are fatter than those from the rapid distortion simulation (run SQF). Consequently, the integral scales from this simulation are bigger than those from the rapid distortion simulation. In other words, nonlinear and viscous effects cause the integral scales to decrease less rapidly than in the rapid distortion case.

Figures 5-18 and 5-19 show the history of the turbulent kinetic energy and its dissipation rate. When the compression rate is large, as in runs SQF and SQG, the flow is immediately affected by the mean strain and both quantities increase throughout the simulation. If the initial value of $|S|q^2/\epsilon$ is 0.1 or less, the mean strain is not strong enough to immediately alter the structure of the flow and the flow retains the character of decaying isotropic turbulence during the initial period. After the strain has been applied for a longer period, the flow gradually reflects the effect of mean strain. There is a transition region in which the decay and strain effects are approximately balanced. In all cases, when the strain has been applied for a long enough period, both the turbulent kinetic energy and its dissipation rate increase.

Figures 5-20 through 5-22 show the evolution of integral length scale, Taylor microscale, and Kolmogorov length scale, respectively. These length scales all behave in roughly the same way. If the compression is fast enough, the length scale immediately begins to decrease; if the mean strain is weaker, the length scale may grow initially as in the case of decaying turbulence. In the latter cases, after the strain has been applied for a while, the length scales start decreasing. Note that the Kolmogorov length scale decreases most rapidly. The increasing density is responsible for the dramatic decrease of the kinematic viscosity. In most cases, the simulations had to be stopped because the small scales could no longer be resolved.

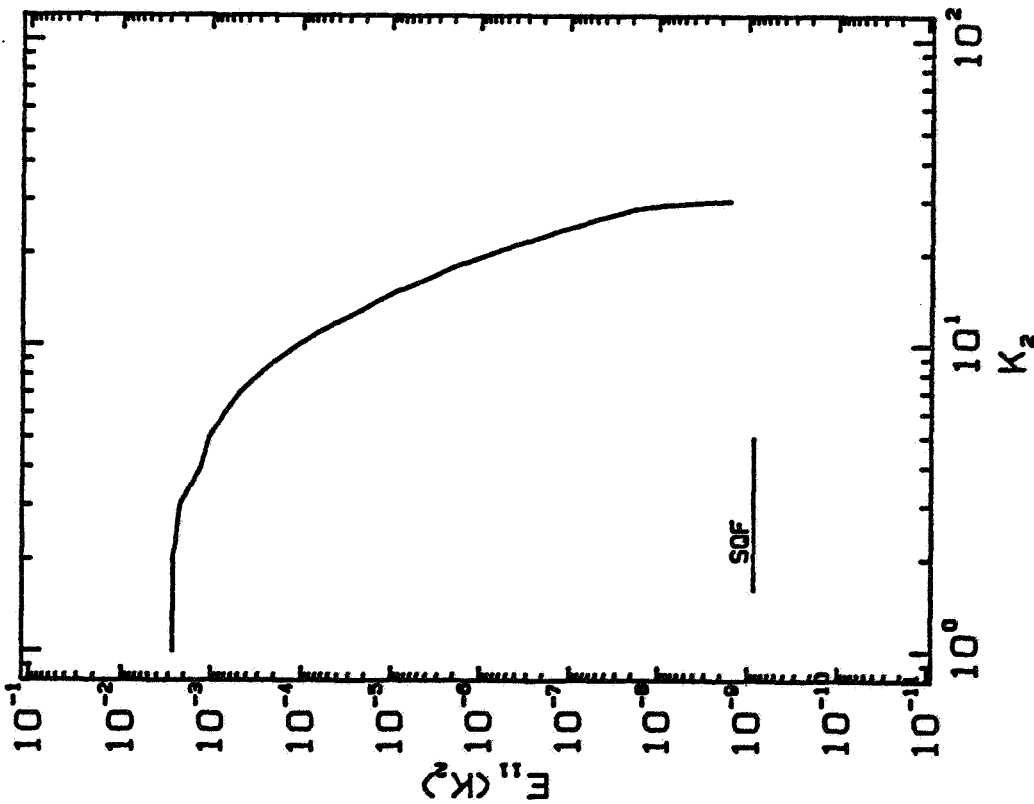


Fig. 5-1. The initial lateral one-dimensional energy spectrum of run SQF.

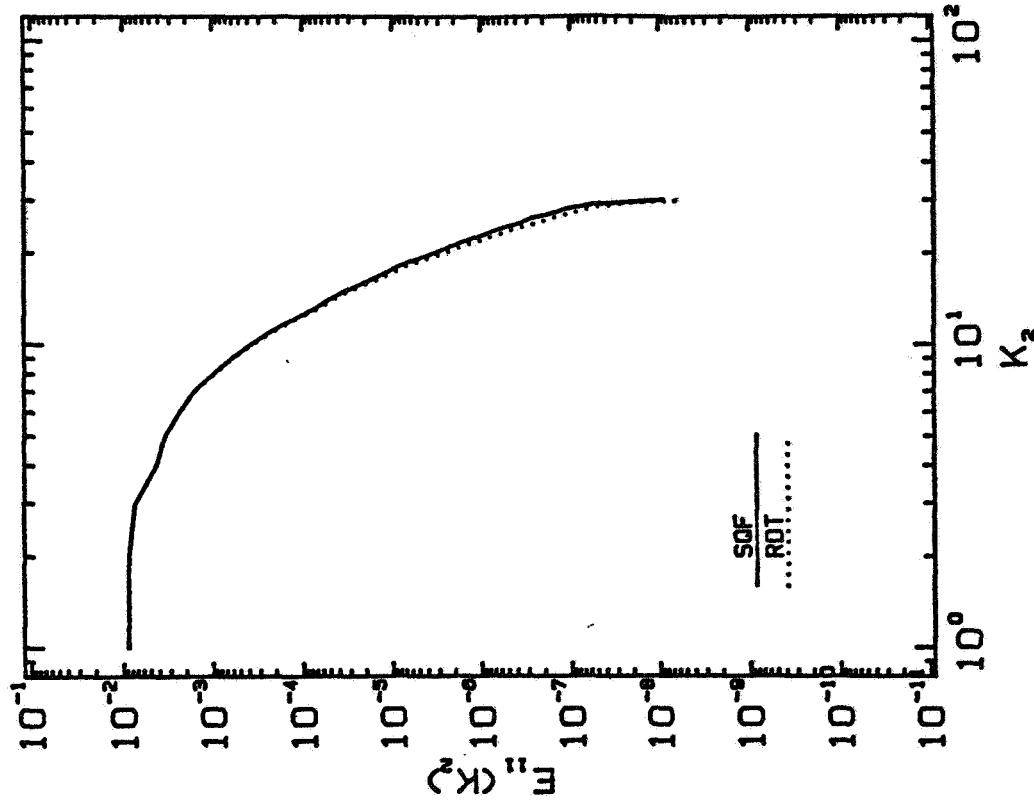


Fig. 5-2. The lateral one-dimensional energy spectra of run SQF and RDT analysis at total strain 0.552.

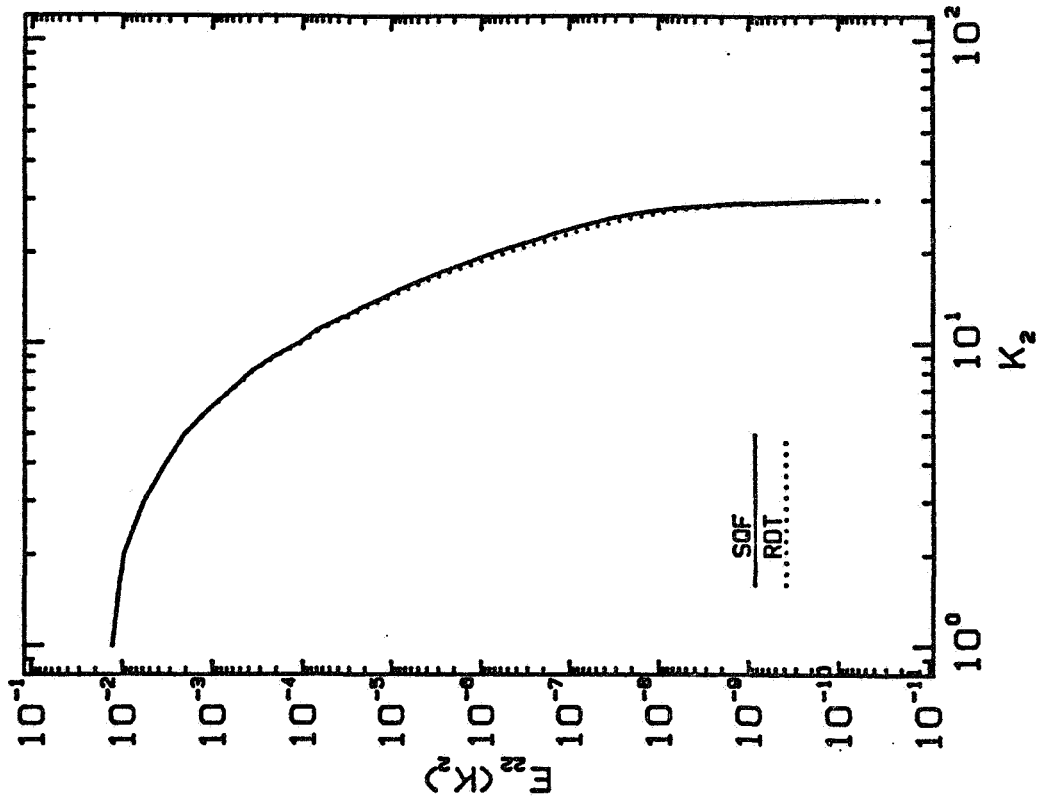


Fig. 5-4. The longitudinal one-dimensional energy spectra of run SQF and RDT analysis at total strain 0.552.

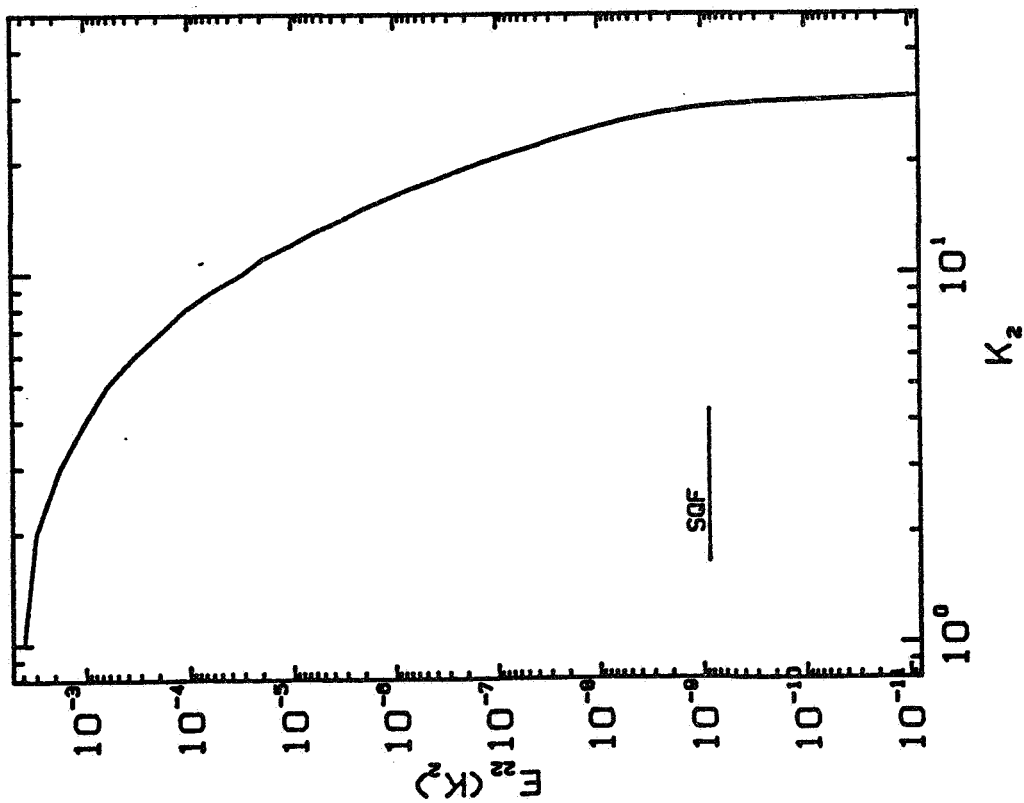


Fig. 5-3. The initial longitudinal one-dimensional energy spectrum of run SQF.

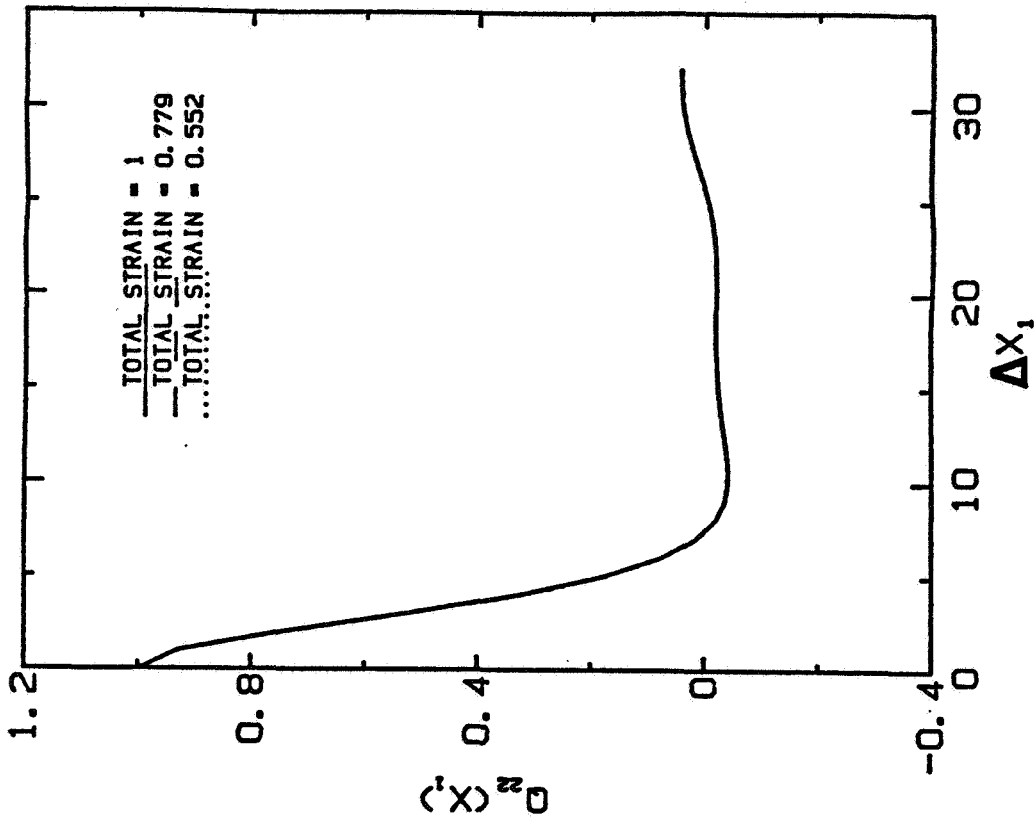


Fig. 5-6. The lateral two-point velocity correlations of run SQF at total strain 1, 0.779, and 0.552.

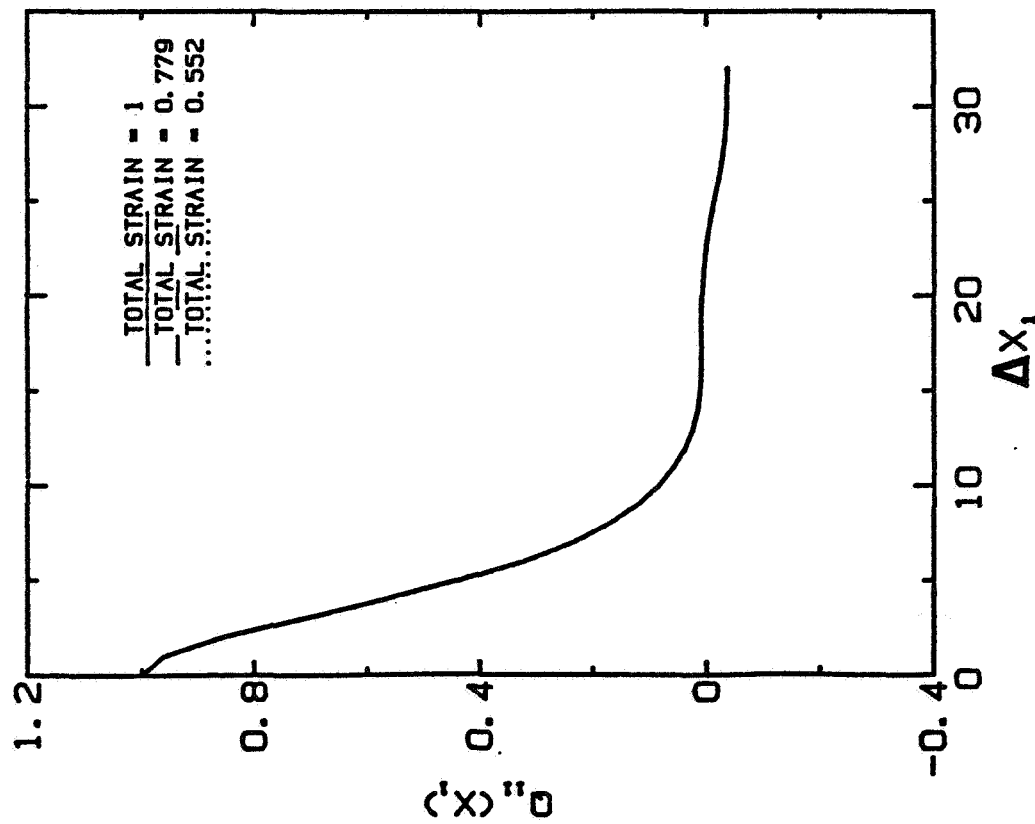


Fig. 5-5. The longitudinal two-point velocity correlations of run SQF at total strain 1, 0.779, and 0.552.

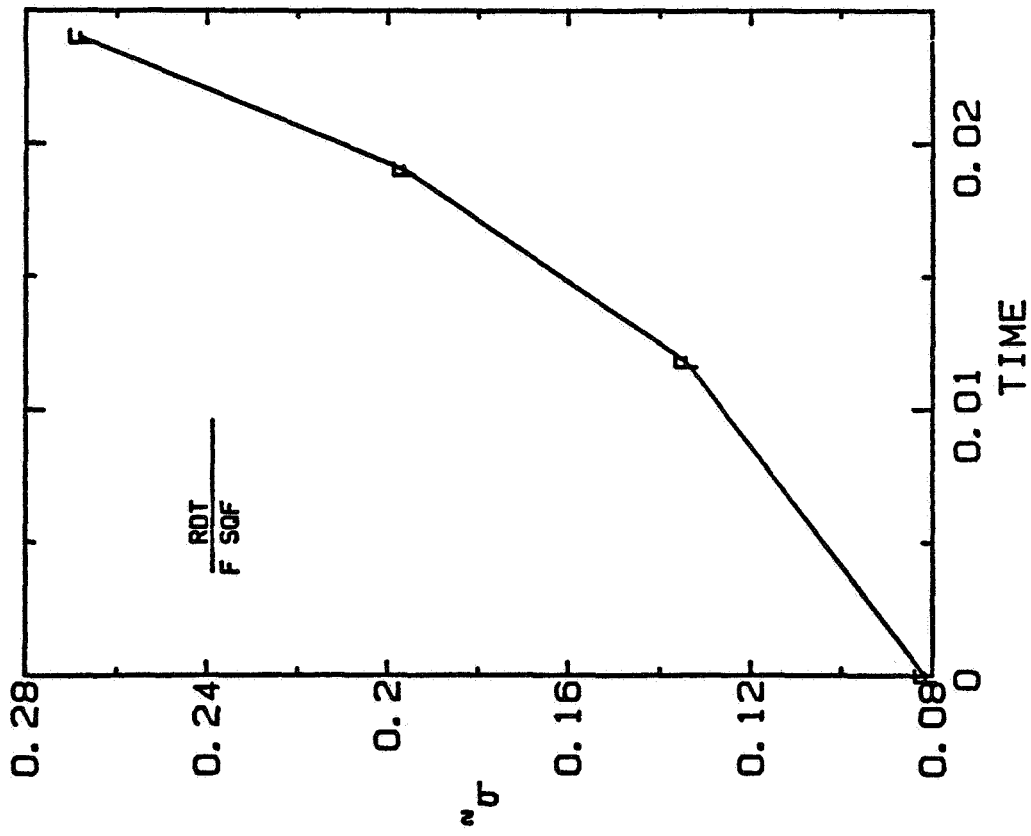


Fig. 5-7. The evolution of twice the turbulent kinetic energy of run SQF and RDT analysis.

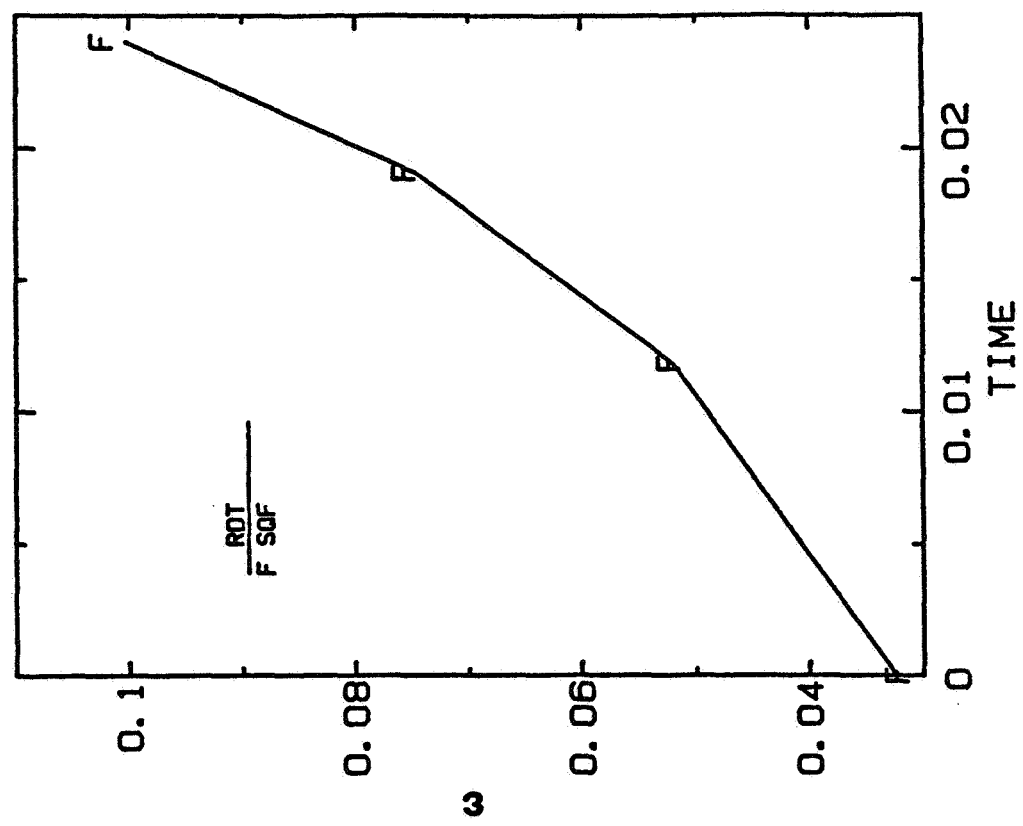


Fig. 5-8. The evolution of the dissipation rate of run SQF and RDT analysis.

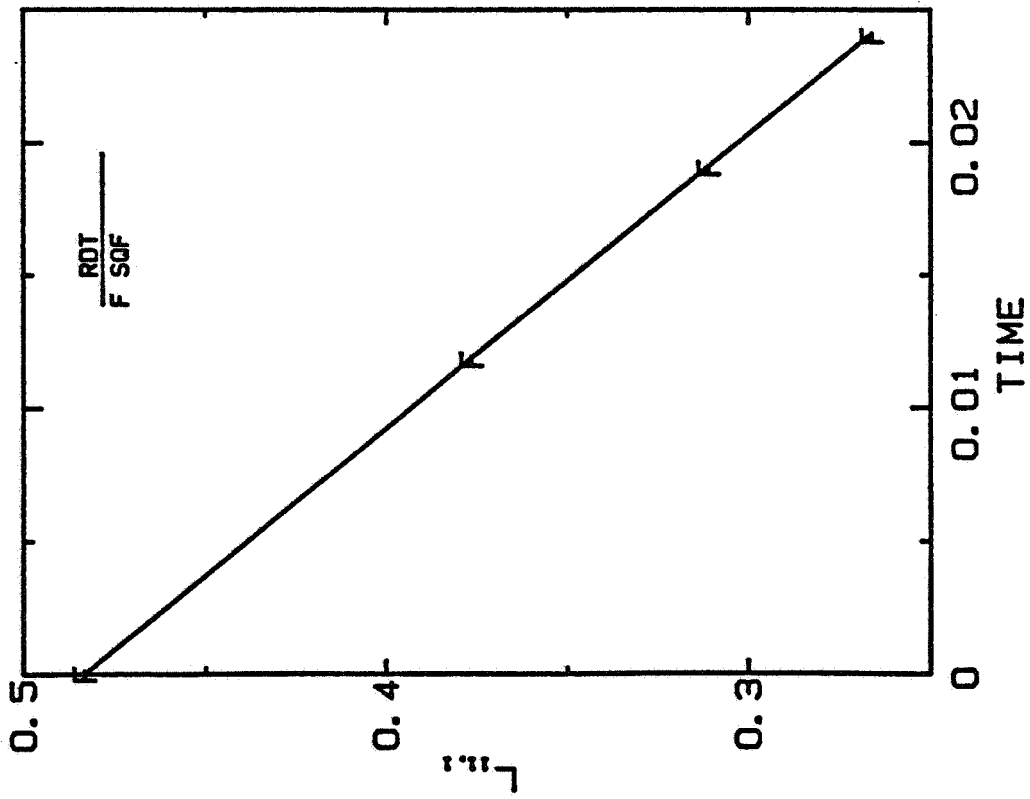


Fig. 5-9. The evolution of a longitudinal integral length scale of run SQF and RDT analysis.

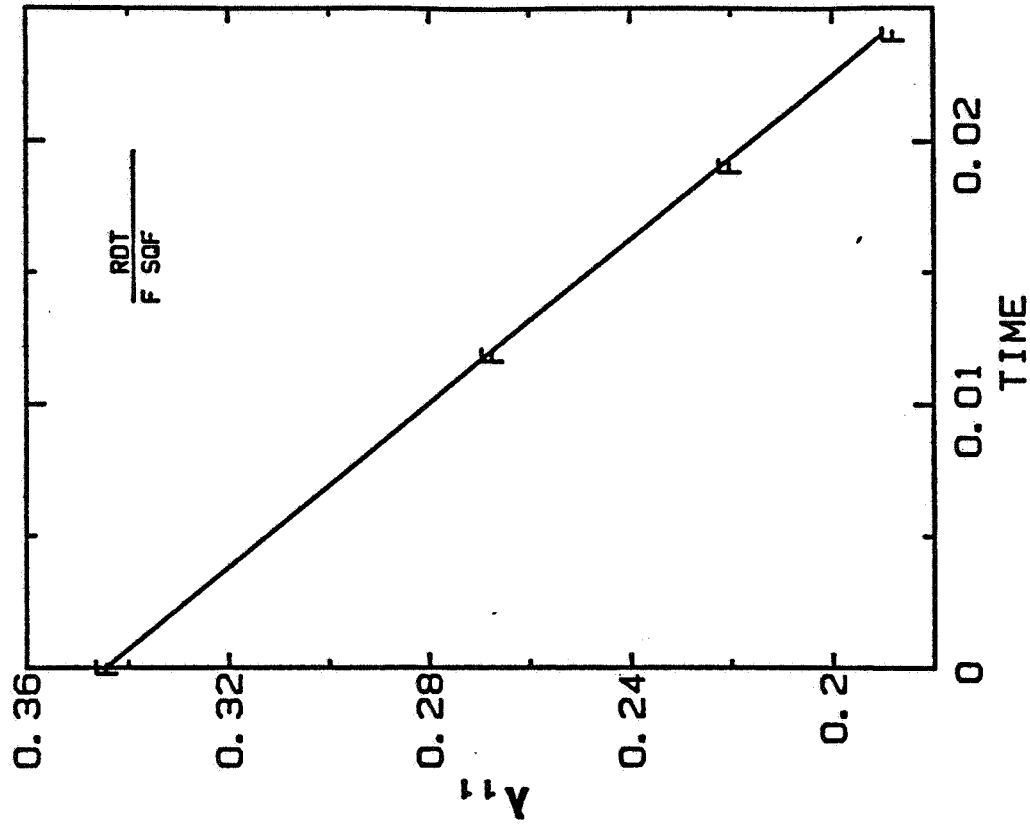


Fig. 5-10. The evolution of a Taylor microscale of run SQF and RDT analysis.

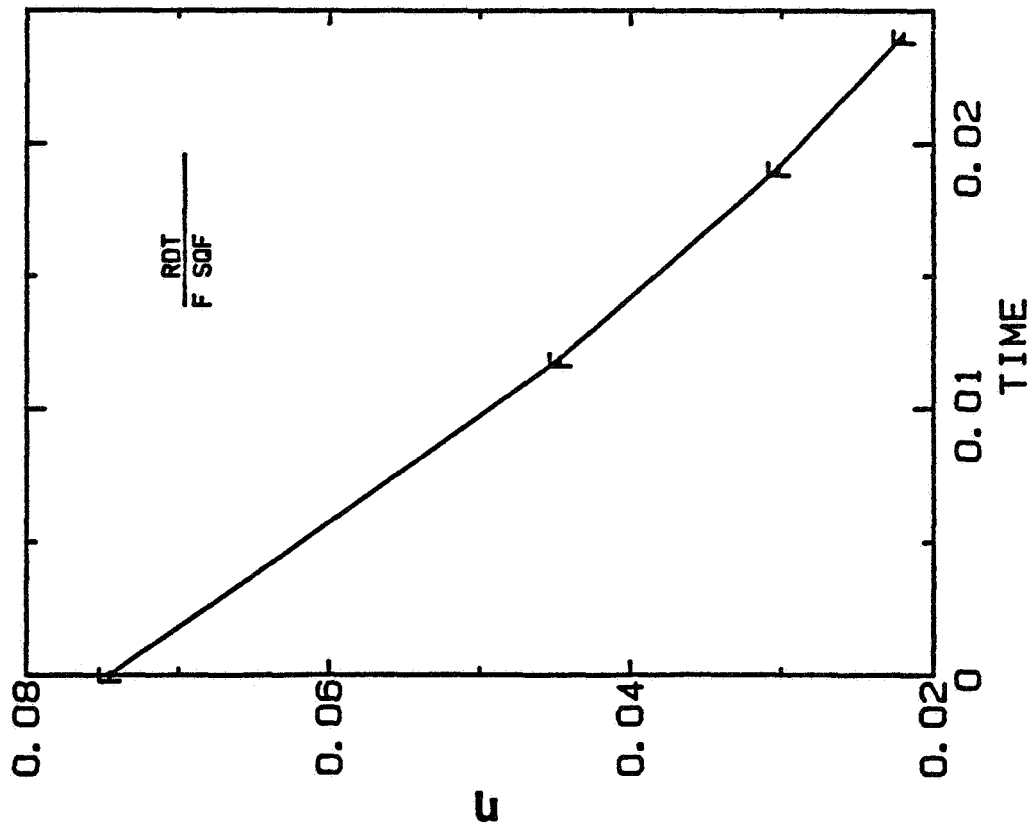


Fig. 5-11. The evolution of the Kolmogorov length scale of run SQF and RDT analysis.

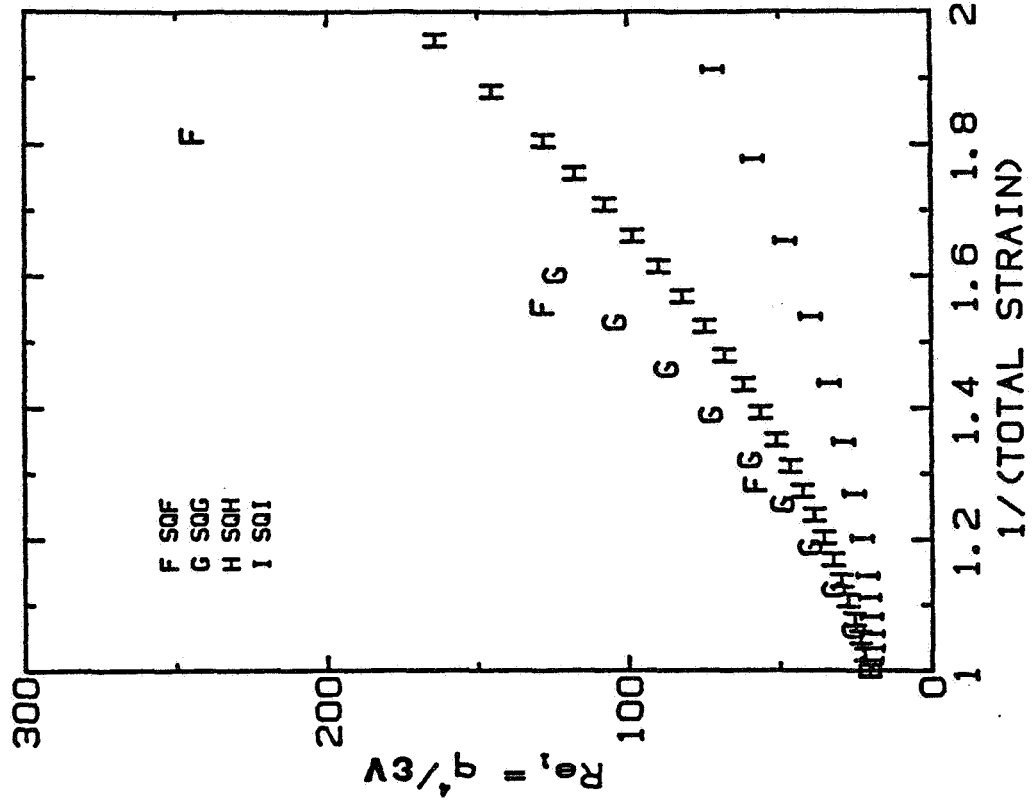


Fig. 5-12. The evolution of the turbulent Reynolds number for four isotropic compression simulations.

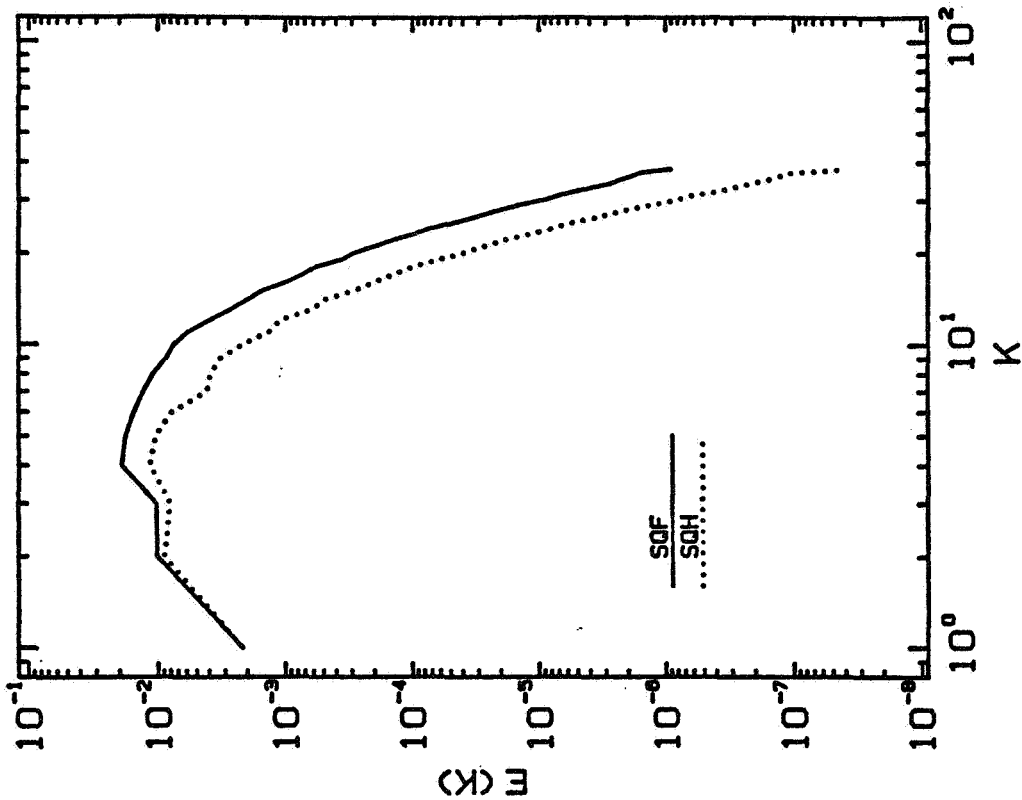


Fig. 5-14. The three-dimensional energy spectra of runs SQF and SQH at total strain 0.785.

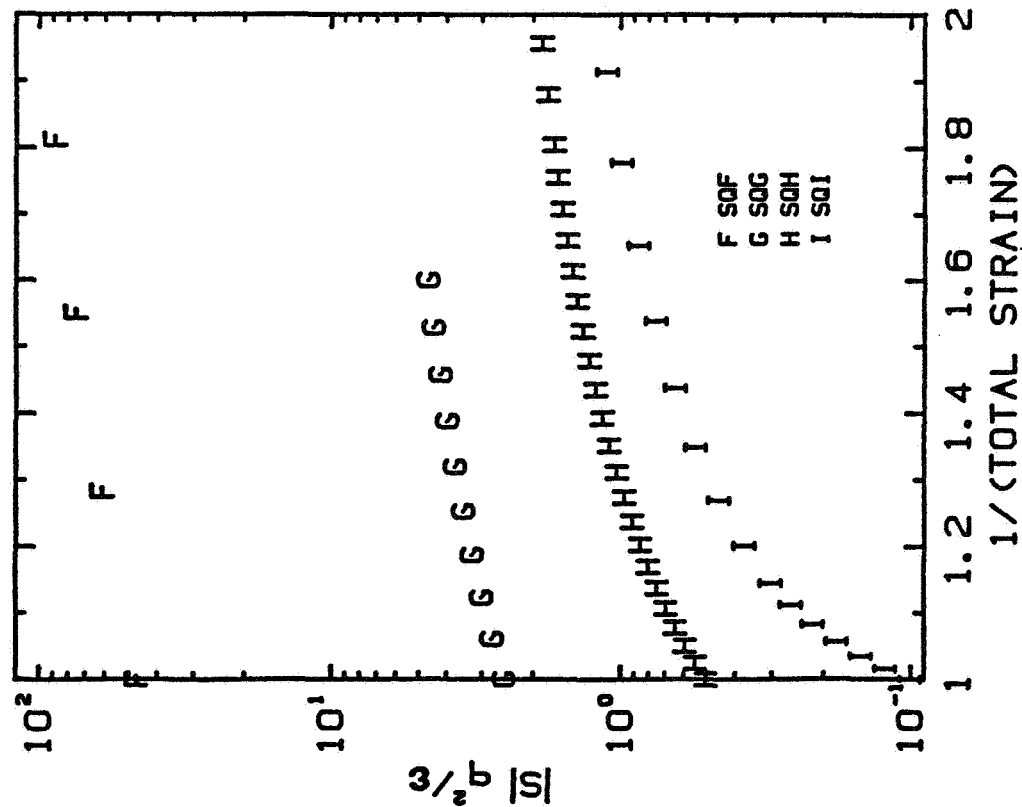


Fig. 5-13. The range of $|S|q^2/\epsilon$ covered in four isotropic compression simulations.

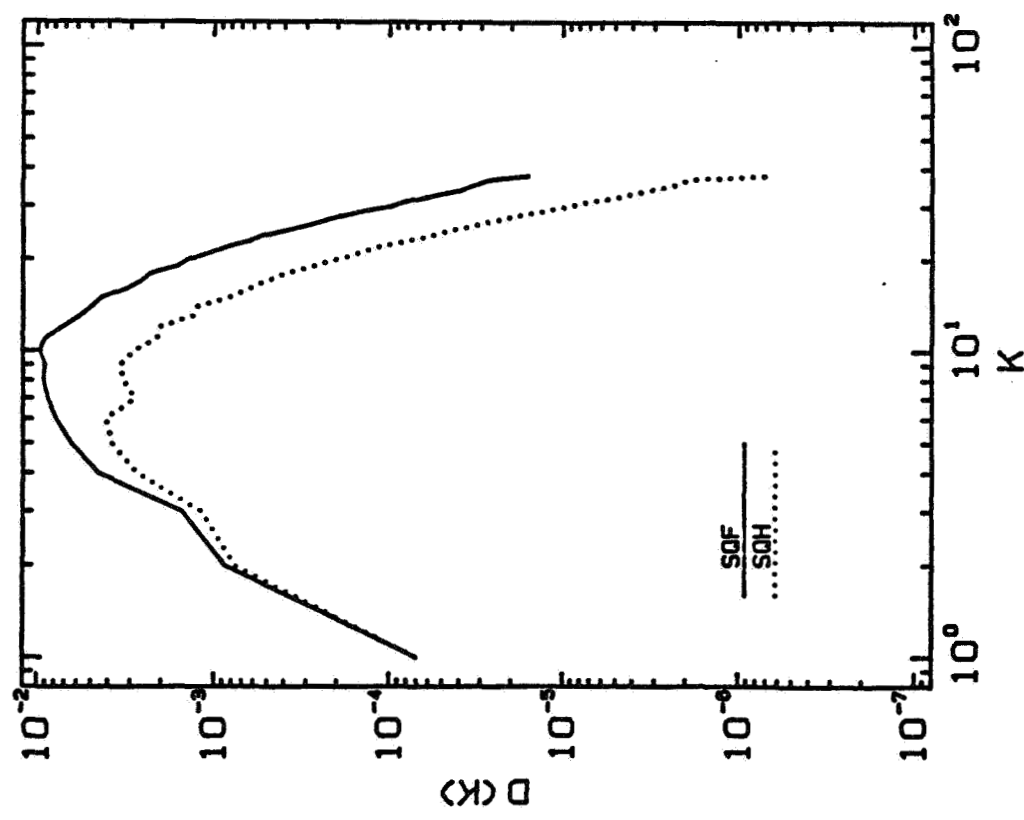


Fig. 5-15. The three-dimensional dissipation spectra of runs SQF and SQH at total strain 0.785.

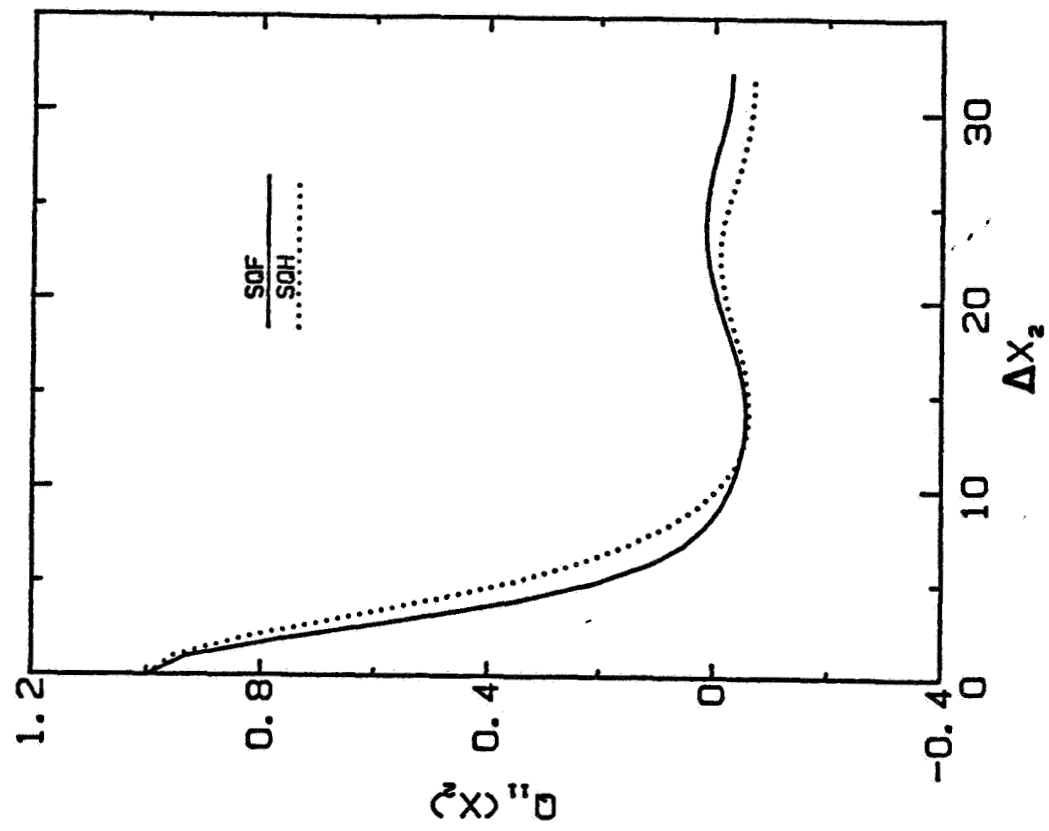


Fig. 5-16. The lateral two-point velocity correlations of runs SQF and SQH at total strain 0.785

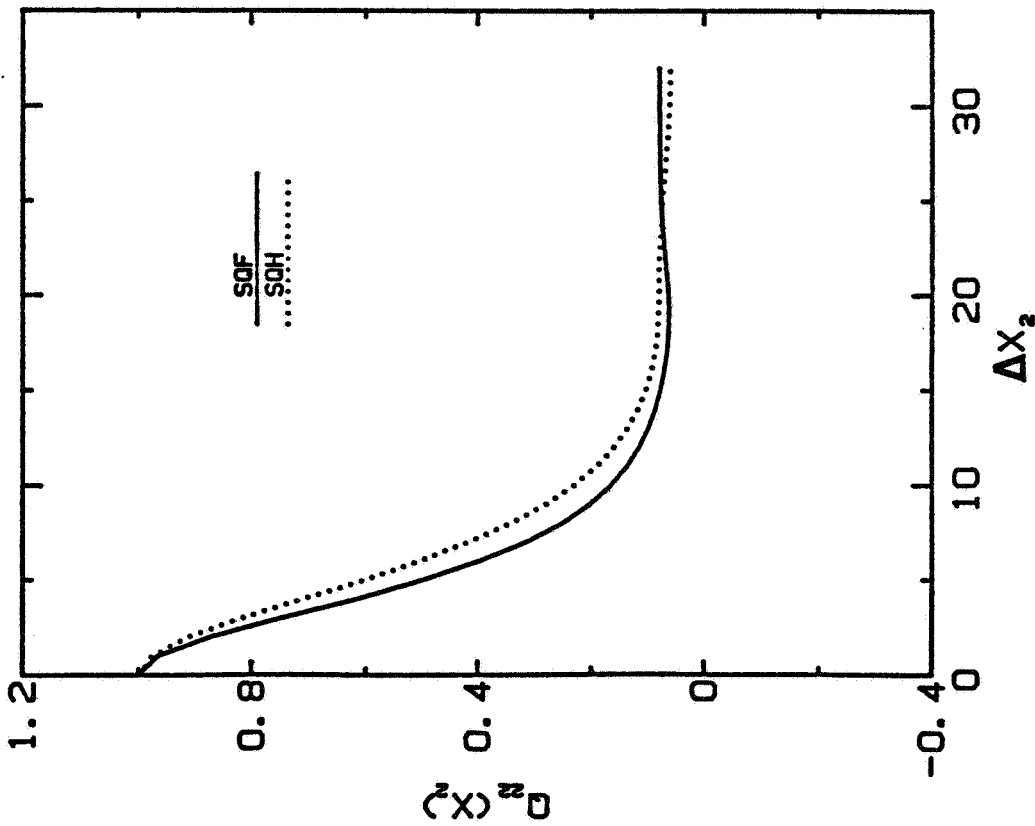


Fig. 5-17. The longitudinal two-point velocity correlations of runs SQF and SQH at total strain 0.785.

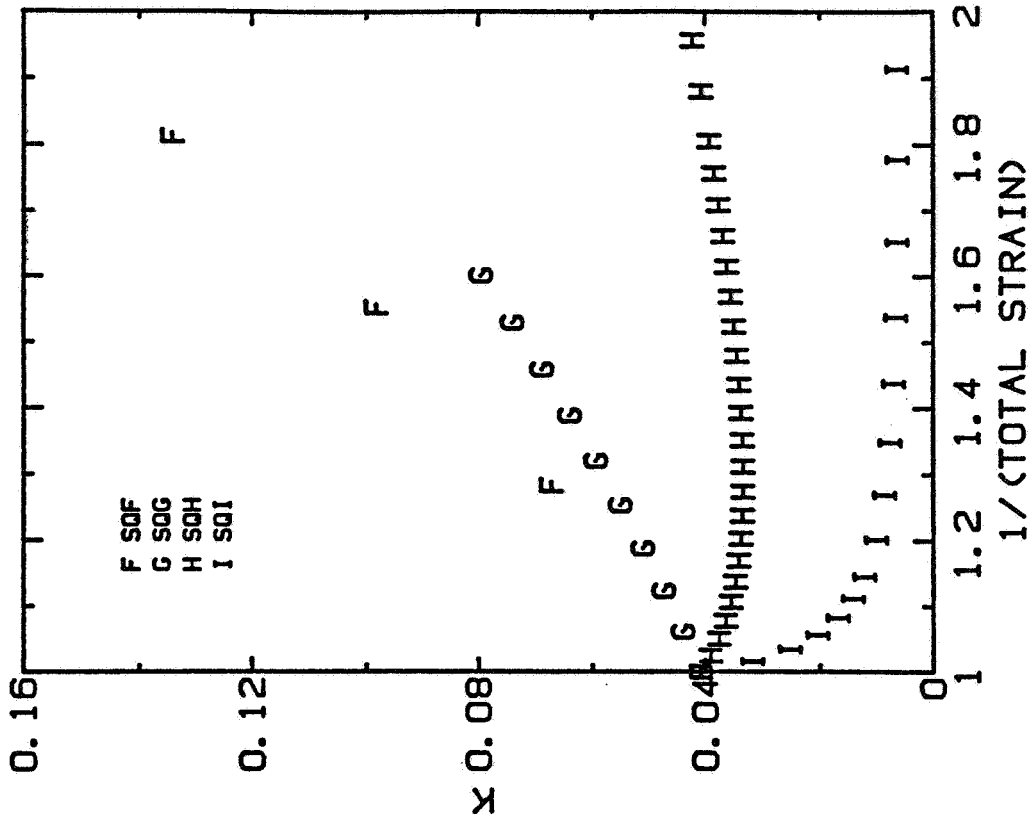


Fig. 5-18. The evolution of the turbulent kinetic energy for four isotropic compression simulations.

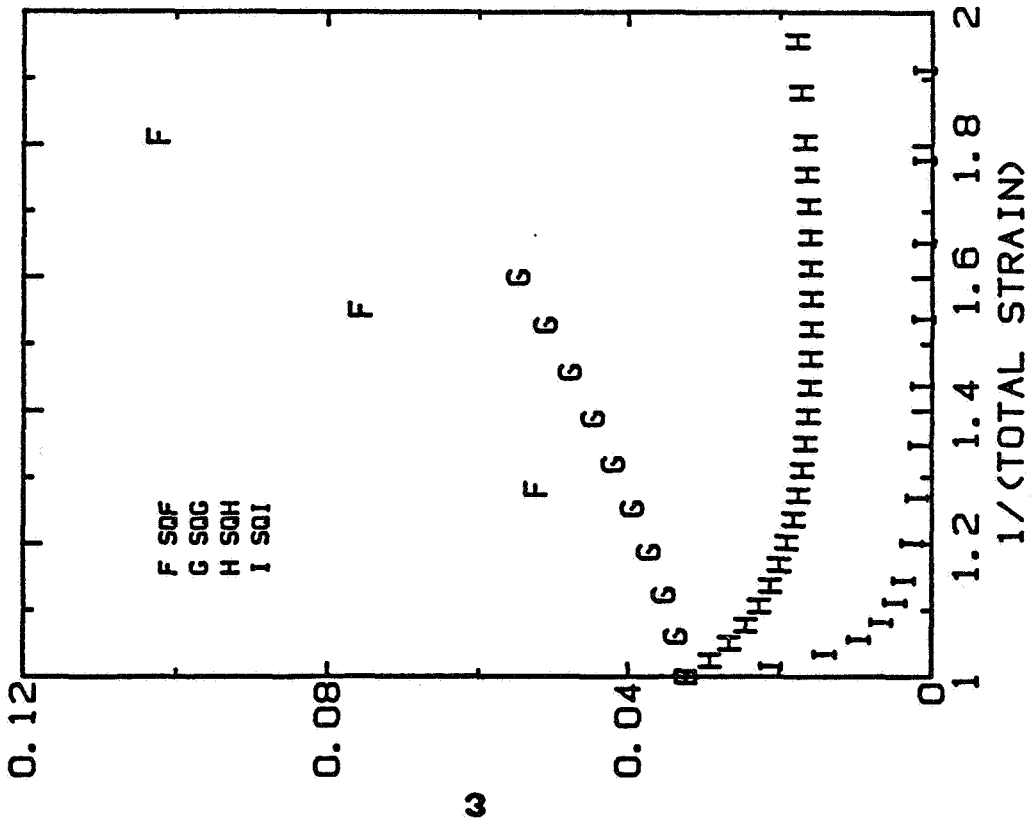


Fig. 5-19. The evolution of the dissipation rate for four isotropic compression simulations.

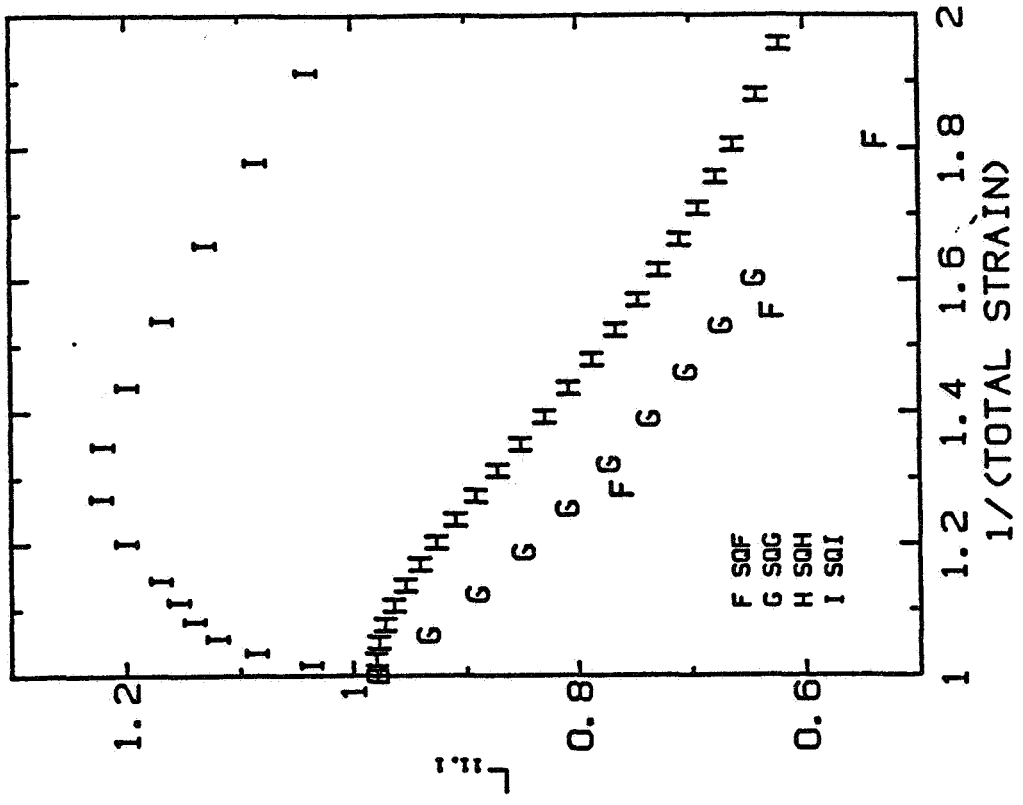


Fig. 5-20. The evolution of a longitudinal integral length scale for four isotropic compression simulations.

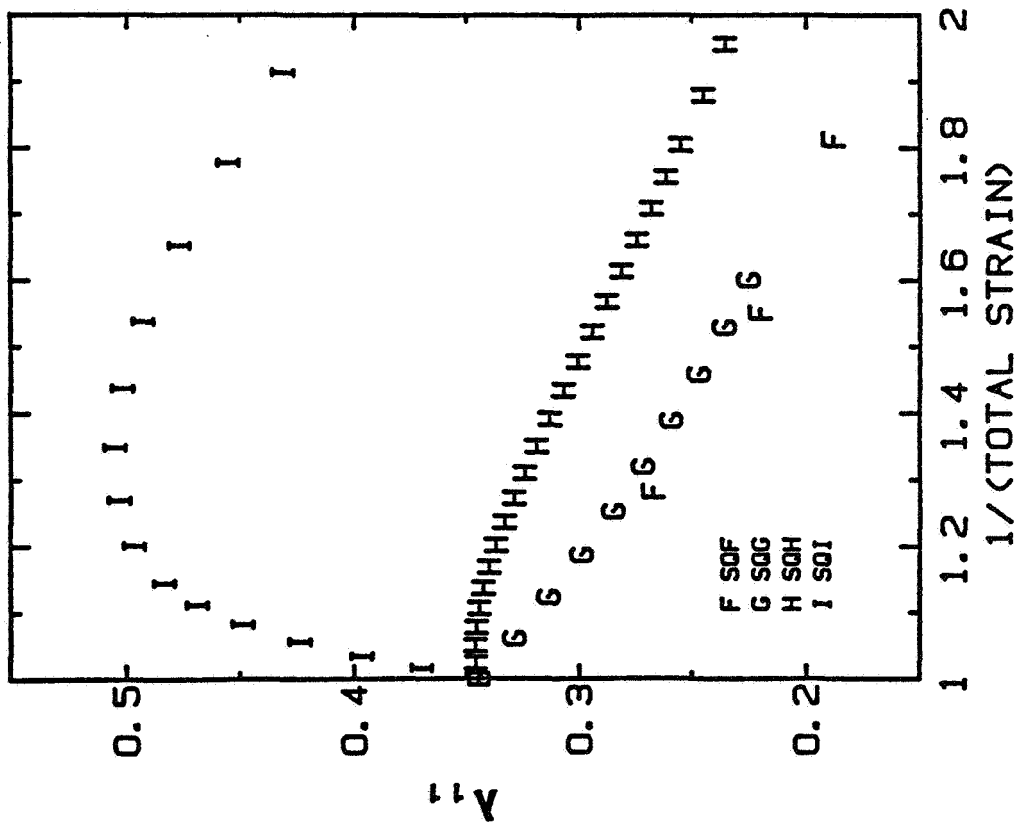


Fig. 5-21. The evolution of a Taylor microscale for four isotropic compression simulations.

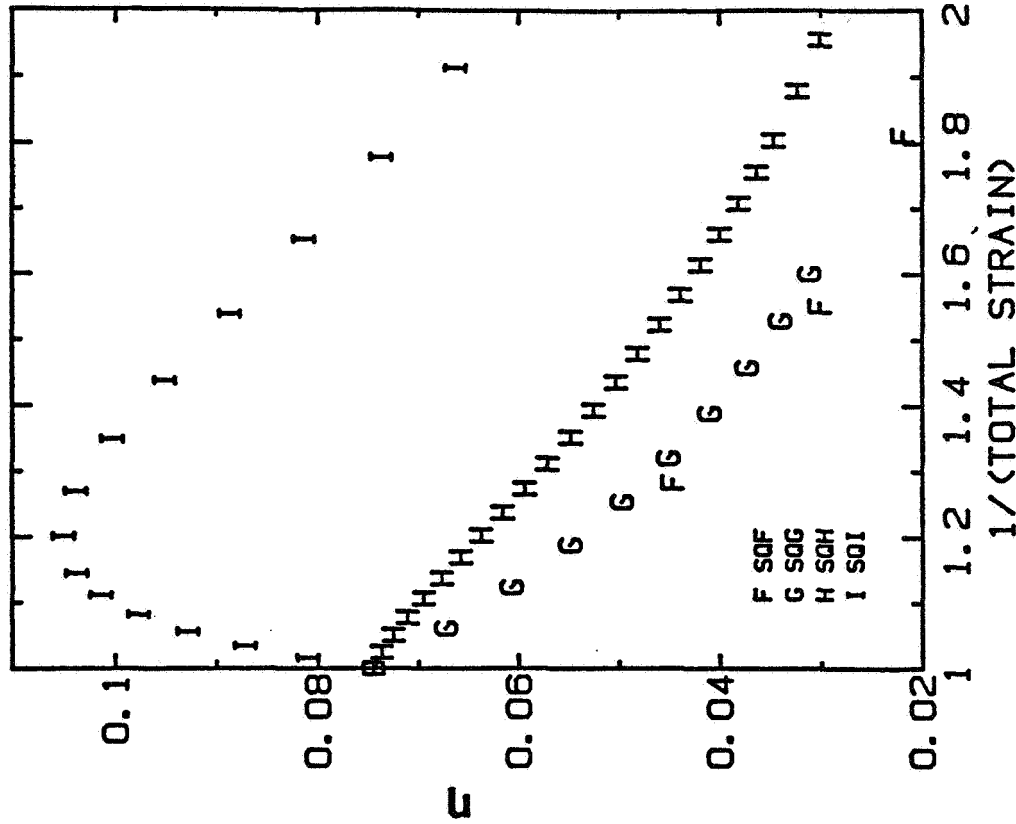


Fig. 5-22. The evolution of the Kolmogorov length scale for four isotropic compression simulations.

Chapter VI

RESULTS FOR HOMOGENEOUS TURBULENCE UNDERGOING ONE-DIMENSIONAL COMPRESSION

In this chapter we present the results for homogeneous turbulence undergoing one-dimensional compression and expansion, irrotational, axisymmetric strain. Four one-dimensional compression and three axisymmetric strain simulations are presented and discussed in some detail. The axisymmetric strain simulations were carried out by Lee and Reynolds (1985); we are grateful for permission to use their results prior to publication.

6.1 Description of The Flows

In this section we describe the flows that are simulated numerically. We consider a fixed mass of turbulent fluid contained within a rectangular parallelepiped. If one opposed pair of sides of the parallelepiped moves inward, as illustrated in Figure 2-2, the fluid in the box undergoes a one-dimensional compression similar to that experienced in an engine cylinder with a flat piston. If one opposed pair of sides moves inward at twice the rate the other two pairs move outward, the fluid experiences an expansion type of axisymmetric strain. This case is illustrated in Figure 6-1. Both flows are axisymmetric. Indeed, the one-dimensional compression can be considered as a combination of the axisymmetric strain and the isotropic compression studied in the preceding chapter. Formally, one can decompose the strain-rate tensor for the one-dimensional case into those for the other two cases:

$$\begin{pmatrix} S & 0 & 0 \\ 0 & 0 & 0 \\ 0 & 0 & 0 \end{pmatrix} = \begin{pmatrix} S/3 & 0 & 0 \\ 0 & S/3 & 0 \\ 0 & 0 & S/3 \end{pmatrix} + \begin{pmatrix} 2S/3 & 0 & 0 \\ 0 & -S/3 & 0 \\ 0 & 0 & -S/3 \end{pmatrix} \quad (6-1)$$

Tables 6.1 and 6.2 present the range of independent dimensionless parameters covered in each simulation. The run identification is given in Column 1. The initial and final $|S|q^2/\epsilon$ are given in Columns 2 and 3, respectively. A wide range of $|S|q^2/\epsilon$ was covered in each type of

simulation so that the effect of strain rate on turbulence could be studied. Columns 4 and 5 show the initial and final turbulent Reynolds numbers for each simulation. Each run covers much the same range of Reynolds number. The anisotropy tensor b_{ij} is defined as

$$b_{ij} = \frac{R_{ij}}{R_{kk}} - \frac{\delta_{ij}}{3} \quad (6-2)$$

where R_{ij} is the Reynolds stress tensor and δ_{ij} is the Kronecker delta. Three invariants can be formed from b_{ij} :

$$I = b_{ii} \quad (6-3)$$

$$-2II = b_{ij}b_{ji} \quad (6-4)$$

$$3III = b_{ij}b_{jk}b_{ki} \quad (6-5)$$

The first invariant (Eq. (6-3)) is zero as a consequence of the definition of b_{ij} . II and III are measures of the anisotropy of R_{ij} or the magnitude of b_{ij} . The initial and final values of II and III are shown in Columns 6 through 9 of Tables 6.1 and 6.2. Since both types of strain are axisymmetric, $b_{22} = b_{33} = -b_{11}/2$. The final total strain ratio is shown in Column 10.

The same initial state was used for every simulation and was taken from a simulation of decaying, homogeneous, isotropic turbulence that had been run long enough to allow the energy cascade to become established. The one-dimensional, compressed turbulence simulations were performed on a grid of $64 \times 64 \times 64$ mesh points. Initially, the computational cell has $\Delta x_1 = 2\Delta x_2 = 2\Delta x_3$, where x_1 is the compression axis. The total strain ratio achieved is approximately 0.25; higher strains result in inadequate resolution, because the box becomes too small in the compression direction. The expansional, axisymmetric strain simulations were done by Lee and Reynolds (1985) and were performed on a grid containing $128 \times 128 \times 128$ mesh points. At the initial state, the computational cell has $\Delta x_1 = 2\sqrt{2}\Delta x_2 = 2\sqrt{2}\Delta x_3$. The total strain ratio achieved is close to 2. Results of these two types of simulations are described and discussed in the following sections.

6.2 Simulation Results

A. Summary of One-Dimensional Compression Simulations

Four simulations of one-dimensional, compressed turbulence were performed. All started with the same isotropic turbulence initial condition, but differed in compression rate. Some details of the initial field are shown in Table 6.3. Some overall data characterizing the four one-dimensional compression simulations are compiled in Table 6.1 and discussed in this section.

The mean strain-rate tensor for one-dimensional compression is

$$S_{ij} = \begin{pmatrix} S(t) & 0 & 0 \\ 0 & 0 & 0 \\ 0 & 0 & 0 \end{pmatrix}$$

where $S(t) = V_p/x_p(t)$, V_p is the compression speed, and $x_p(t)$ is the instantaneous box length. Summarized results are shown in Figures 6-2 through 6-15 and discussed below.

Figures 6-2 and 6-3 show the behavior of the Reynolds number and time-scale ratio as functions of the total strain, which is an appropriate nondimensional time for this flow, for the four simulations. As can be seen in Figure 6-3, the time-scale ratio increases with time in each case. A wide range of $|S|q^2/\epsilon$ was covered by these four simulations to allow study of the effect of time-scale ratio on turbulence. As shown in Figure 6-2 for the cases with small initial $|S|q^2/\epsilon$ (runs ODD and ODE), the Reynolds number decreases in the initial stages of the simulation, and then increases. In the large initial $|S|q^2/\epsilon$ cases (runs ODB and ODC), the Reynolds number increases monotonically with time.

The evolution of the three-dimensional energy and dissipation spectra of a typical run are shown in Figures 6-4 and 6-5. These particular spectra are taken from run ODD at the initial time and at total strain 0.494. The 3-D energy and dissipation spectra evolve as the simulation proceeds. Apparently, viscosity is dissipating the small scales while the large scales are absorbing energy from the applied strain.

Figure 6-6 shows the three-dimensional spectra of the three components of the turbulent kinetic energy in run ODD at total strain ratio

0.494. Anisotropy occurs at the low and moderate wavenumbers. The 3-D energy spectrum of E_{11} is greater than that of the other two components, due to the fact that x_1 is the compression axis. E_{22} and E_{33} are almost equal, as expected.

Figure 6-7 shows two 3-D energy spectra of runs ODB and ODD at total strain 0.847. Run ODB has a higher compression rate than run ODD. Both spectra evolve from the same initial spectrum, but differences develop. The differences can be attributed to the viscous dissipation of the small scales and nonlinear interactions.

For runs ODB and ODD at total strain ratio 0.847, the longitudinal two-point correlations in Lagrangian coordinates are shown in Figures 6-8 and 6-9. Note that x_1 is the compression axis and x_2 is a non-compression axis. As can be seen, curves from run ODD are slightly broader than those from run ODB. Consequently, the integral scales from run ODD are larger than those from run ODB in all three directions. Nonlinear and viscous effects cause the integral scales to decrease less rapidly in the small $|S|q^2/\epsilon$ than in the large $|S|q^2/\epsilon$ case.

Figures 6-10 and 6-11 show the history of twice the turbulent kinetic energy (q^2) and its dissipation rate (ϵ). Both quantities show the same behavior as in isotropically compressed turbulence. When the compression rate is large, as in runs ODB and ODC, the flow is immediately affected by the mean strain and both quantities increase throughout the simulation. If the initial value of $|S|q^2/\epsilon$ is 0.5 or less, as in runs ODD and ODE, the mean strain is not strong enough to immediately alter the structure of the flow and the flow retains the character of decaying isotropic turbulence during the initial period. After the strain has been applied for a longer period, the flow gradually reflects the effect of mean strain and both quantities increase.

Figure 6-12 shows the evolution of b_{11} , which is defined by Eq. (6-2). It appears that there may be an asymptotic value of this quantity in each simulation, although the asymptote is not reached in the time covered by the simulations. The asymptotic value of b_{11} decreases as $|S|q^2/\epsilon$ increases. Furthermore, for fixed total strain, b_{11} increases as time scale ratio ($|S|q^2/\epsilon$) decreases. The reasons

for these results, which appear to conflict with intuition, are not known at present.

Figures 6-13 through 6-15 show the evolution of integral length scale, Taylor microscale, and Kolmogorov length scale, respectively. These length scales all behave in roughly the same way and are similar to those in isotropically compressed turbulence. If the compression is fast enough, the length scale immediately begins to decrease; if the mean strain is weaker, the length scale may grow initially as in the case of decaying turbulence. In the latter case, after the strain has been applied for a while, the length scales start decreasing. Note that the rate of decrease of the Kolmogorov length scale in this flow is smaller than in the isotropic compression cases, due to the fact that the density increases linearly with the inverse of the total strain in this flow rather than cubically, as in the isotropic compression cases.

B. Summary of Incompressible Axisymmetric Expansion Simulations

One-dimensional compression can be considered as a combination of isotropic compression and axisymmetric expansion (see Eq. (6-1)). If S is negative, the left-hand side of Eq. (6-1) is the mean strain-rate tensor for one-dimensional compression flow. The first term on the right-hand side is the mean strain-rate tensor for the isotropic compression, and the second term is the mean strain-rate tensor for axisymmetric expansion. Although the mean strains are related by Eq. (6-1), the turbulence they generate may not be related to each other. The isotropic and one-dimensional compression simulations were described in detail in Chapter V and the preceding section. The relationship among the mean strains for the three flows suggests that there might be a relationship among the turbulence generated in the two compression flows and the one generated by the application of the mean strain corresponding to the last term in Eq. (6-1). To study this, we need the data from the results of the axisymmetric expansion simulations of Lee and Reynolds (1985); they will be introduced in this section. The results introduced in this section will be used later in turbulence model testing.

The mean strain-rate tensor for axisymmetric expansion flow is

$$S_{ij} = \begin{pmatrix} -2S & 0 & 0 \\ 0 & S & 0 \\ 0 & 0 & S \end{pmatrix}$$

where S is a positive constant. The turbulence is compressed in the x_1 direction at twice the rate that it is stretched in the other two directions. The mean velocity is divergence-free, so the density remains constant throughout the simulation. Figure 6-1 illustrates this type of flow. In Section 6.1 we present a general description of the simulations. Table 6.2 shows the range of independent, dimensionless parameters covered in each run. Some details of the isotropic-turbulence initial condition are shown in Table 6.4. Summarized results are shown in Figures 6-16 through 6-23 and discussed below.

Figure 6-16 shows the behavior of the Reynolds number as a function of the total strain ratio for each run. In the low-strain-rate run (run EX0) the Reynolds number decreases in the initial period of the simulation and later increases. In the late stages of the simulations, the highest strain-rate run (run EXQ) has the lowest Reynolds number and the lowest strain-rate run has the highest Reynolds number. This contrasts with the 1-D compression flow.

The behavior of the time-scale ratio ($|S|q^2/\epsilon$) as a function of the total strain ratio is shown in Figure 6-17. As can be seen, a wide range of $|S|q^2/\epsilon$ is covered in these simulations. Since the mean strain rate (S) remains constant throughout each simulation, the change of the time-scale ratio is caused by the change of the turbulence time scale (q^2/ϵ) only. It is found that the turbulence time scale increases during run EX0, which has the lowest strain rate. The turbulence time scale decreases slowly in the highest strain-rate run (run EXQ), and it is approximately a constant throughout run EXP.

Figures 6-18 and 6-19 show the time evolution of twice the turbulent kinetic energy (q^2) and its dissipation rate (ϵ). The behavior of both quantities is similar to that in one-dimensional compression cases. If the mean strain is strong enough, the structure of the flow

is immediately altered and both quantities increase throughout the simulation. Otherwise, the flow retains the character of decaying isotropic turbulence until it reflects the effect of mean strain.

The evolution of b_{11} is shown in Figure 6-20. Its behavior is also very similar to that found in the one-dimensional compression case. The asymptotic value of b_{11} in run EXQ is 1/6, which agrees with RDT analysis. At the same total strain ratio, the flow which has the smaller value of $|S|q^2/\epsilon$ is more anisotropic than the one that has larger $|S|q^2/\epsilon$.

Figures 6-21 through 6-23 show the evolution of integral length scale, Taylor microscale, and Kolmogorov length scale, respectively. The behaviors of these three length scales are similar to each other and to those of the one-dimensional compression flow. The behavior of the Kolmogorov length scale is closer to that of the other length scales in this flow (in contrast to the case of the one-dimensional compression flow), because the kinematic viscosity remains constant in this flow.

Important results from three types of simulated flows--isotropic compression, one-dimensional compression, and axisymmetric expansion flows--have been given and discussed in this and the previous chapters. In the next chapter we shall use these results to test the validity of turbulence models.

Table 6.1
Description of Simulations of One-Dimensionally Compressed Turbulence

Run ID	$ S q^2/\epsilon$		$q^4/\epsilon\nu$		II		III		Total Strain Ratio	
	Initial	Final	Initial	Final	Initial	Final	Initial	Final	Initial	Final
ODB	47.04	143.58	34.55	197.94	-2.865×10^{-4}	-1.490×10^{-2}	-1.791×10^{-6}	6.993×10^{-4}	0.277	
ODC	2.50	11.54	34.55	197.51	-2.865×10^{-4}	-2.510×10^{-2}	-1.791×10^{-6}	1.530×10^{-3}	0.261	
ODD	0.50	5.92	34.55	164.71	-2.865×10^{-4}	-3.926×10^{-2}	-1.791×10^{-6}	2.992×10^{-3}	0.254	
ODE	0.10	4.04	34.55	80.15	-2.865×10^{-4}	-4.783×10^{-2}	-1.791×10^{-6}	3.887×10^{-3}	0.275	

Table 6.2
Description of Simulations of Axisymmetric Expansion Flow

Run ID	$ S q^2/\epsilon$		$q^4/\epsilon\nu$		II		III		Total Strain Ratio	
	Initial	Final	Initial	Final	Initial	Final	Initial	Final	Initial	Final
EXQ	40.83	27.46	58.19	56.69	-1.536×10^{-5}	-1.896×10^{-2}	-1.090×10^{-8}	1.004×10^{-3}		1.919
EXP	4.083	8.512	58.19	84.34	-1.536×10^{-5}	-2.985×10^{-2}	-1.090×10^{-8}	1.983×10^{-3}		2.007
EXO	0.408	1.746	58.19	88.54	-1.536×10^{-5}	-5.618×10^{-2}	-1.090×10^{-8}	5.122×10^{-3}		2.000

Table 6.3

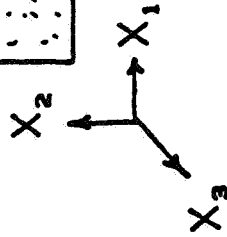
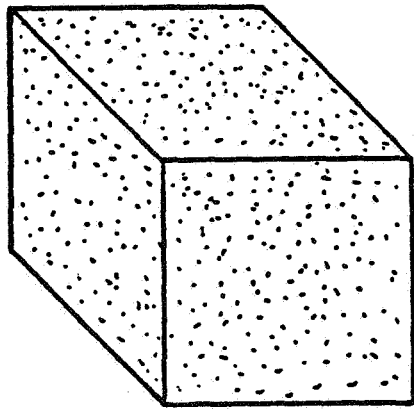
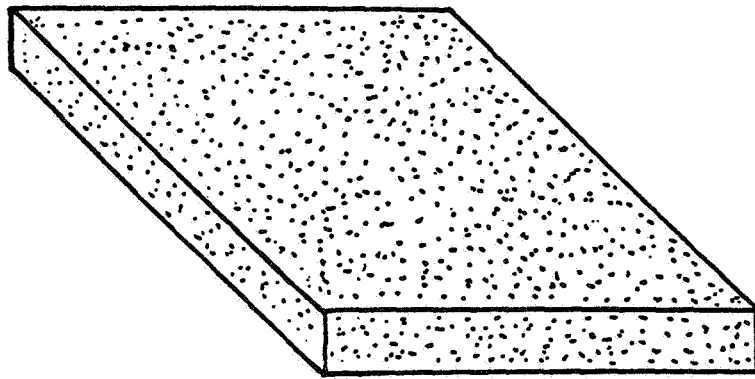
Some Details of the Initial Condition
of the One-Dimensionally Compressed Turbulence Simulations
(consistent units)

Turbulence velocity q	0.9447
Dissipation rate ϵ	1.5369
Integral length scale $L_{11,1}$	0.3227
Taylor microscale λ_{11}	0.2146
Kolmogorov length scale η	0.0385
Kinematic viscosity ν	0.0150

Table 6.4

Some Details of the Initial Condition
of the Axisymmetric Expansion Flow Simulations
(consistent units)

Turbulence velocity q	0.4688
Dissipation rate ϵ	0.1931
Integral length scale $L_{11,1}$	0.2271
Taylor microscale λ_{11}	0.1556
Kolmogorov length scale η	0.0253
Kinematic viscosity ν	0.0043



$1 \times 1 \times 1$

$1/4 \times 2 \times 2$

Fig. 6-1. Schematic description of homogeneous, incompressible, axisymmetric expansion flow.

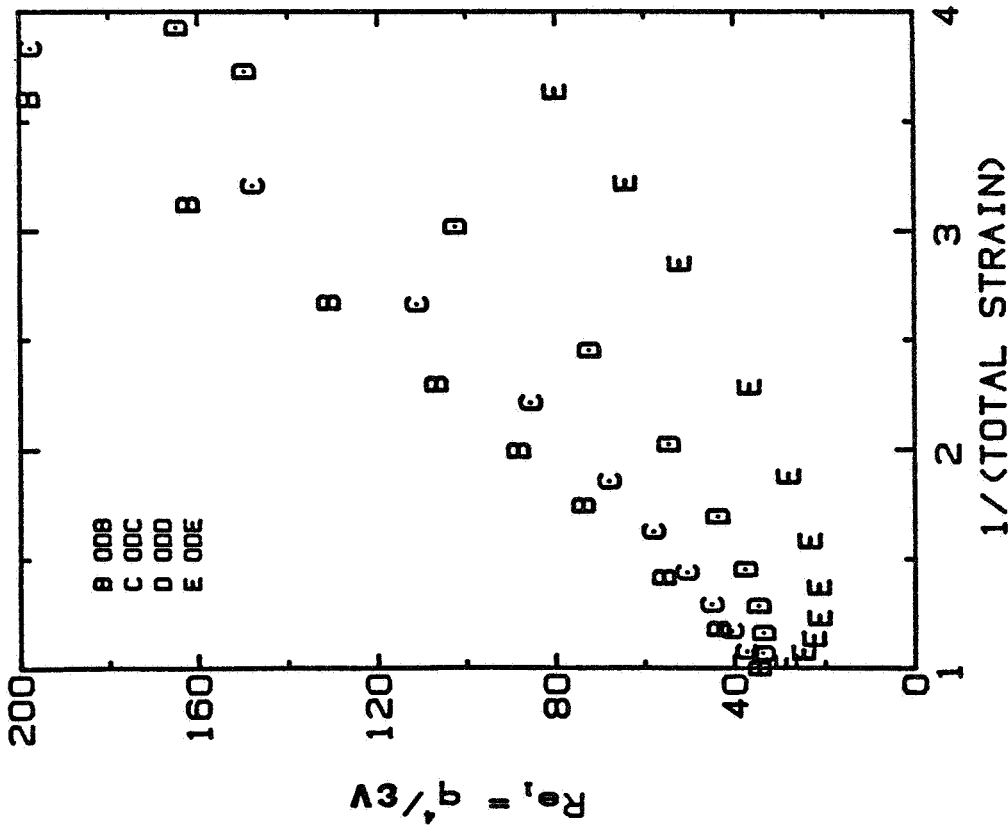


Fig. 6-2. The evolution of the turbulent Reynolds number for four one-dimensional compression simulations.

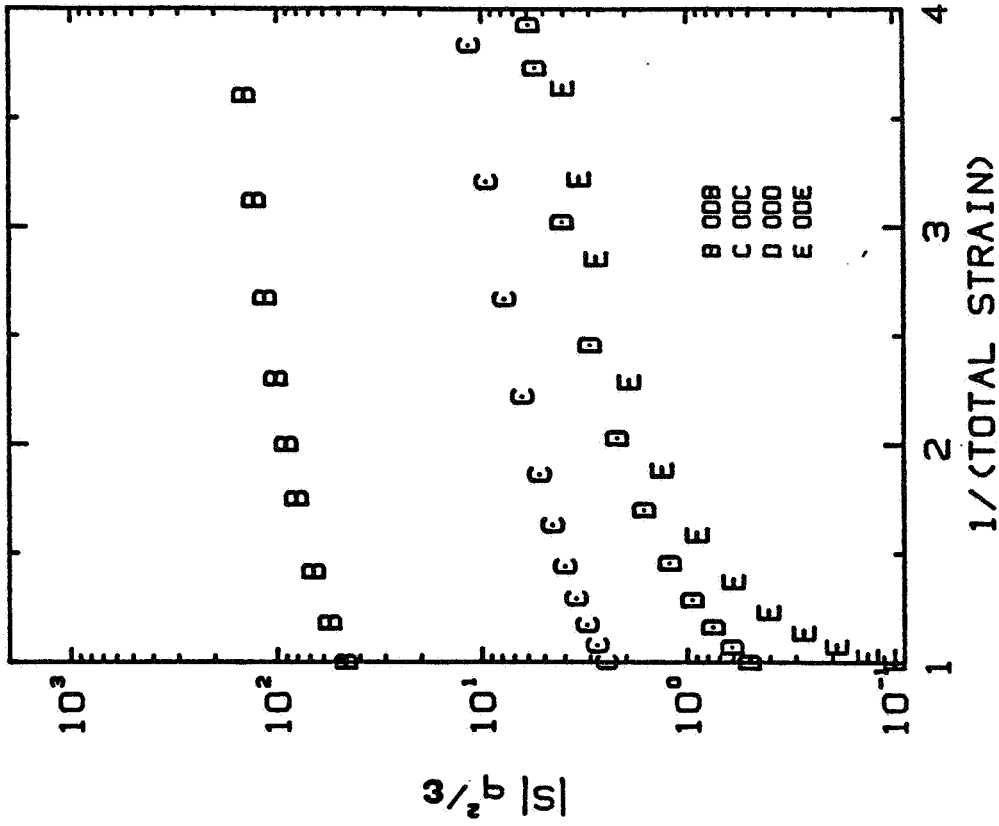


Fig. 6-3. The range of $|S|q^2/\epsilon$ covered in four one-dimensional compression simulations.

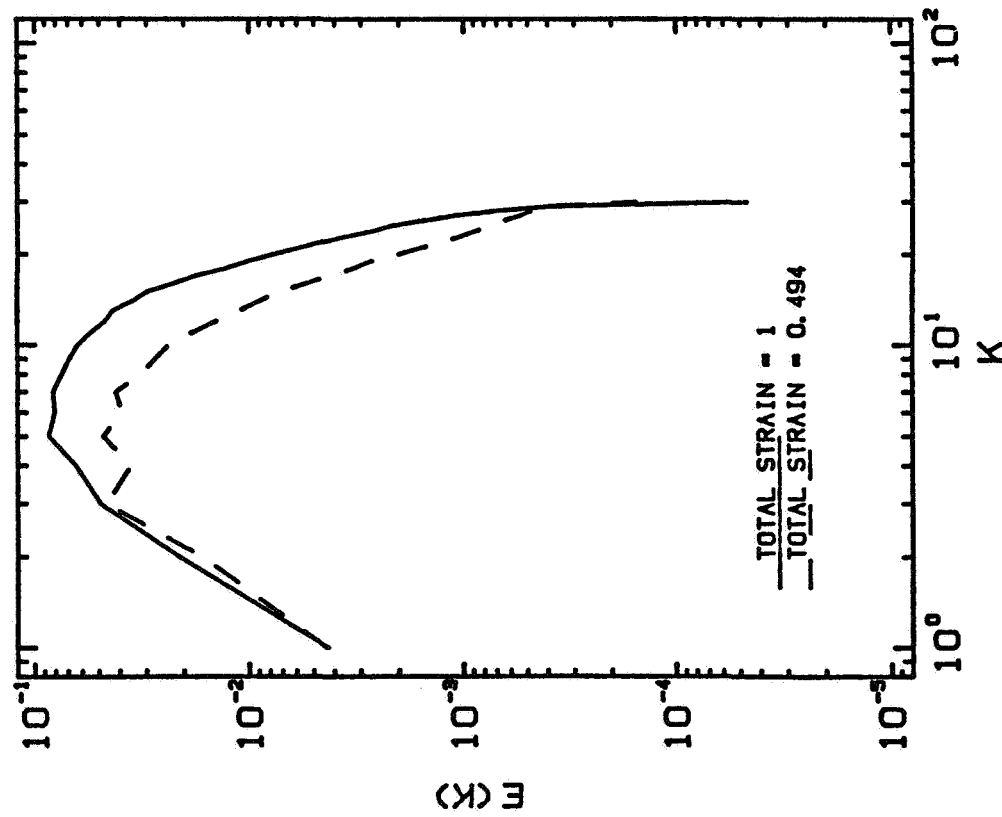


Fig. 6-4. The three-dimensional energy spectra of run ODD at total strain 1 and 0.494.

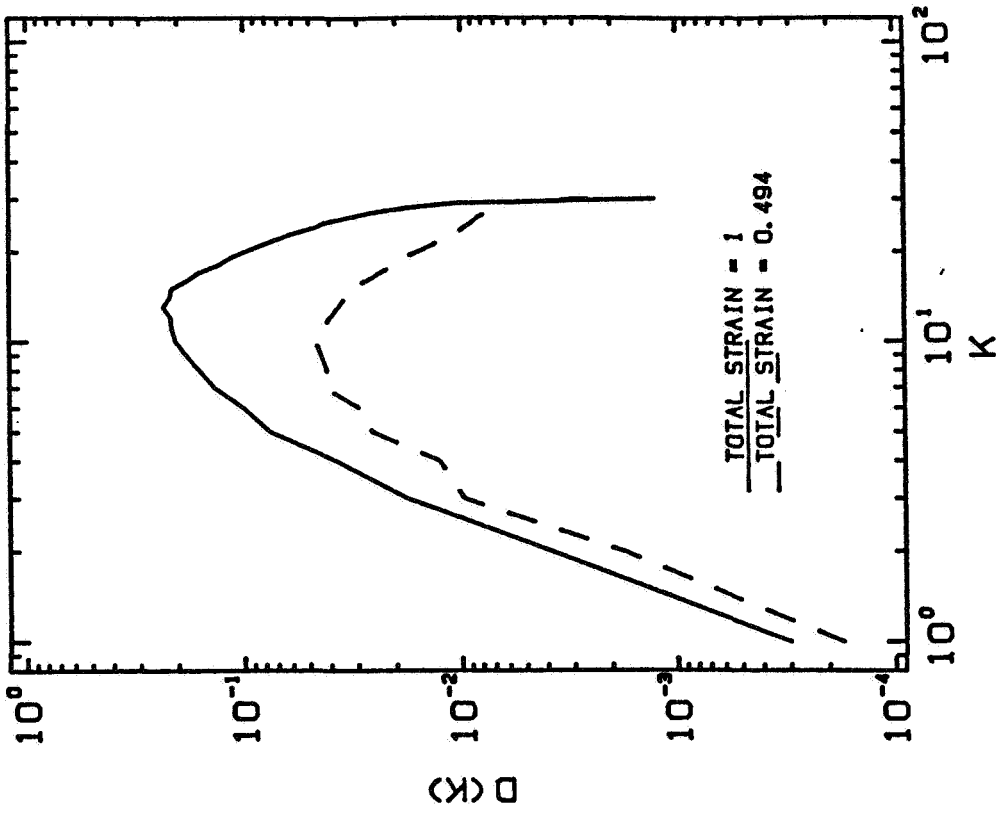


Fig. 6-5. The three-dimensional dissipation spectra of run ODD at total strain 1 and 0.494.

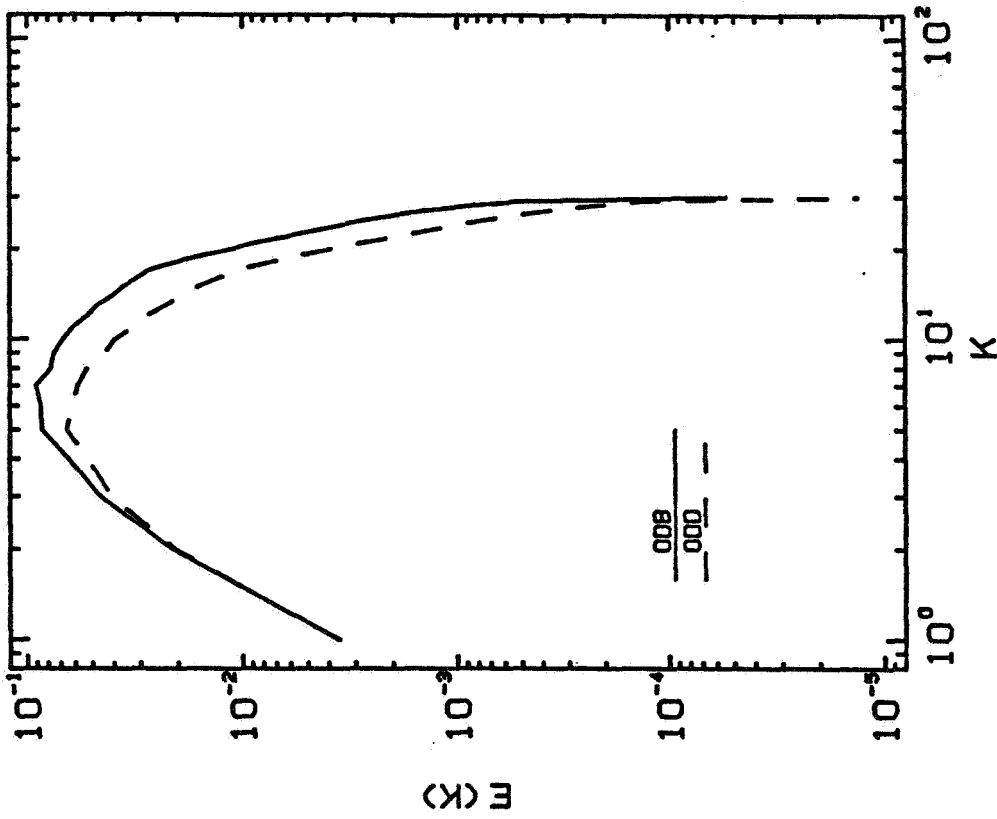


Fig. 6-7. The three-dimensional energy spectra of runs ODB and ODD at total strain 0.847.

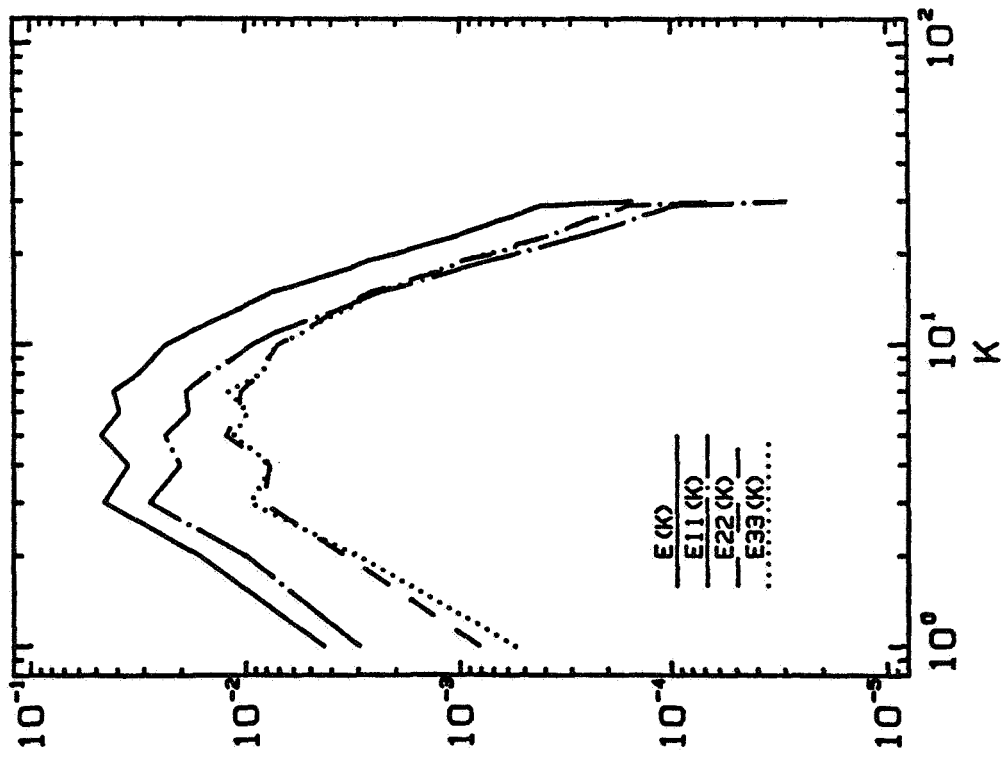
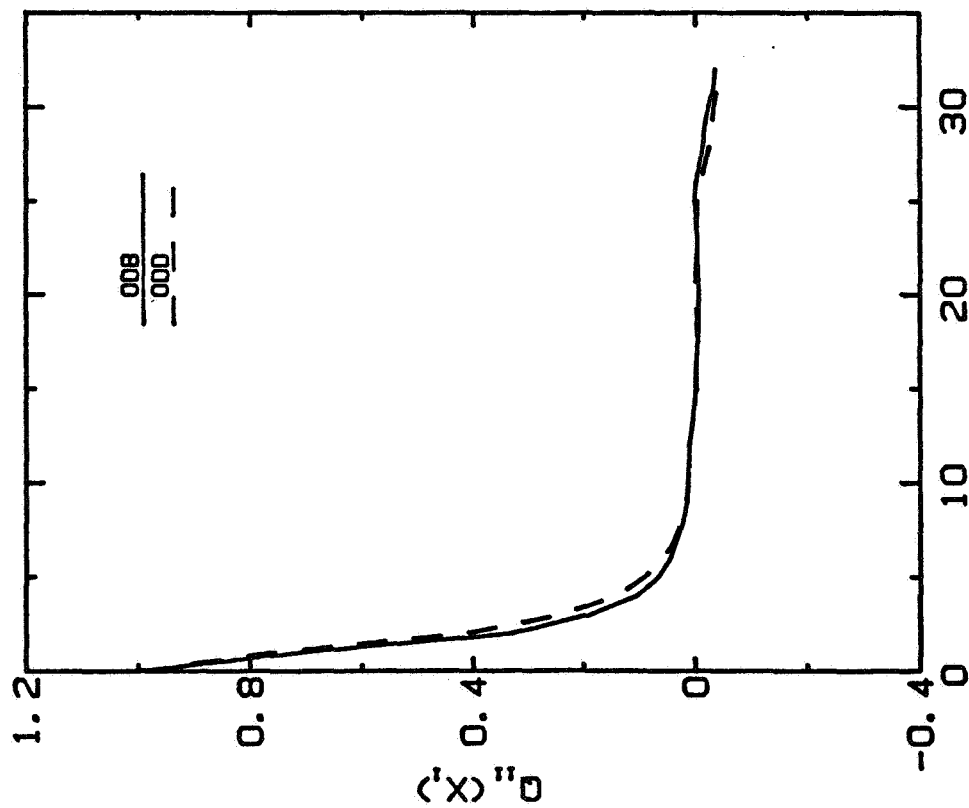
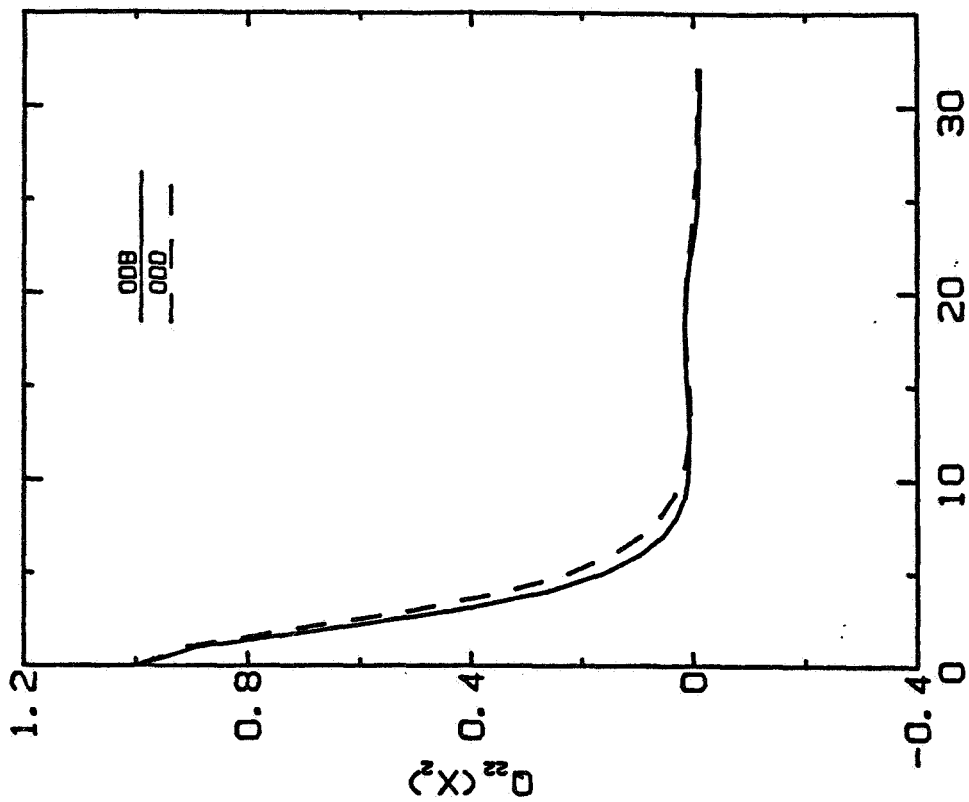


Fig. 6-6. The three-dimensional spectra of the three normal energy components of run ODD at total strain 0.494.



ΔX_1

Fig. 6-8. The longitudinal two-point velocity correlations in the compression direction of runs ODB and ODD at total strain 0.847.



ΔX_2

Fig. 6-9. The longitudinal two-point velocity correlations in the noncompression direction of runs ODB and ODD at total strain 0.847.

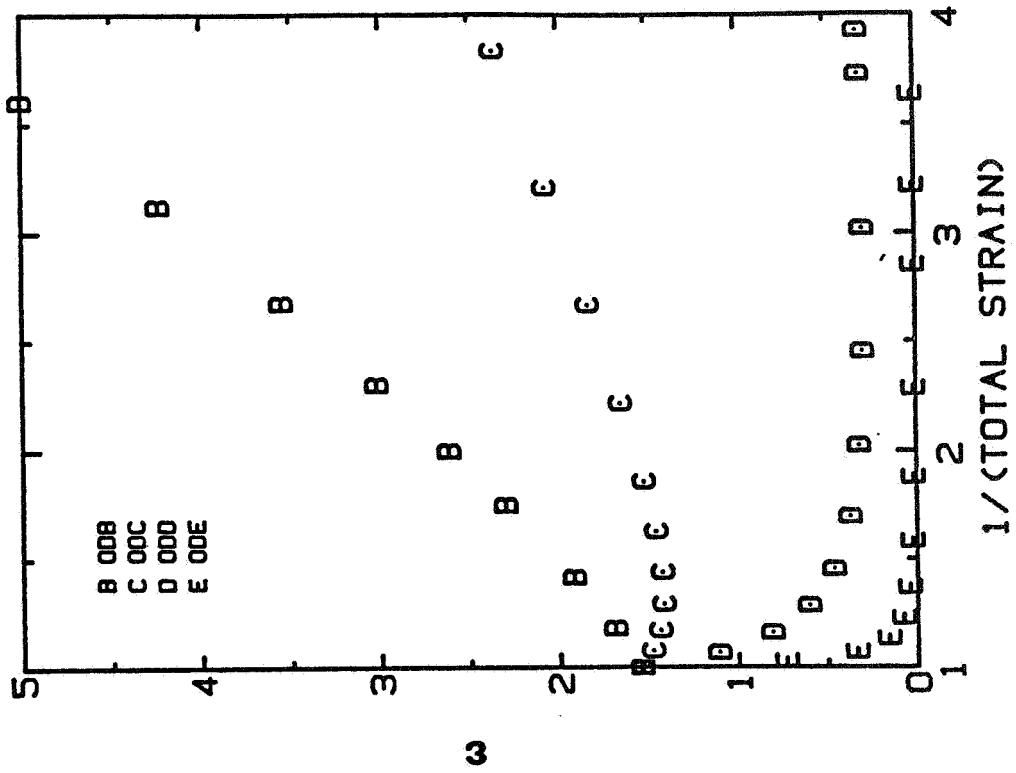


Fig. 6-11. The evolution of the dissipation rate for four one-dimensional compression simulations.

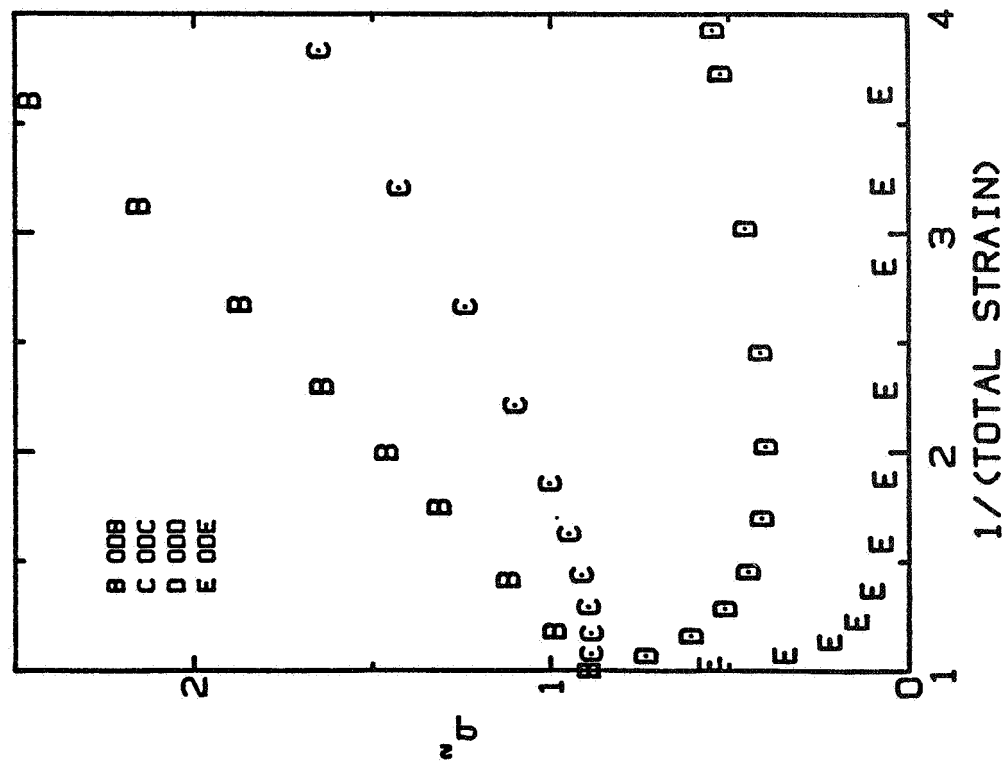


Fig. 6-10. The evolution of twice the turbulent kinetic energy for four one-dimensional compression simulations.

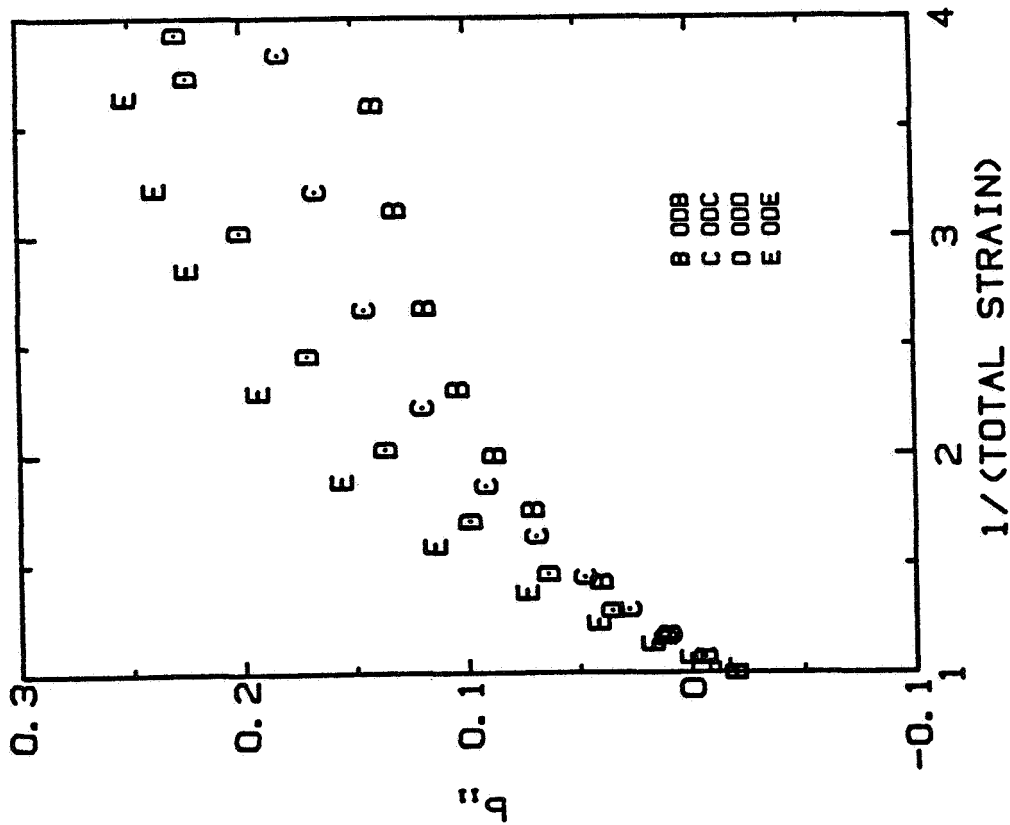


Fig. 6-12. The evolution of $b_{||}$ for four one-dimensional compression simulations.

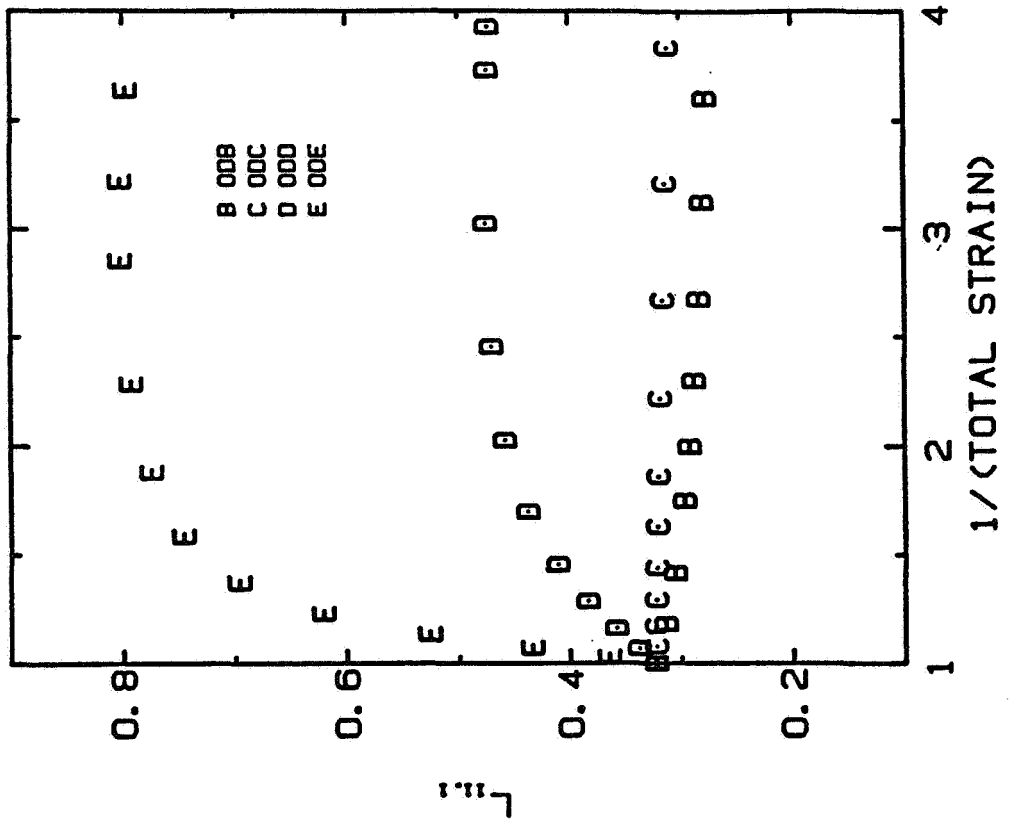


Fig. 6-13. The evolution of the longitudinal integral length scale in the compression direction for four one-dimensional compression simulations.

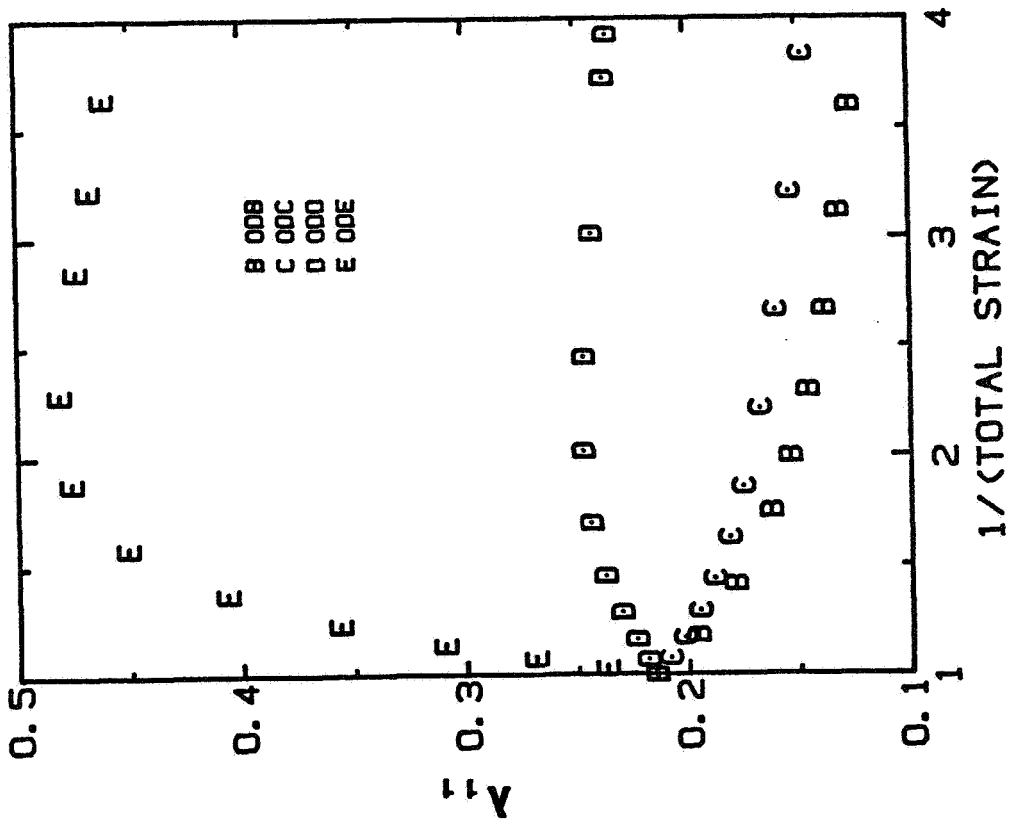


Fig. 6-14. The evolution of a Taylor microscale for four one-dimensional compression simulations.

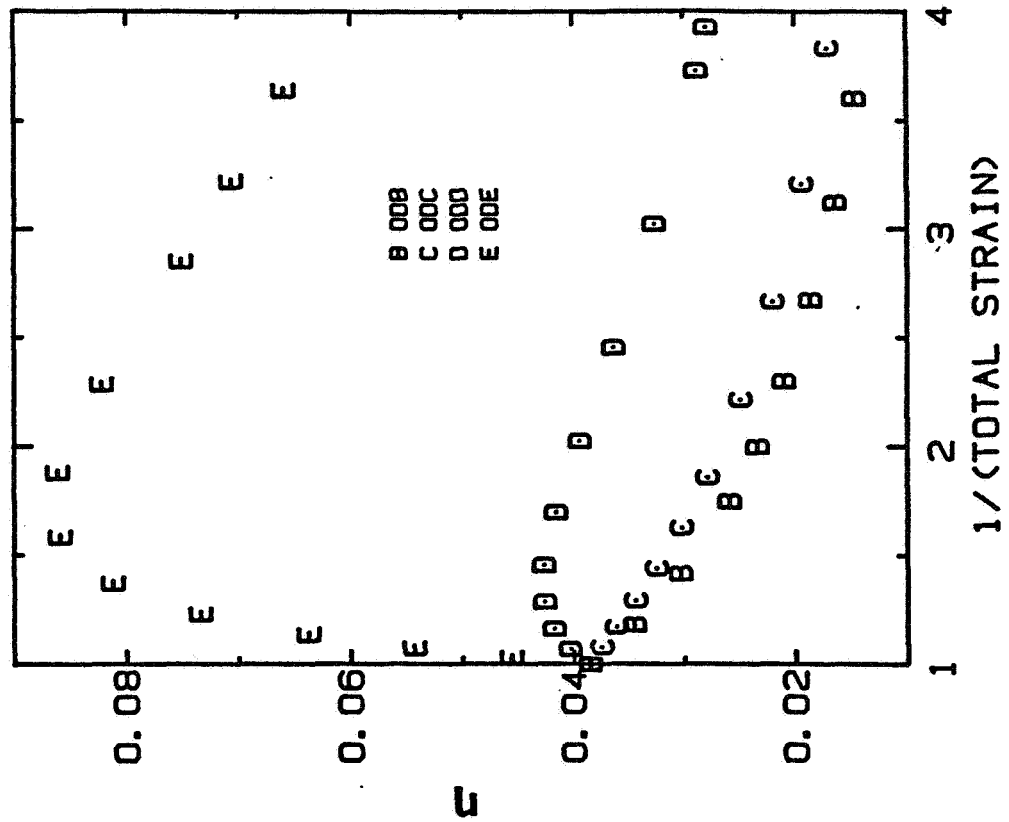


Fig. 6-15. The evolution of the Kolmogorov length scale for four one-dimensional compression simulations.

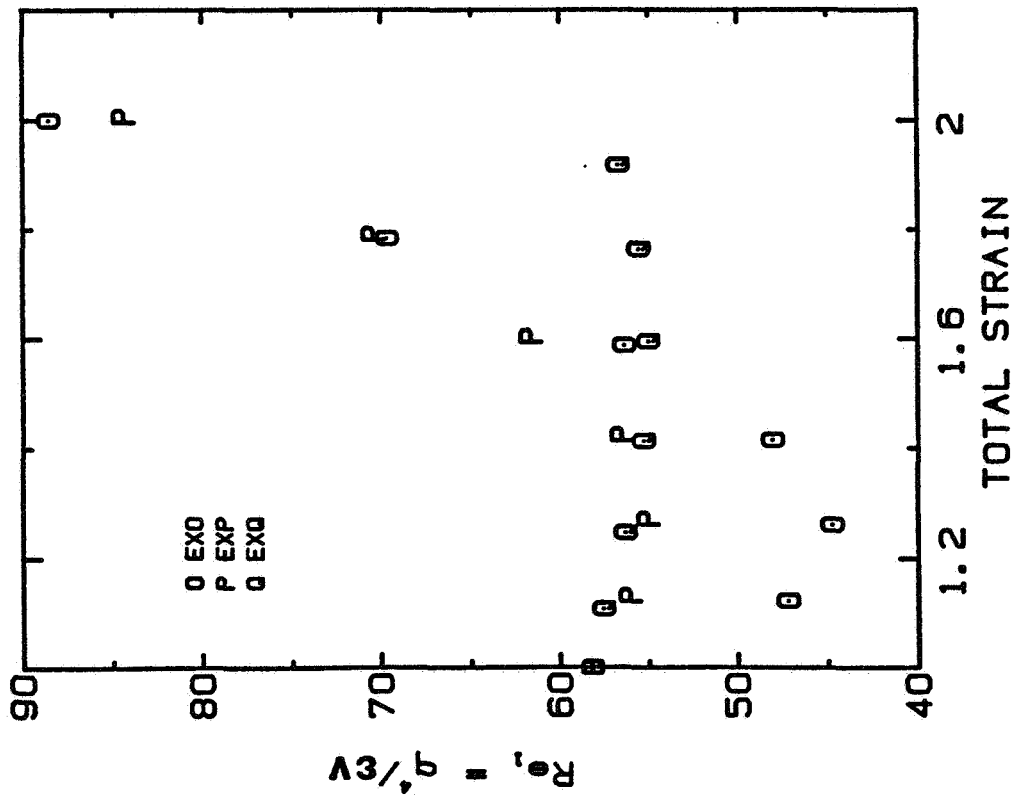


Fig. 6-16. The evolution of the turbulent Reynolds number for three axisymmetric expansional strain simulations.

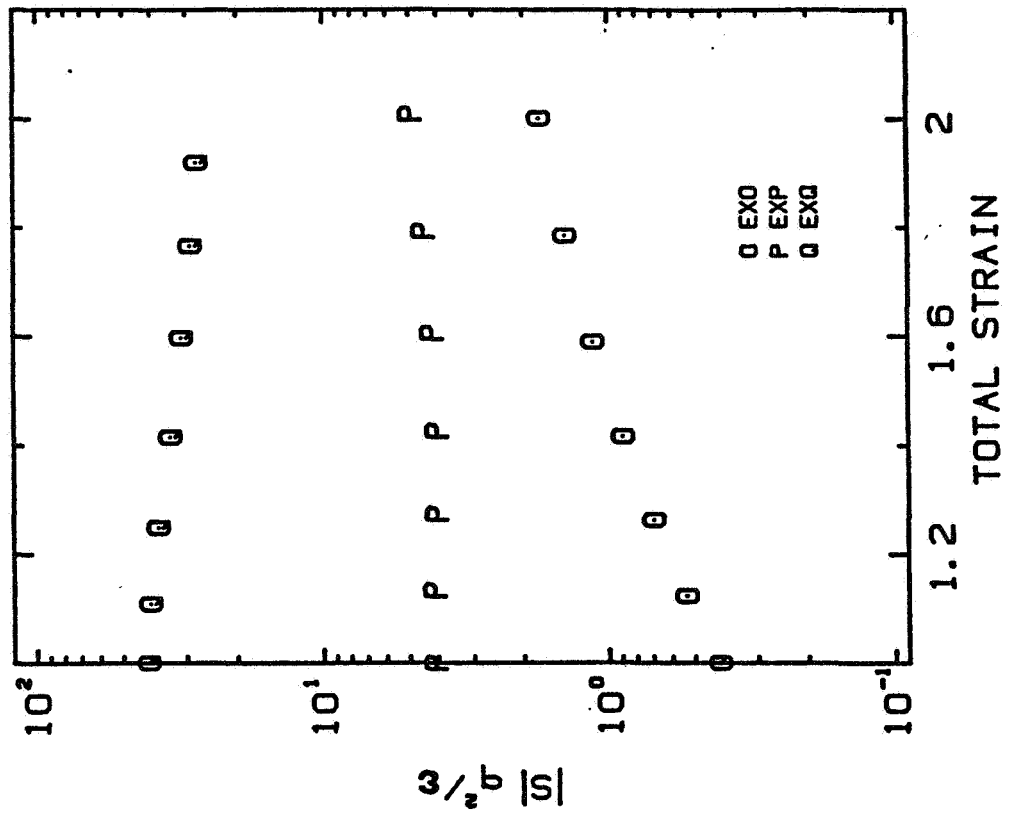


Fig. 6-17. The range of $|S|q^2/\epsilon$ covered in three axisymmetric expansional strain simulations.

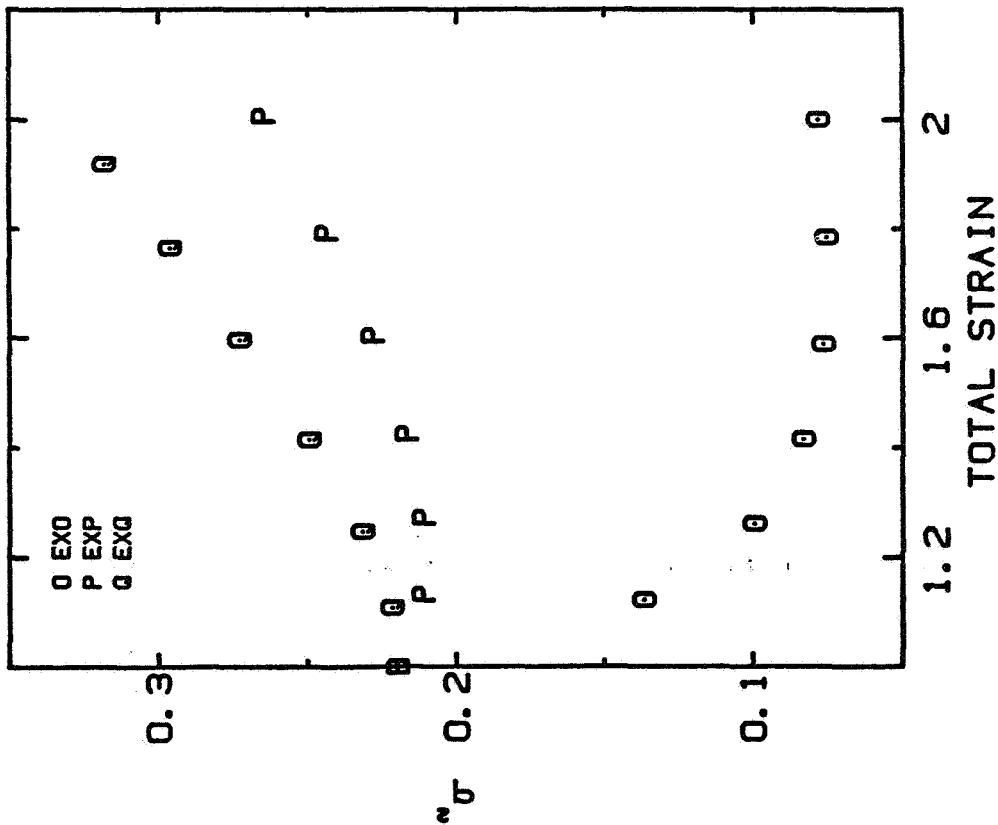


Fig. 6-18. The evolution of twice the turbulent kinetic energy for three axisymmetric expansional strain simulations.

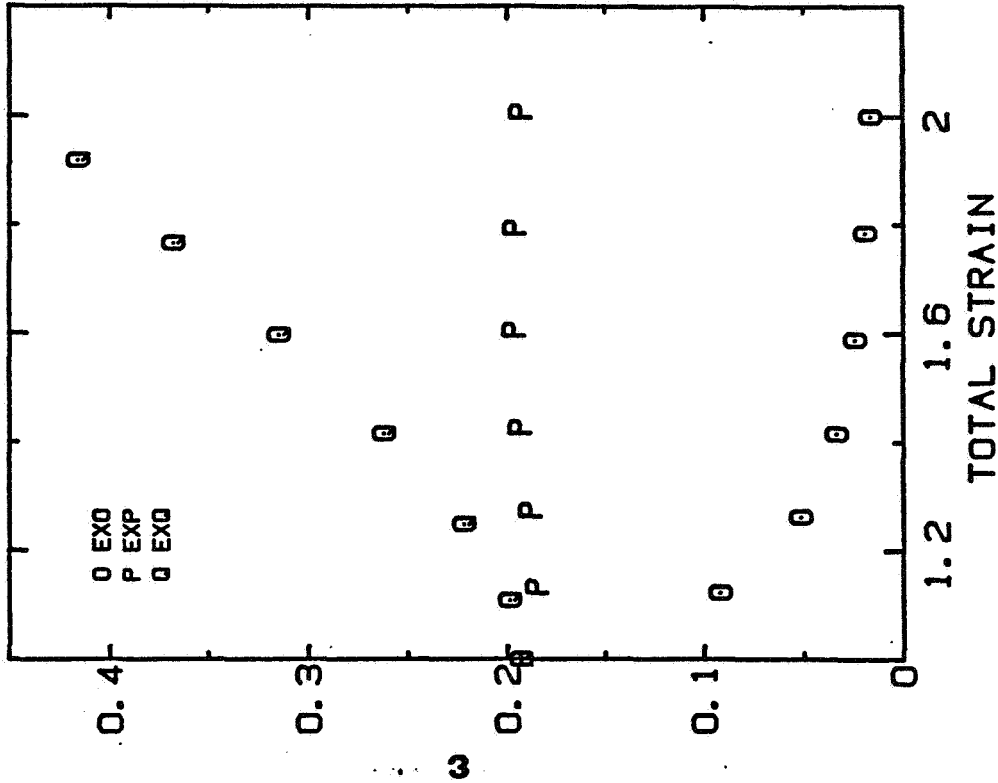


Fig. 6-19. The evolution of the dissipation rate for three axisymmetric expansional strain simulations.

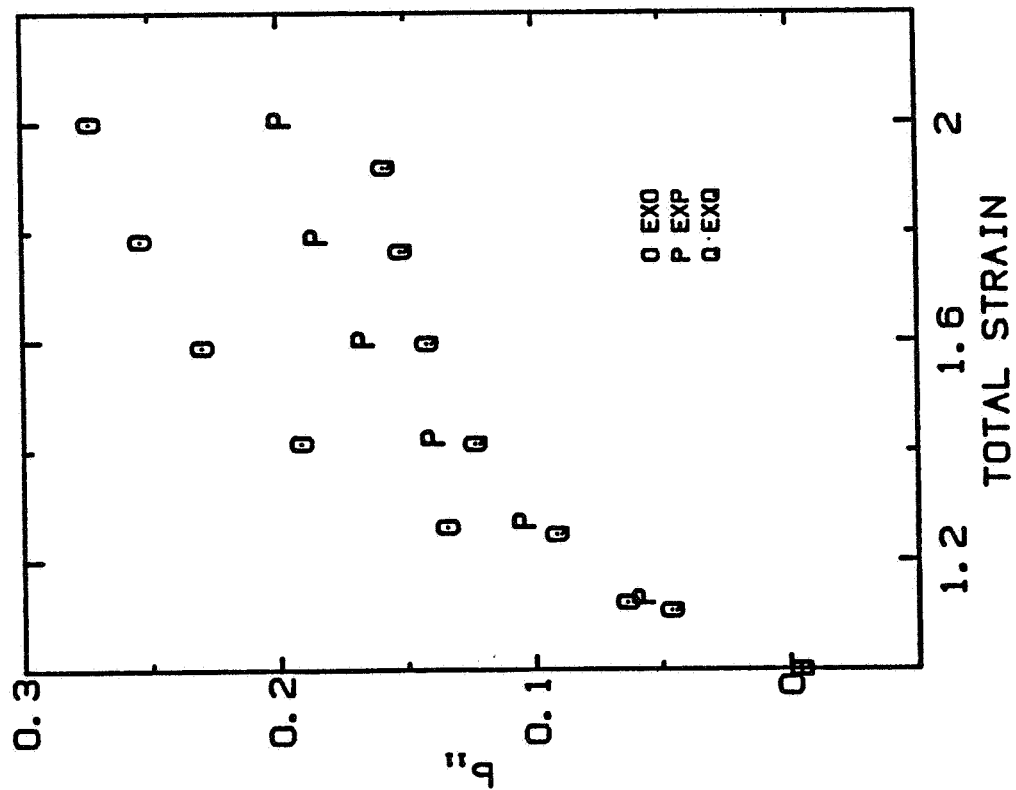


Fig. 6-20. The evolution of b_{11} for three axisymmetric expansional strain simulations.

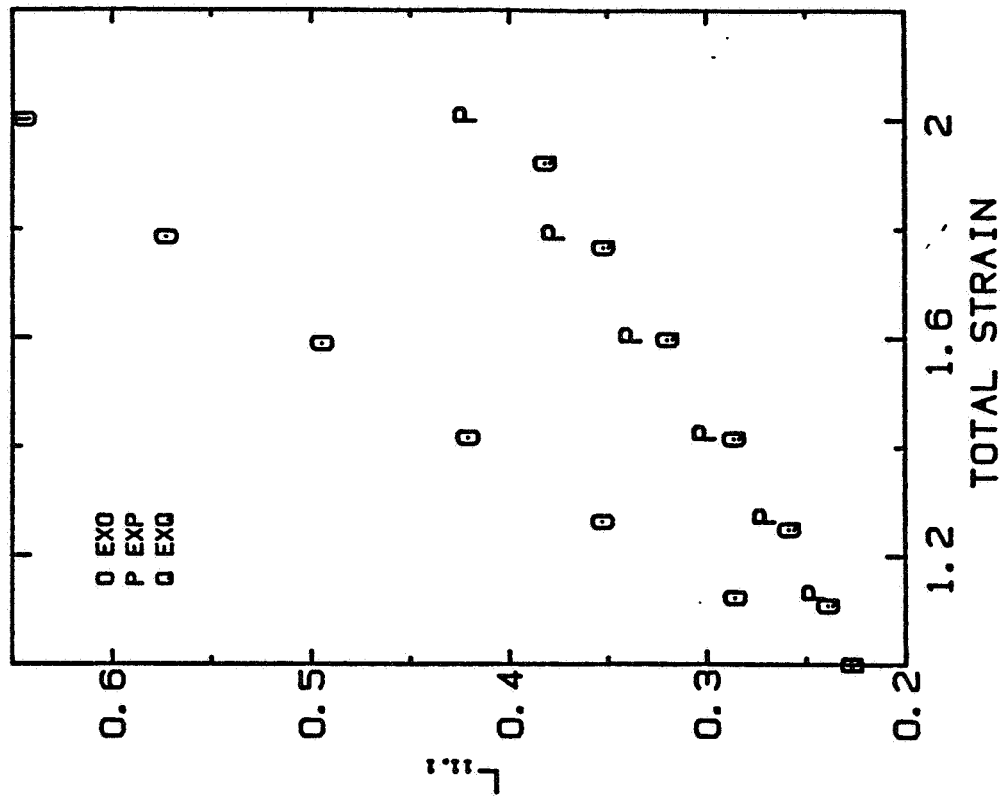


Fig. 6-21. The evolution of the longitudinal integral length scale in the compression direction for three axisymmetric expansional strain simulations.

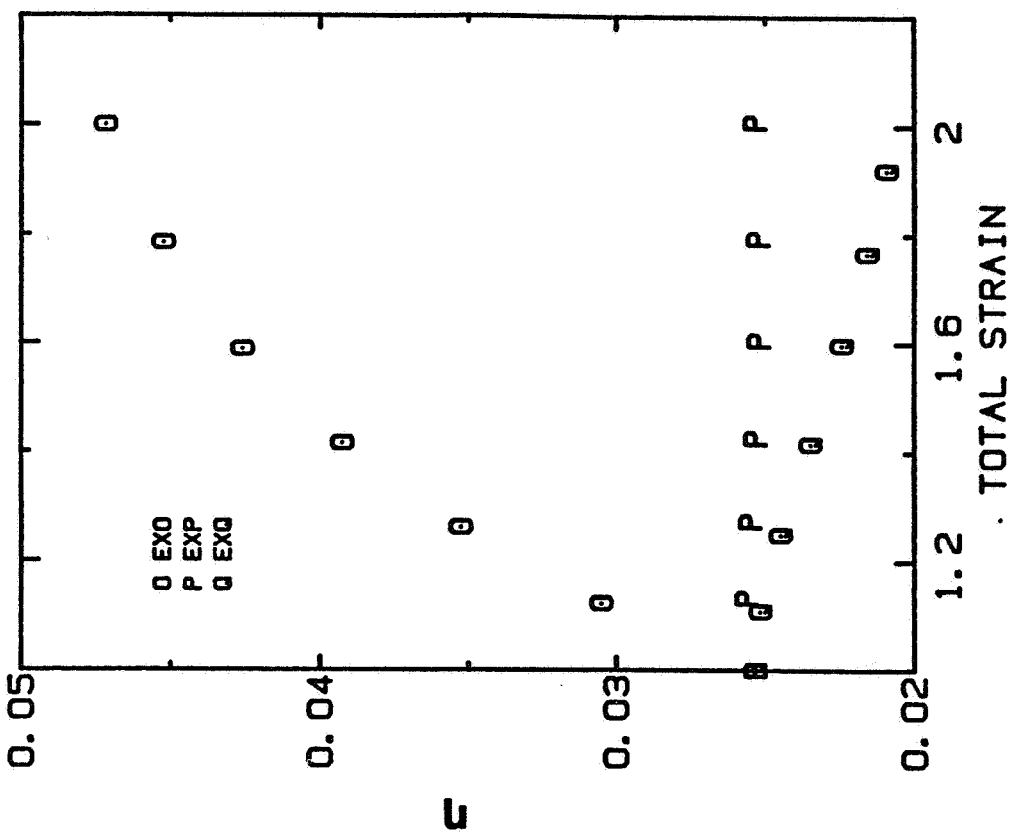


Fig. 6-22. The evolution of a Taylor microscale length scale for three axisymmetric strain simulations.

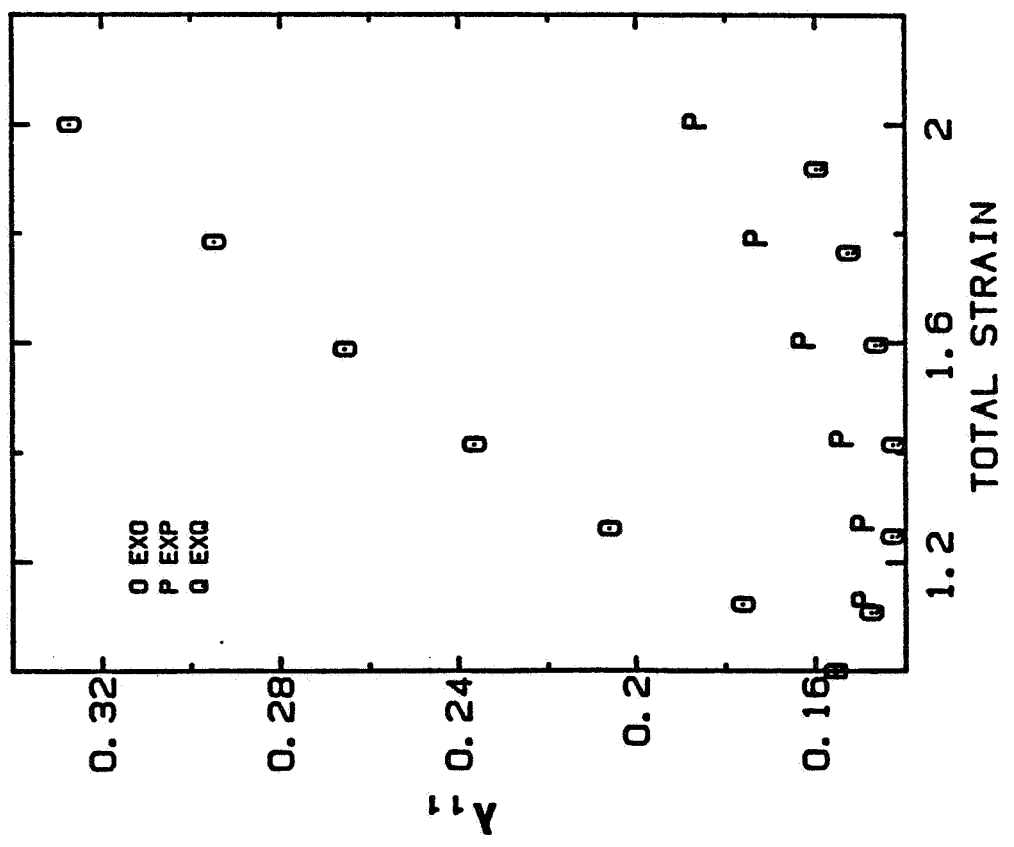


Fig. 6-23. The evolution of the Kolmogorov length scale for three axisymmetric expansional strain simulations.

Chapter VII

$k-\epsilon$ TURBULENCE MODEL TESTING AND MODIFICATIONS

Results from isotropic compression, axisymmetric expansional straining, and one-dimensional compression simulations are used to test the validity of $k-\epsilon$ turbulence models in this chapter. The model is found to be defective. To correct the deficiency, a three-equation ($k-\epsilon-\tau$) turbulence model which models four types of flows (isotropic decay, isotropic compression, axisymmetric expansional straining, and one-dimensional compression flows) with a wide range of strain rates is proposed. A method of determining the model constants is developed and discussed.

7.1 Introduction

Since turbulence phenomena are highly nonlinear, they are not amenable to classical analytical approaches, and modeling needs to be used. As technology advances, greater accuracy is needed and more complex prediction methods, including more sophisticated turbulence models, are required.

Methods of simulating turbulent flows can be classified according to the following scheme (Kline et al., 1981):

1. Correlations
2. Integral methods
3. One-point closure methods
4. Two-point closure methods
5. Large-eddy simulation
6. Full simulation

As one moves down the list, each method requires less modeling than those above it. The range of flows that may be simulated with a single model broadens as the level increases. Turbulence models at each level can be validated using results from higher levels. Two-equation models (and $k-\epsilon$ models in particular) based on one-point closure are among the most popular turbulence models at present. They are able to simulate a wide variety of flows with reasonable accuracy, including flows that are difficult to treat with other one-point closure models.

The isotropic and one-dimensional compression simulations described in the preceding chapters are full simulations, i.e., numerical solutions of the exact Navier-Stokes equations. These results will be used to investigate both the physics of turbulence and turbulence models. In the next section we shall use the simulation results to test the validity of $k-\epsilon$ two-equation turbulence models; they will be shown to be inadequate. In Section 7.3, a new one-point-closure, three-equation turbulence model is proposed to overcome the shortcomings of $k-\epsilon$ models. The rationale for constructing the three-equation model is discussed, a method for evaluating the model constants is described, and the performance of this three-equation model is presented.

7.2 Testing $k-\epsilon$ Turbulence Models

A. Background

The $k-\epsilon$ two-equation model was developed by Jones and Launder (1972) and has been used in many applications. In addition to the equations for the mean flow, this model uses two partial differential equations which describe the evolution of the turbulence kinetic energy ($k = q^2/2$) and its dissipation rate (ϵ). In this model, the length scale is taken to be $k^{3/2}/\epsilon$.

The equation which describes the turbulence kinetic energy can be derived by: taking the scalar product of Eq. (2-10) with the fluctuating velocity (u'_i) and taking the ensemble average. For homogeneous turbulence, the result is:

$$\frac{dk}{dt} = P - \epsilon \quad (7-1)$$

where $P = -R_{ij} \bar{u}'_i \bar{u}'_j$ is the rate of production of turbulence energy and $\epsilon = \nu \overline{u'_{i,j} u'_{i,j}}$ is the rate of viscous dissipation of turbulent kinetic energy; all quantities are per unit mass. $R_{ij} = \overline{u'_i u'_j}$; $-\rho R_{ij}$ is the Reynolds stress tensor.

One can derive an equation for the dissipation rate (ϵ) from the Navier-Stokes equations. The resulting equation is so complicated (El Tahry, 1983) that one has to model all of the terms in it. For homogen-

eous turbulence, the most commonly used model equation for the dissipation rate (ϵ) has the following form:

$$\frac{d\epsilon}{dt} = -C_2 \frac{\epsilon^2}{k} + C_1 \frac{P\epsilon}{k} + C_3 \epsilon S_{kk} \quad (7-2)$$

where the C_i are model constants. The first term on the right-hand side of Eq. (7-2) is the only one active in isotropic decaying turbulence, and the constant, C_2 , can be fixed by fitting it to that flow. The second term accounts for production by incompressible strain and/or shear, and C_1 is adjusted to produce the correct behavior for incompressible homogeneous straining and shearing flows (Reynolds, 1976). The third term accounts for production due to dilatation; the evaluation of C_3 requires data for compression flow; the results of Chapter V provide the necessary data (Reynolds, 1980).

Watkins (1977) suggested that the constant C_3 be unity as a natural outcome of his derivation. Houtt and Wong (1980) argued that the angular momentum of the turbulence should be conserved in rapid compression. Using this notion, Reynolds (1980) suggested that the the product of the turbulence length and velocity scales should remain fixed during fast compression, i.e.:

$$k^2/\epsilon = \text{constant} \quad (7-3)$$

To obtain the proper behavior of turbulent length scale in rapid isotropic compression, Reynolds proposed $C_3 = -2/3$.

Two sets of model constants are tabulated in Table 7.1. One was proposed by Launder and Spalding (1974) and extended by Watkins (1977) (hereafter denoted by LSW), and the other was proposed by Reynolds (1980). Note that not only are the magnitudes of model constant C_3 different in the two sets, but the signs disagree. Resolution of this discrepancy was one of the original goals of this work.

Table 7.1

The Values of the Model Constants in the k-ε Models

	C_1	C_2	C_3	C_μ
Launder, Spalding, (LSW) Watkins	1.44	1.92	1.00	0.09
Reynolds	1.0	11/6	-2/3	0.09

To close equations (7-1) and (7-2), additional equations must be provided for Reynolds stress tensor R_{ij} . In the k-ε model, R_{ij} is assumed to obey the Boussinesq constitutive equation:

$$R_{ij} = \frac{2}{3} k \delta_{ij} - 2\nu_t (S_{ij} - \frac{1}{3} S_{kk} \delta_{ij}) \quad (7-4)$$

where $2k = R_{ii}$, $S_{ij} = \frac{1}{2} (\bar{U}_{i,j} + \bar{U}_{j,i})$, ν_t is the eddy viscosity, and δ_{ij} is the Kronecker delta. The eddy viscosity ν_t is given by:

$$\nu_t = C_\mu \frac{k^2}{\epsilon} \quad (7-5)$$

where C_μ is chosen to be 0.09 to fit the ratio of shear stress to turbulence kinetic energy in local-equilibrium free shear layers, in which production and dissipation are equal.

Tests of k-ε models for isotropic compression, axisymmetric expansion, and one-dimensional compression flows will be described below. In these tests, Eqs. (7.1) and (7.2) were solved with given initial values of k and ϵ and the strain-rate tensor (S_{ij}) was prescribed as a function of time. The model (Eqs. (7-4) and (7-5)) for the Reynolds stress is used to compute the production.

B. Isotropic Compression Flow

The strain-rate tensor S_{ij} for isotropic compression is

$$S_{ij} = \begin{pmatrix} S(t) & 0 & 0 \\ 0 & S(t) & 0 \\ 0 & 0 & S(t) \end{pmatrix} \quad (7-6)$$

where $S < 0$. The model (Eqs. (7-4) and (7-5)) for the Reynolds stress is not needed, because the turbulence remains isotropic throughout the simulation. Predictions of the two $k-\epsilon$ models described above for four different strain rates, which correspond to runs SQF through SQI of Table 5.2, are shown in Figures 7-1 through 7-4, respectively. In the high strain-rate test (run SQF), both models predict k correctly but ϵ is badly predicted. In this case, the production dominates the dissipation, so the prediction of energy is good because the production is correctly computed (the Boussinesq relation, Eq. (7-4), is not needed in this flow). The dissipation is poorly predicted but has no effect on the prediction of the kinetic energy. In the moderate strain-rate runs shown in Figures 7-2 and 7-3, Reynolds' model predicts too high a dissipation rate causing the predicted energy (k) to be low. The LSW model predicts too low a dissipation rate and overpredicts the energy. In the slow compression rate test (run SQI), Reynolds' model produces good results while the LSW model overpredicts the energy. In these cases (except run SQF), the energy production and dissipation are nearly equal, so accurate prediction of dissipation rate is required for a good simulation.

The turbulence length scale is defined in $k-\epsilon$ model as

$$l = k^{3/2}/\epsilon \quad (7-7)$$

and is supposed to represent the integral length scale. Figure 5-20 shows the behavior of the integral length scale in this flow. Figures 7-5 and 7-6 show the behavior of the model length scale (l) predicted by the LSW and Reynolds' models, respectively. The LSW model predicts growth of the length scale during compression no matter how fast the flow is compressed. Morel and Mansour (1982) found that, in an engine simulation, the length scale predicted by the LSW model reached values several times the cylinder height near top dead center. This is clearly incorrect. The behavior of the length scale predicted by Reynolds' model is much more plausible. However, in order to get proper length scale behavior, Reynolds' model predicts too much dissipation in the fast compression case.

C. Incompressible Axisymmetric Expansion Flow

The strain-rate tensor S_{ij} for incompressible axisymmetric expansion flow is

$$S_{ij} = \begin{pmatrix} -2S & 0 & 0 \\ 0 & S & 0 \\ 0 & 0 & S \end{pmatrix} \quad (7-8)$$

where S is a positive constant. The Reynolds stress model, Eqs. (7-4) and (7-5), is needed to model the production. Results for three different strain rates, which correspond to runs EXQ, EXP, and EXO of Table 6.2, are shown in Figures 7-7 through 7-9, respectively. In the high and intermediate strain-rate tests (runs EXQ and EXP), predictions of k and ϵ by both models behave badly. This is mainly due to overprediction of the production which is, in turn, due to overprediction of the Reynolds stress in the high and intermediate strain-rate cases. The Reynolds stress model, Eqs. (7-4) and (7-5), causes the production of energy to be proportional to the square of the instantaneous strain rate and predicts a sudden jump in Reynolds stress when strain is turned on; neither of these predictions is correct. In the low strain-rate test (run EXO), the predictions of both models are good and there is almost no difference between them.

Figures 7-10 and 7-11 show the behavior of the turbulence length scale, defined by Eq. (7-7), predicted by the k - ϵ models. Again, both k - ϵ models predict growth of the length scale during the straining process no matter how large the strain rate. Figure 6-21 shows the evolution of the integral scale in this flow. As can be seen, both models perform poorly.

D. One-Dimensional Compression Flow

The strain-rate tensor S_{ij} for one-dimensional compression is

$$S_{ij} = \begin{pmatrix} S(t) & 0 & 0 \\ 0 & 0 & 0 \\ 0 & 0 & 0 \end{pmatrix} \quad (7-9)$$

where S is negative. The Reynolds stress model (Eqs. (7-4) and (7-5)) is used to calculate the production. Results for four strain rates, which correspond to runs ODB through ODE of Table 6.1, are shown in Figures 7-12 through 7-15, respectively. In the high strain-rate test (run ODB), both k and ϵ are badly missed due to incorrect modeling of the Reynolds stress. In the intermediate strain rate case (run ODC), Reynolds' model predicts too much dissipation but the energy is in good agreement with the simulation results. The LSW model does not behave as well as Reynolds' model. In the slow strain-rate tests (runs ODD and ODE), Reynolds' model does an excellent job of predicting the turbulence energy (k), dissipation rate (ϵ), and Reynolds stress (R_{11}). The LSW model behaves better than in the high strain-rate tests, but is not as good as Reynolds' model.

The evolution of the integral length scale for this flow is shown in Figure 6-13. Figures 7-16 and 7-17 show the behavior of the turbulence length scale predicted by the two models. The LSW model predicts growing length scales during compression which is not correct, while Reynolds' model shows plausible turbulence length-scale behavior (except in case ODB).

E. Comments on Turbulence Length Scale Model

The turbulence length scale, which is supposed to represent the integral length scale, is modeled as $k^{3/2}/\epsilon$. Figures 7-18 through 7-20 show the evolution of $k^{3/2}/\epsilon$, based on the exact quantities obtained from the full simulations, as a function of total strain in isotropic compression, axisymmetric expansion, and one-dimensional compression flows, respectively. The longitudinal integral length scale in the compression direction for each flow is shown for comparison. As can be seen, this turbulence length-scale model behaves more or less correctly only in the axisymmetric expansion flow. For the compression flows, this model does not represent the integral length scale, because of the decrease in the dissipation in compression flows.

F. Testing Constants in Modeled Dissipation Equation

The following is a method of deriving the model constants in the dissipation equation from the data. For homogeneous turbulent flows, the model equation for the dissipation rate is Eq. (7-2). In the isotropic compression flow, Eq. (7-2) can be rewritten:

$$-\frac{k}{2} \frac{d\epsilon}{\epsilon dt} = (-2C_1 + 3C_3) \left(\frac{P}{\epsilon}\right) + C_2 \quad (7-10)$$

While in incompressible axisymmetric expansion flow, it can be rearranged to

$$-\frac{k}{2} \frac{d\epsilon}{\epsilon dt} = -C_1 \left(\frac{P}{\epsilon}\right) + C_2 \quad (7-11)$$

We can use the simulation results to evaluate the validity of the model. The turbulence kinetic energy, dissipation, and production rate are obtained from the full-turbulence simulations. The time derivative of the dissipation is obtained by spline fitting the dissipation and differentiating the result; the derivatives obtained in this way contain considerable uncertainty. Despite the uncertainty, we should be able to discern trends; however, quantitative results need to be accepted with care.

Equations (7-10) and (7-11) suggest that plots of $-\frac{k}{2} \frac{d\epsilon}{\epsilon dt}$ against P/ϵ should be straight lines if model constants are indeed pure constants. Figures 7-21 and 7-22 show this kind of plots for isotropic compression and incompressible axisymmetric expansion flows. The high strain-rate simulations (runs SQF and EXQ) are not used here, due to unacceptable uncertainty caused by too few data points. As can be seen from Fig. 7-21, for isotropic compression, the slopes $(-2C_1 + 3C_3)$ are the same for the various runs, but the intercepts (C_2) are not. We conclude that the model needs modification. Figure 7-22 shows that the situation is even worse for incompressible axisymmetric strain flow.

Thus, the parameters in modeled dissipation equation cannot be pure constants if these data are to be fit. Dependence of the parameters on P/ϵ is precluded by the linearity of Fig. 7-21. We considered the possibility that the model constants depend on Reynolds number.

However, the Reynolds number is large enough that the model constants should not depend on this parameter. Furthermore, when the "constants" were plotted vs. Reynolds number, the variation of C_2 was opposite what one would expect. The remaining possibility is that the parameters are functions of the total strain ratio.

To test this possibility, we re-sorted the data from the various runs according to the value of the total strain. For each total strain, a least squares fit to the data was made. Good fits were obtained, indicating that the model constants can be considered functions of total strain. $k-\epsilon$ models that incorporate this dependence would require solution of several additional differential equations which describe the evolution of model constants. This procedure is cumbersome and not good modeling practice.

We have now tested the $k-\epsilon$ models as thoroughly as we can. The summarized results will be presented in the next section.

G. Summary of $k-\epsilon$ Model Testing

We found that $k-\epsilon$ models perform well in low strain-rate flows in which the production of energy is of about the same order of magnitude as the dissipation, i.e., the turbulence is in an "equilibrium" state. When the strain is so strong that the flow structure is out of equilibrium, $k-\epsilon$ models do not perform well. Furthermore, the model turbulence length scale does not represent the integral length scale well in the compression cases. Finally, the "constants" in the modeled dissipation equation cannot be pure constants.

Thus $k-\epsilon$ models do not perform well for high strain rate. A turbulence model capable of predicting flows accurately with a wide range of strain rates is needed. In the next section we shall propose a three-equation turbulence model which meets this need.

7.3 A One-Point-Closure Three-Equation Turbulence Model

A. Motivation

In two-equation (k - ϵ) models, the turbulence kinetic energy determines the turbulence velocity scale, while the dissipation plays two roles: it is the rate of destruction of turbulence kinetic energy, (Eq. (7-1)), and it determines the turbulence length scale (Eq. (7-7)). The dissipation cannot do both jobs simultaneously in high strain-rate flows in which the flow structure is out of equilibrium. To decouple the dissipation and the length and time scales and introduce the minimum of additional complexity, a one-point-closure, three-equation turbulence model is proposed. In particular, a model equation for a turbulence time scale (τ) is introduced. It is to be solved together with the dynamic equations for the turbulence kinetic energy (k) and its dissipation rate (ϵ). At present, this model equation is limited to homogeneous flows. The method of evaluating the constants of this model is discussed and tests of the performance of the model are presented below.

B. Homogeneous Isotropic Decay Flow

We begin by looking at the model as applied to isotropic decay. The three-equation model consists of three differential equations. For isotropic-decay, the exact dynamic equation of the turbulence kinetic energy (Eq. (7-1)) reduces to:

$$\frac{dk}{dt} = -\epsilon \quad (7-12)$$

The model equation for the dissipation rate is modified to include the new time scale:

$$\frac{d\epsilon}{dt} = -\frac{\epsilon}{\tau} \quad (7-13)$$

where τ is the new turbulence time scale; this equation replaces Eq. (7-2).

We need a model equation for τ to close this set of equations; for isotropic decay it can be derived as follows.

The turbulence kinetic energy decays according to the power law (Reynolds, 1976):

$$k \sim (t - t_0)^{-n} \quad (7-14)$$

The exponent (n) is reasonably well established as 1.2 at high Reynolds number; t_0 is an effective origin. The dissipation rate (ϵ) then decays as

$$\epsilon \sim -\frac{dk}{dt} \sim n(t - t_0)^{-n-1} \quad (7-15)$$

Then Eq. (7-13) requires

$$\tau = \frac{1}{n+1} (t - t_0) \quad (7-16)$$

or, in differential form:

$$\frac{d\tau}{dt} = \frac{n}{n+1} = \frac{5}{11} \quad (7-17)$$

Equations (7-12), (7-13), and (7-17) give the correct behavior of the turbulence in isotropic-decay. Of course, the added complication is unnecessary in this case. Also the constant in Eq. (7-17) should be a function of Reynolds number; this function could be evaluated using the data of Shirani et al. (1981).

C. Return to Equilibrium

When strain is applied to the flow, all the turbulence quantities are modified. In particular, the turbulence time scale (τ) is pushed away from equilibrium, (cf. Eq. (7-16)). After the strain is removed, the turbulence tends to return to an equilibrium state. The simplest modification of the time-scale equation that will accomplish this (and be dimensionally correct) is:

$$\frac{d\tau}{dt} = \frac{5}{11} + C_5 \left(\frac{\epsilon\tau}{k} - \frac{6}{11} \right) \quad (7-18)$$

The form of the second term is selected because, in isotropic turbulence, $\epsilon\tau/k = 6/11$. Defining $z = \epsilon\tau/k$ and manipulating Eqs. (7-12), (7-13), and (7-18), we obtain

$$\frac{dz}{dt} = \frac{\epsilon}{k} (1 + C_5) \left(z - \frac{6}{11}\right) \quad (7-19)$$

In isotropic-decay, Eq. (7-19) becomes trivial. Thus, in the $(z, dz/dt)$ phase plane $(6/11, 0)$ is an equilibrium point.

If z is perturbed from its equilibrium point in the direction of larger z and $1 + C_5 > 0$, then dz/dt will be positive and z will be driven away from the equilibrium state; if z is displaced in the opposite direction and $1 + C_5 > 0$, z will also be driven away from the equilibrium state. Therefore,

$$C_5 < -1 \quad (7-20)$$

is required to assure return to equilibrium.

D. Isotropic Compression Flow

When turbulence is subjected to strain, the large eddies interact with the mean flow and extract kinetic energy from the mean motion. For isotropic-compression flows, the mean-deformation tensor $\bar{U}_{i,j}$ is shown in Eq. (2-26). The turbulence energy production is $P_{DIL} = -\frac{2}{3} k \bar{U}_{k,k}$. In the presence of homogeneous isotropic compression, the three-equation model can be written

$$\frac{dk}{dt} = P_{DIL} - \epsilon \quad (7-21)$$

$$\frac{d\epsilon}{dt} = -\frac{\epsilon}{\tau} + C_4 \frac{P_{DIL}\epsilon}{k} \quad (7-22)$$

$$\frac{d\tau}{dt} = \frac{5}{11} + C_5 \left(\frac{\epsilon\tau}{k} - \frac{6}{11}\right) + C_{6,ISO} S_{ISO}\tau \quad (7-23)$$

The additional terms reflect the effects of the mean flow on turbulence quantities. Note that one could use $1/\tau$ in place of ϵ/k in the last term of Eq. (7-22). The choice used in Eq. (7-22) was tried first and worked; other authors may wish to try the other possibility.

The three model constants (C_4 , C_5 , and $C_{6,ISO}$) can be evaluated from the results of isotropic-compression simulations. A method of accomplishing this follows. The turbulence kinetic energy, dissipation rate, and production used here are obtained from full-turbulence simulations. The time derivative of the dissipation is obtained by spline fitting the dissipation and differentiating the result. The slope of the curves in Fig. 7-21 suggests $C_4 = 1$. If this value is accepted, the turbulence time scale (τ) is the only remaining unknown in Eq. (7-22) and can be evaluated.

The model constants C_5 and $C_{6,ISO}$ are then evaluated from Eq. (7-23). The turbulence kinetic energy, dissipation rate, and mean strain rate (S_{ISO}) are obtained from full-turbulence simulations. The turbulence time scale (τ) is obtained from Eq. (7-22) as described above, and its time derivative is obtained by spline fitting the time scale and differentiating the result. The model constants C_5 and $C_{6,ISO}$ are the remaining unknowns in Eq. (7-23) and can be evaluated. Keeping in mind that model constant C_5 must be less than -1 (Eq. (7-20)), we find that $C_5 = -1.1$ and $C_{6,ISO} = -0.5$.

The performance of the three-equation model for isotropic compression with four different compression rates (runs SQF through SQI) is shown in Figures 7-23 through 7-26, respectively. The predictions of the $k-\epsilon$ models are plotted for comparison. The evolution of the model time scale for each simulation is shown in Figure 7-27. As can be seen, the three-equation model is better than both the LSW and Reynolds' models at all strain-rates. This is not surprising, because we fit the model constants to this flow.

E. Incompressible Axisymmetric Expansion Flow

In incompressible axisymmetric expansion flow, the mean-deformation tensor is

$$\bar{U}_{1,j} = \begin{pmatrix} -2S & 0 & 0 \\ 0 & S & 0 \\ 0 & 0 & S \end{pmatrix} \quad (7-24)$$

where S is a positive constant. The turbulence energy production through mean motion is $P_{INC} = -R_{ij} \bar{U}_{i,j}$. The three-equation model in the presence of homogeneous incompressible mean strain can be written

$$\frac{dk}{dt} = P_{INC} - \epsilon \quad (7-25)$$

$$\frac{d\epsilon}{dt} = -\frac{\epsilon}{\tau} + C_1 \frac{P_{INC} \epsilon}{k} \quad (7-26)$$

$$\frac{d\tau}{dt} = \frac{5}{11} + C_5 \left(\frac{\epsilon \tau}{k} - \frac{6}{11} \right) + C_{6,AXI} S \tau \quad (7-27)$$

The constants multiplying the strain terms are allowed to differ from those used in the isotropic compression case. The model constant C_5 was determined to be -1.1 in the preceding section. The remaining two unknown model constants (C_1 and $C_{6,AXI}$) can be evaluated from the results of homogeneous, incompressible, axisymmetric, expansion flow simulations.

The method used to evaluate the model constants C_1 and $C_{6,AXI}$ is similar to that presented in the preceding section. The turbulence kinetic energy, dissipation rate, and production are obtained from full-turbulence simulations. The time derivative of the dissipation is obtained by spline fitting the dissipation and differentiating the result. This leaves two unknowns (C_1 and τ) to be determined in Eq. (7-26). It was found that, for incompressible axisymmetric expansion flows, the "production of dissipation" predicted by $k-\epsilon$ models is too weak and the dissipation is underpredicted in high strain-rate flows. This means that C_1 must be larger than 1.44 (the value in the LSW model) for this type of flow. By numerical experiments, we found $C_1 = 2$. Equation (7-26) then provides τ . Given the evolution of turbulence kinetic energy, dissipation rate, strain rate (from full-turbulence simulations), turbulence time scale (from Eq. (7-26)), and the time derivative of the turbulence time scale (from numerical differentiation), model constant $C_{6,AXI}$ of Eq. (7-27) is found to be -2 .

Since the model constants are evaluated from the "actual production", one needs an accurate Reynolds stress model to have a satisfactory prediction. The Boussinesq Reynolds stress model does not work well when the strain rate is high; its drawbacks were discussed in the preceding section. Therefore, a Reynolds stress model has been developed for this flow. It will also be applied to the one-dimensional compression flow in the next section.

F. Reynolds Stress Model

An exact transport equation for the components of the Reynolds stress tensor can be obtained by multiplying Eq. (2-10) by u'_j , adding the result to the equation obtained by switching the subscripts i and j , and averaging the result:

$$\frac{\partial R_{ij}}{\partial t} + \bar{U}_k R_{ij,k} = P_{ij} + T_{ij} - D_{ij} + J_{ijk,k} \quad (7-28)$$

where $\rho R_{ij} = \rho \overline{u'_i u'_j}$ is the Reynolds stress tensor.

The first term on the right side of Eq. (7-28), called the "production tensor", is the creation of Reynolds stress from the mean flow.

$$P_{ij} = - (R_{ik} S_{kj} + R_{jk} S_{ki}) + (R_{ik} \Omega_{kj} + R_{jk} \Omega_{ki}) \quad (7-29)$$

here $S_{ij} = \frac{1}{2} (\bar{U}_{i,j} + \bar{U}_{j,i})$ is the mean strain rate tensor and $\Omega_{ij} = \frac{1}{2} (\bar{U}_{i,j} - \bar{U}_{j,i})$ is the mean rotation tensor.

T_{ij} is the "transfer tensor",

$$T_{ij} = \frac{1}{\rho} \overline{p' (u'_{i,j} + u'_{j,i})} \quad (7-30)$$

It has zero trace in an incompressible turbulence field and is supposedly responsible for intercomponent redistribution of the Reynolds stress. It has the form of a correlation between the fluctuating pressure and the fluctuating strain rate.

D_{ij} is the "dissipation tensor",

$$D_{ij} = 2\nu \overline{u'_{i,k} u'_{j,k}} \quad (7-31)$$

It dissipates turbulent kinetic energy through viscous action.

The tensor J_{ijk} is the diffusive flux of R_{ij} ,

$$J_{ijk} = \frac{1}{\rho} (\overline{p'u'_i} \delta_{jk} + \overline{p'u'_j} \delta_{ik}) + \overline{u'_i u'_j u'_k} - \nu R_{ij,k} \quad (7-32)$$

By definition, homogeneous flows have no convection or diffusion, and Eq. (7-28) reduces to

$$\frac{dR_{ij}}{dt} = P_{ij} + T_{ij} - D_{ij} \quad (7-33)$$

P_{ij} is explicitly determined from the Reynolds stress, but models are needed for T_{ij} and D_{ij} .

We first address the pressure-strain terms. An exact equation for the fluctuating pressure, p' , can be derived by taking the divergence of Eq. (2-10). We get

$$\frac{1}{\rho} p'_{,ii} = -2\overline{u'_{i,j} u'_{j,i}} - \overline{u'_{i,j} u'_{j,i}} \quad (7-34)$$

The source term in this Poisson equation can be split into two parts, giving rise to two components of the pressure: a "rapid" part $p^{(1)}$ given by

$$\frac{1}{\rho} p^{(1)}_{,ii} = -2\overline{u'_{i,j} u'_{j,i}} \quad (7-35)$$

and a "slow" part $p^{(2)}$ given by

$$\frac{1}{\rho} p^{(2)}_{,ii} = -\overline{u'_{i,j} u'_{j,i}} \quad (7-36)$$

Note that the "rapid" pressure, $p^{(1)}$, involves the mean deformation explicitly. Hence the imposition of a mean deformation immediately changes the "rapid" pressure. Solving Eq. (7-35) for $p^{(1)}$ (see Reynolds, 1984), we get

$$\frac{1}{\rho} \overline{p^{(1)} u'_{i,q}} = 2\overline{u'_{p,j} M_{ijpq}} \quad (7-37)$$

where

$$M_{ijpq} = \int \frac{k^k p^k}{k^2} E_{ij}(k, t) dk \quad (7-38)$$

Models for M_{ijpq} have been proposed by various modelers (Hanjalic and Launder, 1972; Launder, Reece, and Rodi, 1975; Hanjalic and Launder, 1976; Lumley, 1978; and Lumley, 1979). The particular model we use was proposed by Reynolds (1984) and is similar to the others. It has the following form for divergence-free turbulence field.

$$M_{ijpq} = q^2 \left\{ \frac{2}{15} \delta_{ij} \delta_{pq} - \frac{1}{30} (\delta_{ip} \delta_{jq} + \delta_{iq} \delta_{jp}) - \left(\frac{1}{3} + \frac{11}{3} A_1 \right) \delta_{ij} b_{pq} \right. \\ \left. + A_1 (\delta_{ip} b_{jq} + \delta_{iq} b_{jp} + \delta_{jp} b_{iq} + \delta_{jq} b_{ip}) + \left(\frac{1}{3} - \frac{4}{3} A_1 \right) \delta_{pq} b_{ij} \right\} \quad (7-39)$$

where $q^2 = 2k$, b_{ij} , defined in Eq. (6-2), is the Reynolds stress anisotropy tensor, δ_{ij} is the Kronecker delta, and A_1 is the model constant. The rapid part of the pressure-strain term is then modeled as

$$T_{ij}^{(1)} = q^2 \left\{ \frac{2}{5} S_{ij} - \frac{2}{15} S_{kk} \delta_{ij} + 4A_1 S_{kk} b_{ij} - 6A_1 (b_{ik} S_{kj} + b_{jk} S_{ki} \right. \\ \left. - \frac{2}{3} b_{nm} S_{nm} \delta_{ij}) - \left(\frac{4}{3} + \frac{14}{3} A_1 \right) (b_{ik} \Omega_{kj} + b_{jk} \Omega_{ki}) \right\} \quad (7-40)$$

By insisting that this model agree with rapid distortion theory, the constant A_1 is found to be $-2/7$ (Reynolds, 1984). For slower mean deformation rates, Reynolds (1984) added quadratic terms in b_{ij} to M_{ijpq} . This complicates the model.

In order to keep the model simple without losing the essence of modeling philosophy, we model $T_{ij}^{(1)}$ by using linear terms in b_{ij} only (Eq. (7-40)), but allow the coefficient A_1 to be a function of the ratio of production to dissipation to compensate.

In one-dimensional compression or axisymmetric expansion flow, $T_{ij}^{(1)}$ is diagonal. Furthermore, since $T_{22}^{(1)} = T_{33}^{(1)}$ and $T_{ij}^{(1)}$ is traceless, the entire tensor can be expressed in terms of $T_{11}^{(1)}$, for which the model (Eq. (7-40)) becomes:

$$T_{11}^{(1)} = -\frac{8}{5} kS + 4A_1 (3R_{11} - 2k) S \quad (7-41)$$

where S is the mean strain rate of Eq. (7-24). Full-turbulence simulation (Lee and Reynolds, 1985) provides the actual rapid pressure-strain ($T_{11}^{(1)}$), turbulence kinetic energy (k), Reynolds stress (R_{11}), and mean strain rate (S). These data allow us to evaluate the model coefficient A_1 as a function of the ratio of energy production to dissipation ($P/\epsilon = (3R_{11} - 2k)S/\epsilon$). We found

$$A_1 = -0.34 + 0.12 \exp(-0.3 P/\epsilon) \quad (7-42)$$

Figure 7-28 shows how Eq. (7-42) fits the full-turbulence simulation data. As can be seen, Reynolds' value ($A_1 = -2/7$) is good for moderate and high strain rates (runs EXP and EXQ), to which rapid distortion theory may be applied.

It is customary to model the combination of the slow pressure-strain term and dissipation anisotropy tensor together (Lumley and Newman, 1977; Lumley, 1978; Lumley, 1979; Rogallo, 1981; and Reynolds, 1984). This tensor ϕ_{ij} is defined as

$$\phi_{ij} \equiv -\frac{1}{\epsilon} \left[\frac{1}{\rho} p^{(2)} (\overline{u'_{i,j} + u'_{j,i}}) - (D_{ij} - D_{kk} \delta_{ij}/3) \right] \quad (7-43)$$

where $D_{kk} = 2\epsilon$. ϕ_{ij} is modeled by

$$\phi_{ij} = A_0 b_{ij} \quad (7-44)$$

where b_{ij} is the anisotropy tensor of R_{ij} and A_0 is a model constant. In this flow, ϕ_{11} is the only independent component of ϕ_{ij} . We evaluated A_0 from ϕ_{11} and b_{11} obtained from full simulations. Figure 7-29 shows the evolution of A_0 for flows with a wide range of strain rates. As can be seen, there is a considerable scatter. However, ϕ_{11} is not important in moderate and high strain-rate cases (runs EXP and EXQ), because the mean strain rate is so high that mean flow dictates the evolution of turbulence. We chose $A_0 = 1$ to fit the low strain-rate flow. Note that this choice might not give accurate modeling of the relaxation following removal of strain. For further results on modeling this term, see Lee and Reynolds (1985).

Combining Eqs. (7-33), (7-29), and (7-43), the modeled Reynolds stress transport equation for homogeneous flow is written as

$$\frac{dR_{ij}}{dt} = P_{ij} + T_{ij}^{(1)} - \epsilon \phi_{ij} - \frac{2}{3} \epsilon \delta_{ij} \quad (7-45)$$

where P_{ij} , T_{ij} , ϕ_{ij} are given by Eqs. (7-29), (7-40), and (7-44), respectively. When this Reynolds stress model is applied to incompressible axisymmetric flow, it further reduces to the following form (bear in mind that only dR_{11}/dt is needed).

$$\frac{dR_{11}}{dt} = P_{11} + T_{11}^{(1)} - \epsilon \phi_{11} - \frac{2}{3} \epsilon$$

where

$$\left. \begin{aligned} P_{11} &= 4R_{11}S \\ T_{11}^{(1)} &= -\frac{8}{5}kS + 4A_1(3R_{11} - 2k)S \\ A_1 &= -0.34 + 0.12 \exp(-0.3 P/\epsilon) \\ P &= (3R_{11} - 2k)S \\ \phi_{11} &= A_0(R_{11}/2k - 1/3) \\ A_0 &= 1 \end{aligned} \right\} (7-46)$$

Note that $R_{22} = R_{33} = (2k - R_{11})/2$ in this type of flow.

The performance of this model (Eqs. (7-25), (7-26), (7-27), and (7-46)) for axisymmetric expansion flow at three strain-rates (runs EXQ through EXO) are shown in Figures 7-30 through 7-32, respectively. The predictions of the $k-\epsilon$ models are plotted for comparison. The evolution of the model time scale for each simulation is shown in Figure 7-33. In high and moderate strain-rate flows (runs EXQ and EXP), the better performance of the $k-\epsilon-\tau$ model can be attributed largely to the introduction of the new Reynolds stress model. In low strain-rate flow (run EXO), the $k-\epsilon-\tau$ model is slightly better than $k-\epsilon$ models, and there is no distinct difference between the LSW and Reynolds' models. Again, the $k-\epsilon-\tau$ model is tuned to the full simulation results for this flow. It is expected to perform well.

G. One-Dimensional Compression Flow

The mean-deformation tensor for one-dimensional compression is

$$\bar{U}_{1,j} = \begin{pmatrix} S(t) & 0 & 0 \\ 0 & 0 & 0 \\ 0 & 0 & 0 \end{pmatrix} \quad (7-47)$$

where S is negative. One-dimensional compression can be considered as a combination of the isotropic-compression and axisymmetric expansion. Formally,

$$\begin{pmatrix} S & 0 & 0 \\ 0 & 0 & 0 \\ 0 & 0 & 0 \end{pmatrix} = \begin{pmatrix} S/3 & 0 & 0 \\ 0 & S/3 & 0 \\ 0 & 0 & S/3 \end{pmatrix} + \begin{pmatrix} 2S/3 & 0 & 0 \\ 0 & -S/3 & 0 \\ 0 & 0 & -S/3 \end{pmatrix} \quad (7-48)$$

Both the dilatation and divergence-free parts of the mean flow contribute to the energy production. The $k-\epsilon-\tau$ model has the following form

$$\frac{dk}{dt} = P_{INC} + P_{DIL} - \epsilon \quad (7-49)$$

$$\frac{d\epsilon}{dt} = -\frac{\epsilon}{\tau} + C_1 \frac{P_{INC}\epsilon}{k} + C_4 \frac{P_{DIL}\epsilon}{k} \quad (7-50)$$

$$\frac{d\tau}{dt} = \frac{5}{11} + C_5 \left(\frac{\epsilon\tau}{k} - \frac{6}{11} \right) + C_{6,ISO} \frac{S}{3} \tau + C_{6,AXI} \frac{S}{3} \tau \quad (7-51)$$

where $P_{INC} = (2k - 3R_{11})S/3$ and $P_{DIL} = -2kS/3$. The model constants obtained from the isotropic-compression and axisymmetric expansion flows will be used without modification. They are given in Table 7.2. The Reynolds stress model tuned to incompressible axisymmetric expansion flow (Eq. (7-46)) is also employed here. Since the dilatation part of the production, P_{DIL} , does not contribute to the rapid pressure-strain tensor, the production in the expression for the model coefficient A_1 , Eq. (7-42), should be P_{INC} . This model (Eqs. (7-46), (7-49), (7-50), and (7-51)) reduces to those for the two preceding cases in the appropriate limits.

Table 7.2

The Values of the Model Constants in the $k-\epsilon-\tau$ Model

C_1	2.0
C_4	1.0
C_5	-1.1
$C_{6,ISO}$	-0.5 (for isotropic compression flow)
$C_{6,AXI}$	-2.0 (for axisymmetric expansion flow)

The three-equation model (Eqs. (7-49) through (7-51)) and the Reynolds stress model (Eq. (7-46)) were used to predict one-dimensional compression simulations with four strain rates (runs ODB through ODE). The predictions are shown in Figures 7-34 through 7-37. The predictions of the two-equation models are plotted for comparison. The evolution of the model time scale for each simulation is shown in Figure 7-38. In the rapid distortion case (run ODB), the $k-\epsilon-\tau$ model is superior to the $k-\epsilon$ models, due to the introduction of an accurate Reynolds stress model. In moderate strain-rate cases (runs ODC and ODD), the three-equation model reflects the behavior of the turbulence better than do the two-equation models. In slow strain-rate case (run ODE), there is little difference between the $k-\epsilon-\tau$ and $k-\epsilon$ models.

It is encouraging that a model derived from other flows can be used to predict these flows and, in particular, that the effects of the various strains appear to be additive.

H. Summary

In this section we summarize the one-point-closure, three-equation, turbulence model. For homogeneous flows, this model is

$$\frac{dk}{dt} = P_{INC} + P_{DIL} - \epsilon \quad (7-49)$$

$$\frac{d\epsilon}{dt} = -\frac{\epsilon}{\tau} + C_1 \frac{P_{INC}\epsilon}{k} + C_4 \frac{P_{DIL}\epsilon}{k} \quad (7-50)$$

$$\frac{d\tau}{dt} = \frac{5}{11} + C_5 \left(\frac{\epsilon\tau}{k} - \frac{6}{11} \right) + C_{6,ISO} S_{ISO} \tau + C_{6,AXI} S_{AXI} \tau \quad (7-52)$$

where $P_{INC} = -R_{ij}(\bar{U}_{i,j} - \frac{1}{3}\bar{U}_{k,k}\delta_{ij})$, $P_{DIL} = -\frac{2}{3}k\bar{U}_{k,k}$, S is the strain rate, and the C_i are the model constants tabulated in Table 7.2. Equation (7-49) is an exact equation for turbulence kinetic energy.

Equation (7-50) is a model equation for the dissipation rate (ϵ). The first term on the right side of Eq. (7-50) is the destruction term. The second and third terms are the "production of dissipation" due to the incompressible and dilatation parts of the mean flow. The model constants C_1 and C_4 are evaluated from the results of axisymmetric expansion and isotropic-compression flow simulations, respectively. It was found that $C_1 = 2$ and $C_4 = 1$.

Equation (7-52) describes the evolution of the turbulence time scale (τ). The first term on the right gives the correct behavior of the turbulence quantities in isotropic-decay flow. The second term is a return-to-equilibrium term, and the rest of the terms represent the influence of the mean strain on the turbulence time scale. Stability analysis shows that model constant C_5 must be less than -1. We chose C_5 to be -1.1 from numerical experiments. The new model constants are $C_{6,ISO} = -0.5$ and $C_{6,AXI} = -2$. Three independent strain flows are needed to complete the model of the effect of strain on the turbulence time scale. In this work we covered two independent strains (isotropic compression and incompressible axisymmetric expansion), so one additional term may be needed in Eq. (7-52) to produce a complete model. The effects of the strains appear to be additive. One more building-block flow such as axisymmetric contraction or plane strain is needed to calibrate the remaining model constant in the turbulence time-scale equation.

A new Reynolds stress model was developed by fitting the simulation results for incompressible axisymmetric expansion flow. It has the form

$$\frac{dR_{ij}}{dt} = P_{ij} + T_{ij}^{(1)} - \epsilon\phi_{ij} - \frac{2}{3}\epsilon\delta_{ij} \quad (7-45)$$

$$\left. \begin{aligned}
 P_{ij} &= - (R_{ik} S_{kj} + R_{jk} S_{ki}) + (R_{ik} \Omega_{kj} + R_{jk} \Omega_{ki}) \\
 S_{ij} &= \frac{1}{2} (\bar{U}_{1,j} + \bar{U}_{j,1}) \\
 \Omega_{ij} &= \frac{1}{2} (\bar{U}_{1,j} - \bar{U}_{j,1})
 \end{aligned} \right\} (7-29)$$

$$\begin{aligned}
 T_{ij}^{(1)} &= q^2 \left\{ \frac{2}{5} S_{ij} - \frac{2}{15} S_{kk} \delta_{ij} + 4A_1 S_{kk} b_{ij} - 6A_1 (b_{ik} S_{kj} + b_{jk} S_{ki} \right. \\
 &\quad \left. - \frac{2}{3} b_{nm} S_{nm} \delta_{ij}) - \left(\frac{4}{3} + \frac{14}{3} A_1 \right) (b_{ik} \Omega_{kj} + b_{jk} \Omega_{ki}) \right\} \quad (7-40)
 \end{aligned}$$

$$\left. \begin{aligned}
 A_1 &= -0.34 + 0.12 \exp(-0.3 P_{INC}/\epsilon) \\
 b_{ij} &= \frac{R_{ij}}{R_{kk}} - \frac{\delta_{ij}}{3}
 \end{aligned} \right\} (7-42)$$

$$\left. \begin{aligned}
 \phi_{ij} &= A_0 b_{ij} \\
 A_0 &= 1
 \end{aligned} \right\} (7-44)$$

Model constants A_0 and A_1 are tuned to fit incompressible axisymmetric expansion flow; they were also used in predicting one-dimensional compression flow, and their performance was good. This model has not been tested in flows with rotation, and so should be used with caution in shear flows.

The performance of the $k-\epsilon-\tau$ model is slightly better than that of the $k-\epsilon$ models in low strain-rate flows. In high strain-rate flows, the flow structure is out of equilibrium and the $k-\epsilon-\tau$ model reflects the changing physics much better than do the $k-\epsilon$ models. Some engineering flows occur in the range in which the differences of the models are significant. In summary, a one-point-closure, three-equation turbulence model which accurately calculates four types of flows— isotropic decay, isotropic compression, axisymmetric expansion, and one-dimensional compression flows— for a wide range of strain rates has been developed.

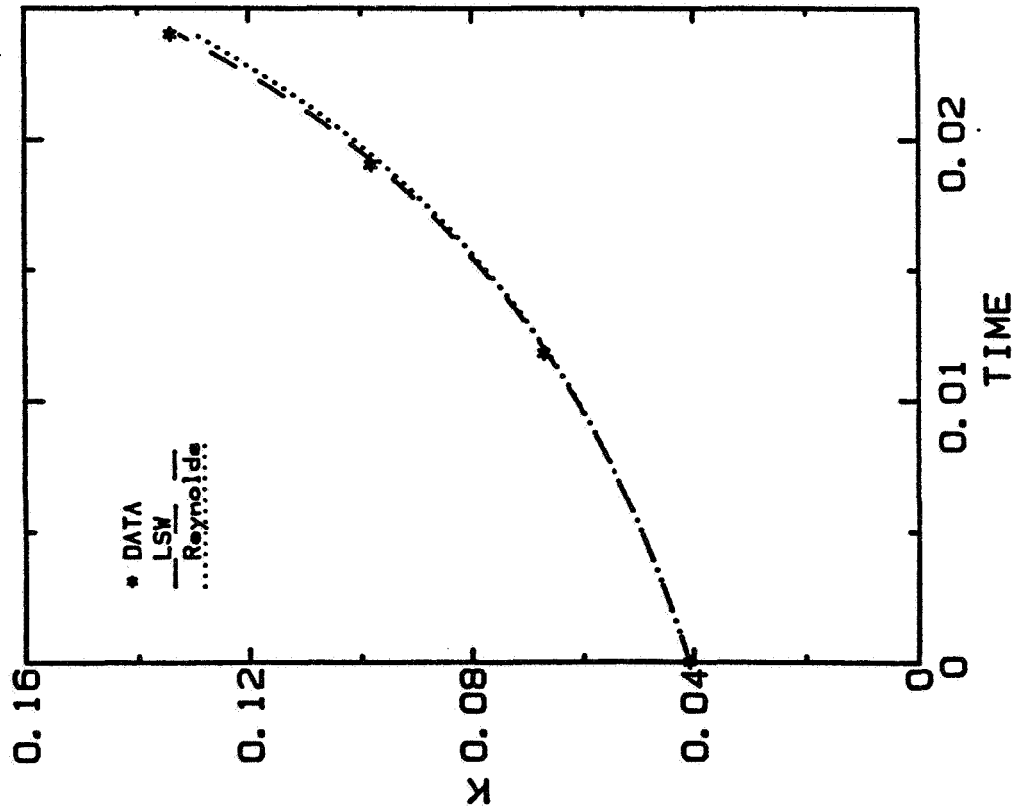


Fig. 7-1(a). The prediction of the turbulent kinetic energy by k- ϵ models for run SQF.

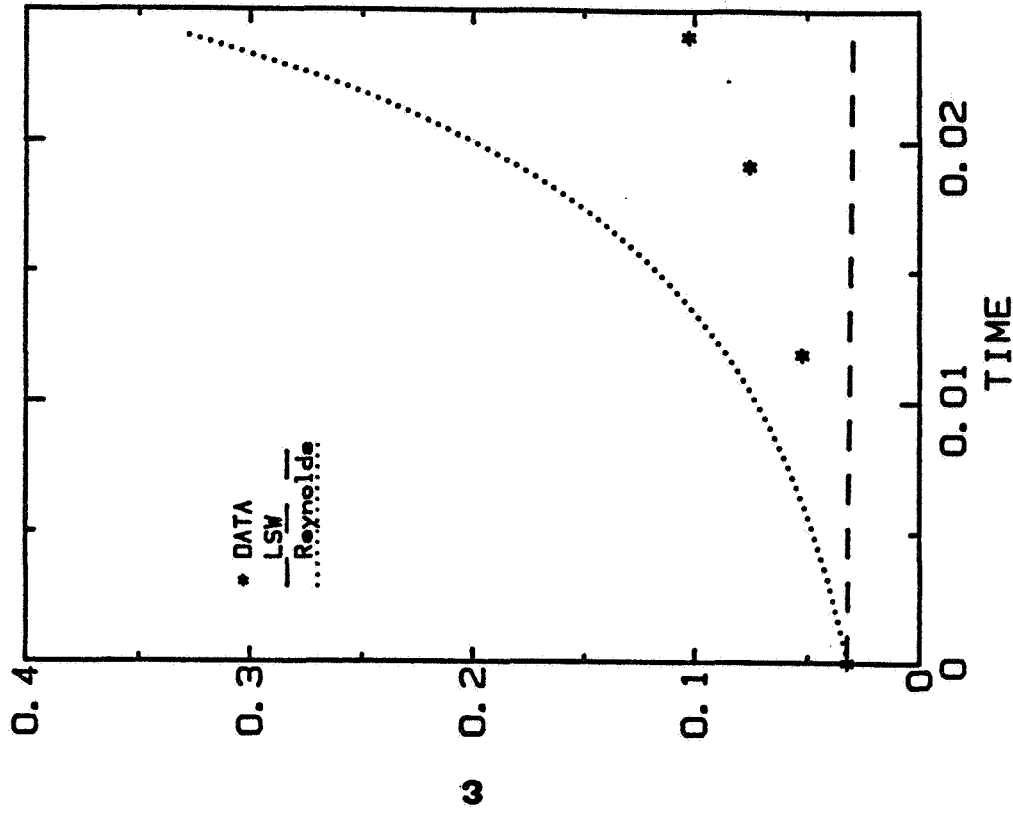


Fig. 7-1(b). The prediction of the dissipation rate by k- ϵ models for run SQF.

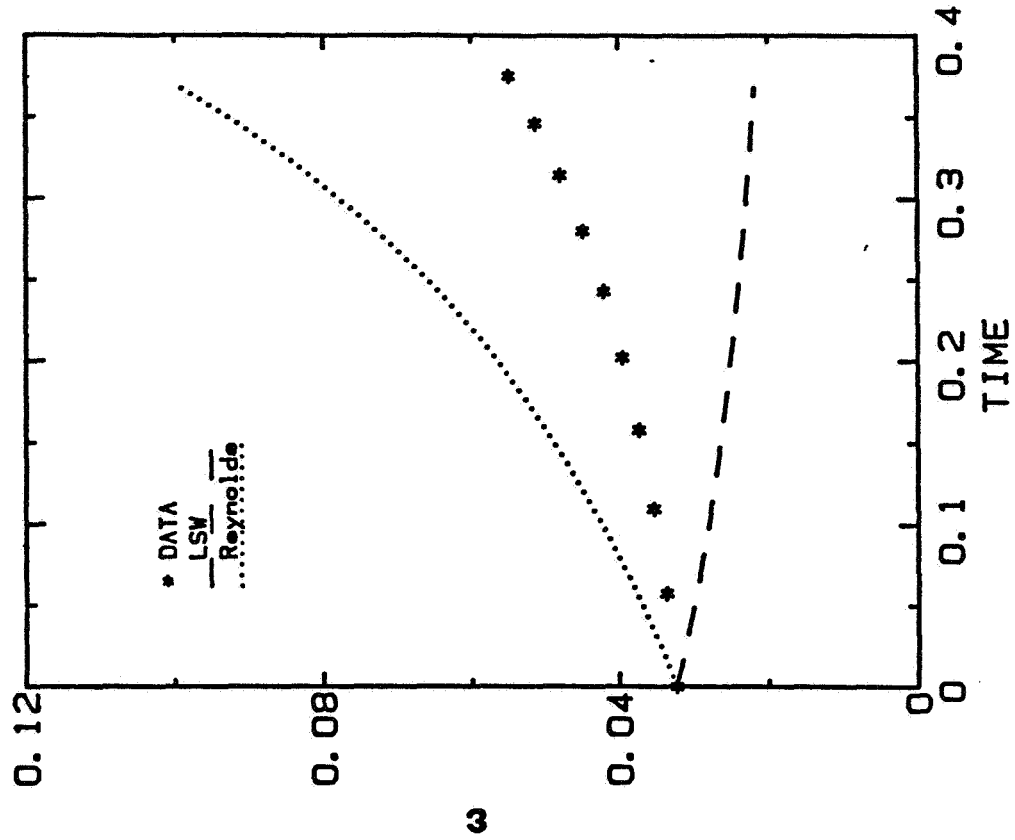


Fig. 7-2(b). The prediction of the dissipation rate by k-ε models for run SQG.

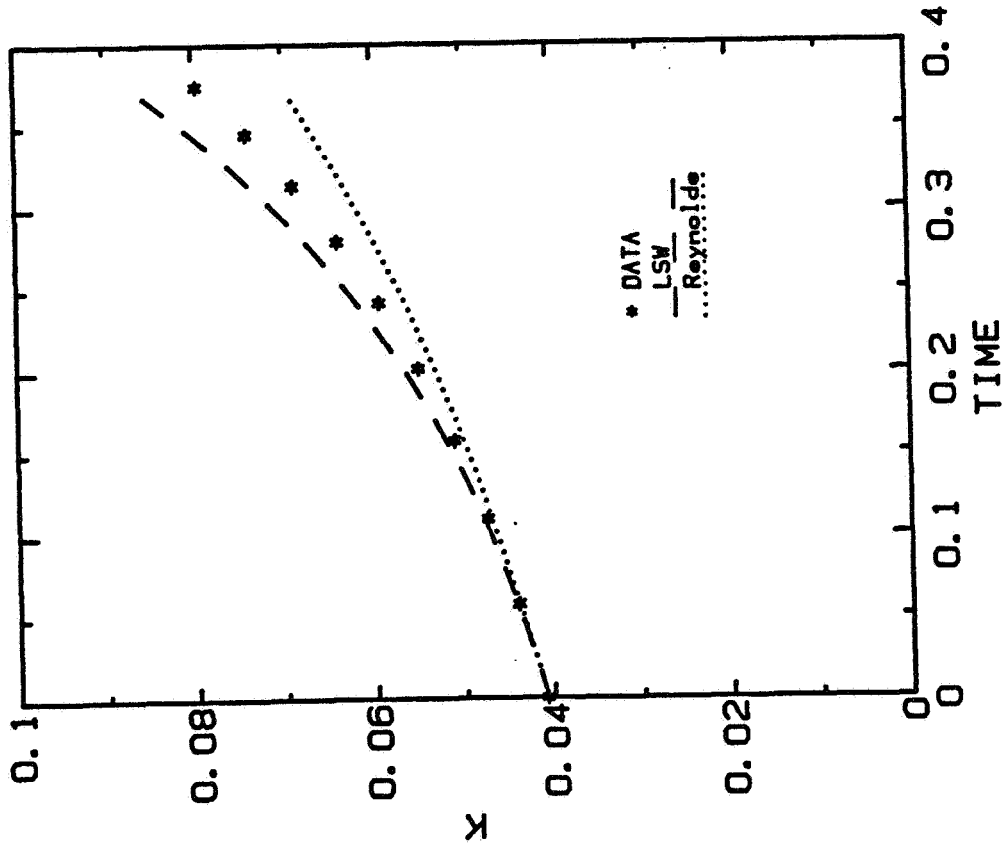


Fig. 7-2(a). The prediction of the turbulent kinetic energy by k-ε models for run SQG.

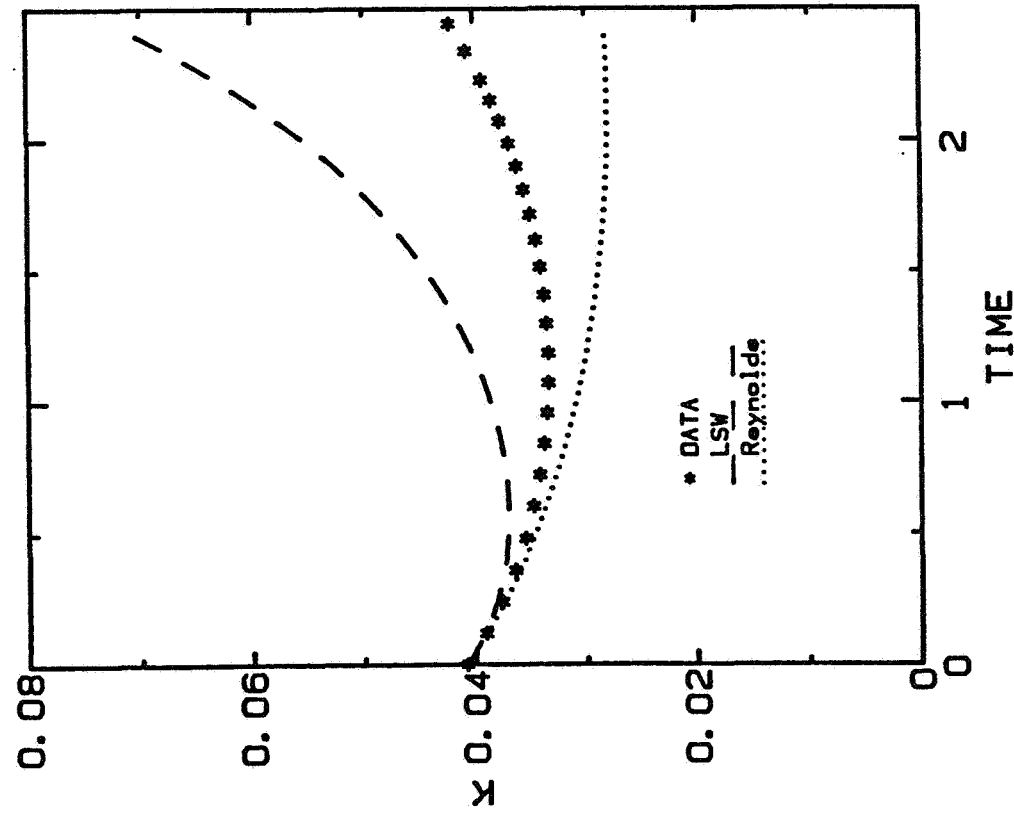


Fig. 7-3(a). The prediction of the turbulent kinetic energy by k- ϵ models for run SQH.

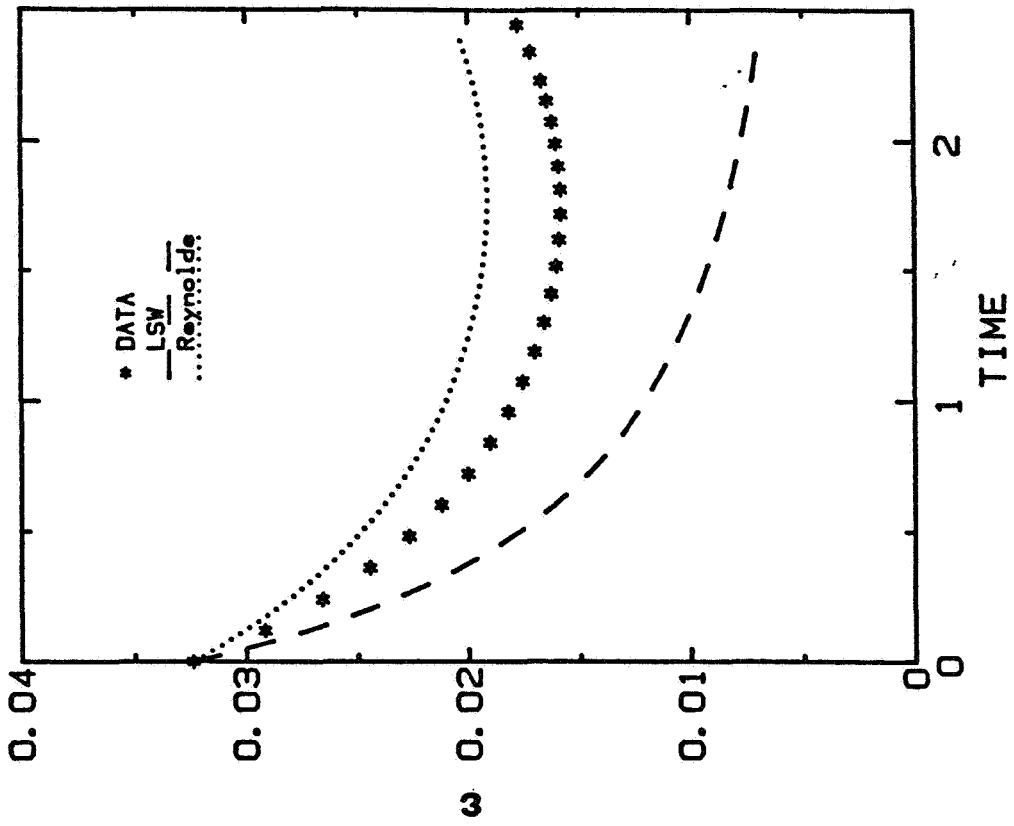


Fig. 7-3(b). The prediction of the dissipation rate by k- ϵ models for run SQH.

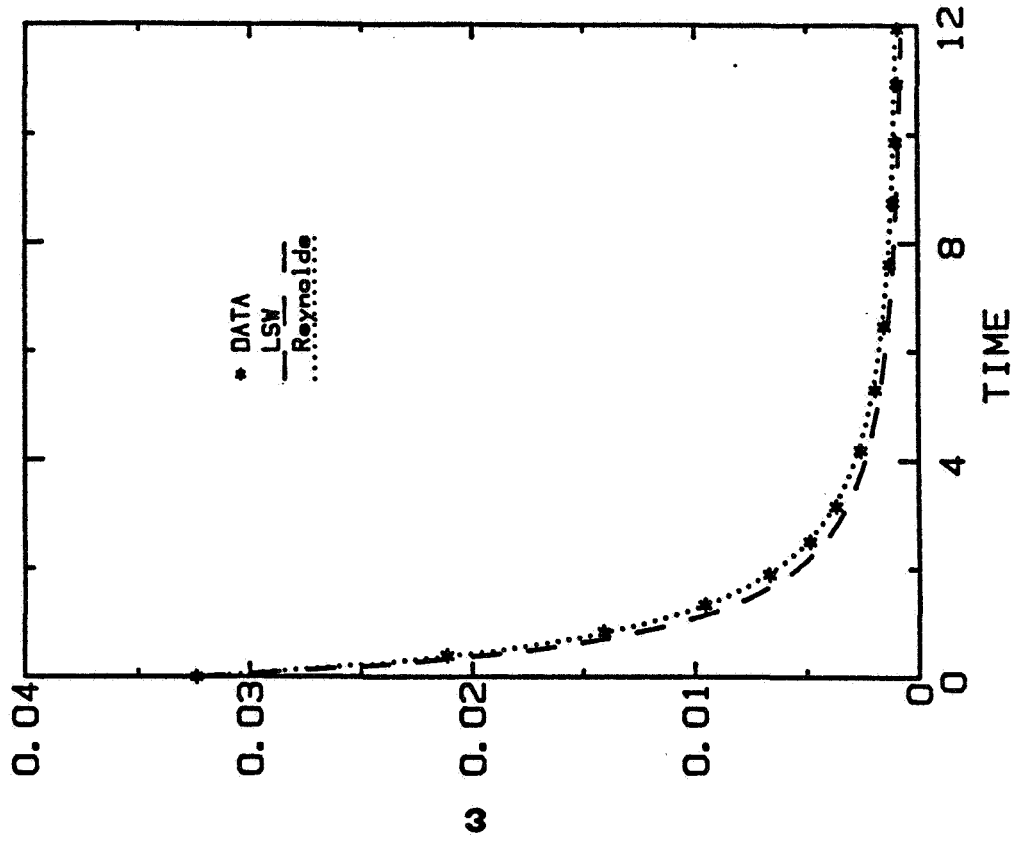


Fig. 7-4(b). The prediction of the dissipation rate by k- ϵ models for run SQ1.

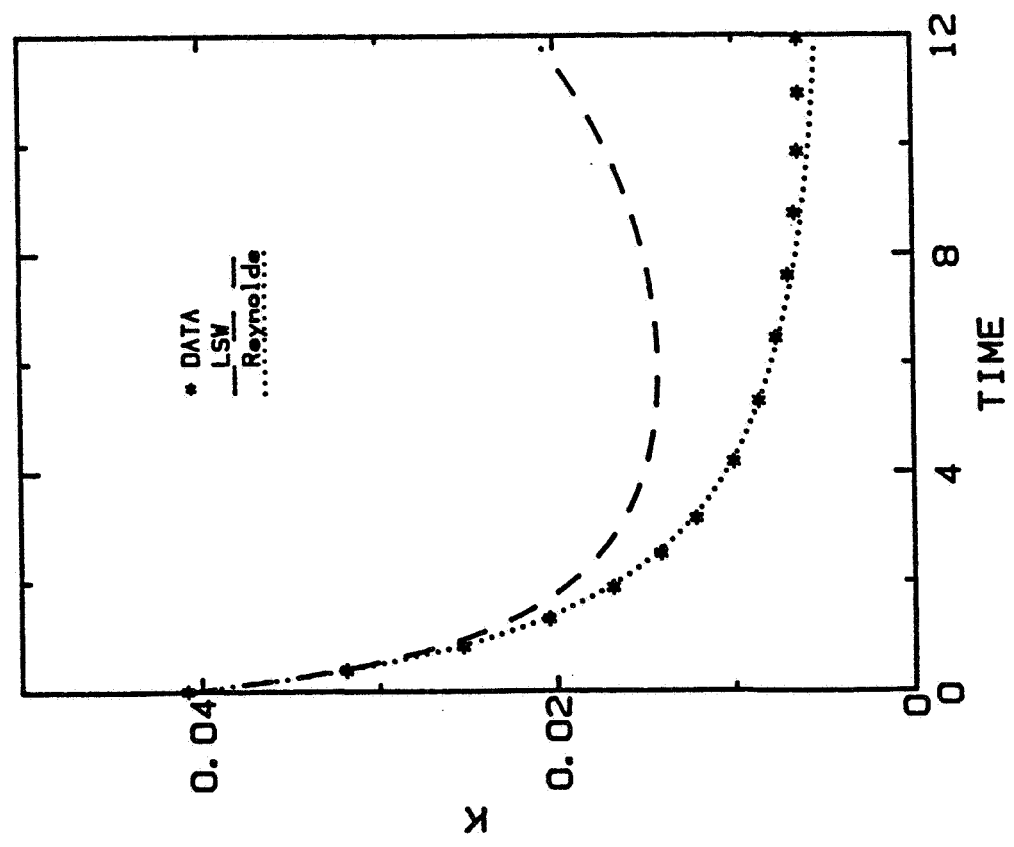


Fig. 7-4(a). The prediction of the turbulent kinetic energy by k- ϵ models for run SQ1.

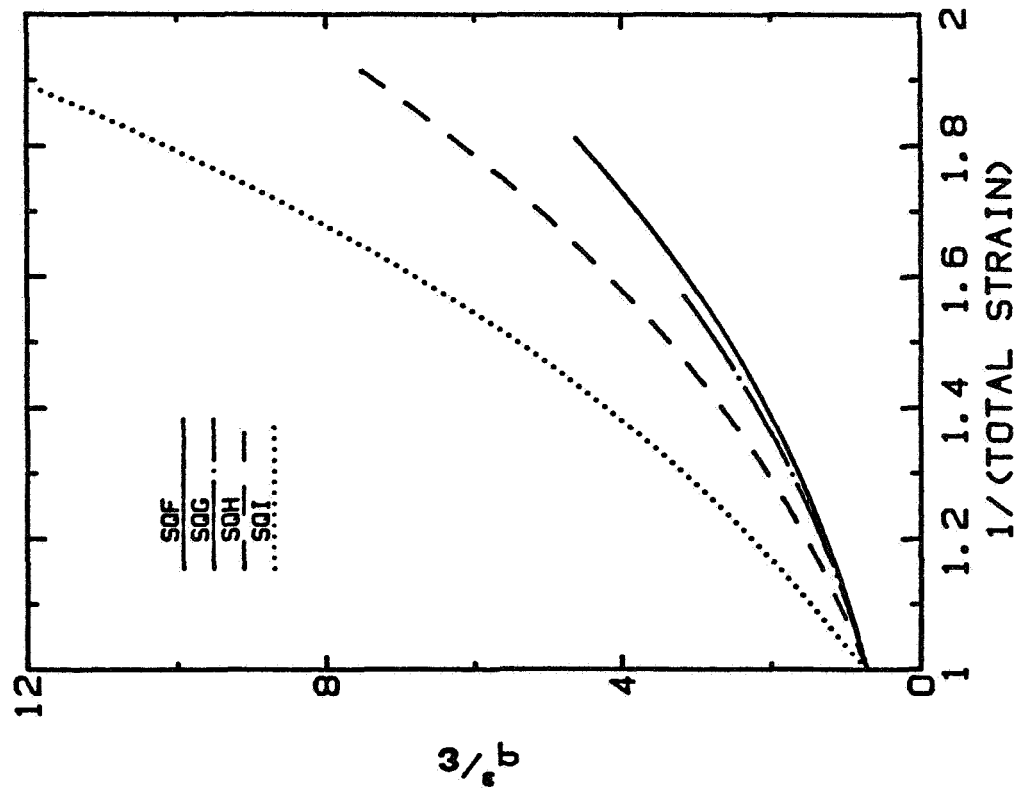


Fig. 7-5. The prediction of the turbulence length scale by the LSW model for isotropic compression simulations.

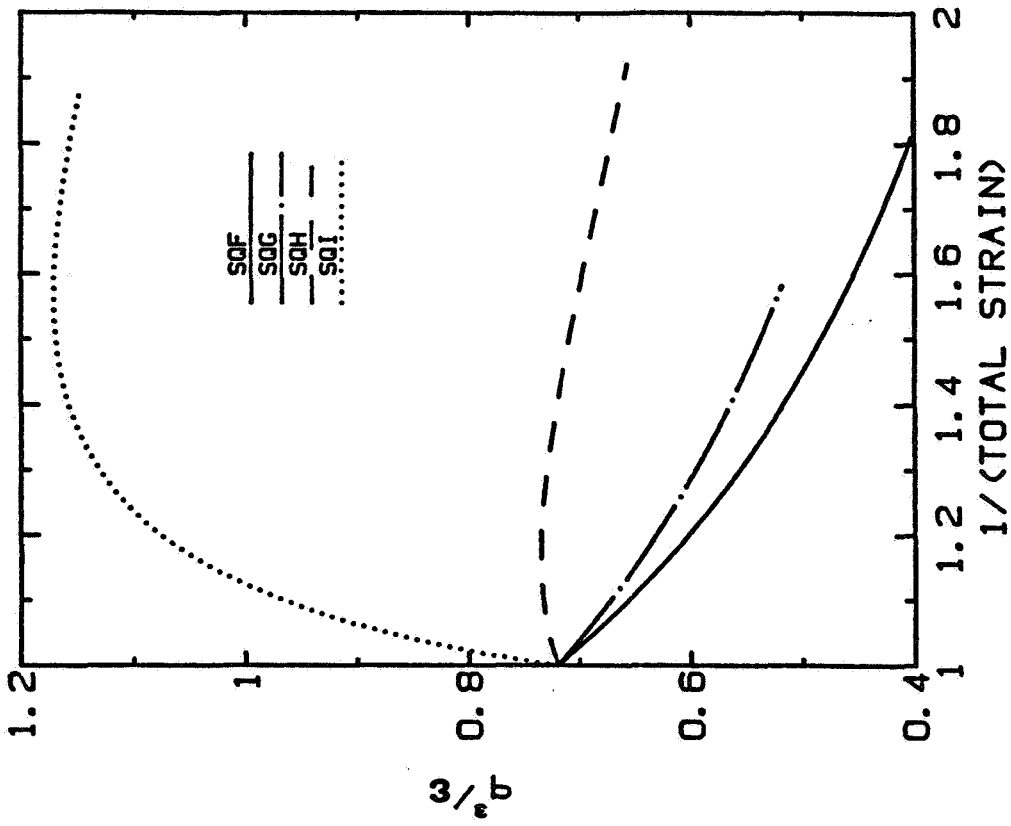


Fig. 7-6. The prediction of the turbulence length scale by Reynolds' model for isotropic compression simulations.

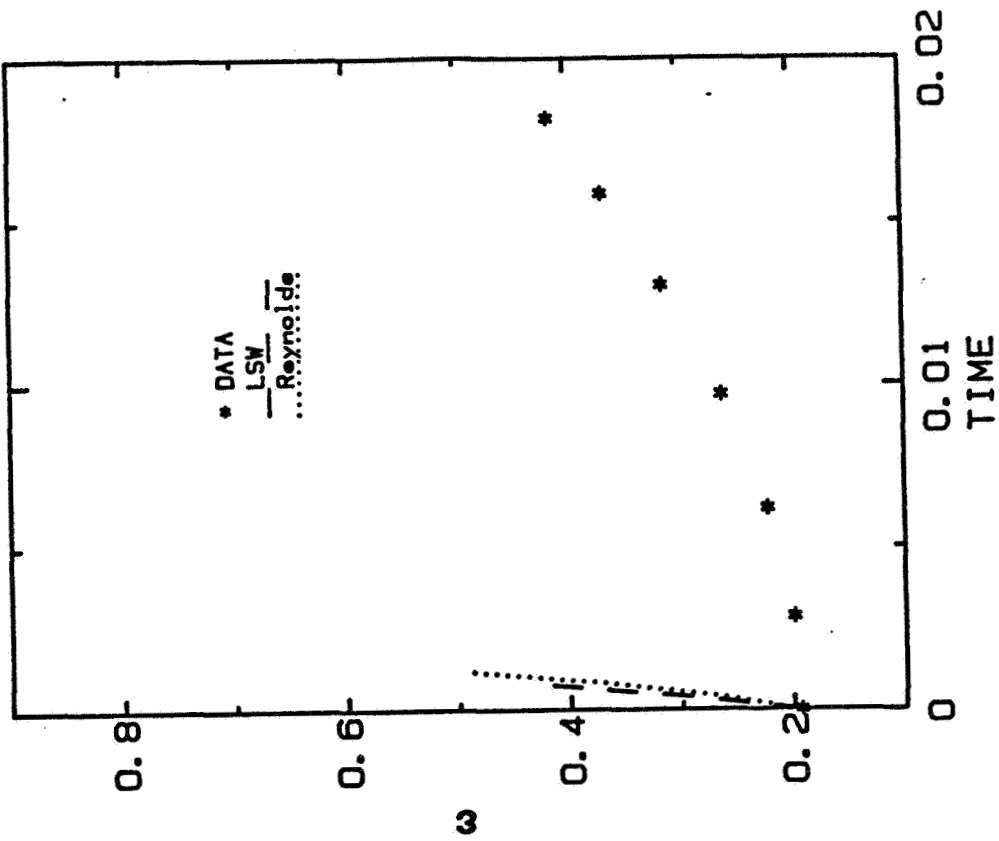


Fig. 7-7(a). The prediction of the turbulent kinetic energy by k- ϵ models for run EXQ.

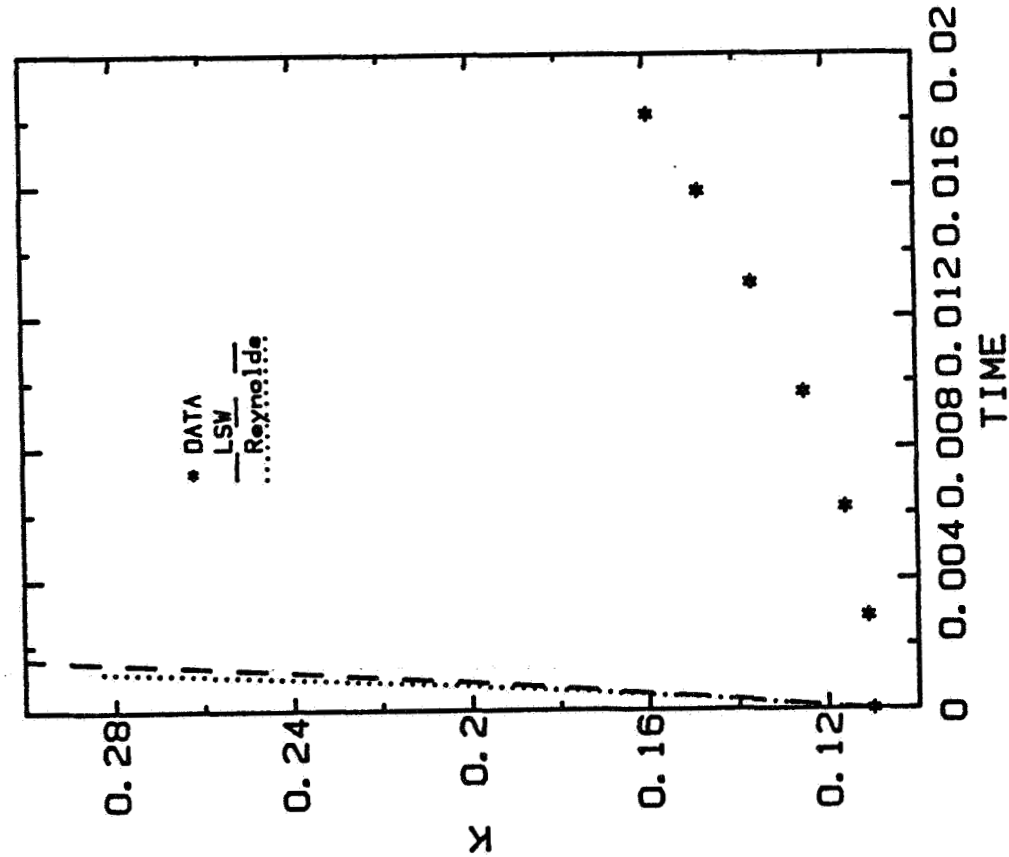


Fig. 7-7(b). The prediction of the dissipation rate by k- ϵ models for run EXQ.

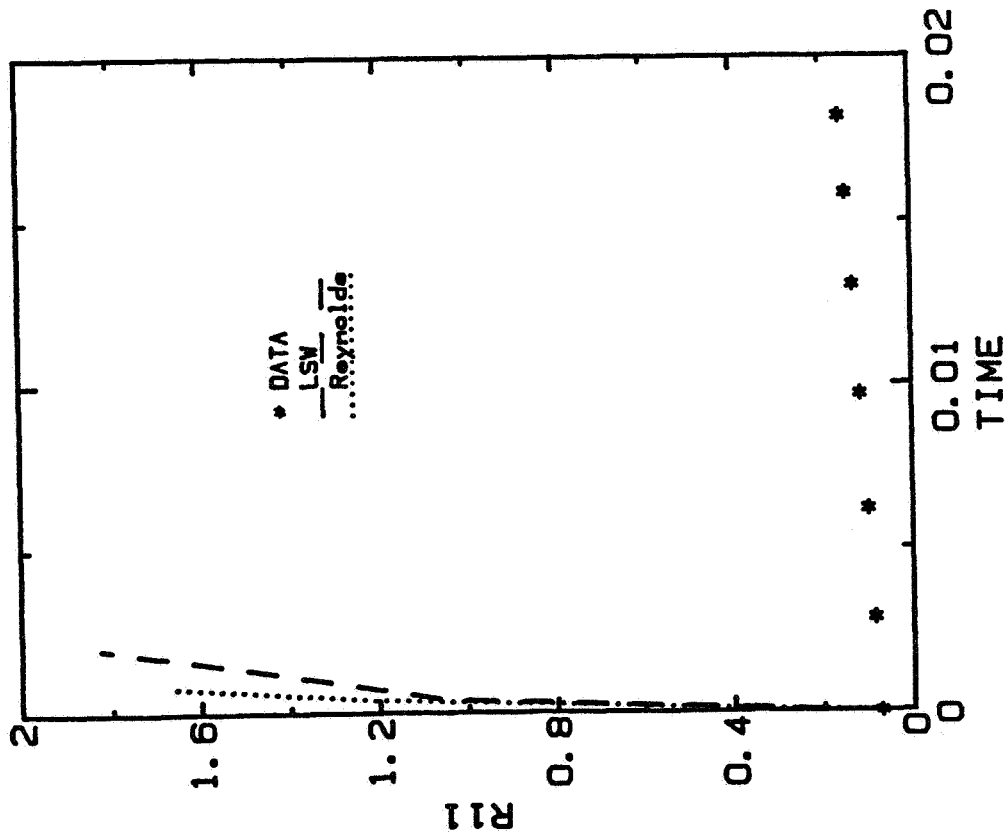


Fig. 7-7(c). The prediction of R_{11} by k- ϵ models for run EXQ.

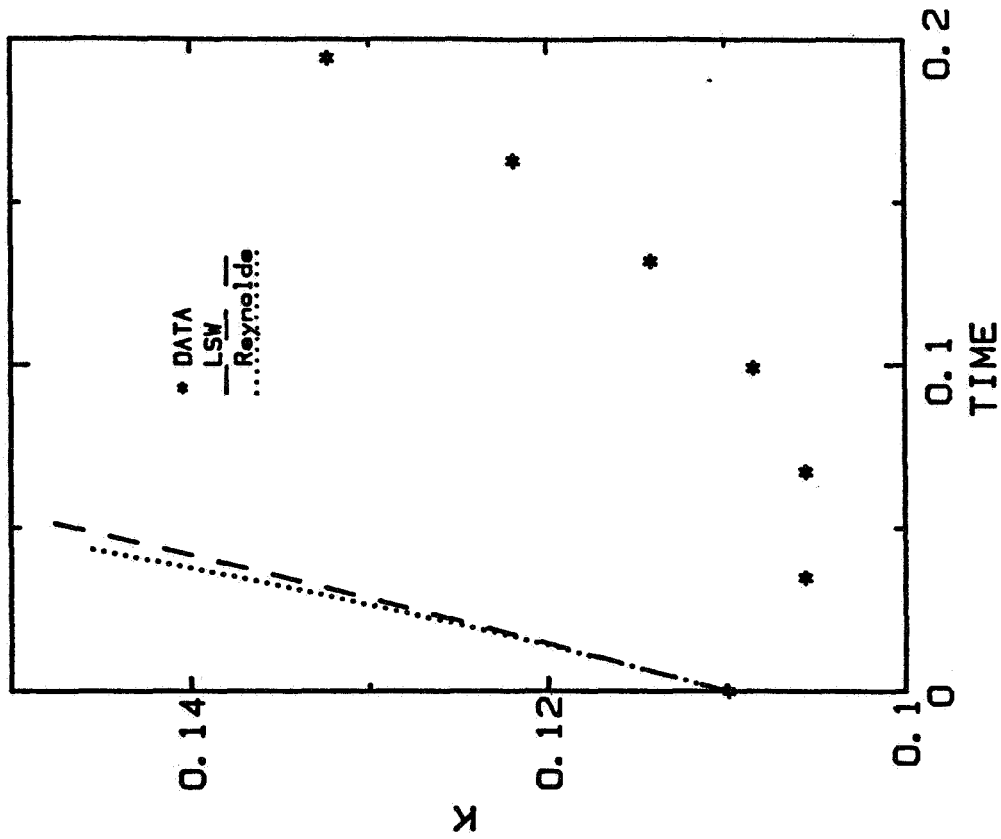


Fig. 7-8(a). The prediction of the turbulent kinetic energy by k- ϵ models for run EXP.

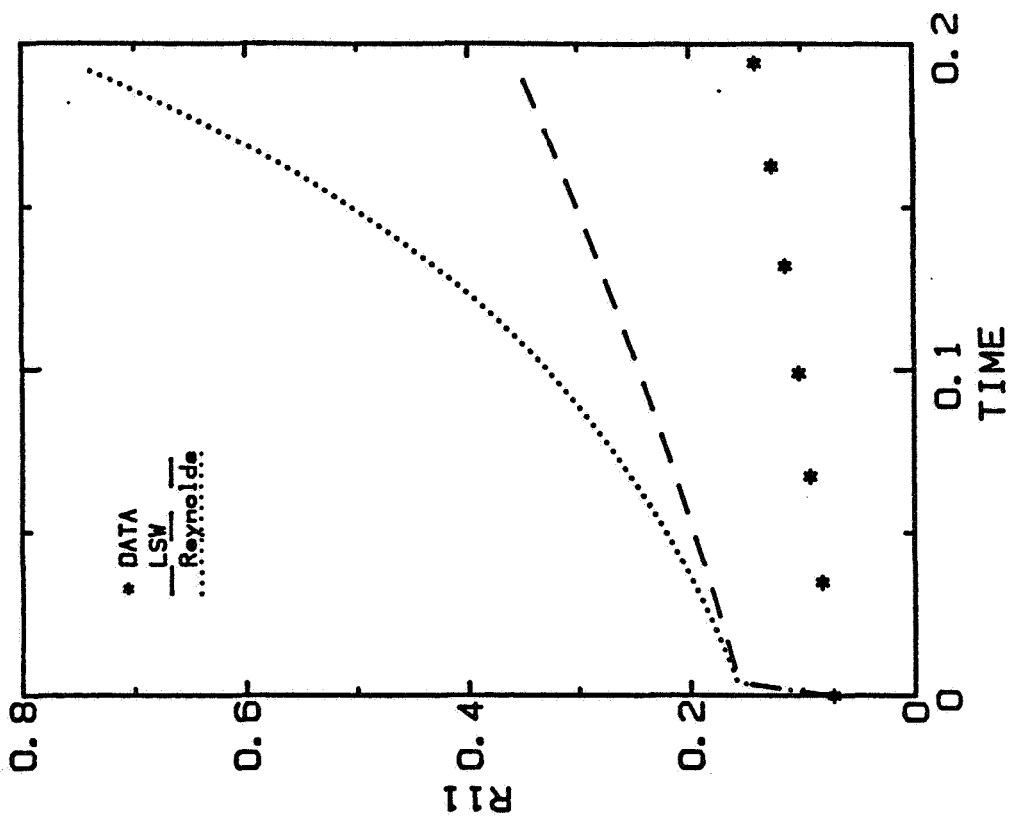


Fig. 7-8(c). The prediction of R_{11} by $k-\epsilon$ models for run EXP.

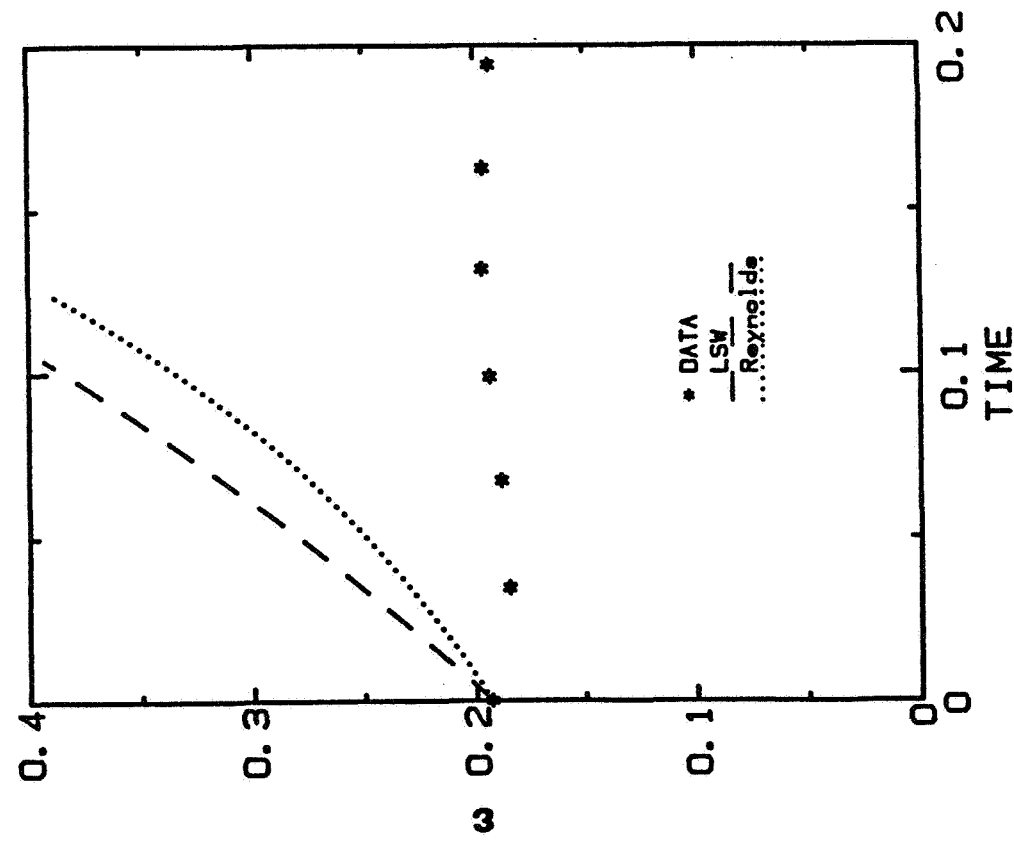


Fig. 7-8(b). The prediction of the dissipation rate by $k-\epsilon$ models for run EXP.

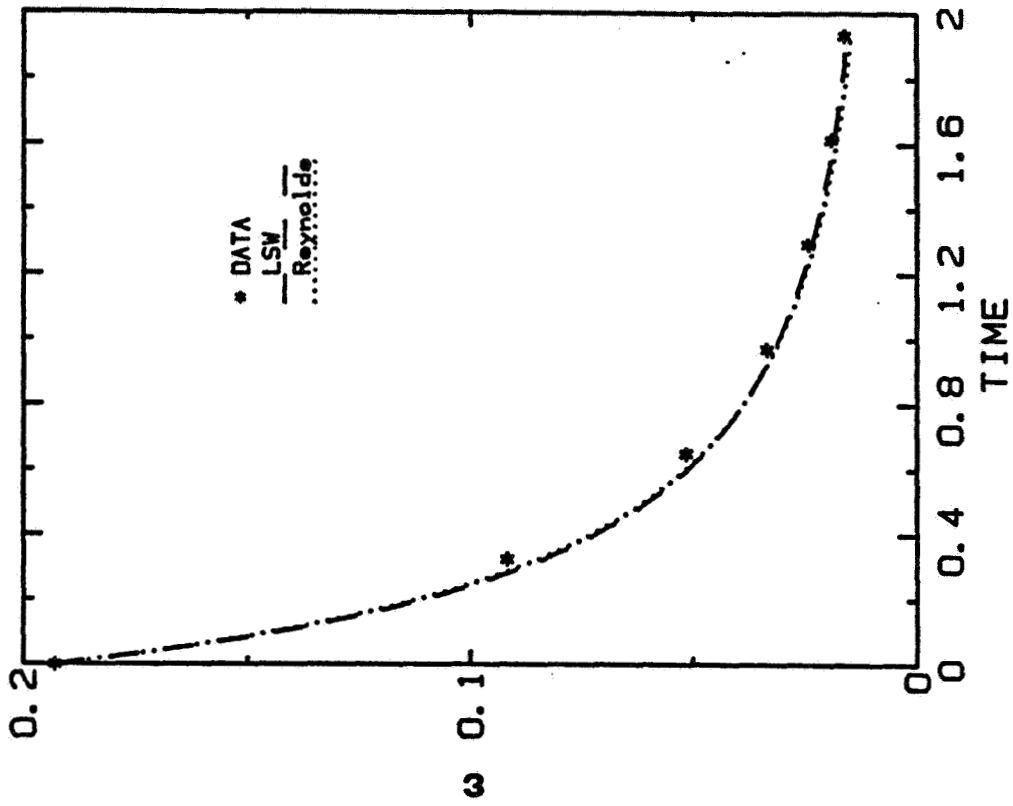


Fig. 7-9(a). The prediction of the turbulent kinetic energy by k- ϵ models for run EXO.

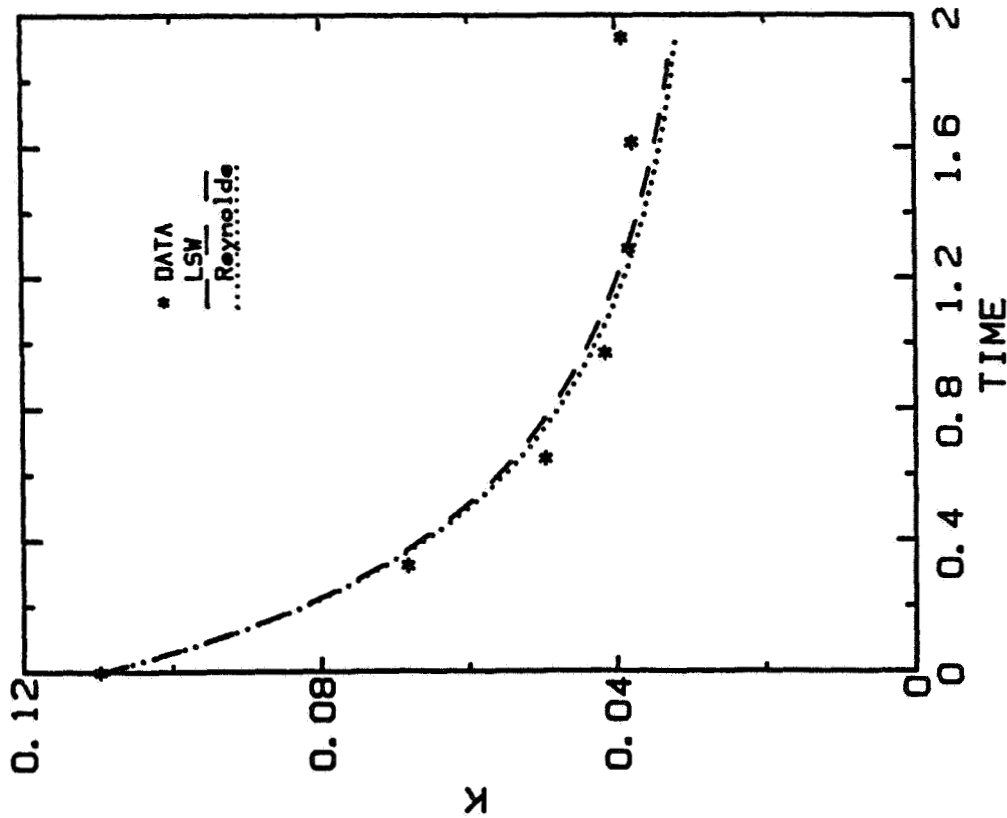


Fig. 7-9(b). The prediction of the dissipation rate by k- ϵ models for run EXO.

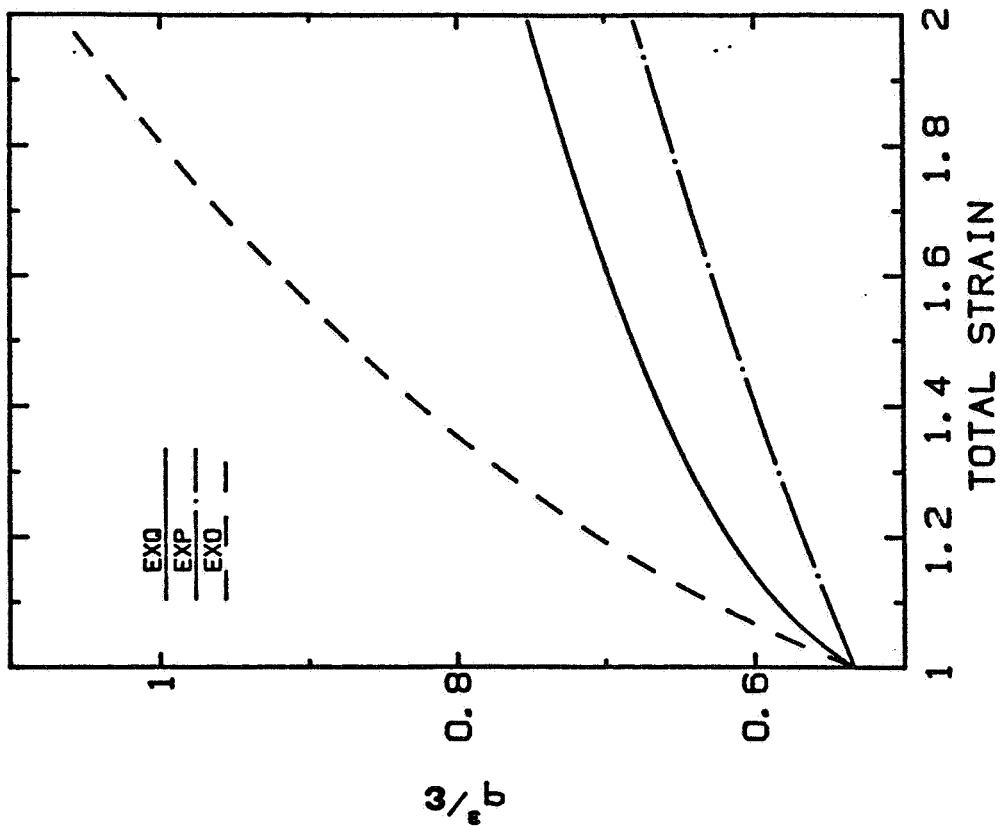


Fig. 7-10. The prediction of the turbulence length scale by the LSW model for three axisymmetric expansional strain simulations.

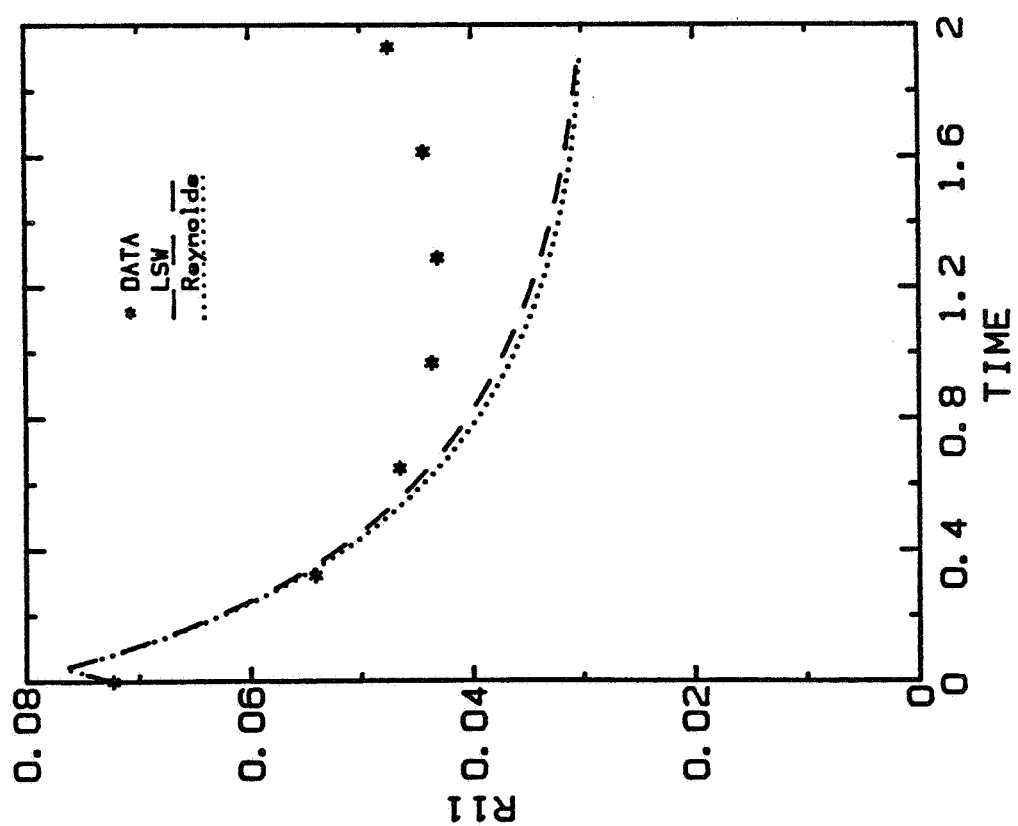


Fig. 7-9(c). The prediction of R_{11} by $k-\epsilon$ models for run EXO.

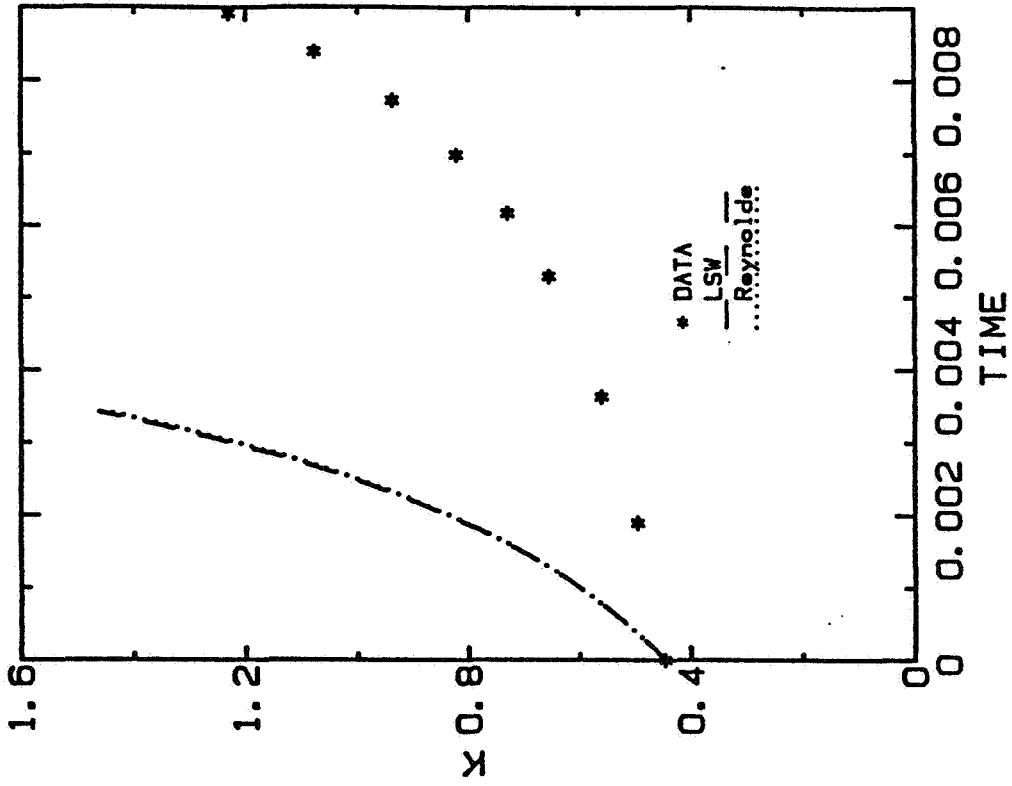


Fig. 7-12(a). The prediction of the turbulent kinetic energy by k-e models for run ODB.

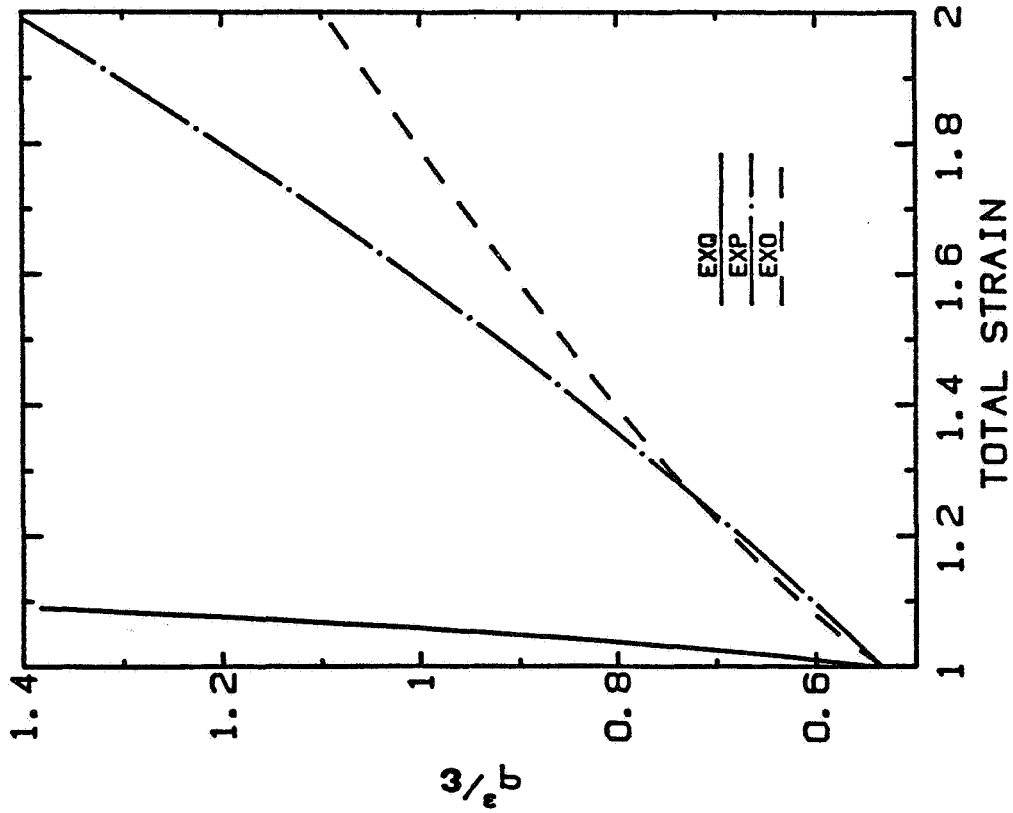


Fig. 7-11. The prediction of the turbulence length scale by Reynolds' model for three axisymmetric expansional strain simulations.

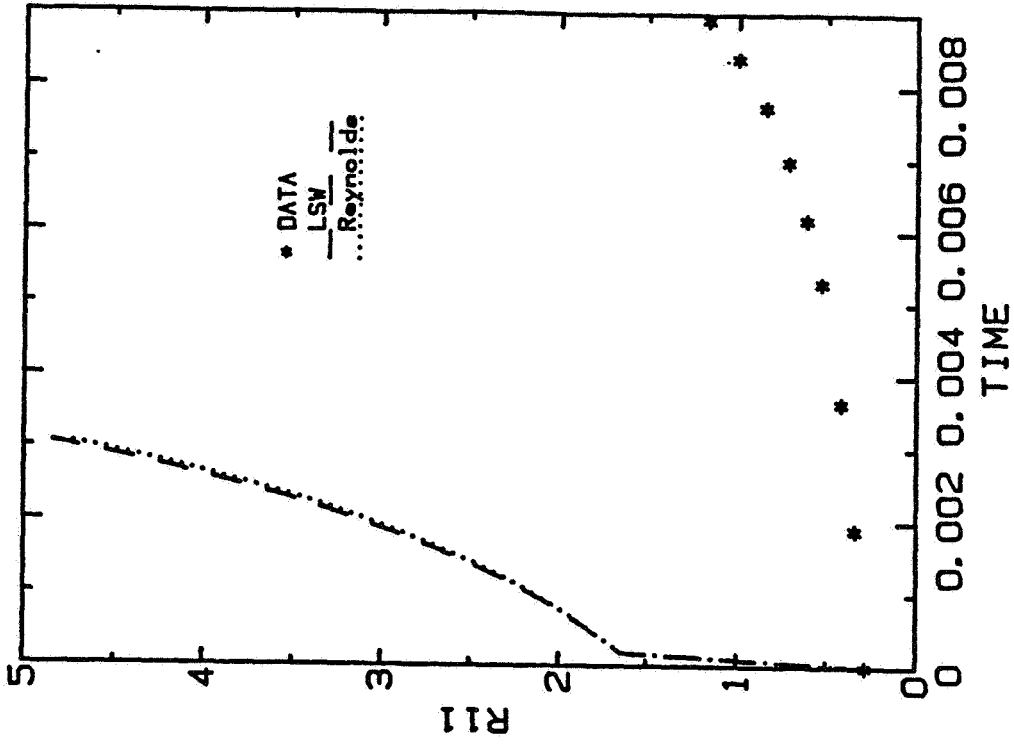


Fig. 7-12(c). The prediction of R_{11} by $k-\epsilon$ models for run ODB.

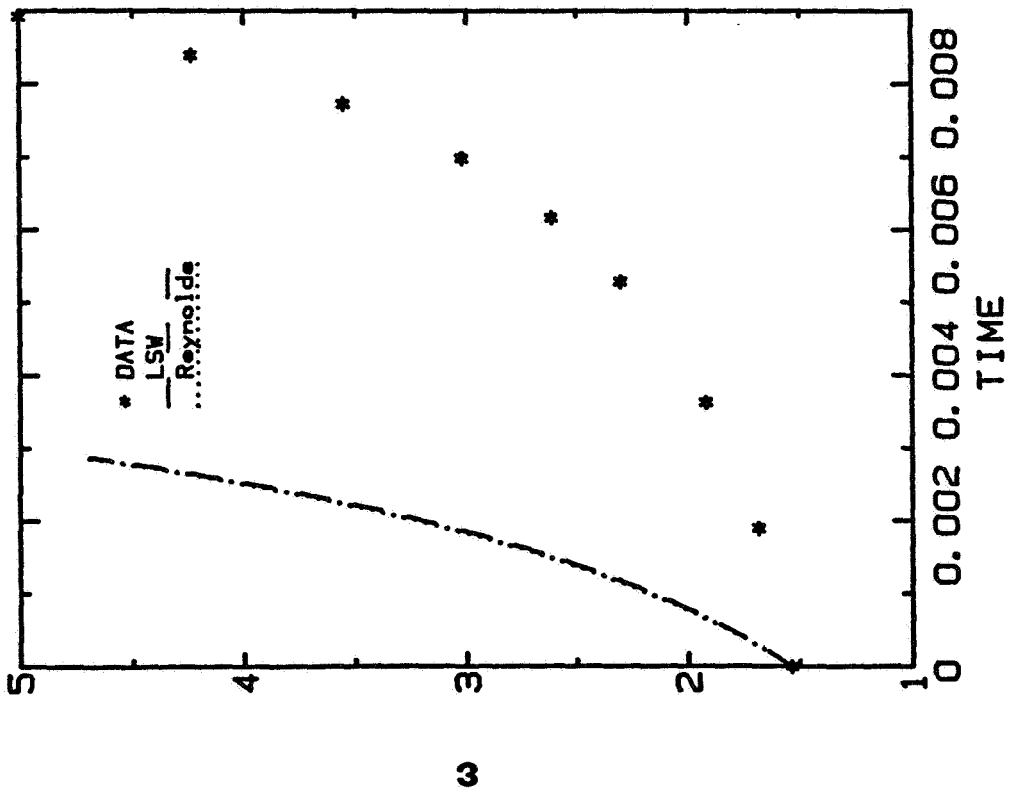


Fig. 7-12(b). The prediction of the dissipation rate by $k-\epsilon$ models for run ODB.

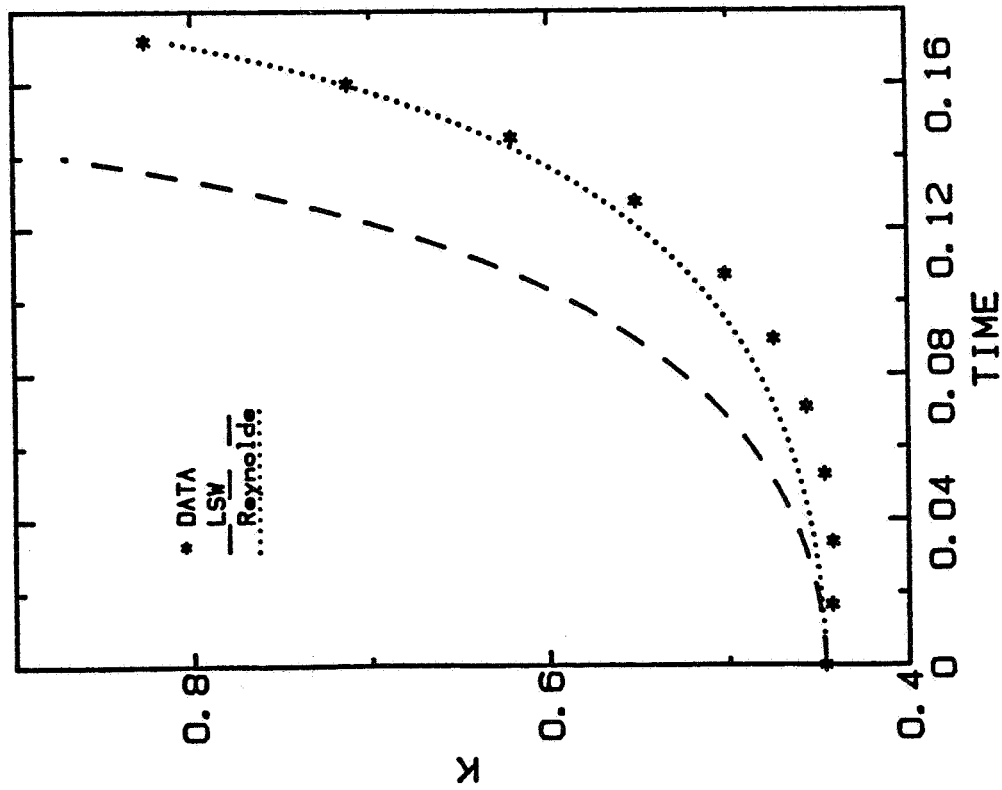


Fig. 7-13(a). The prediction of the turbulent kinetic energy by k - ϵ models for run ODC.

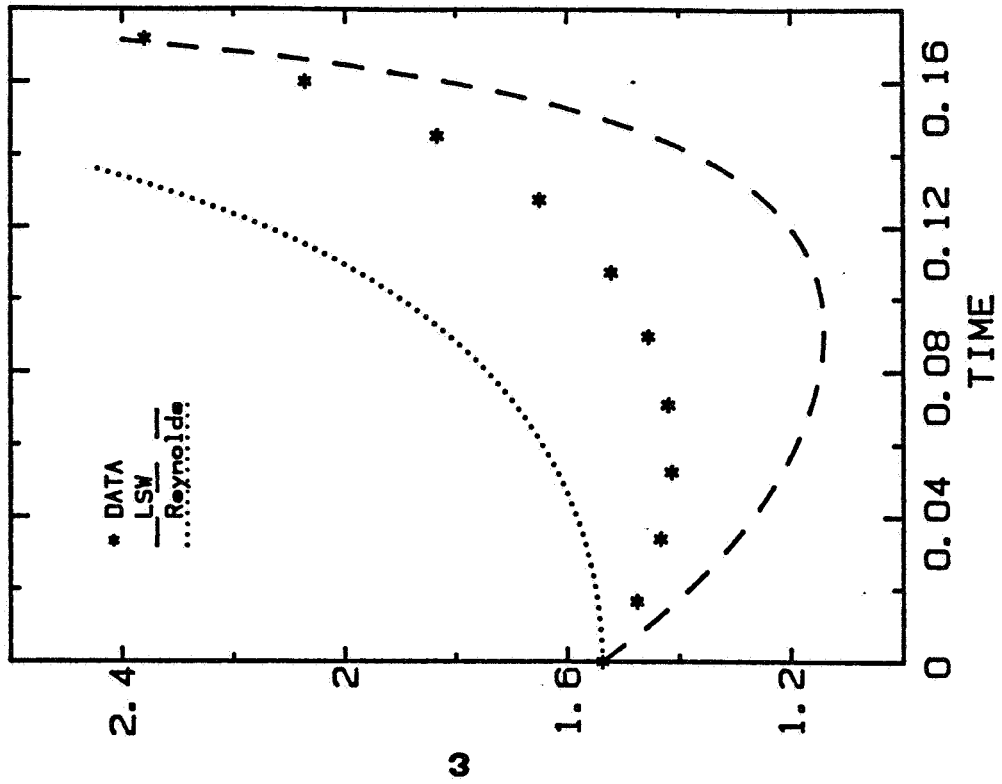


Fig. 7-13(b). The prediction of the dissipation rate by k - ϵ models for run ODC.

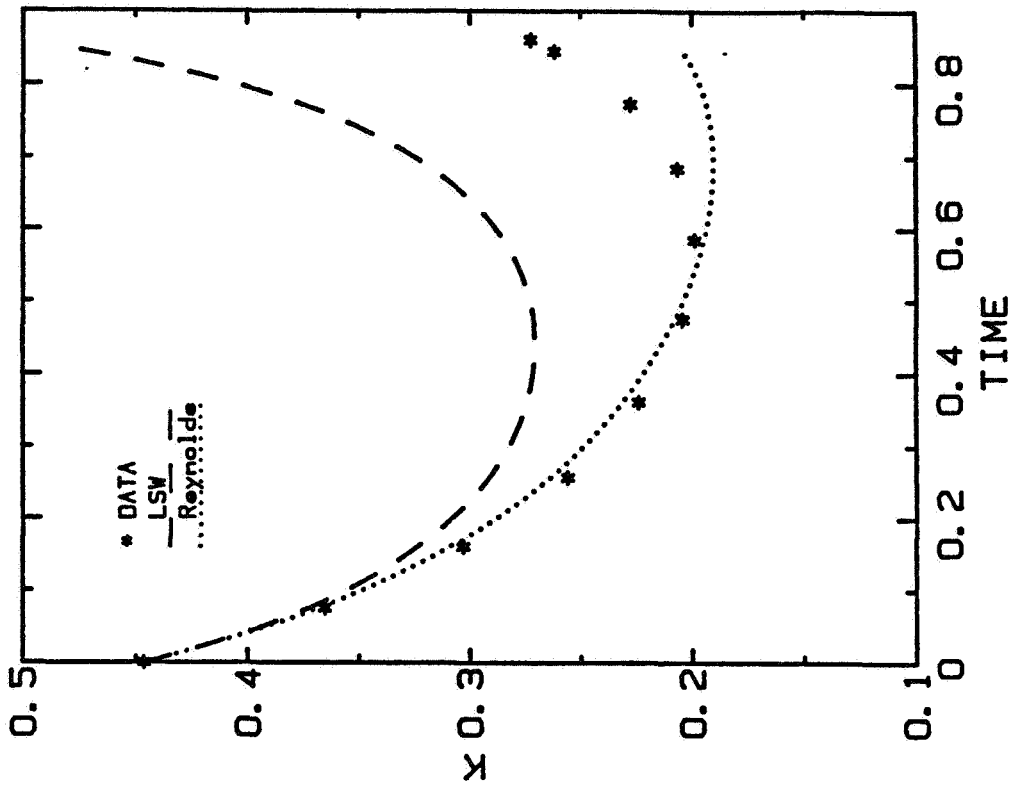


Fig. 7-14(a). The prediction of the turbulent kinetic energy by k-ε models for run ODD.

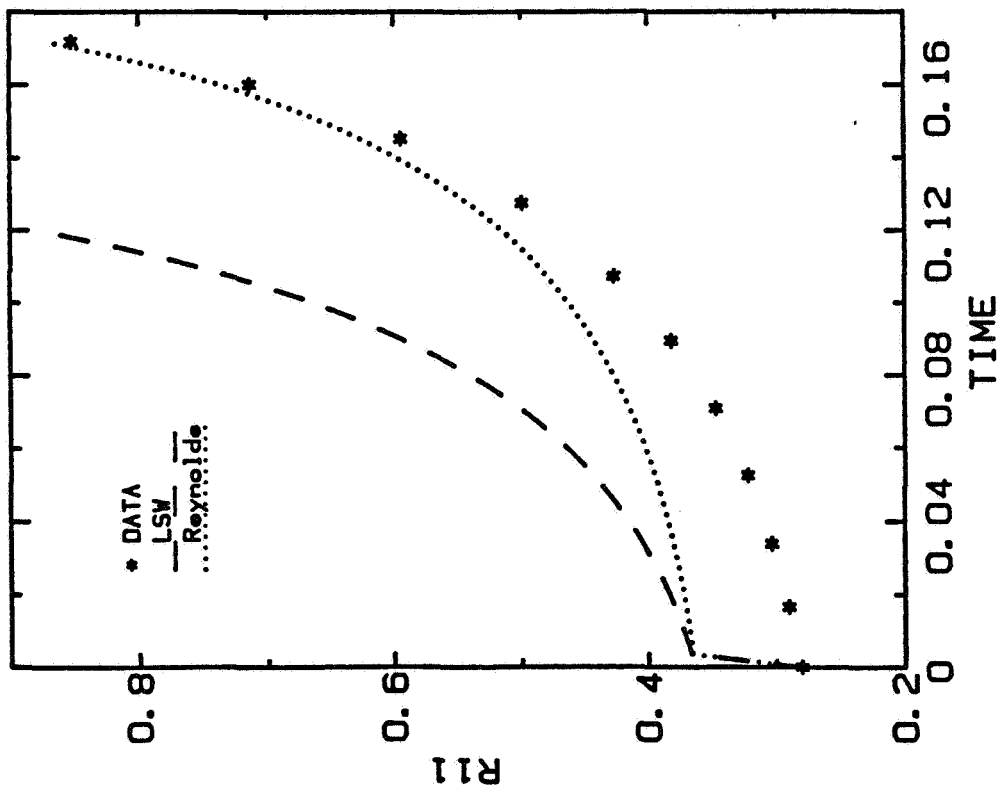


Fig. 7-13(c). The prediction of R_{11} by k-ε models for run ODC.

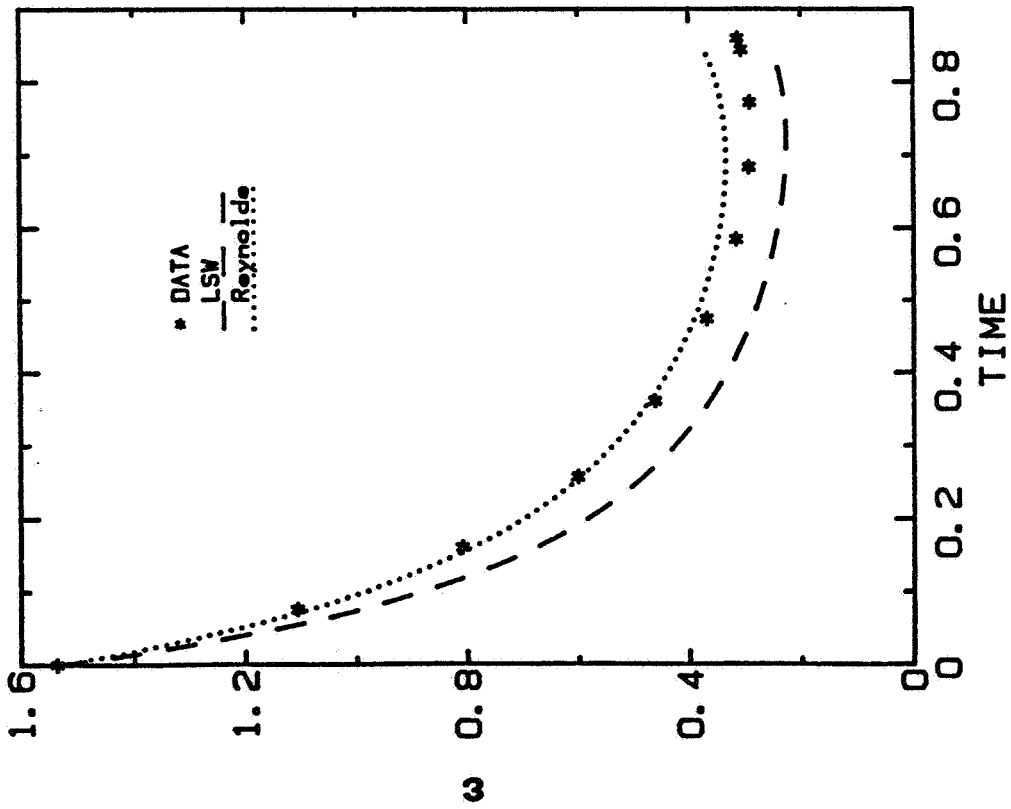


Fig. 7-14(b). The prediction of the dissipation rate by k-ε models for run ODD.

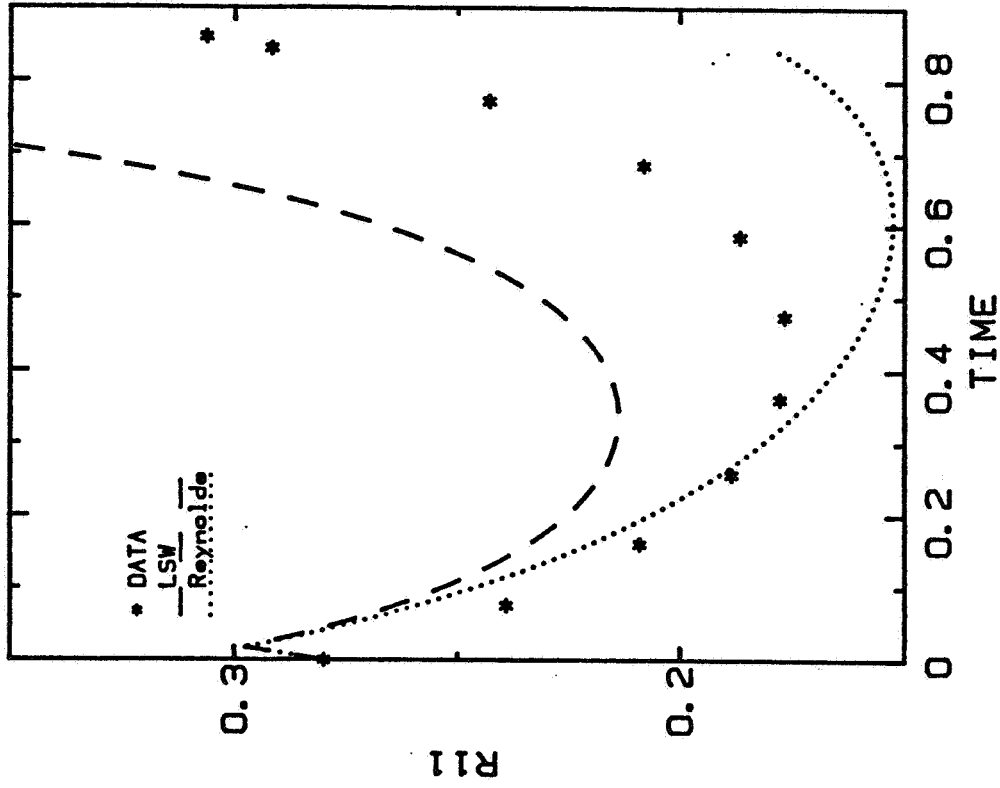


Fig. 7-14(c). The prediction of R_{11} by k-ε models for run ODD.

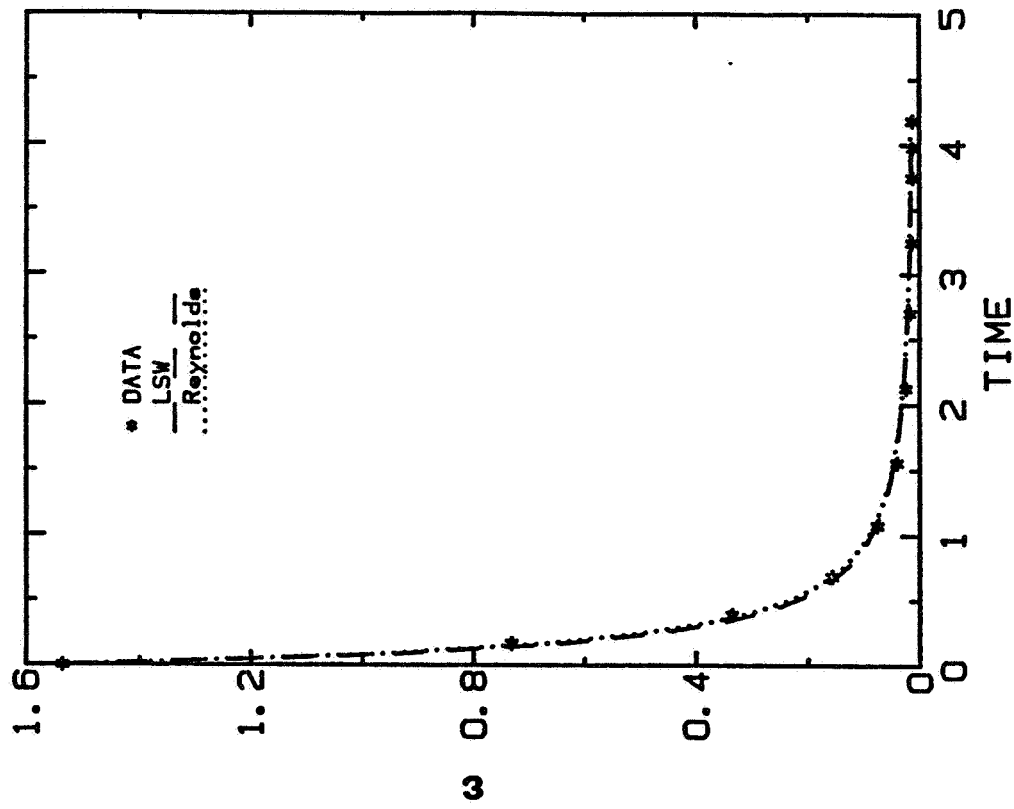


Fig. 7-15(b). The prediction of the dissipation rate by k- ϵ models for run ODE.

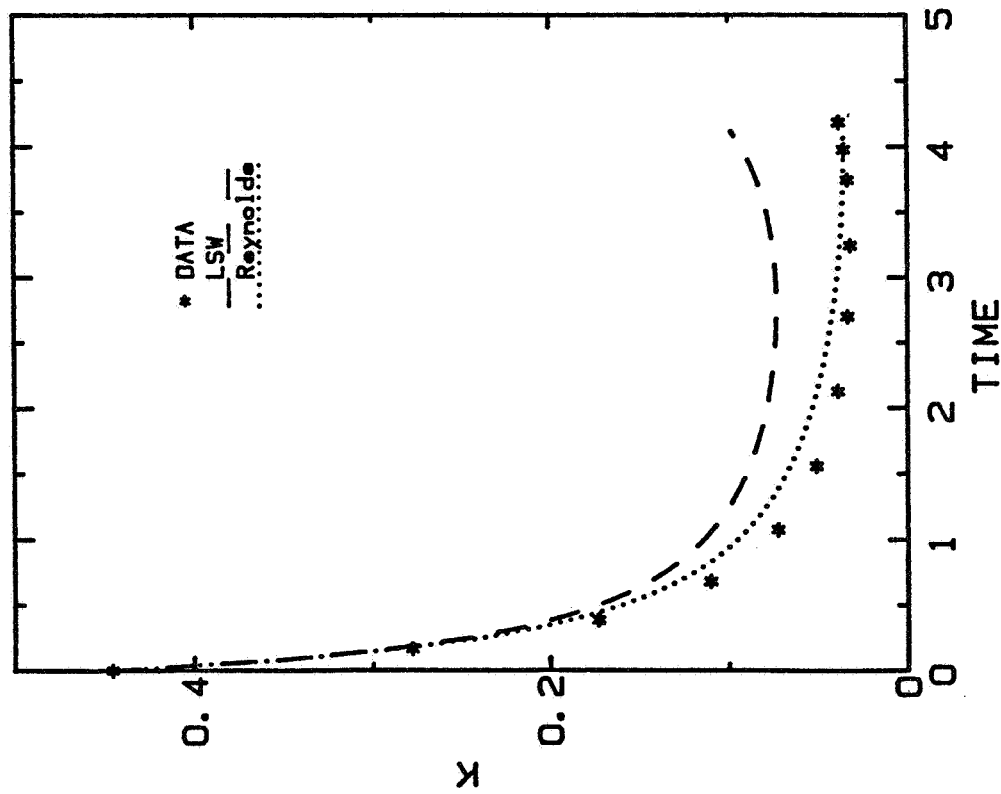


Fig. 7-15(a). The prediction of the turbulent kinetic energy by k- ϵ models for run ODE.

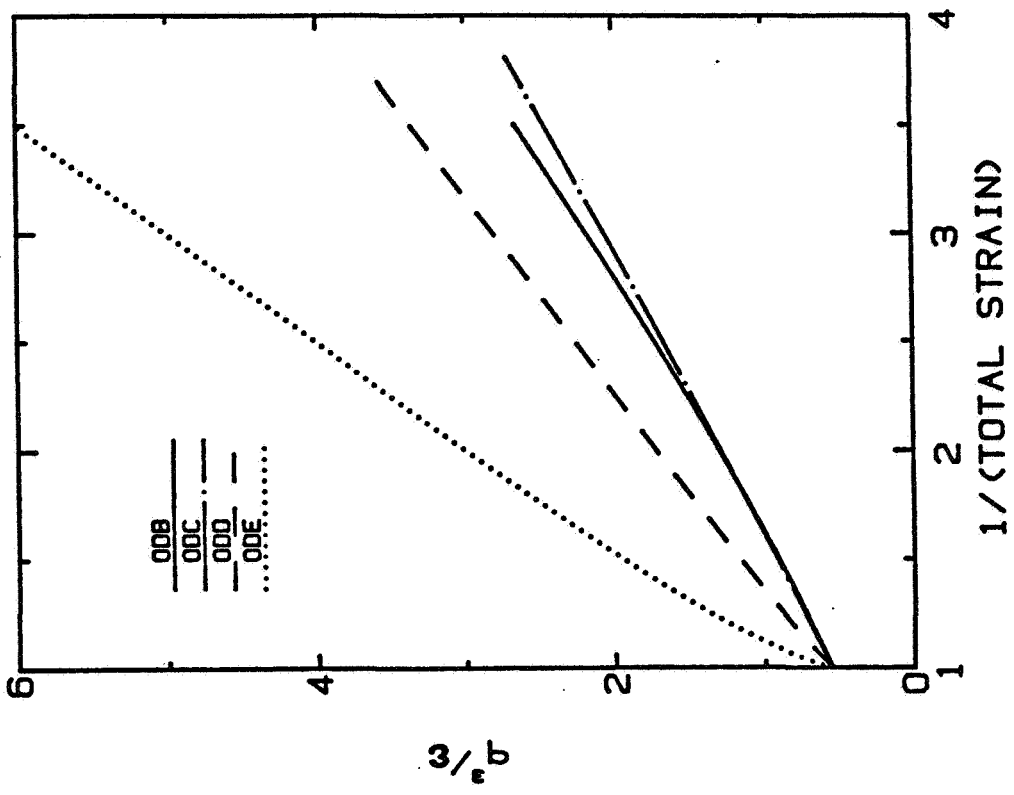


Fig. 7-16. The prediction of the turbulence length scale by the LSW model for one-dimensional compression simulations.

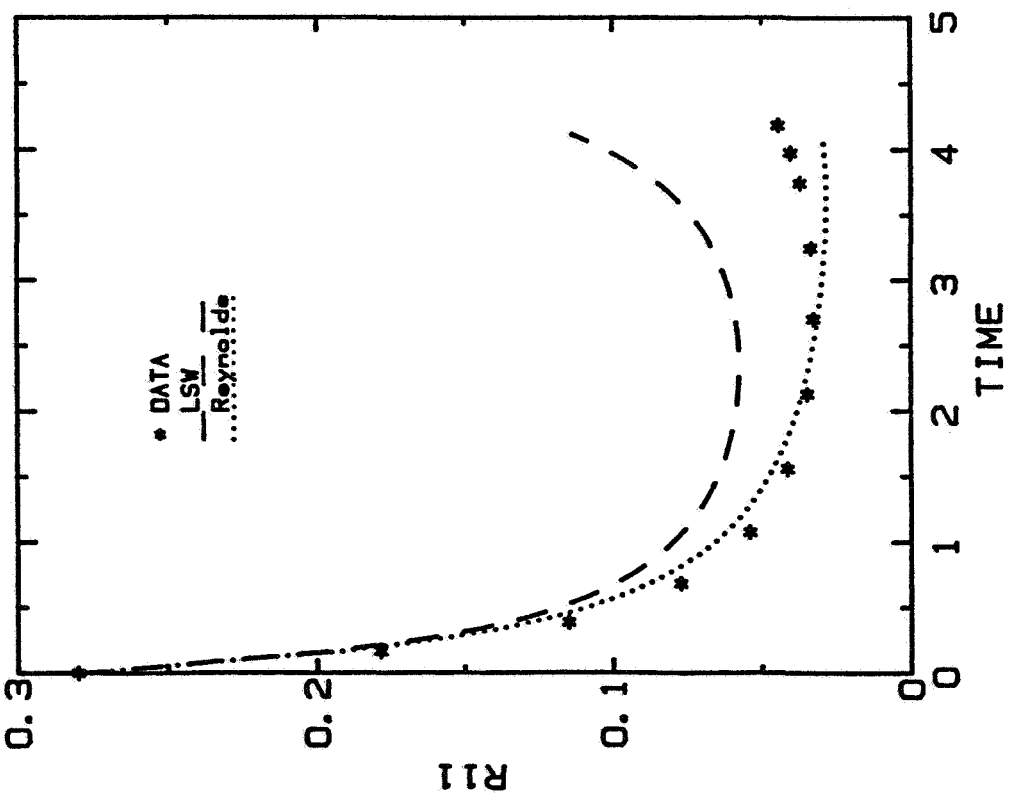


Fig. 7-15(c). The prediction of R_{11} by $k-\epsilon$ models for run ODE.

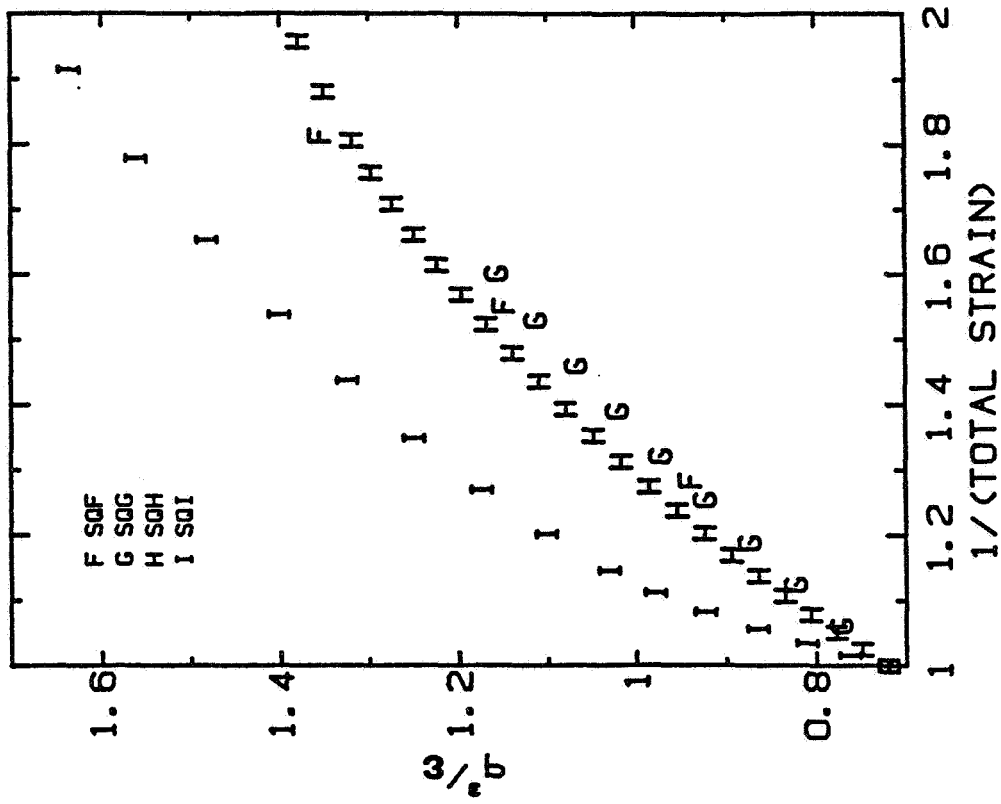


Fig. 7-18(a). The evolution of q^3/ϵ in isotropic compression simulations.

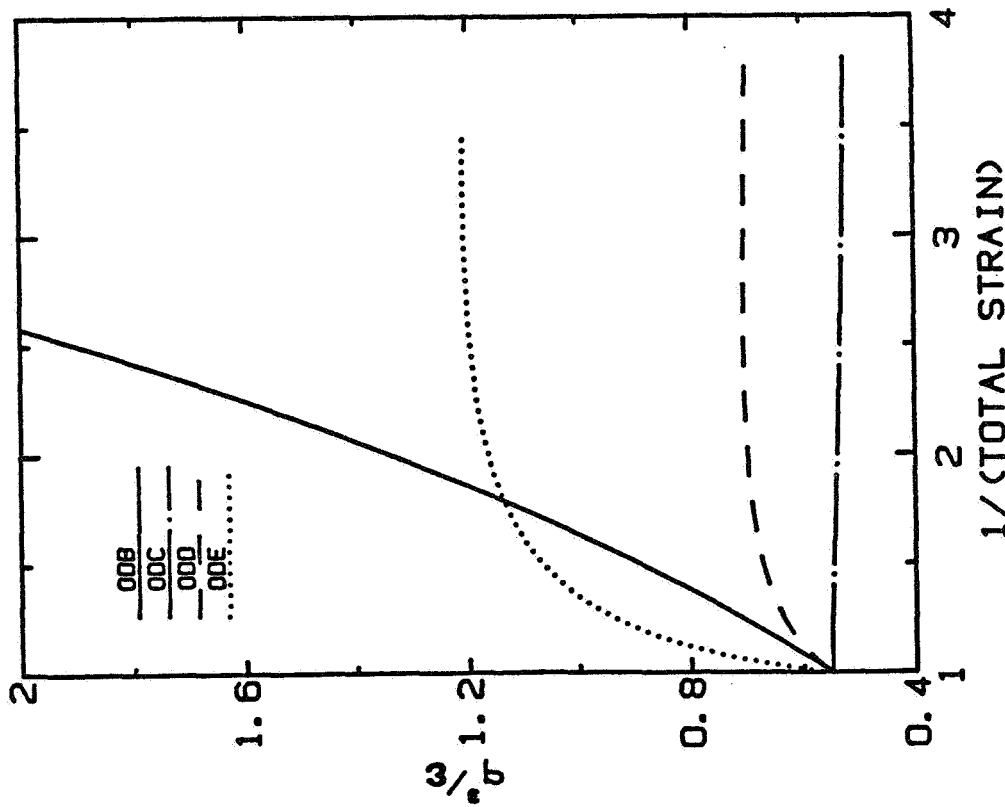


Fig. 7-17. The prediction of the turbulence length scale by Reynolds' model for one-dimensional compression simulations.

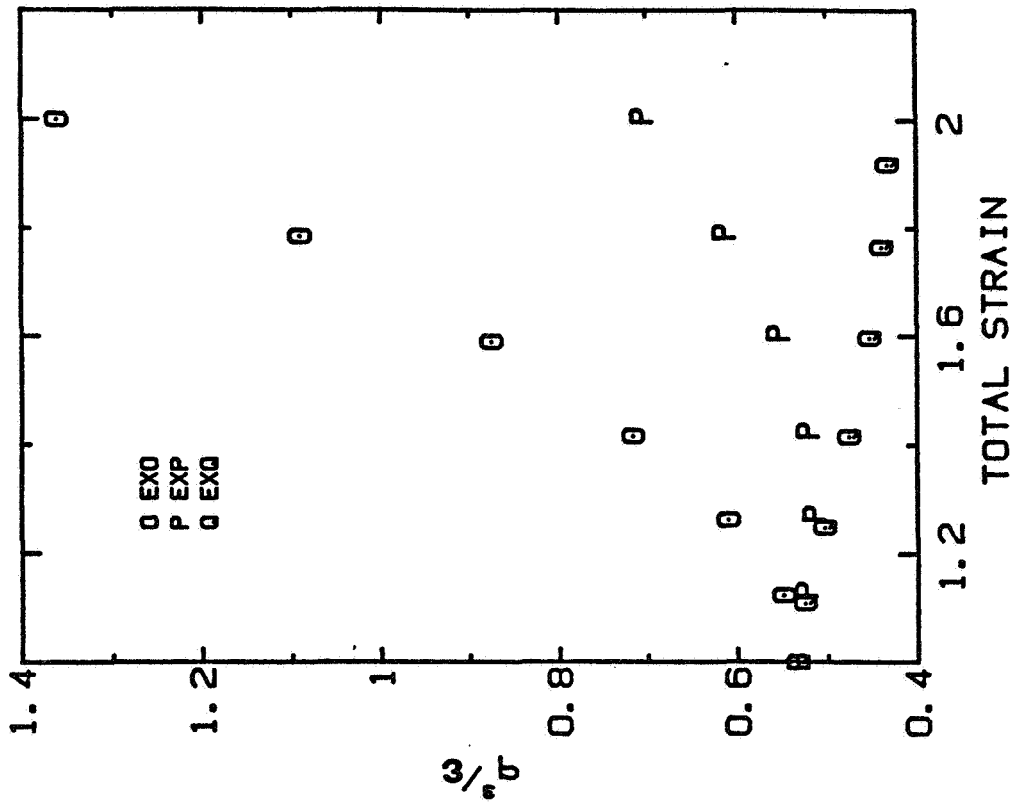


Fig. 7-19(a). The evolution of q^3/ϵ in incompressible, axisymmetric expansional strain simulations.

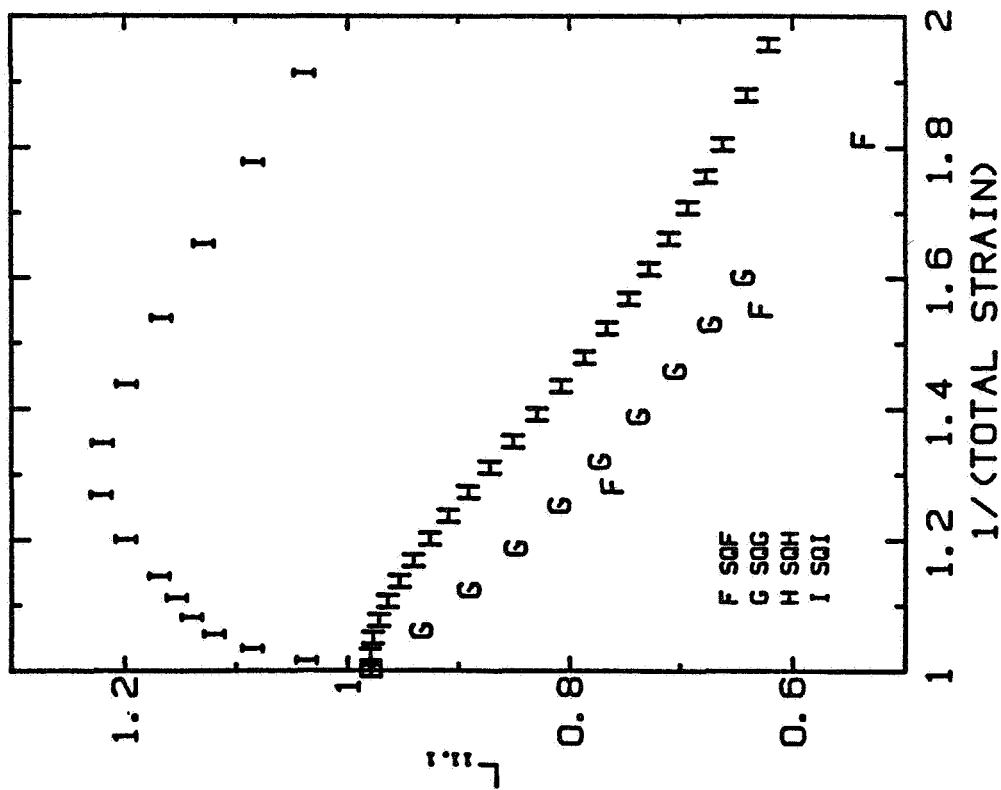


Fig. 7-18(b). The evolution of a longitudinal integral length scale in isotropic compression simulations.

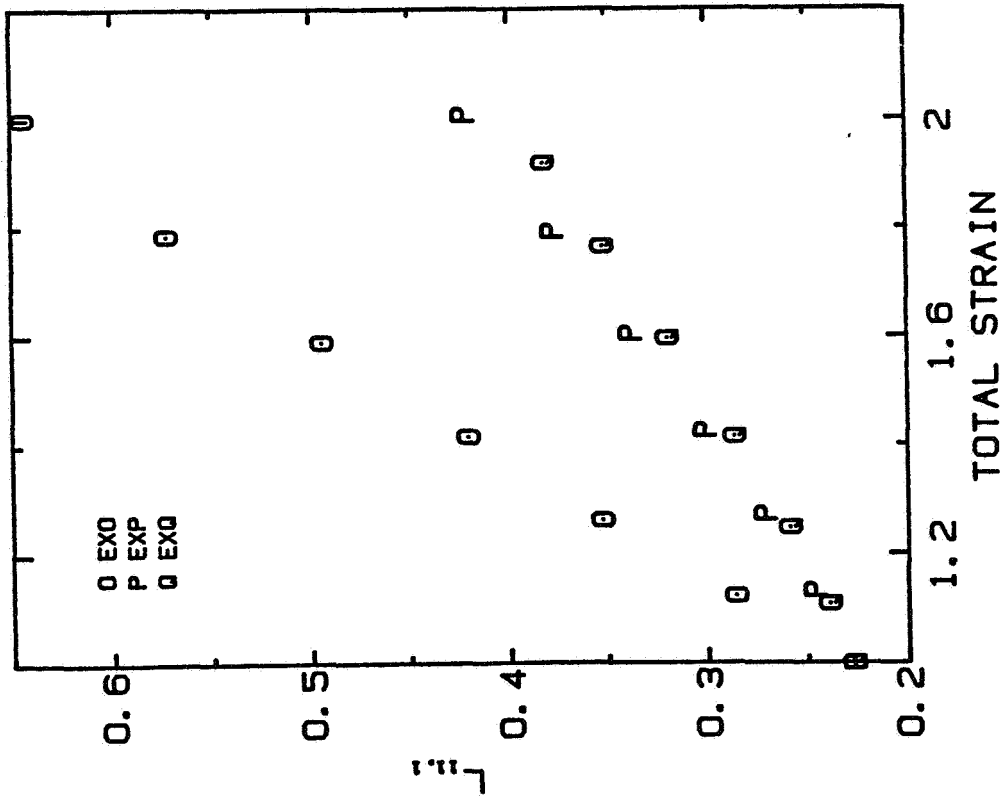


Fig. 7-19(b). The evolution of the longitudinal integral length scale in the compression direction for incompressible, axisymmetric expansional strain simulations.

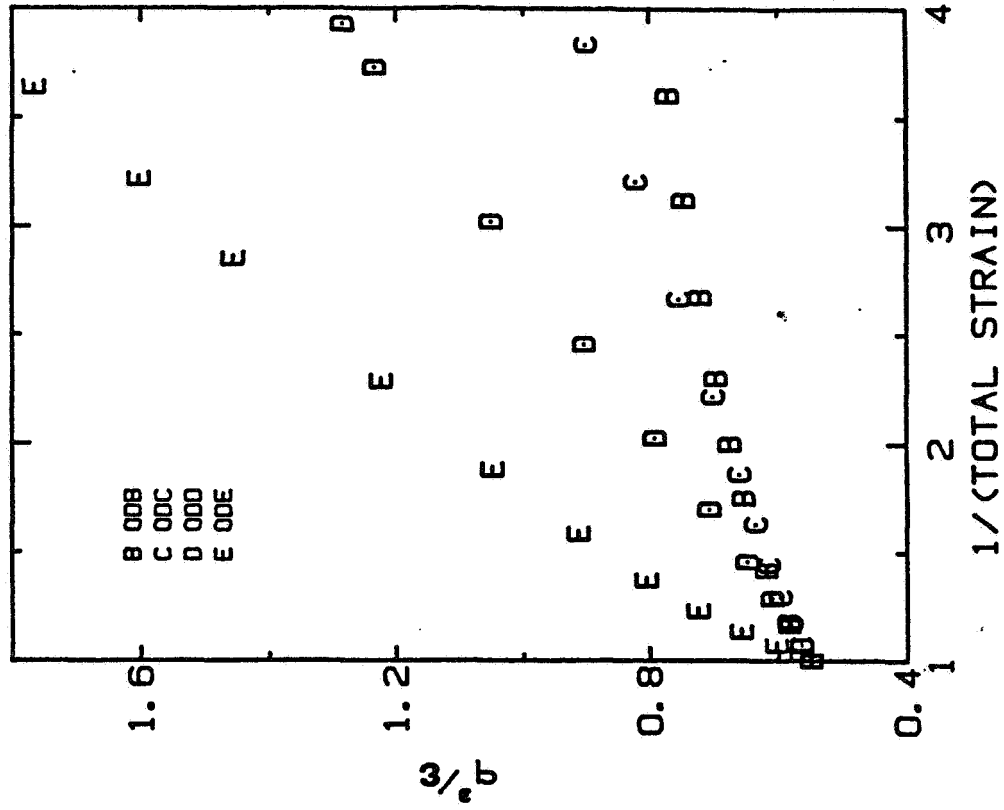


Fig. 7-20(a). The evolution of q^3/ϵ in one-dimensional compression simulations.

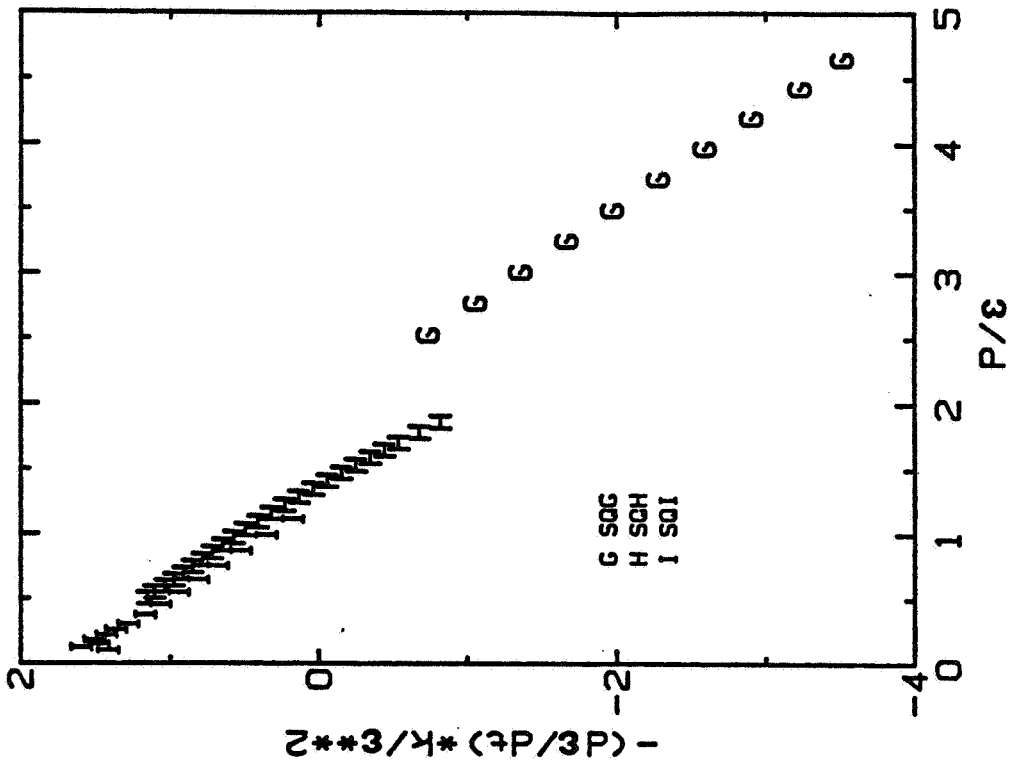


Fig. 7-21. A plot of $-\frac{1}{k/\epsilon^2} \frac{d\epsilon}{dt}$ against P/ϵ for isotropic compression simulations.

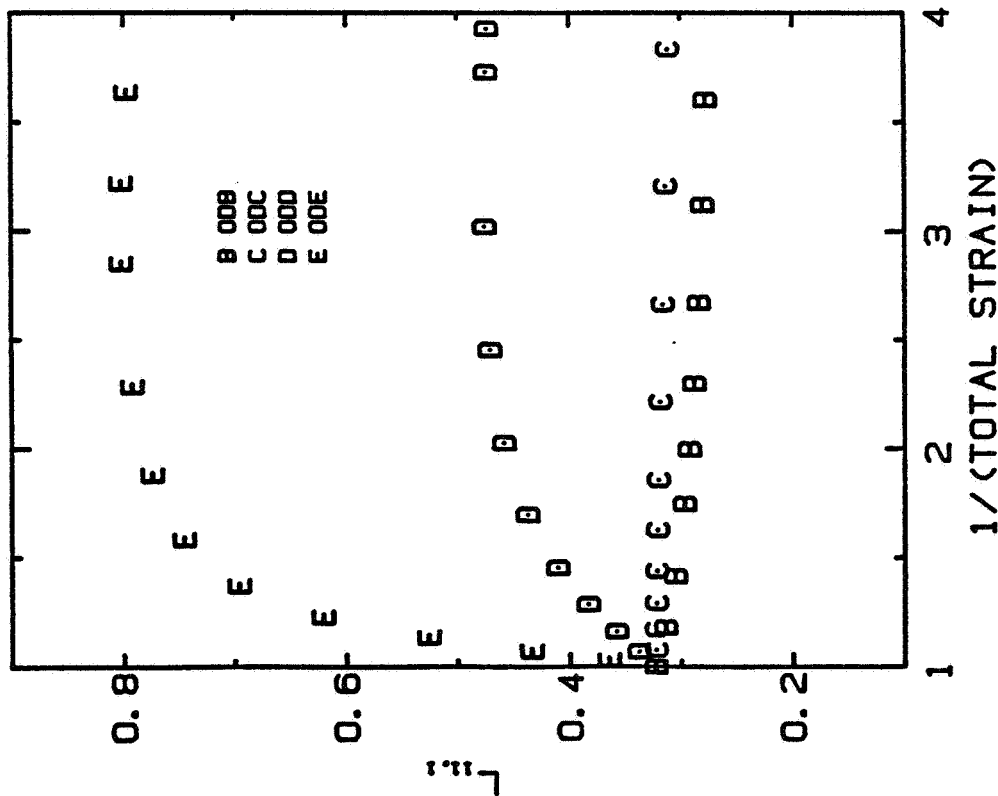


Fig. 7-20(b). The evolution of the longitudinal integral length scale in the compression direction for one-dimensional compression simulations.

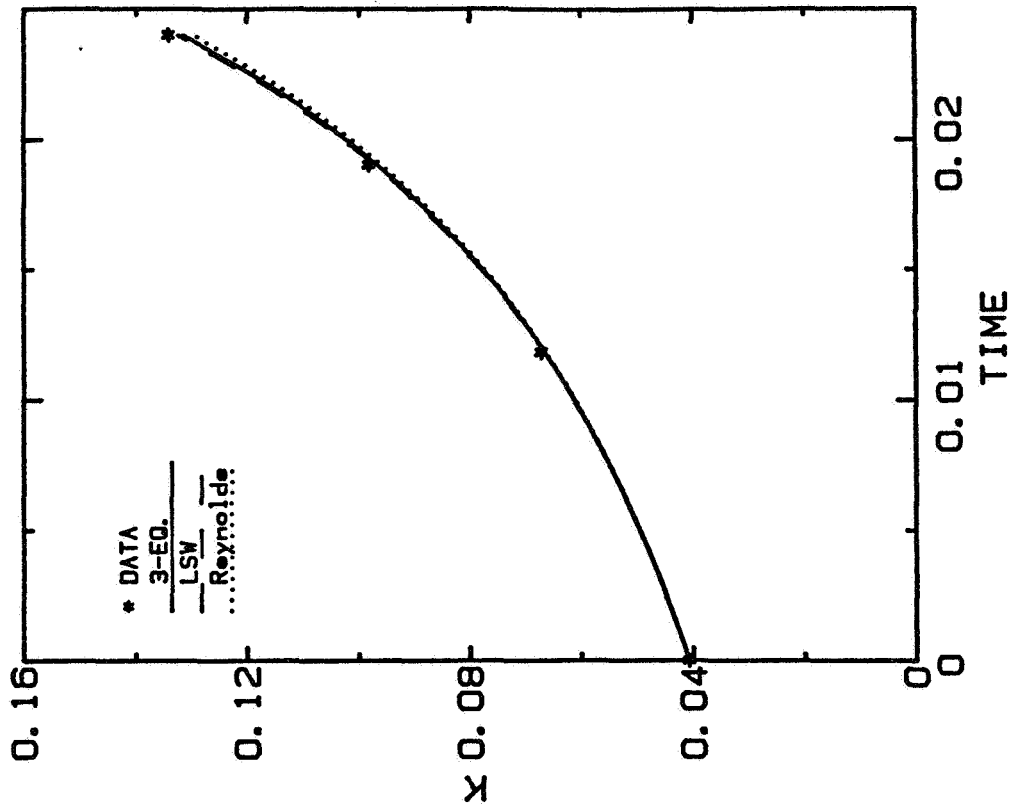


Fig. 7-23(a). The prediction of the turbulent kinetic energy by $k-\epsilon$ and $k-\epsilon$ models for run SQF.

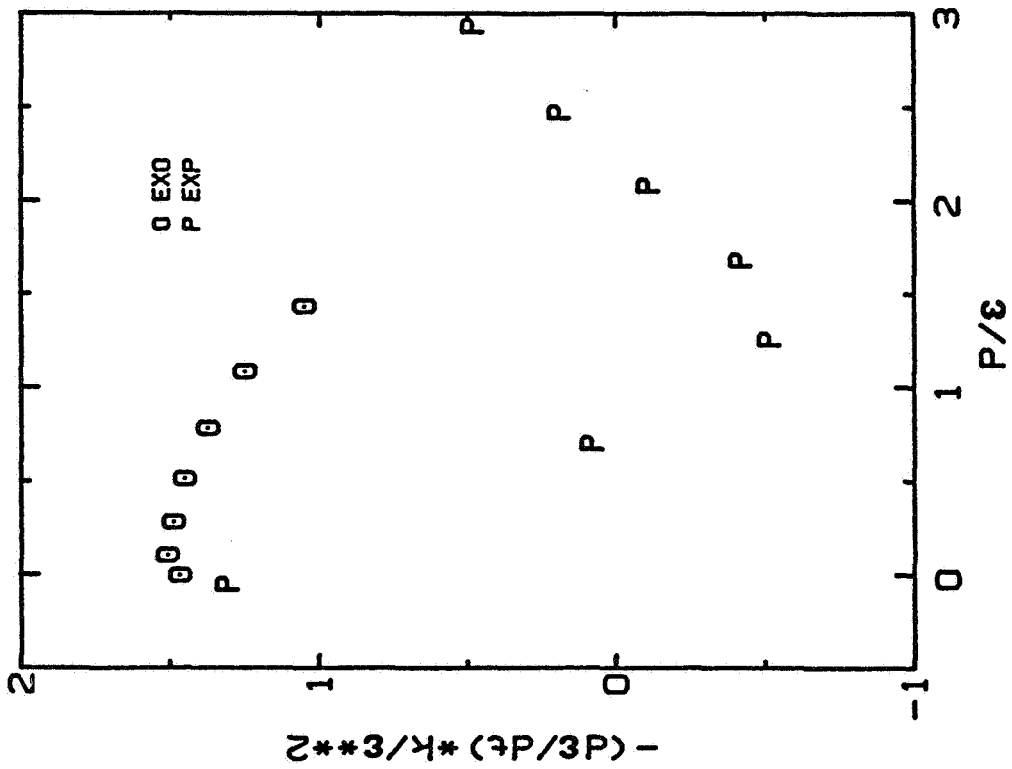


Fig. 7-22. A plot of $-\frac{2}{3} \frac{dP}{dt} \epsilon$ against P/ϵ for incompressible, axisymmetric expansional strain simulations.

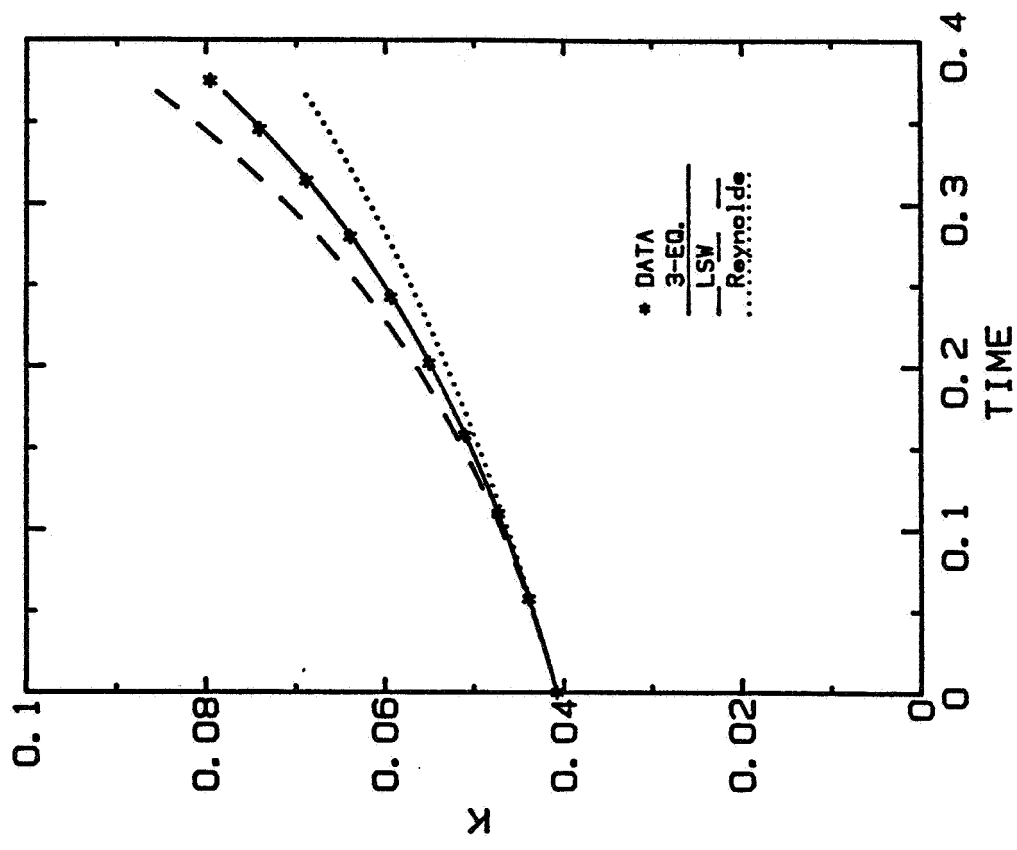


Fig. 7-24(a). The prediction of the turbulent kinetic energy by $k-\epsilon-\tau$ and $k-\epsilon$ models for run SQF.

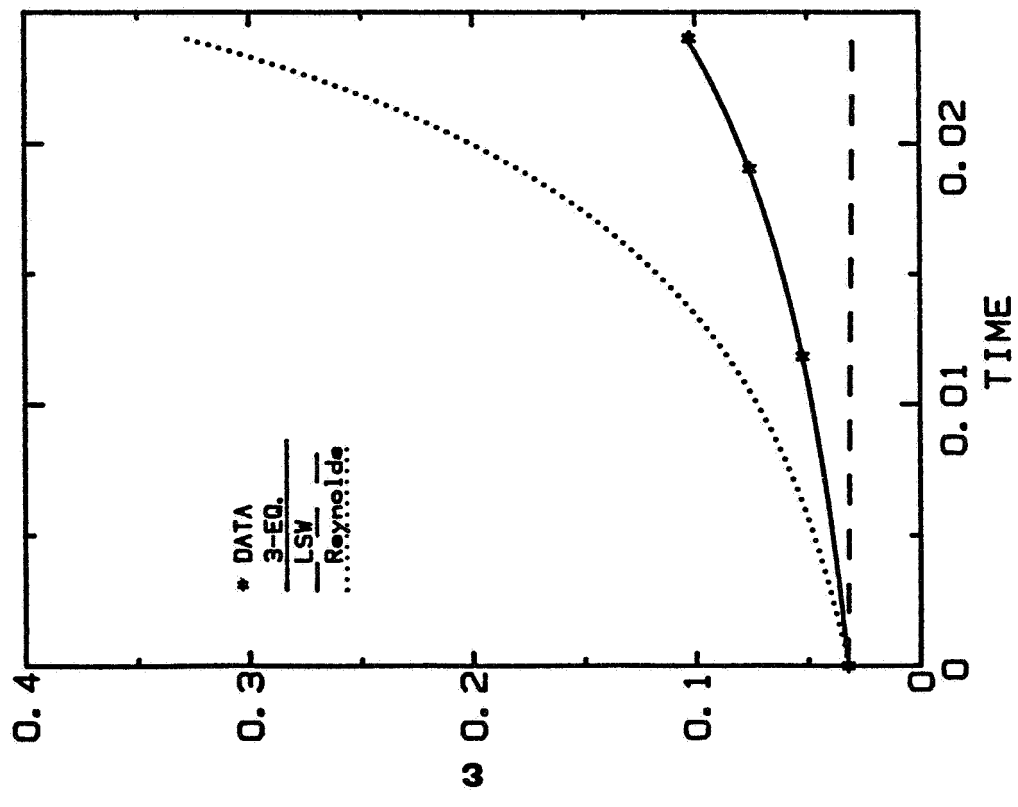


Fig. 7-23(b). The prediction of the dissipation rate by $k-\epsilon-\tau$ and $k-\epsilon$ models for run SQF.

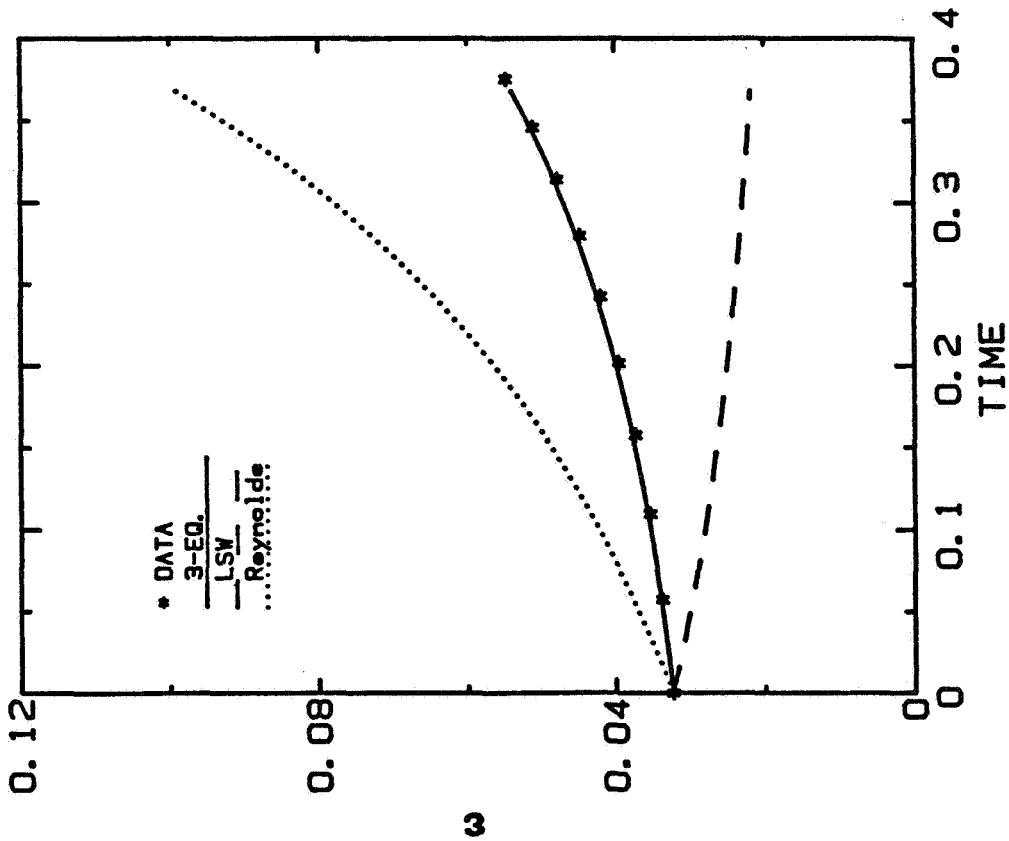


Fig. 7-24(b). The prediction of the dissipation rate by $k-\epsilon-\tau$ and $k-\epsilon$ models for run SQG.

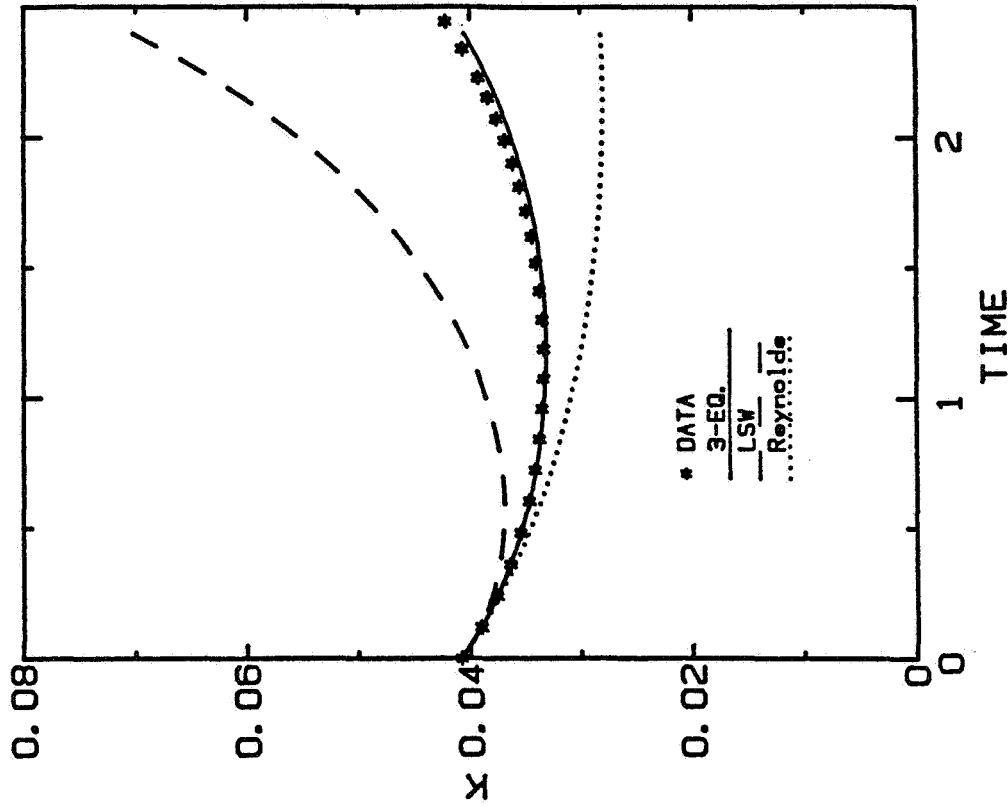


Fig. 7-25(a). The prediction of the turbulent kinetic energy by $k-\epsilon-\tau$ and $k-\epsilon$ models for run SQH.

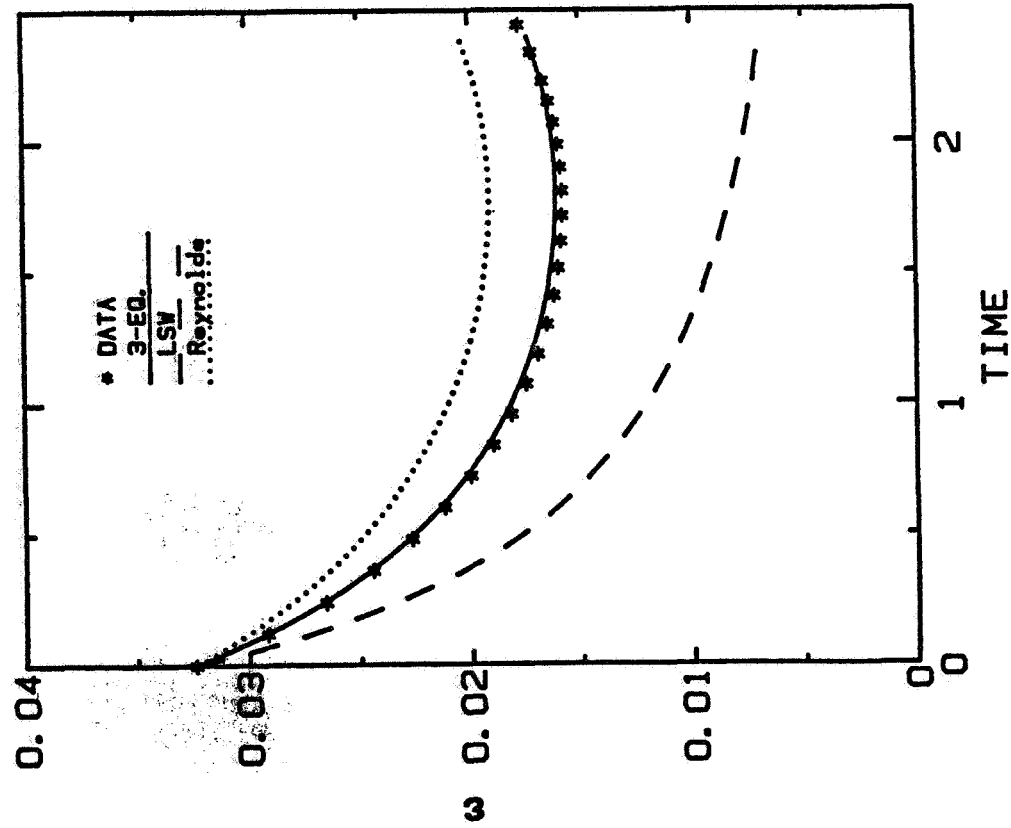


Fig. 7-25(b). The prediction of the dissipation rate by $k-\epsilon-\tau$ and $k-\epsilon$ models for run SQH.

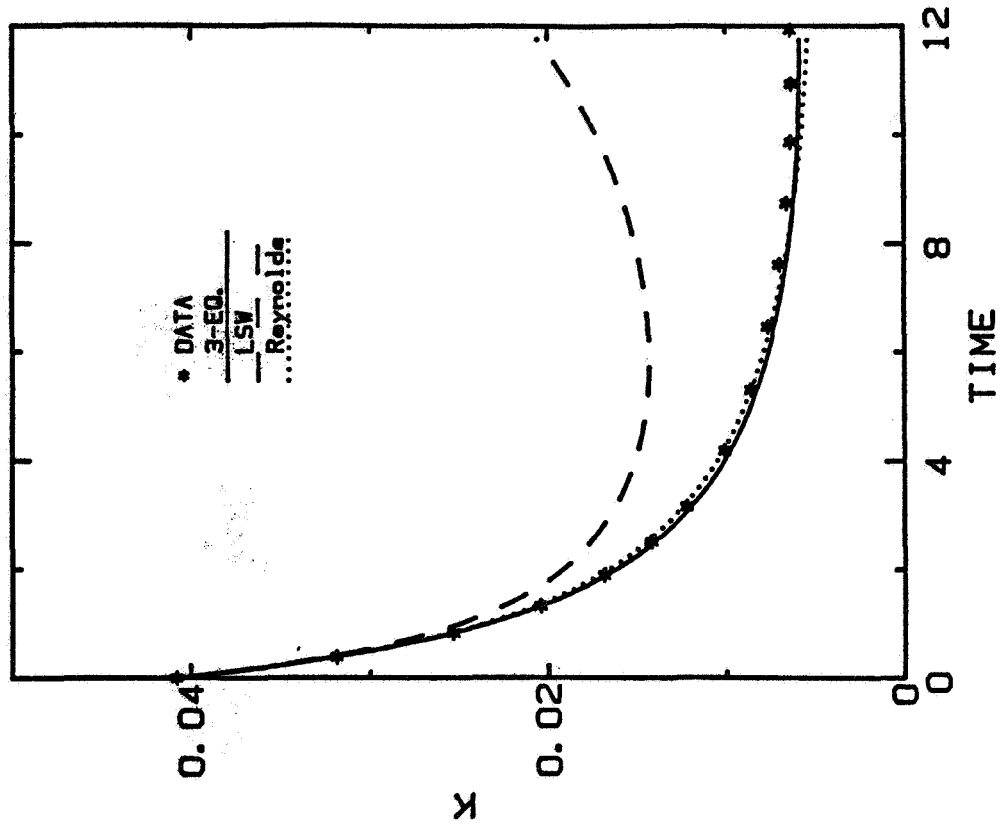


Fig. 7-26(a). The prediction of the turbulent kinetic energy by $k-\epsilon-\tau$ and $k-\epsilon$ models for run SQL.

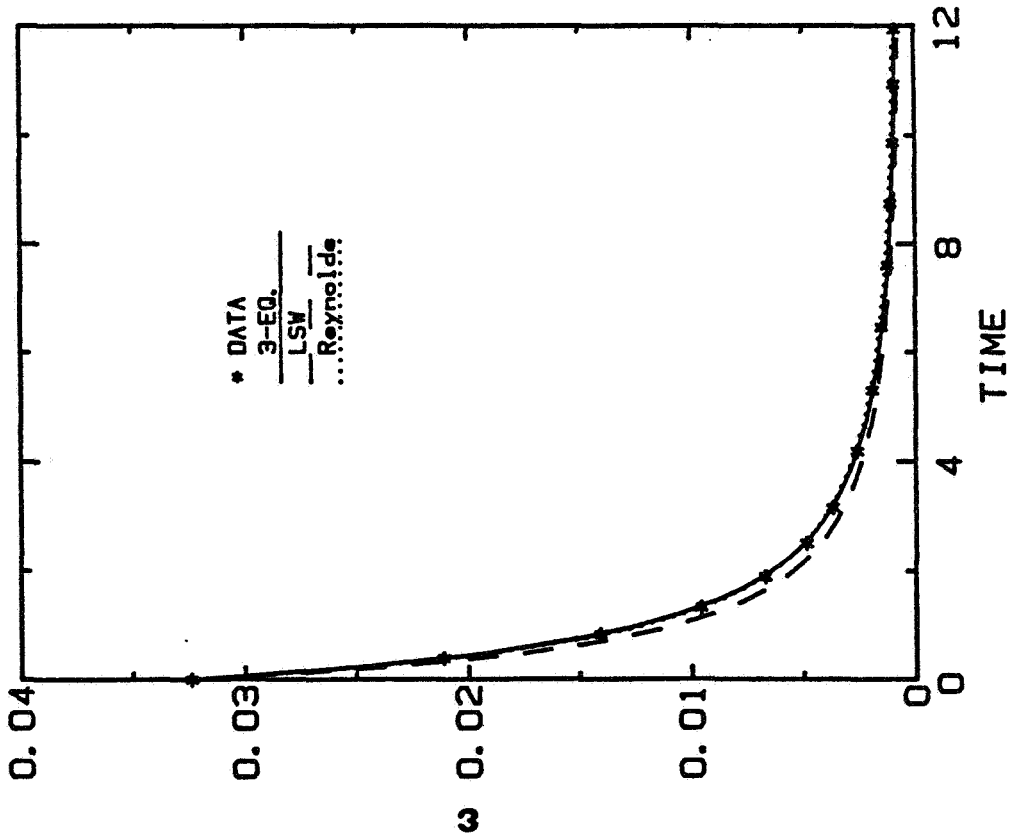


Fig. 7-26(b). The prediction of the dissipation rate by $k-\epsilon-\tau$ and $k-\epsilon$ models for run SQI.

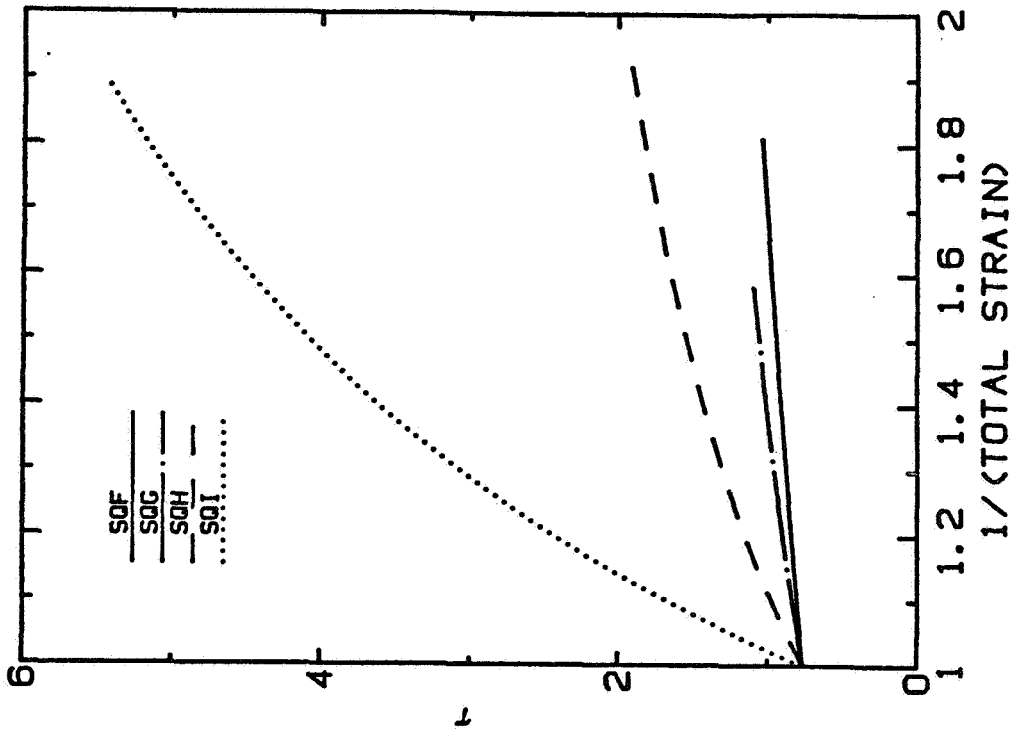


Fig. 7-27. The evolution of the modeled turbulence time scale in isotropic compression simulations.

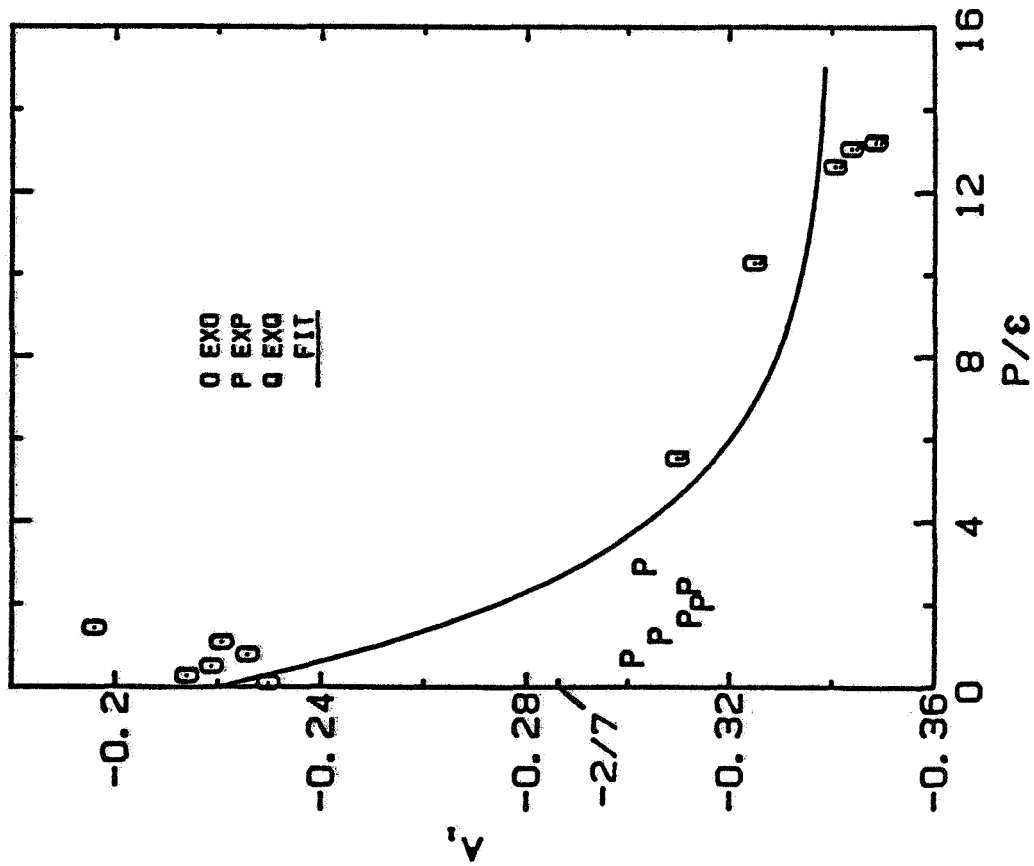


Fig. 7-28. A plot of the model coefficient A_1 as a function of P/ϵ and its fitting in incompressible, axisymmetric expansional strain flow.

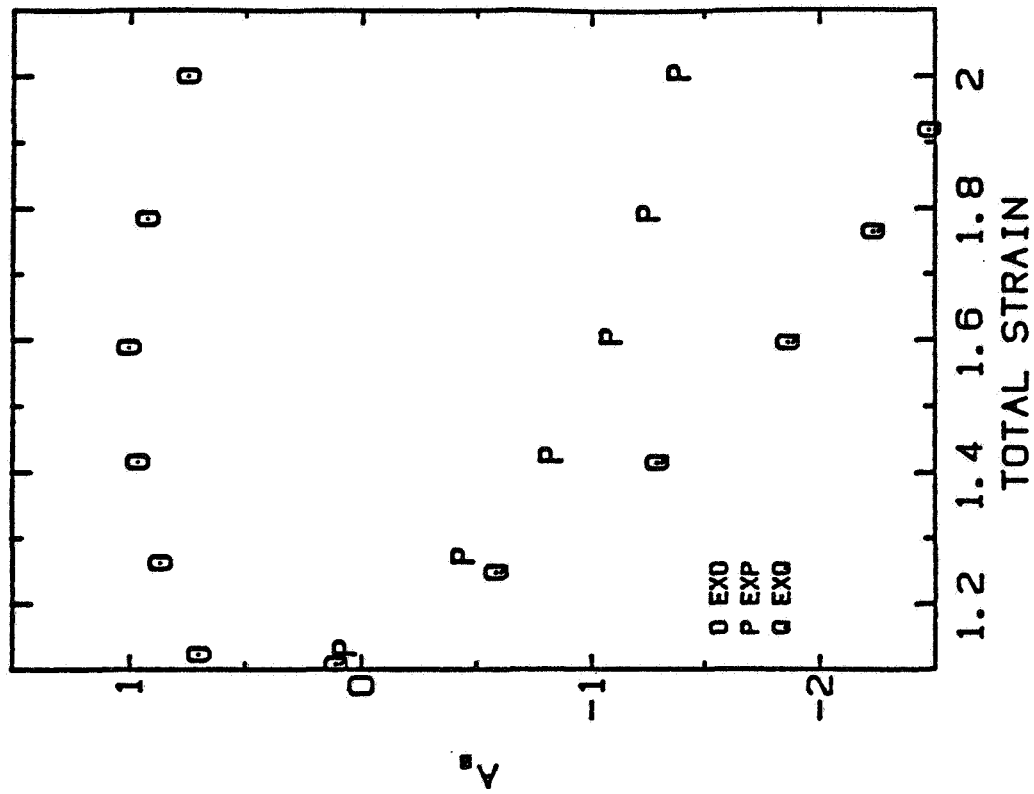


Fig. 7-29. The evolution of the model coefficient A_0 in incompressible, axisymmetric expansional strain flow.

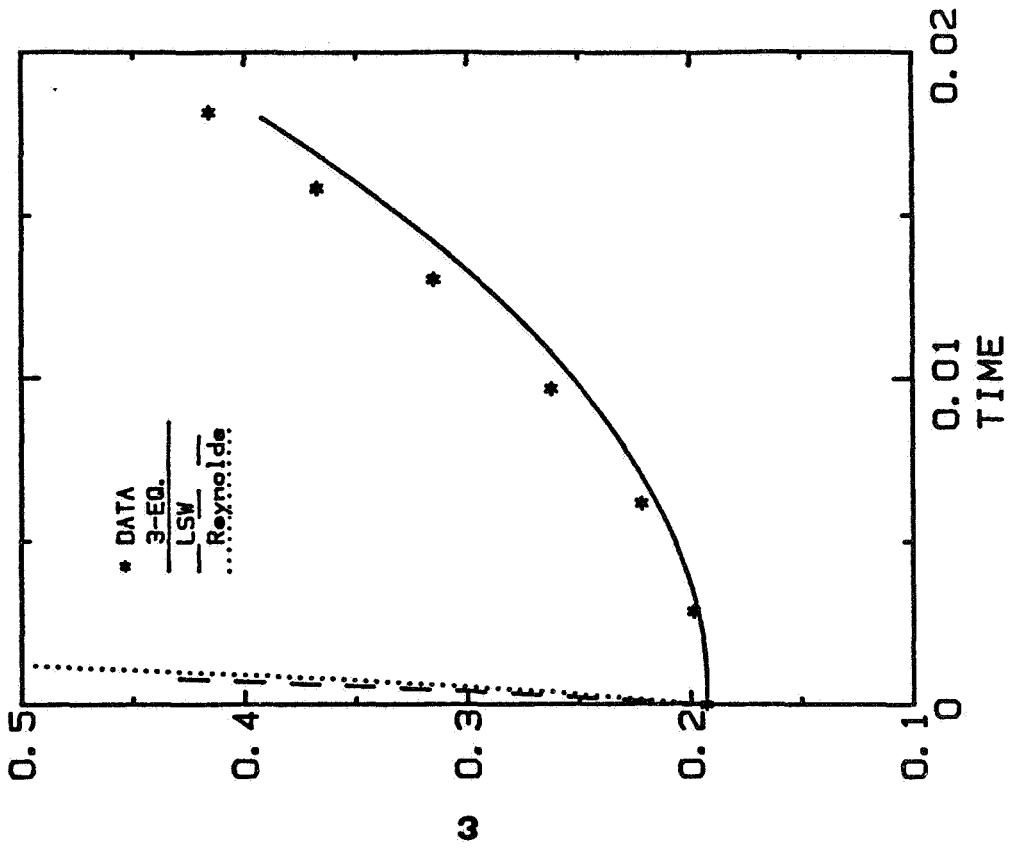


Fig. 7-30(a). The prediction of the turbulent kinetic energy by $k-\epsilon-r$ and $k-\epsilon$ models for run EXQ.

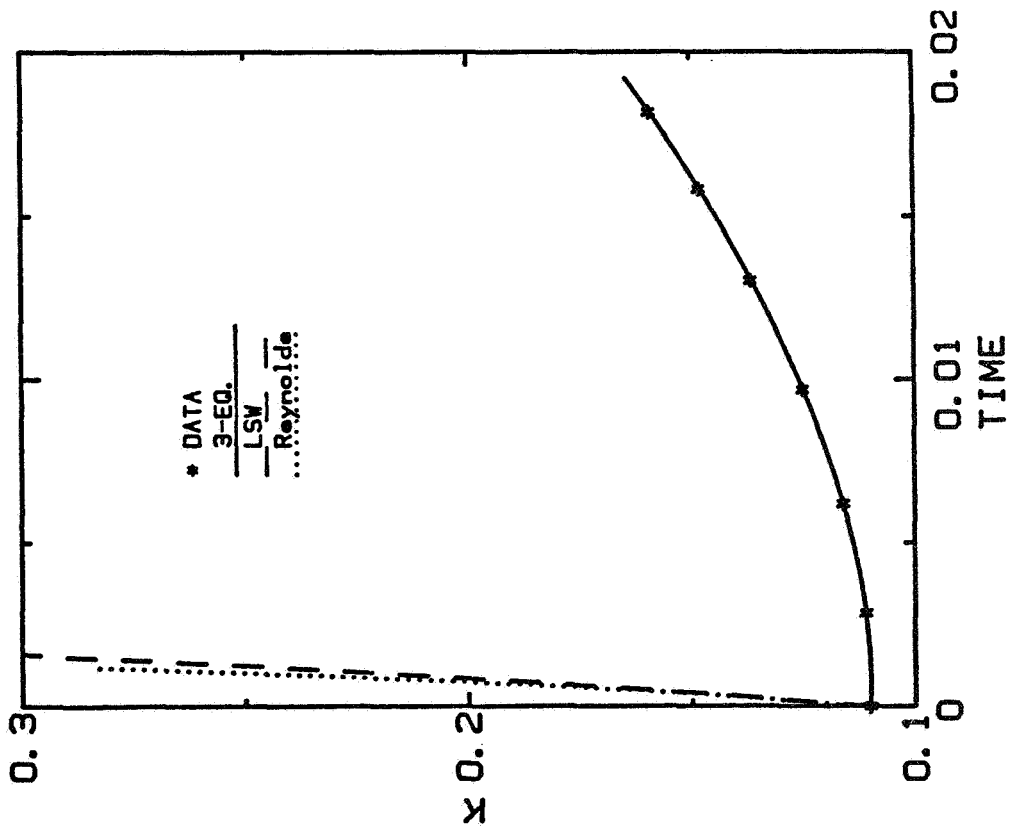


Fig. 7-30(b). The prediction of the dissipation rate by $k-\epsilon-r$ and $k-\epsilon$ models for run EXQ.

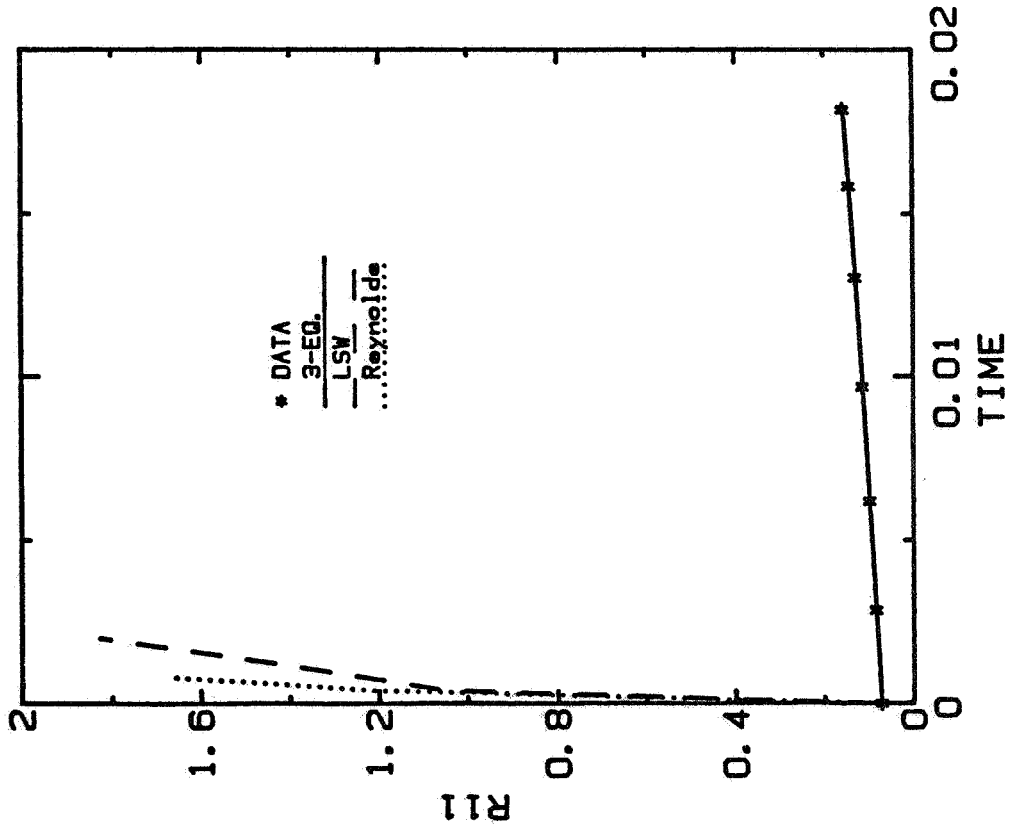


Fig. 7-30(c). The prediction of R_{11} by $k-\epsilon-\tau$ and $k-\epsilon$ models for run EXQ.

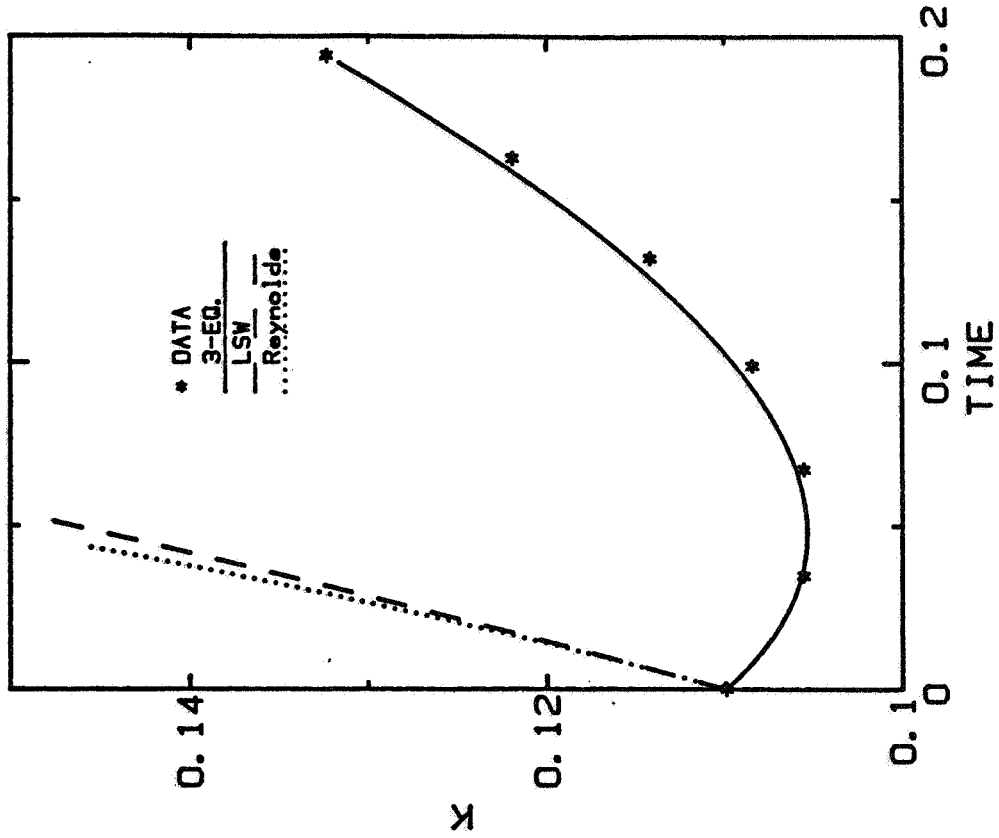


Fig. 7-31(a). The prediction of the turbulent kinetic energy by $k-\epsilon-\tau$ and $k-\epsilon$ models for run EXP.

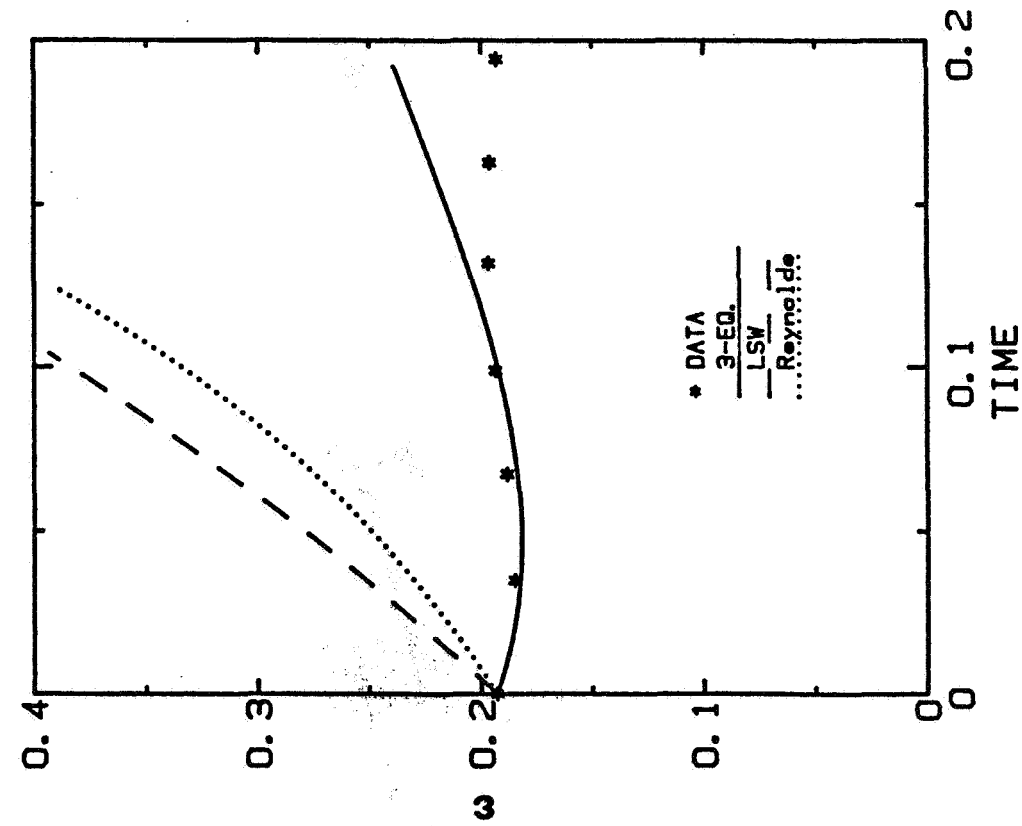


Fig. 7-31(b). The prediction of the dissipation rate by $k-\epsilon-\tau$ and $k-\epsilon$ models for run EXP.

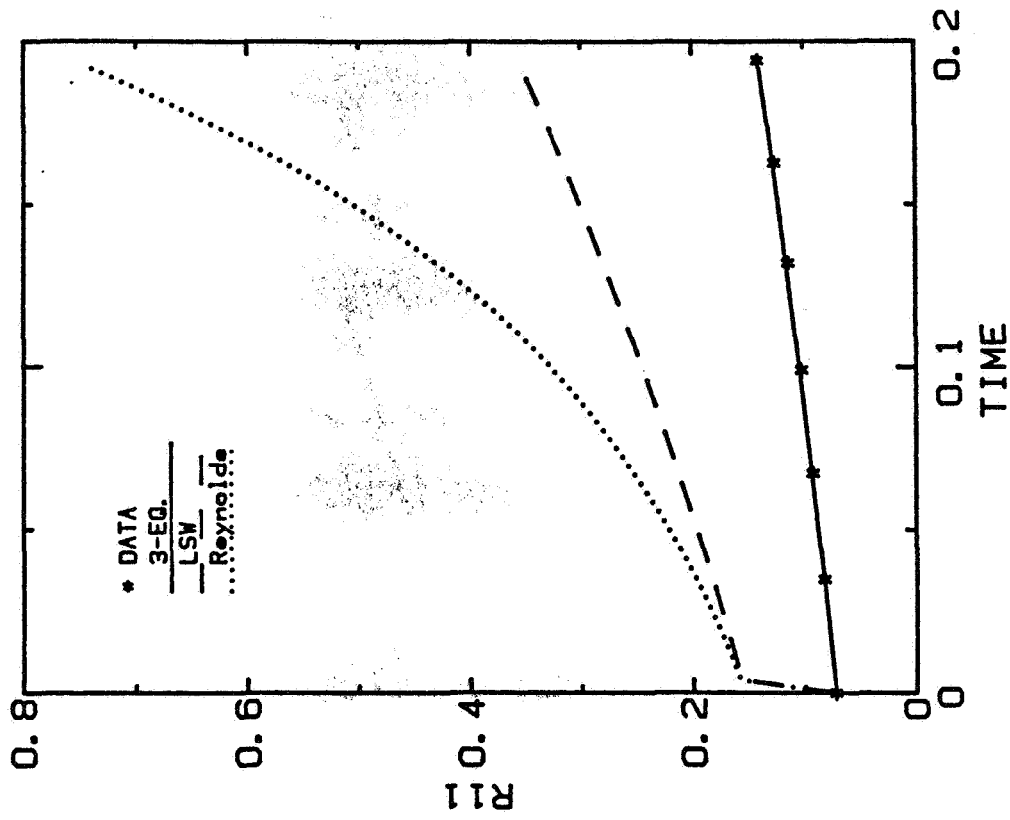


Fig. 7-31(c). The prediction of R_{11} by $k-\epsilon-\tau$ and $k-\epsilon$ models for run EXP.

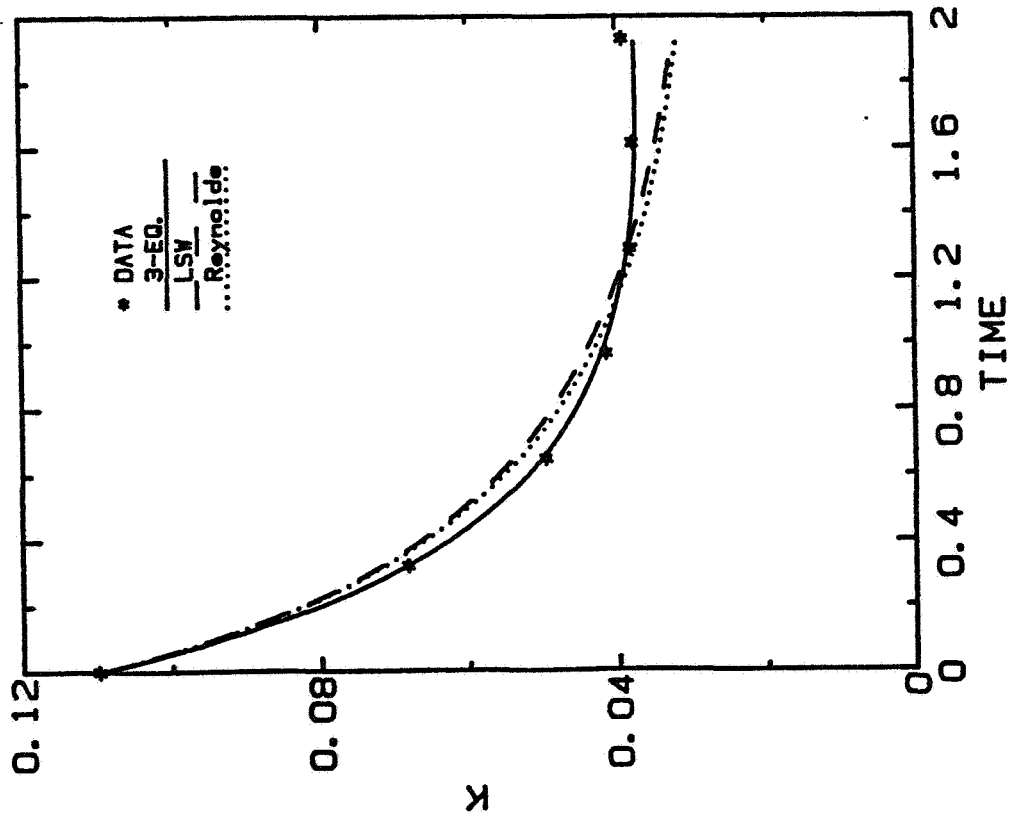


Fig. 7-32(a). The prediction of the turbulent kinetic energy by $k-\epsilon-\tau$ and $k-\epsilon$ models for run EXO.

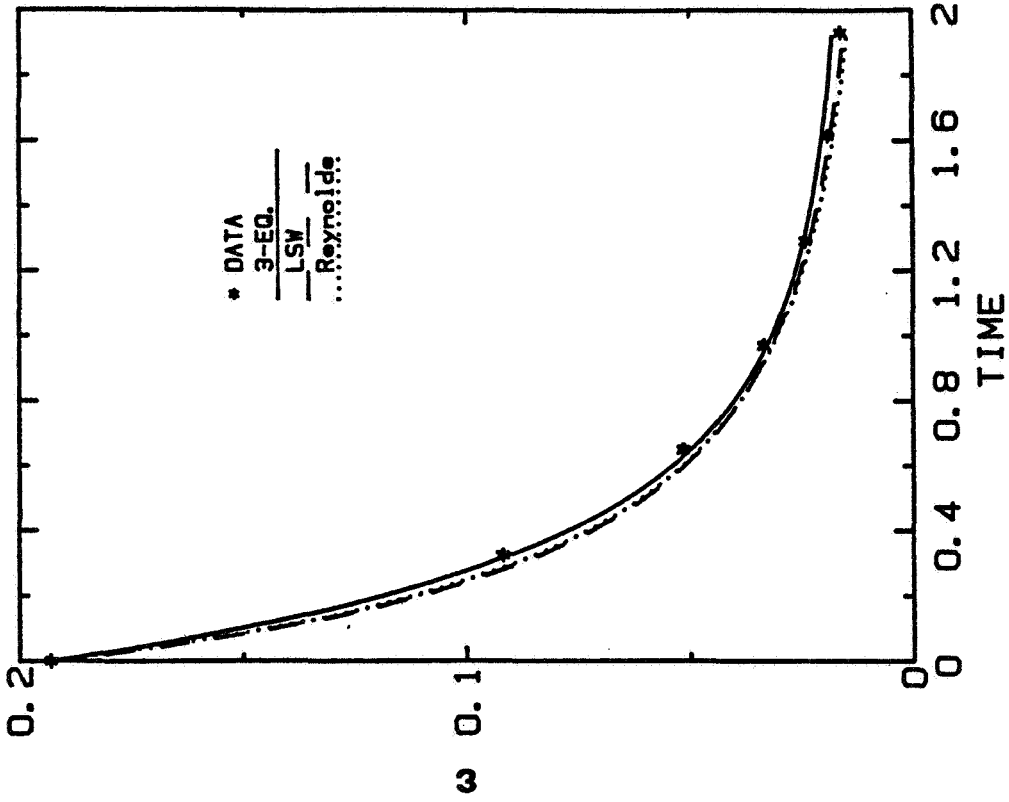


Fig. 7-32(b). The prediction of the dissipation rate by $k-\epsilon-\tau$ and $k-\epsilon$ models for run EXO.

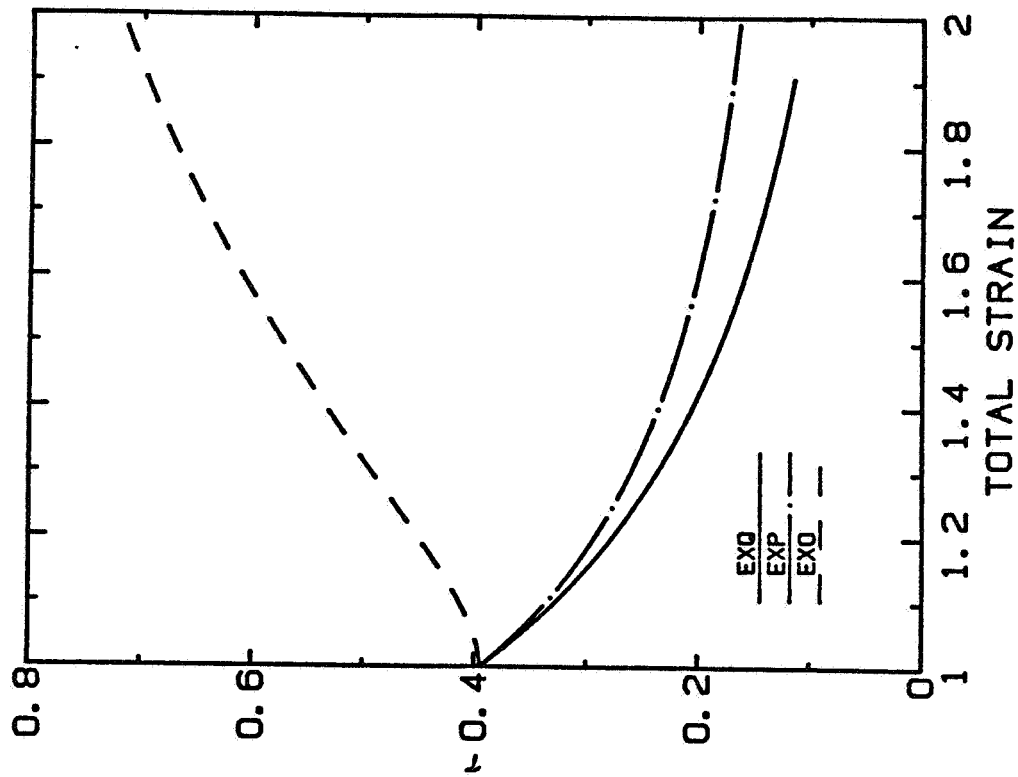


Fig. 7-33. The evolution of the modeled turbulence time scale in incompressible, axisymmetric expansional strain flow.

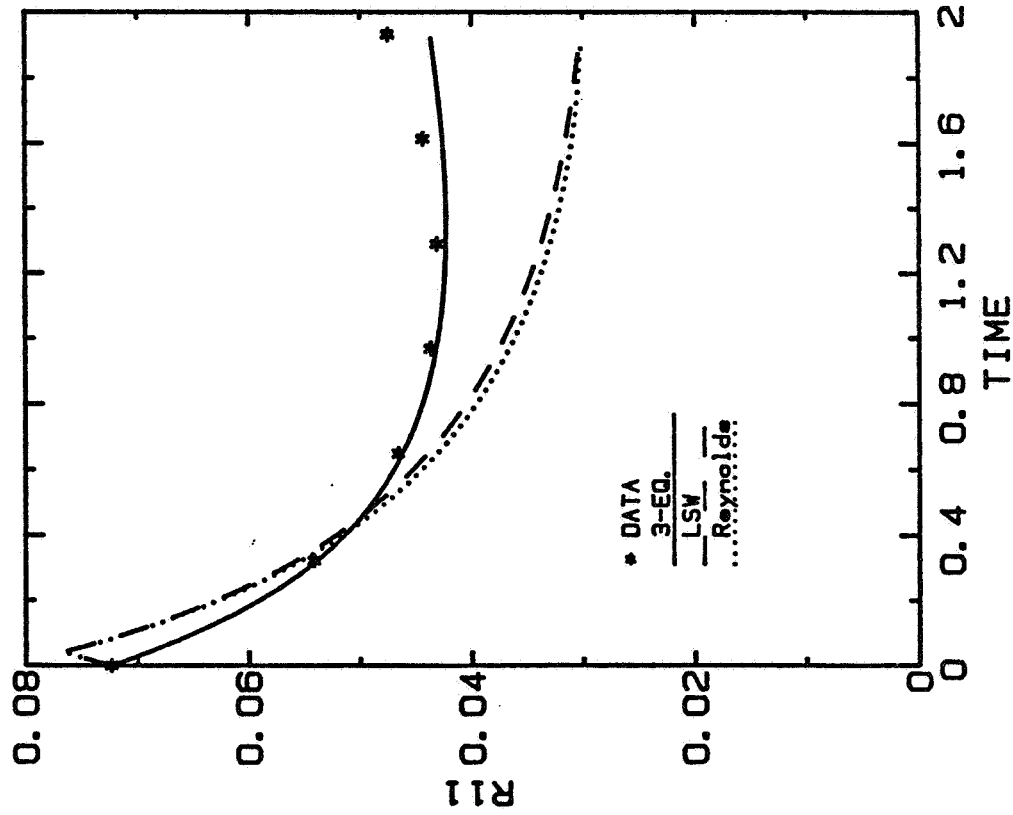


Fig. 7-32(c). The prediction of R_{11} by $k-\epsilon-\tau$ and $k-\epsilon$ models for run EXO.

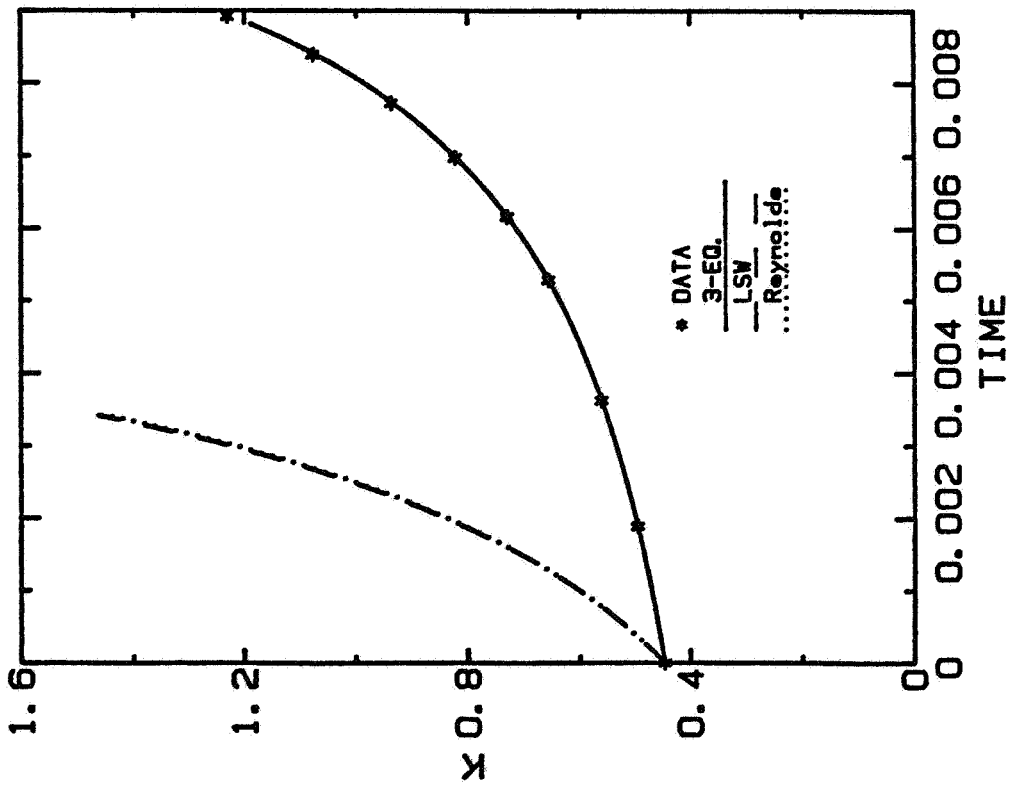


Fig. 7-34(a). The prediction of the turbulent kinetic energy by k - ϵ - τ and k - ϵ models for run ODB.

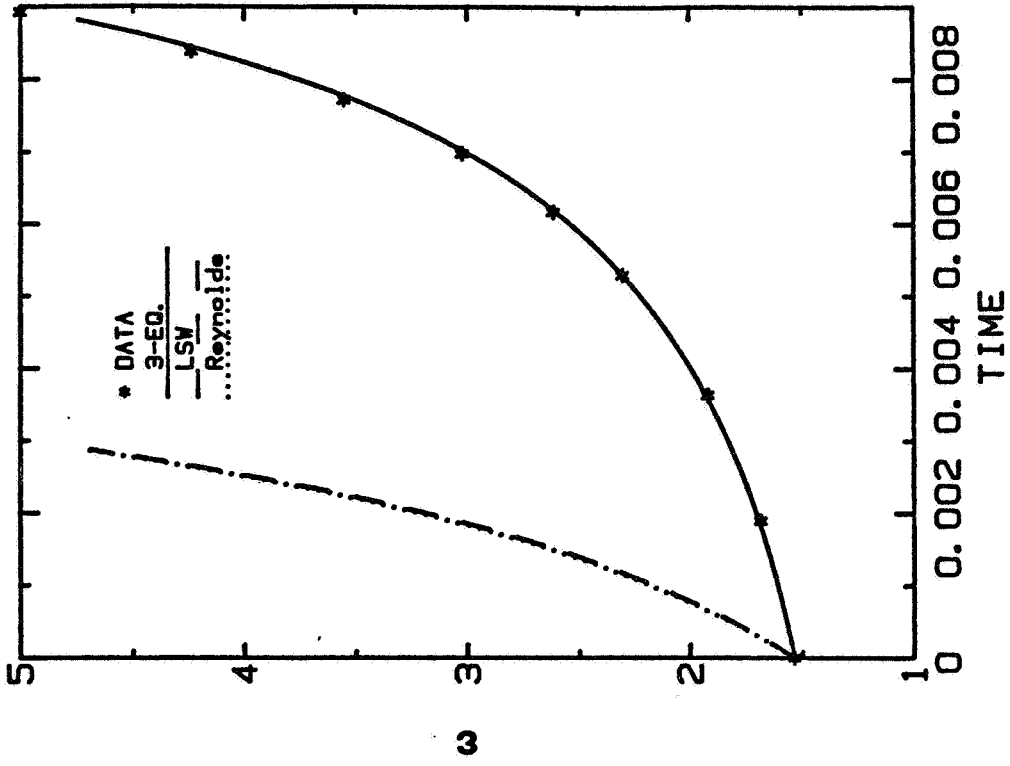


Fig. 7-34(b). The prediction of the dissipation rate by k - ϵ - τ and k - ϵ models for run ODB.

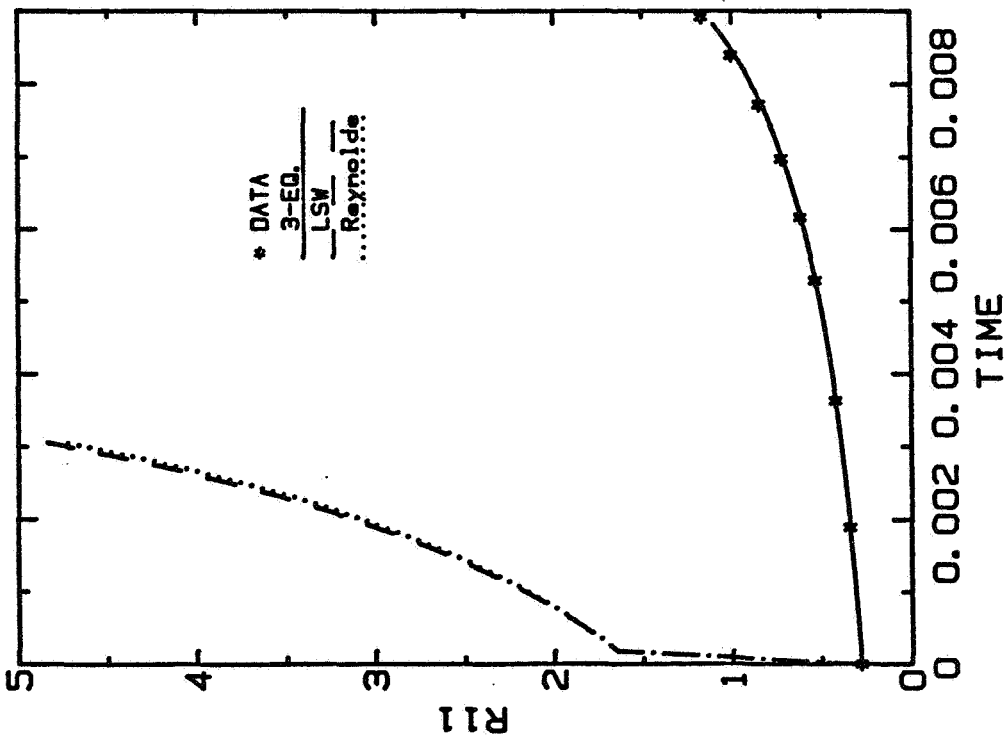


Fig. 7-34(c). The prediction of R_{11} by $k-\epsilon-\tau$ and $k-\epsilon$ models for run ODB.

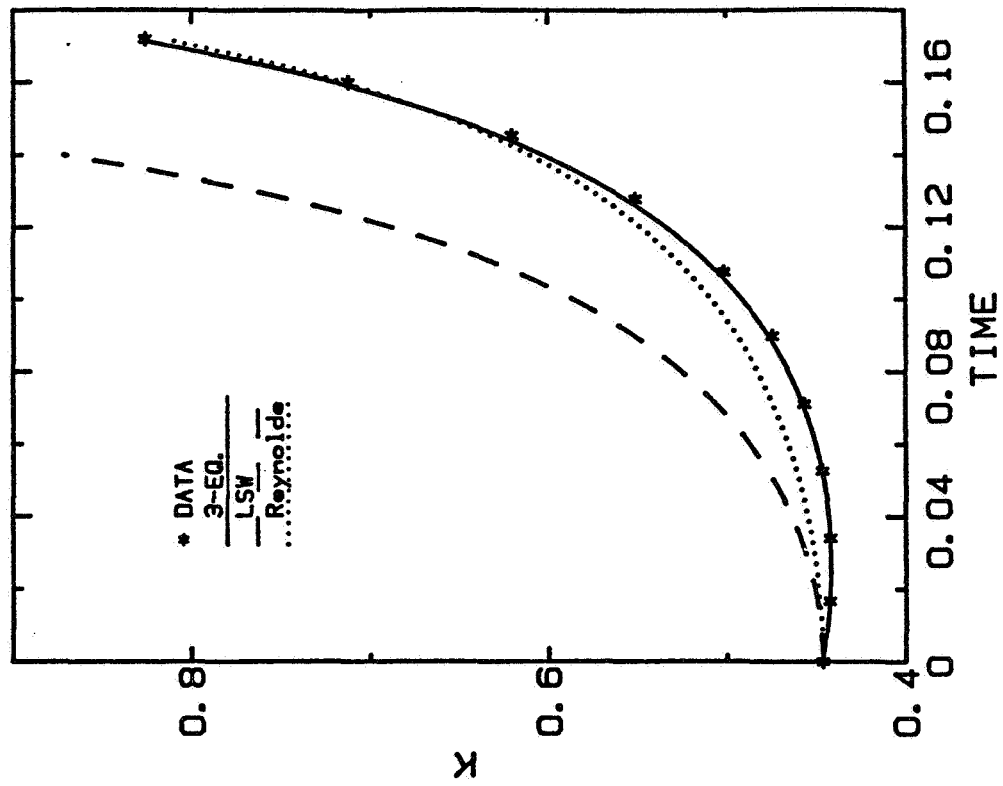


Fig. 7-35(a). The prediction of the turbulent kinetic energy by $k-\epsilon-\tau$ and $k-\epsilon$ models for run ODC.

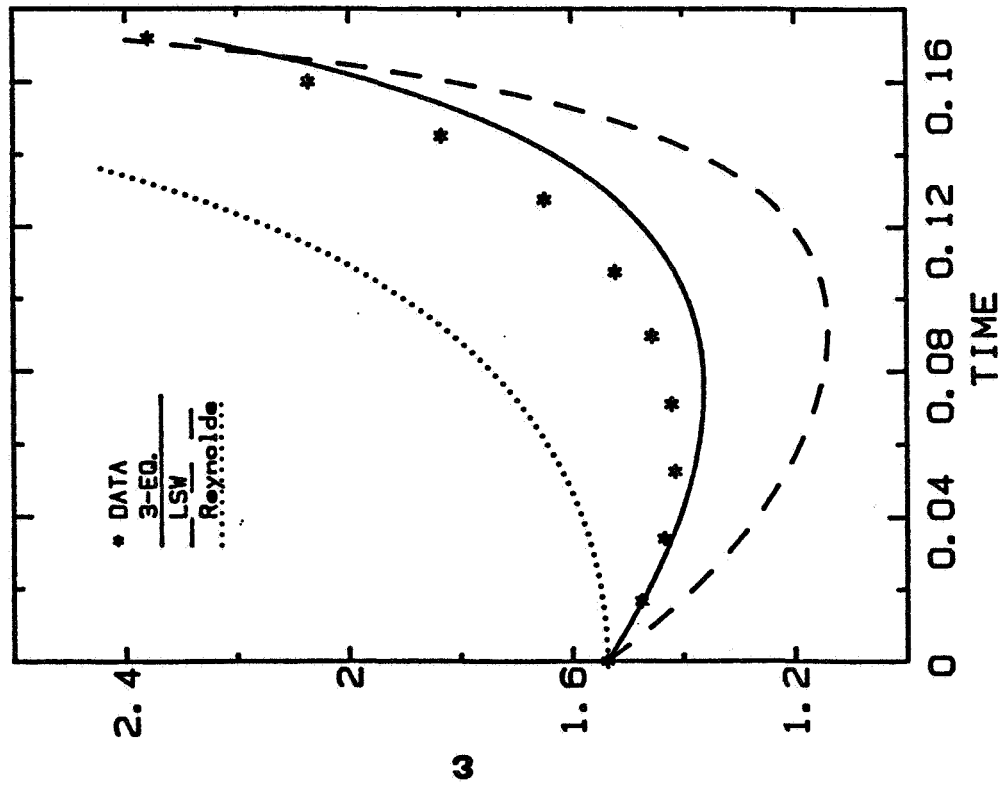


Fig. 7-35(b). The prediction of the dissipation rate by $k-\epsilon-\tau$ and $k-\epsilon$ models for run ODC.

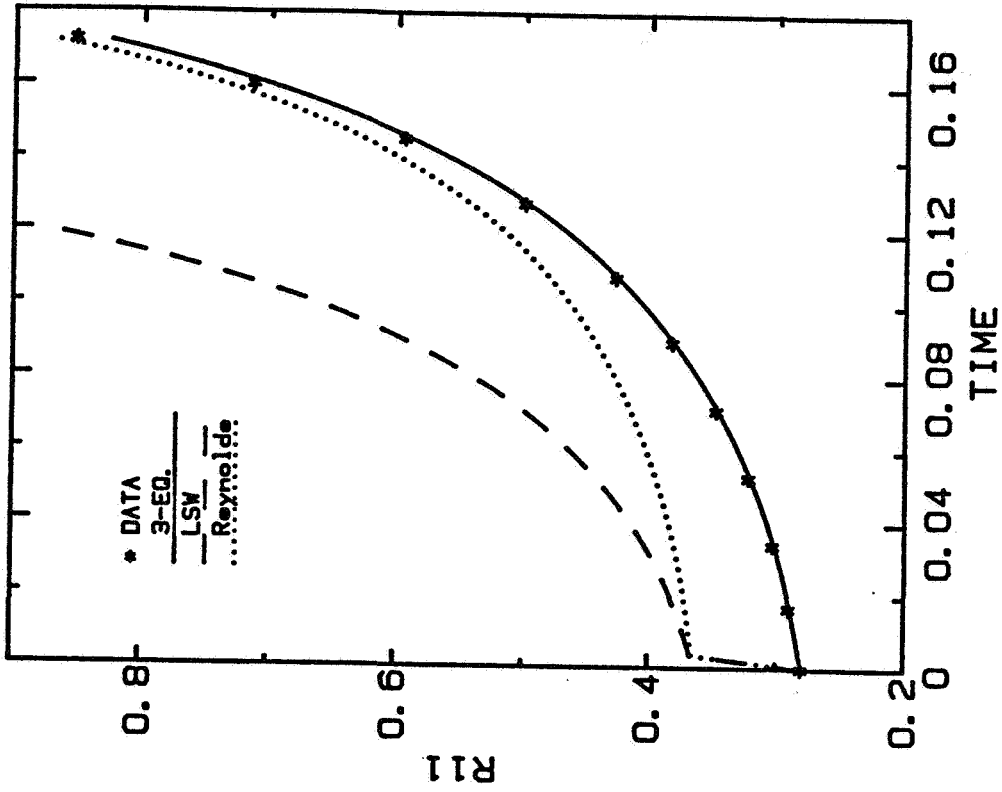


Fig. 7-35(c). The prediction of R_{11} by $k-\epsilon-\tau$ and $k-\epsilon$ models for run ODC.

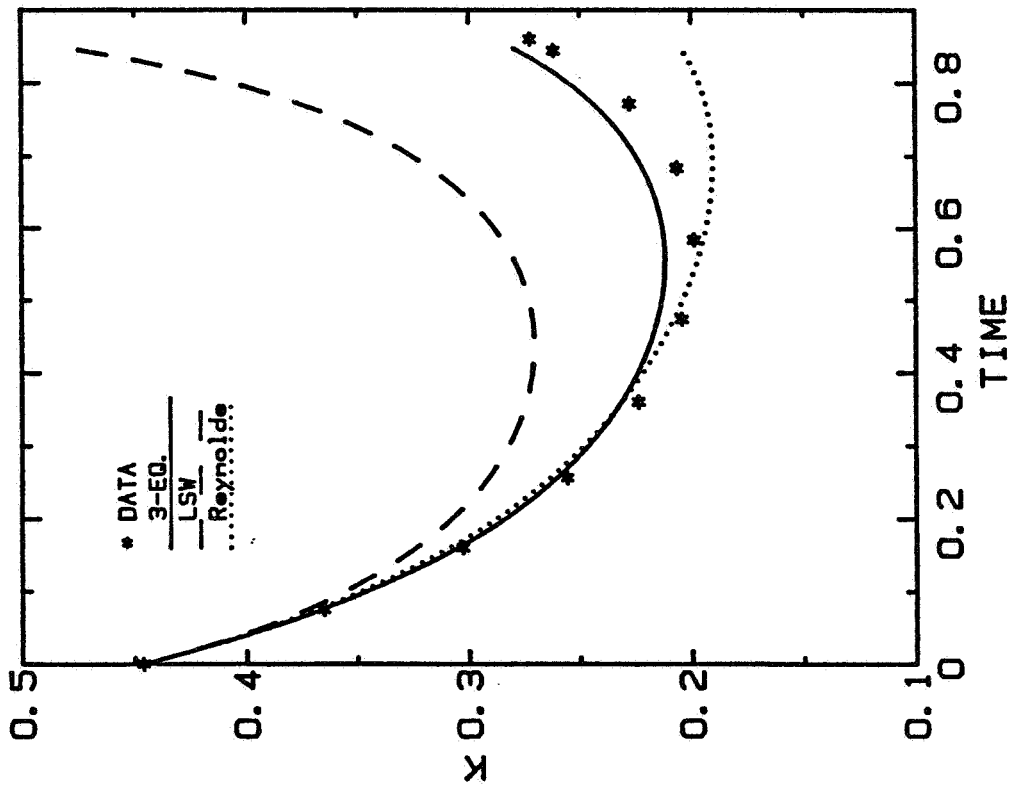


Fig. 7-36(a). The prediction of the turbulent kinetic energy by k - ϵ - τ and k - ϵ models for run ODD.

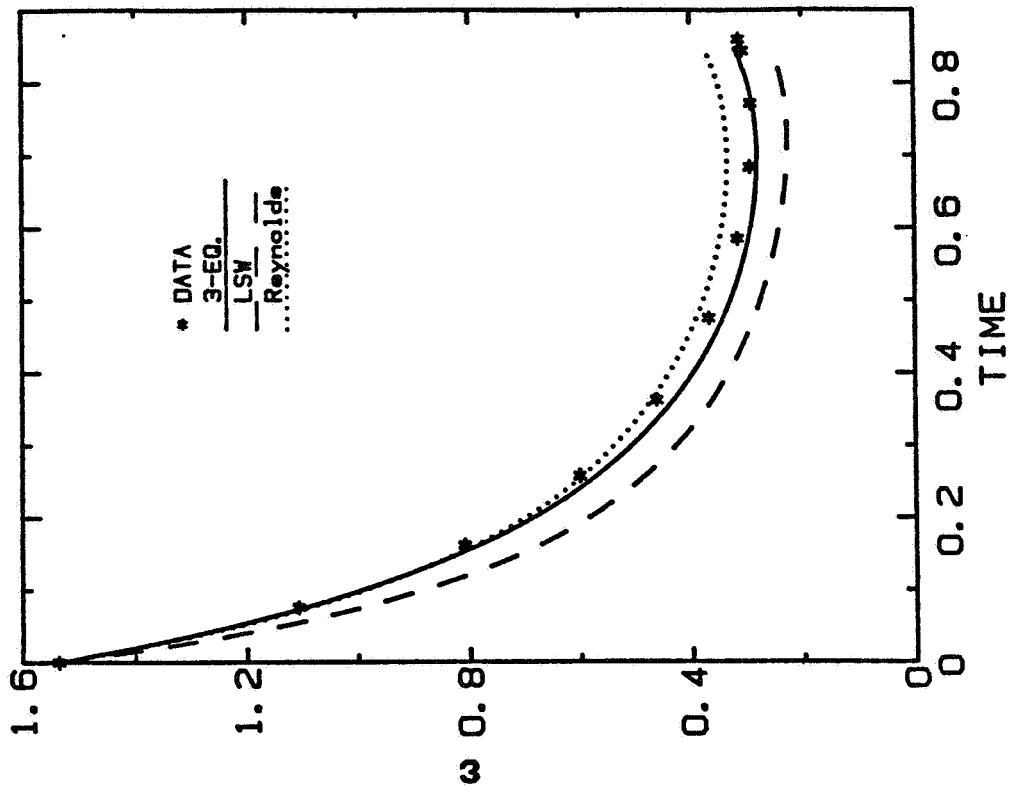


Fig. 7-36(b). The prediction of the dissipation rate by k - ϵ - τ and k - ϵ models for run ODD.

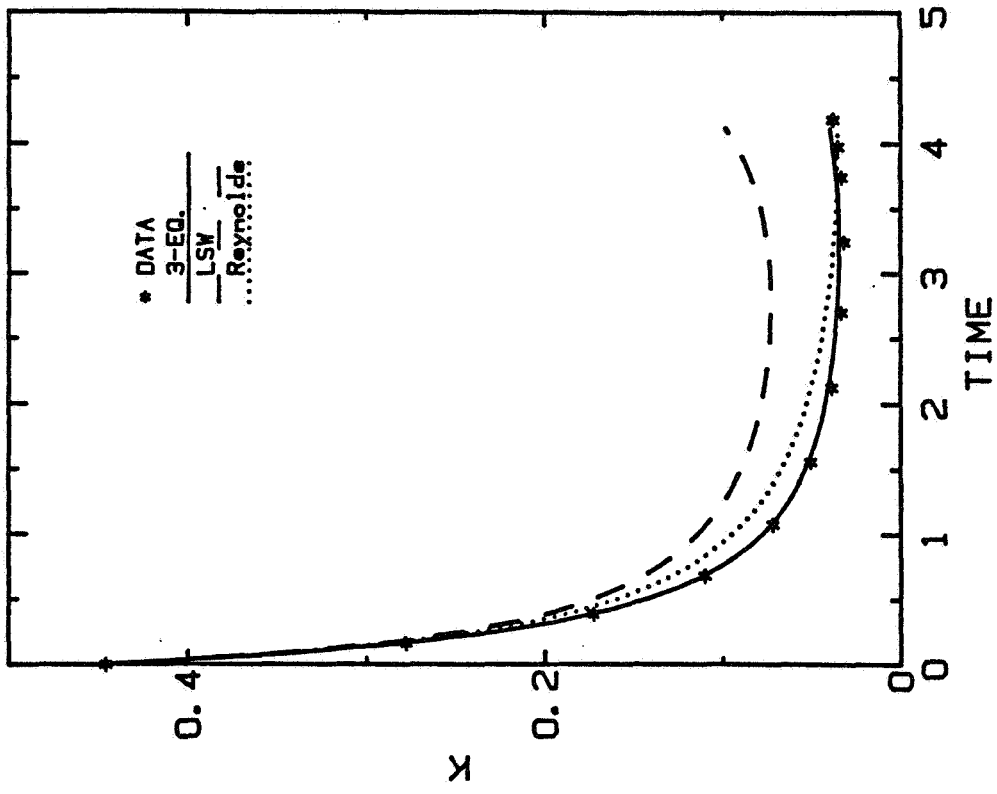


Fig. 7-37(a). The prediction of the turbulent kinetic energy by $k-\epsilon-\tau$ and $k-\epsilon$ models for run ODE.

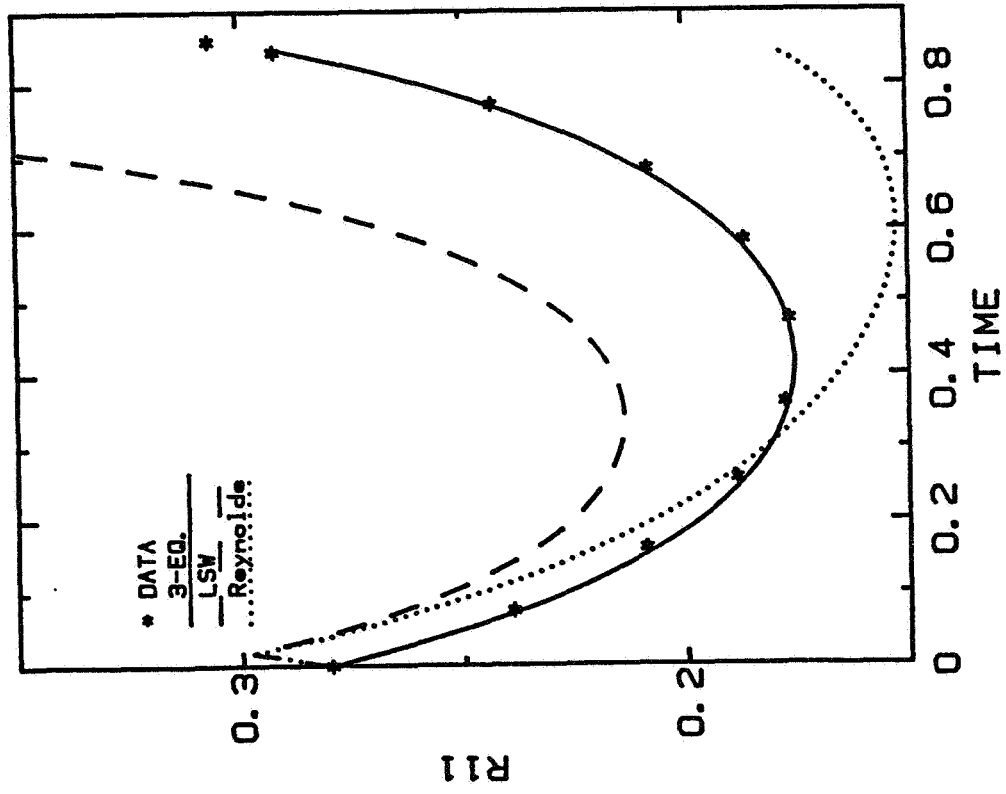


Fig. 7-36(c). The prediction of R_{11} by $k-\epsilon-\tau$ and $k-\epsilon$ models for run ODD.

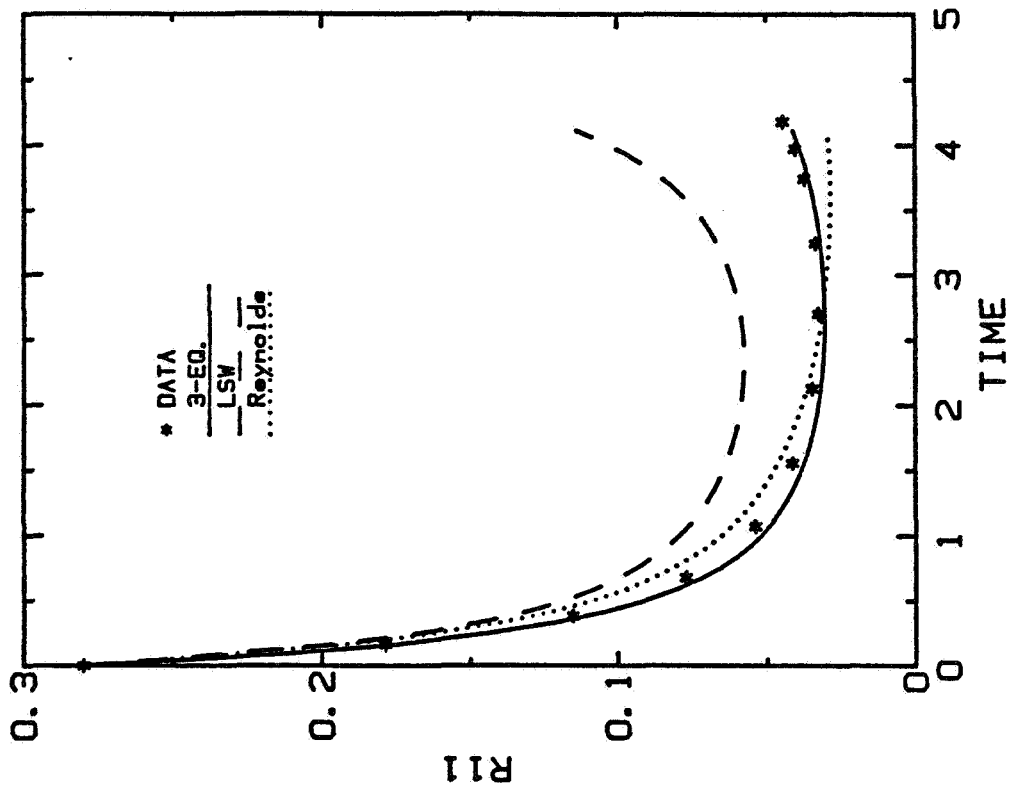


Fig. 7-37(c). The prediction of R_{11} by $k-\epsilon-\tau$ and $k-\epsilon$ models for run ODE.

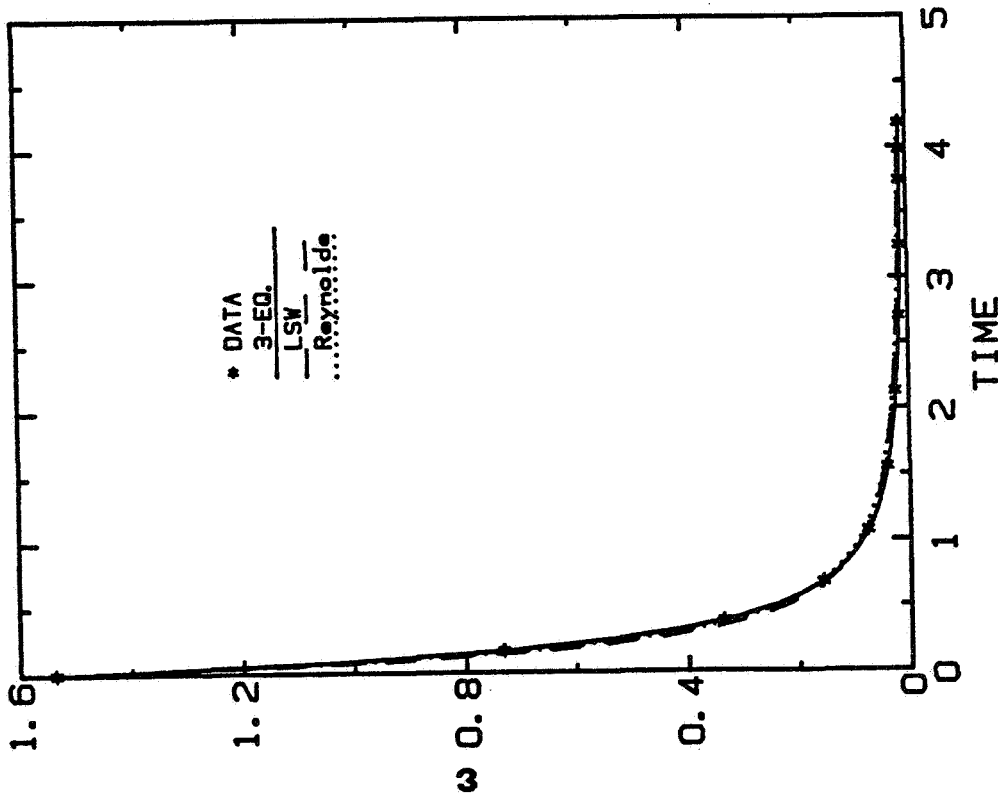


Fig. 7-37(b). The prediction of the dissipation rate by $k-\epsilon-\tau$ and $k-\epsilon$ models for run ODE.

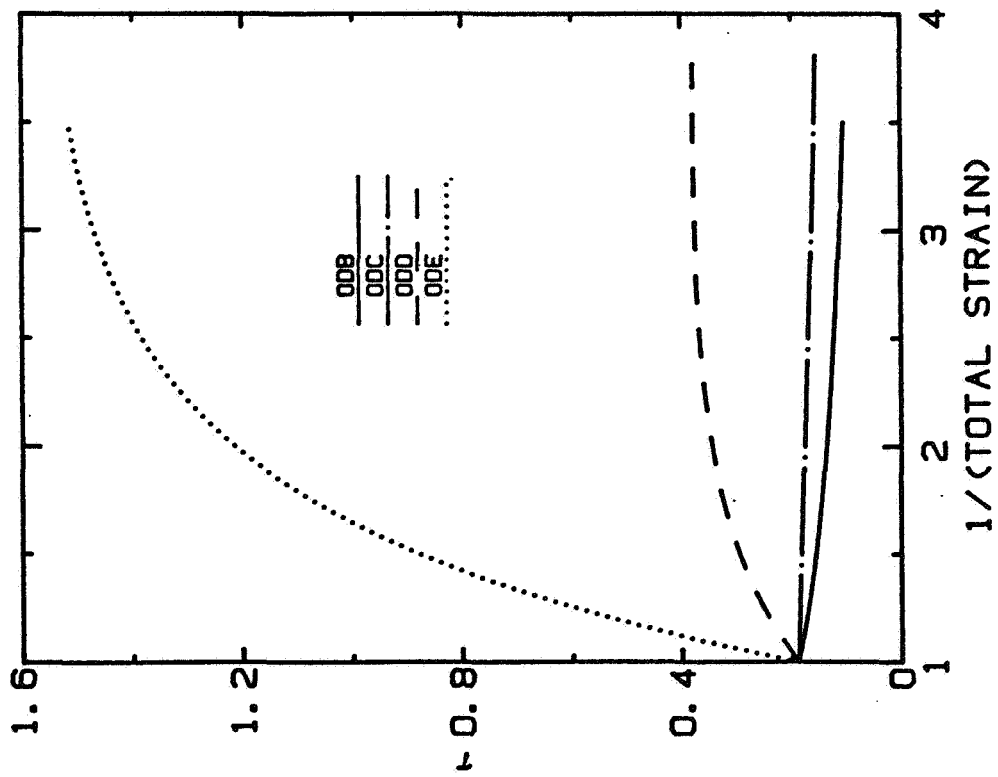


Fig. 7-38. The evolution of the modeled turbulence time scale in one-dimensional compression flow.

Chapter VIII

CONCLUSIONS AND RECOMMENDATIONS

Conclusions and recommendations distilled from the results and discussion presented in the preceding chapters are given in this chapter.

8.1 Conclusions

Numerical methods for solving the three-dimensional, time-dependent, Navier-Stokes equations for homogeneous turbulence undergoing isotropic and one-dimensional compression have been presented along with results obtained from such simulations. The simulations were carried out at low Reynolds number; the limitation on this parameter derives from computer resource availability. The results obtained for fast compression rates have been compared with rapid distortion theory, and good agreement was obtained.

The ratio of the turbulence time scale to the imposed mean-flow time scale was found to be the most important single parameter in these flows. When this ratio is large, the flow is immediately affected by the mean strain in a manner similar to that predicted by rapid distortion theory; i.e., the turbulence kinetic energy and its dissipation rate increase, while the integral length scales immediately decrease. When this ratio is small, the flow initially retains the character of decaying isotropic turbulence; only after the strain has been applied for a long period does the flow begin to reflect the effect of mean strain. In these flows, the Kolmogorov length scale, which is the size of the eddies in which viscous dissipation occurs, decreases rapidly with decreasing total strain, due to the density increase that accompanies compression. This means that these flows have more turbulence energy in the small scales than would be expected on the basis of the models usually used to simulate these flows.

Results from isotropic compression, incompressible axisymmetric expansional strain, and one-dimensional compression simulations were used to test one-point-closure, two-equation ($k-\epsilon$) turbulence models. It was found that $k-\epsilon$ models perform well at low strain rates. When

the strain is so strong that the flow structure is out of equilibrium, these models do not perform well. The parameters in the model dissipation equation cannot be pure constants if the model is to fit the computer-generated data. It was also found that the model turbulence length scale, which is supposed to represent the integral length scale, does so very poorly in these flows. In compressed turbulence, the rapidly decreasing Kolmogorov scale caused by the density increase drives the flow out of equilibrium. The dissipation can no longer satisfactorily fulfill the two functions that $k-\epsilon$ models require of it; it cannot simultaneously be both the rate of destruction of turbulence kinetic energy and the length scale determiner.

To decouple the dissipation and the time scale, a one-point, three-equation turbulence model including a model equation for the turbulence time scale is proposed. The time-scale equation contains terms which account for the decay of isotropic turbulence, the return to isotropic turbulence after a strain has been removed, and the effects of various types of strain. The other two equations of the model govern the evolution of the turbulence kinetic energy and its dissipation rate and are similar to those in $k-\epsilon$ models. The essential change is that the time scale in the destruction term in the modeled dissipation equation is replaced by the new time scale. It is encouraging that the effects of various strains appear to be additive, i.e., only few building-block flows are needed to calibrate the model constants. The new model accurately calculates four types of flows--isotropic decay, isotropic compression, axisymmetric expansion, and one-dimensional compression flows--for a wide range of strain rates.

8.2 Recommendations

As the speed and memory size of supercomputers advance, it will become possible to do simulations of turbulence on a $256 \times 256 \times 256$ grid. This will allow us to study the evolution of turbulence which has an inertial subrange in the spectrum and may eliminate the questions associated with the low Reynolds numbers of the present simulations.

Not all of the flows needed to calibrate the new three-equation turbulence model were simulated in this work. The present code (with

slight modifications) could be used to simulate all the building-block flows needed to calibrate the new model. The model should also be tested by applying it to the simulation of inhomogeneous flows.

Swirl is deliberately generated in the intake stroke by design inlet port shape and orientation and persists through to top-dead-center (TDC) of the compression stroke, at which point the mean flow pattern approximates solid-body rotation. The effect of swirl on turbulence is not well understood. It could be studied by modifying the present code to include a Coriolis force term in the Navier-Stokes equations.

Finally, homogeneous turbulence undergoing expansion could be simulated with the present code with minimum modifications. Results from such simulations could help explain the turbulence behavior during the expansion stroke in an internal combustion engine.

Appendix

TABULATED DATA

Data tabulated in this appendix were obtained from computed turbulence fields described in Chapters V and VI. Fields from the following runs are included.

Run ID	Strain Type	Mean-Deformation Tensor $\bar{U}_{i,j}$
SQF	Isotropic compression	Eq. (2-26) with $L_o = 0.3, V_p = -5.6$
SQG	" "	" " " $L_o = 1.0, V_p = -1.0$
SQH	" "	" " " $L_o = 0.3, V_p = -0.06$
SQI	" "	" " " $L_o = 0.3, V_p = -0.012$
EXQ	Incomp. axisym. exp.	Eq. (7-24) with $S = 35.87$
EXP	" " "	" " " $S = 3.587$
EXO	" " "	" " " $S = 0.3587$
ODB	1-D compression	Eq. (2-30) with $L_o = 0.3, V_p = -24.3$
ODC	" "	" " " $L_o = 0.3, V_p = -1.29$
ODD	" "	" " " $L_o = 0.3, V_p = -0.26$
ODE	" "	" " " $L_o = 0.3, V_p = -0.052$

The following data are presented for each field:

- t = time with units [T]
- S = mean strain rate [T⁻¹]
- $TS = \text{total strain} = \exp\left(\int_{t_0}^t S(t') dt'\right)$ dimensionless
- ν = kinematic viscosity [L²T⁻¹]

Strain Type	S	TS	ν
Isotropic compression	$S(t) = \frac{V_p}{L_o + V_p t}$	$\frac{L_o + V_p t}{L_o}$	$\nu(t) = \nu(0)(TS)^{2.1}$
Incompressible, axisymmetric expansion	constant	$\exp(S(t-t_0))$ $t_0 = 0.58789$	constant
1-D compression	$S(t) = \frac{V_p}{L_o + V_p t}$	$\frac{L_o + V_p t}{L_o}$	$\nu(t) = \nu(0)(TS)^{0.7}$

$$R_{11} = \overline{u'_1 u'_1} \quad (\text{no summation}) \quad \text{with units} \quad [L^2 T^{-2}]$$

$$D_{11} = 2\nu \overline{u'_{1,j} u'_{1,j}} \quad (\text{no summation on } 1) \quad [L^2 T^{-3}]$$

$$q^2 = R_{11} + R_{22} + R_{33} = \text{twice the turbulent kinetic energy} \quad [L^2 T^{-2}]$$

$$\epsilon = (D_{11} + D_{22} + D_{33})/2 = \text{dissipation rate} \quad [L^2 T^{-3}]$$

$$L_{ij,m} = \int_0^{L_h} Q_{ij}(x_m) dx_m \quad (L_h = \text{half the computational box}) \quad \text{with units} \quad [L]$$

longitudinal
= integral length scales in x_m -direction
lateral

$$\lambda_{ij} = \left(\frac{\overline{u'_1 u'_1}}{(\partial u'_1 / \partial x_j)^2} \right)^{1/2} \quad (\text{no summation}) \quad [L]$$

= Taylor microscales

The following data are presented for incompressible, axisymmetric expansion simulations only:

$$dR_{11}/dt \quad \text{with units} \quad [L^2 T^{-3}]$$

$$P_{11} = 4R_{11}S \quad [L^2 T^{-3}]$$

$$T_{11}^{(1)} = \frac{2}{\rho} \overline{p^{(1)} u'_{1,1}} \quad [L^2 T^{-3}]$$

$$\phi_{11} = -\frac{1}{\epsilon} \left[\frac{2}{\rho} \overline{p^{(2)} u'_{1,1}} - (D_{11} - 2\epsilon/3) \right] \quad [L^2 T^{-3}]$$

TS	t	v	S	q ²	ε
RUN ID: SGF					
0. 10000E+01	0. 00000E+00	0. 10000E-01	-0. 18667E+02	0. 81598E-01	0. 32383E-01
0. 77931E+00	0. 11823E-01	0. 59236E-02	-0. 23953E+02	0. 13436E+00	0. 52402E-01
0. 64454E+00	0. 19043E-01	0. 39758E-02	-0. 28961E+02	0. 19642E+00	0. 75703E-01
0. 55173E+00	0. 24015E-01	0. 28683E-02	-0. 33833E+02	0. 26806E+00	0. 10243E+00
RUN ID: SRG					
0. 10000E+01	0. 00000E+00	0. 10000E-01	-0. 10000E+01	0. 81598E-01	0. 32383E-01
0. 94257E+00	0. 57431E-01	0. 88320E-02	-0. 10609E+01	0. 87819E-01	0. 33707E-01
0. 89024E+00	0. 10976E+00	0. 78337E-02	-0. 11233E+01	0. 94622E-01	0. 35348E-01
0. 84214E+00	0. 15786E+00	0. 69712E-02	-0. 11874E+01	0. 10205E+00	0. 37290E-01
0. 79816E+00	0. 20184E+00	0. 62285E-02	-0. 12529E+01	0. 11004E+00	0. 39507E-01
0. 75757E+00	0. 24243E+00	0. 55820E-02	-0. 13200E+01	0. 11867E+00	0. 42009E-01
0. 72022E+00	0. 27978E+00	0. 50197E-02	-0. 13885E+01	0. 12789E+00	0. 44785E-01
0. 68585E+00	0. 31415E+00	0. 45299E-02	-0. 14580E+01	0. 13768E+00	0. 47834E-01
0. 65424E+00	0. 34576E+00	0. 41024E-02	-0. 15285E+01	0. 14804E+00	0. 51151E-01
0. 62485E+00	0. 37515E+00	0. 37250E-02	-0. 16004E+01	0. 15903E+00	0. 54773E-01
RUN ID: SRI					
0. 10000E+01	0. 00000E+00	0. 10000E-01	-0. 40000E-01	0. 81598E-01	0. 32383E-01
0. 98466E+00	0. 38350E+00	0. 96806E-02	-0. 40623E-01	0. 63757E-01	0. 21111E-01
0. 96703E+00	0. 32433E+00	0. 93201E-02	-0. 41364E-01	0. 50611E-01	0. 14051E-01
0. 94697E+00	0. 13258E+01	0. 89188E-02	-0. 42240E-01	0. 40886E-01	0. 95618E-02
0. 92426E+00	0. 18936E+01	0. 84755E-02	-0. 43278E-01	0. 33613E-01	0. 66775E-02
0. 89969E+00	0. 25078E+01	0. 80092E-02	-0. 44460E-01	0. 28281E-01	0. 48591E-02
0. 87370E+00	0. 31574E+01	0. 75312E-02	-0. 45782E-01	0. 24326E-01	0. 36833E-02
0. 83251E+00	0. 41873E+01	0. 68048E-02	-0. 48048E-01	0. 20108E-01	0. 25889E-02
0. 78798E+00	0. 53005E+01	0. 60629E-02	-0. 50763E-01	0. 17193E-01	0. 19195E-02
0. 74173E+00	0. 64567E+01	0. 53397E-02	-0. 53928E-01	0. 15226E-01	0. 15035E-02
0. 69570E+00	0. 76076E+01	0. 46675E-02	-0. 57496E-01	0. 13948E-01	0. 12442E-02
0. 65031E+00	0. 87422E+01	0. 40509E-02	-0. 61509E-01	0. 13151E-01	0. 10768E-02
0. 60528E+00	0. 98681E+01	0. 34842E-02	-0. 66086E-01	0. 12710E-01	0. 96738E-03
0. 56248E+00	0. 10938E+02	0. 29869E-02	-0. 71114E-01	0. 12565E-01	0. 90257E-03
0. 52270E+00	0. 11932E+02	0. 25605E-02	-0. 76526E-01	0. 12654E-01	0. 87011E-03

TS	t	v	S	q ²	ε
RUN 1D: SQH					
0. 10000E+01	0. 00000E+00	0. 10000E-01	-0. 20000E+00	0. 81598E-01	0. 32383E-01
0. 97613E+00	0. 11937E+00	0. 95052E-02	-0. 20489E+00	0. 78121E-01	0. 29171E-01
0. 95205E+00	0. 23975E+00	0. 90196E-02	-0. 21007E+00	0. 75250E-01	0. 26565E-01
0. 92770E+00	0. 35111E+00	0. 85434E-02	-0. 21557E+00	0. 72894E-01	0. 24426E-01
0. 90357E+00	0. 48215E+00	0. 80820E-02	-0. 22134E+00	0. 71002E-01	0. 22669E-01
0. 87937E+00	0. 60317E+00	0. 76341E-02	-0. 22744E+00	0. 69510E-01	0. 21212E-01
0. 85541E+00	0. 72297E+00	0. 72038E-02	-0. 23381E+00	0. 68384E-01	0. 20010E-01
0. 83171E+00	0. 84144E+00	0. 67912E-02	-0. 24047E+00	0. 67582E-01	0. 19018E-01
0. 80833E+00	0. 95837E+00	0. 63963E-02	-0. 24742E+00	0. 67072E-01	0. 18201E-01
0. 78525E+00	0. 10738E+01	0. 60189E-02	-0. 25470E+00	0. 66828E-01	0. 17534E-01
0. 76254E+00	0. 11873E+01	0. 56591E-02	-0. 26228E+00	0. 66830E-01	0. 16998E-01
0. 74010E+00	0. 12995E+01	0. 53151E-02	-0. 27023E+00	0. 67064E-01	0. 16575E-01
0. 71810E+00	0. 14095E+01	0. 49887E-02	-0. 27851E+00	0. 67514E-01	0. 16256E-01
0. 69675E+00	0. 15162E+01	0. 46824E-02	-0. 28705E+00	0. 68163E-01	0. 16033E-01
0. 67626E+00	0. 16187E+01	0. 43978E-02	-0. 29575E+00	0. 68986E-01	0. 15896E-01
0. 65656E+00	0. 17172E+01	0. 41331E-02	-0. 30462E+00	0. 69969E-01	0. 15835E-01
0. 63763E+00	0. 18118E+01	0. 38868E-02	-0. 31366E+00	0. 71098E-01	0. 15842E-01
0. 61954E+00	0. 19023E+01	0. 36588E-02	-0. 32282E+00	0. 72355E-01	0. 15909E-01
0. 60215E+00	0. 19892E+01	0. 34465E-02	-0. 33214E+00	0. 73737E-01	0. 16032E-01
0. 58544E+00	0. 20728E+01	0. 32487E-02	-0. 34162E+00	0. 75236E-01	0. 16205E-01
0. 56945E+00	0. 21528E+01	0. 30651E-02	-0. 35122E+00	0. 76839E-01	0. 16426E-01
0. 55405E+00	0. 22297E+01	0. 28937E-02	-0. 36098E+00	0. 78549E-01	0. 16691E-01
0. 53202E+00	0. 23399E+01	0. 26573E-02	-0. 37593E+00	0. 81305E-01	0. 17171E-01
0. 51117E+00	0. 24441E+01	0. 24434E-02	-0. 39126E+00	0. 84286E-01	0. 17744E-01

TS R₁₁ R₂₂ R₃₃ D_{11/2} D_{22/2} D_{33/2}

RUN ID: 500F
 0. 10000E+01 0. 26071E-01 0. 28377E-01 0. 27149E-01 0. 10576E-01 0. 10954E-01 0. 10853E-01
 0. 77931E+00 0. 42938E-01 0. 46714E-01 0. 44707E-01 0. 17115E-01 0. 17726E-01 0. 17560E-01
 0. 64454E+00 0. 62783E-01 0. 68275E-01 0. 65363E-01 0. 24726E-01 0. 25609E-01 0. 25368E-01
 0. 55173E+00 0. 85598E-01 0. 93155E-01 0. 89210E-01 0. 33456E-01 0. 34652E-01 0. 34323E-01

RUN ID: 500G
 0. 10000E+01 0. 26071E-01 0. 28377E-01 0. 27149E-01 0. 10576E-01 0. 10954E-01 0. 10853E-01
 0. 94257E+00 0. 28053E-01 0. 30547E-01 0. 29219E-01 0. 11000E-01 0. 11404E-01 0. 11304E-01
 0. 89024E+00 0. 30225E-01 0. 32914E-01 0. 31484E-01 0. 11526E-01 0. 11960E-01 0. 11861E-01
 0. 84214E+00 0. 32598E-01 0. 35491E-01 0. 33959E-01 0. 12150E-01 0. 12619E-01 0. 12521E-01
 0. 79816E+00 0. 35158E-01 0. 38259E-01 0. 36627E-01 0. 12863E-01 0. 13370E-01 0. 13274E-01
 0. 75757E+00 0. 37921E-01 0. 41237E-01 0. 39508E-01 0. 13668E-01 0. 14217E-01 0. 14124E-01
 0. 72022E+00 0. 40880E-01 0. 44414E-01 0. 42592E-01 0. 14562E-01 0. 15156E-01 0. 15067E-01
 0. 68585E+00 0. 44028E-01 0. 47781E-01 0. 45874E-01 0. 15543E-01 0. 16186E-01 0. 16104E-01
 0. 65424E+00 0. 47358E-01 0. 51330E-01 0. 49346E-01 0. 16611E-01 0. 17306E-01 0. 17233E-01
 0. 62485E+00 0. 50899E-01 0. 55091E-01 0. 53039E-01 0. 17778E-01 0. 18529E-01 0. 18467E-01

RUN ID: 500I
 0. 10000E+01 0. 26071E-01 0. 28377E-01 0. 27149E-01 0. 10576E-01 0. 10954E-01 0. 10853E-01
 0. 98466E+00 0. 20352E-01 0. 22188E-01 0. 21217E-01 0. 68530E-02 0. 71488E-02 0. 71088E-02
 0. 96703E+00 0. 16167E-01 0. 17579E-01 0. 16864E-01 0. 45304E-02 0. 47625E-02 0. 47581E-02
 0. 94697E+00 0. 13092E-01 0. 14150E-01 0. 13644E-01 0. 30637E-02 0. 32401E-02 0. 32580E-02
 0. 92426E+00 0. 10801E-01 0. 11598E-01 0. 11215E-01 0. 21292E-02 0. 22563E-02 0. 22920E-02
 0. 89969E+00 0. 71186E-02 0. 97590E-02 0. 94037E-02 0. 15478E-02 0. 16336E-02 0. 16776E-02
 0. 87370E+00 0. 78594E-02 0. 84292E-02 0. 80375E-02 0. 11771E-02 0. 12317E-02 0. 12745E-02
 0. 83251E+00 0. 64898E-02 0. 70567E-02 0. 65615E-02 0. 83169E-03 0. 86295E-03 0. 89428E-03
 0. 78798E+00 0. 55261E-02 0. 61399E-02 0. 55271E-02 0. 61595E-03 0. 64406E-03 0. 65948E-03
 0. 74173E+00 0. 48818E-02 0. 55286E-02 0. 48154E-02 0. 48057E-03 0. 51045E-03 0. 51251E-03
 0. 69570E+00 0. 44786E-02 0. 51228E-02 0. 43467E-02 0. 39756E-03 0. 42651E-03 0. 42013E-03
 0. 65031E+00 0. 42382E-02 0. 48558E-02 0. 40565E-02 0. 34594E-03 0. 37135E-03 0. 35953E-03
 0. 60528E+00 0. 41119E-02 0. 46956E-02 0. 39022E-02 0. 31287E-03 0. 33536E-03 0. 31915E-03
 0. 56248E+00 0. 40801E-02 0. 46306E-02 0. 38545E-02 0. 29202E-03 0. 31542E-03 0. 29512E-03
 0. 52270E+00 0. 41309E-02 0. 46440E-02 0. 38787E-02 0. 27977E-03 0. 30762E-03 0. 28272E-03

TS R₁₁ R₂₂ R₃₃ D_{11/2} D_{22/2} D_{33/2}

RUN ID: 5001
 0. 10000E+00 0. 26071E-01 0. 28377E-01 0. 27149E-01 0. 10576E-01 0. 10954E-01 0. 10853E-01
 0. 97613E+00 0. 24949E-01 0. 27180E-01 0. 25991E-01 0. 95102E-02 0. 98707E-02 0. 97897E-02
 0. 95205E+00 0. 24077E-01 0. 26184E-01 0. 25039E-01 0. 86441E-02 0. 89921E-02 0. 89292E-02
 0. 92778E+00 0. 23275E-01 0. 25356E-01 0. 24262E-01 0. 79320E-02 0. 82699E-02 0. 82239E-02
 0. 90357E+00 0. 22676E-01 0. 24682E-01 0. 23644E-01 0. 73470E-02 0. 76762E-02 0. 76459E-02
 0. 87937E+00 0. 22209E-01 0. 24139E-01 0. 23162E-01 0. 68618E-02 0. 71830E-02 0. 71674E-02
 0. 85541E+00 0. 21863E-01 0. 23716E-01 0. 22805E-01 0. 64617E-02 0. 67750E-02 0. 67734E-02
 0. 83171E+00 0. 21523E-01 0. 23401E-01 0. 22558E-01 0. 61317E-02 0. 64370E-02 0. 64489E-02
 0. 80833E+00 0. 21179E-01 0. 23184E-01 0. 22409E-01 0. 58606E-02 0. 61577E-02 0. 61827E-02
 0. 78525E+00 0. 21422E-01 0. 23057E-01 0. 22348E-01 0. 56395E-02 0. 59283E-02 0. 59662E-02
 0. 76254E+00 0. 21445E-01 0. 23016E-01 0. 22369E-01 0. 54618E-02 0. 57424E-02 0. 57934E-02
 0. 74010E+00 0. 21544E-01 0. 23055E-01 0. 22465E-01 0. 53219E-02 0. 55946E-02 0. 56582E-02
 0. 71810E+00 0. 21712E-01 0. 23173E-01 0. 22629E-01 0. 52164E-02 0. 54817E-02 0. 55576E-02
 0. 69675E+00 0. 21943E-01 0. 23365E-01 0. 22855E-01 0. 51429E-02 0. 54015E-02 0. 54883E-02
 0. 67626E+00 0. 22229E-01 0. 23623E-01 0. 23134E-01 0. 50983E-02 0. 53506E-02 0. 54469E-02
 0. 65656E+00 0. 22565E-01 0. 23943E-01 0. 23461E-01 0. 50795E-02 0. 53260E-02 0. 54296E-02
 0. 63763E+00 0. 22746E-01 0. 24319E-01 0. 23832E-01 0. 50837E-02 0. 53245E-02 0. 54337E-02
 0. 61954E+00 0. 23366E-01 0. 24747E-01 0. 24242E-01 0. 51087E-02 0. 53438E-02 0. 54567E-02
 0. 60215E+00 0. 23822E-01 0. 25224E-01 0. 24690E-01 0. 51527E-02 0. 53818E-02 0. 54971E-02
 0. 58544E+00 0. 24313E-01 0. 25747E-01 0. 25176E-01 0. 52143E-02 0. 54369E-02 0. 55540E-02
 0. 56945E+00 0. 24833E-01 0. 26312E-01 0. 25695E-01 0. 52921E-02 0. 55075E-02 0. 56261E-02
 0. 55405E+00 0. 25383E-01 0. 26918E-01 0. 26248E-01 0. 53852E-02 0. 55926E-02 0. 57134E-02
 0. 53202E+00 0. 26262E-01 0. 27902E-01 0. 27142E-01 0. 55525E-02 0. 57463E-02 0. 58719E-02
 0. 51117E+00 0. 27204E-01 0. 28973E-01 0. 28109E-01 0. 57511E-02 0. 59297E-02 0. 60631E-02

TS	L11,1	L22,1	L33,1	L11,2	L22,2	L33,2
RUN ID: SQF						
0. 10000E+01	0. 40340E+00	0. 29692E+00	0. 24845E+00	0. 29233E+00	0. 70986E+00	0. 30577E+00
0. 77931E+00	0. 37527E+00	0. 23130E+00	0. 19362E+00	0. 22748E+00	0. 55230E+00	0. 23825E+00
0. 64454E+00	0. 31086E+00	0. 19123E+00	0. 16014E+00	0. 18788E+00	0. 45608E+00	0. 19702E+00
0. 55173E+00	0. 26582E+00	0. 16362E+00	0. 13708E+00	0. 16061E+00	0. 38982E+00	0. 16863E+00
RUN ID: SQG						
0. 10000E+01	0. 40340E+00	0. 29692E+00	0. 24845E+00	0. 29233E+00	0. 70986E+00	0. 30577E+00
0. 94257E+00	0. 46110E+00	0. 28441E+00	0. 23853E+00	0. 27880E+00	0. 67794E+00	0. 29306E+00
0. 89024E+00	0. 44002E+00	0. 27234E+00	0. 22899E+00	0. 26588E+00	0. 64710E+00	0. 28076E+00
0. 84214E+00	0. 42006E+00	0. 26071E+00	0. 21979E+00	0. 25352E+00	0. 61732E+00	0. 26887E+00
0. 79816E+00	0. 40132E+00	0. 24962E+00	0. 21105E+00	0. 24183E+00	0. 58892E+00	0. 25750E+00
0. 75757E+00	0. 38364E+00	0. 23901E+00	0. 20270E+00	0. 23072E+00	0. 56173E+00	0. 24659E+00
0. 72022E+00	0. 36704E+00	0. 22895E+00	0. 19478E+00	0. 22023E+00	0. 53590E+00	0. 23618E+00
0. 68585E+00	0. 35151E+00	0. 21943E+00	0. 18730E+00	0. 21035E+00	0. 51144E+00	0. 22628E+00
0. 65424E+00	0. 33701E+00	0. 21045E+00	0. 18026E+00	0. 20107E+00	0. 48837E+00	0. 21689E+00
0. 62485E+00	0. 32334E+00	0. 20193E+00	0. 17357E+00	0. 19229E+00	0. 46644E+00	0. 20792E+00
RUN ID: SKI						
0. 10000E+01	0. 40340E+00	0. 29692E+00	0. 24845E+00	0. 29233E+00	0. 70986E+00	0. 30577E+00
0. 98466E+00	0. 51493E+00	0. 32189E+00	0. 27400E+00	0. 30900E+00	0. 75474E+00	0. 33116E+00
0. 96703E+00	0. 54761E+00	0. 34407E+00	0. 29886E+00	0. 32040E+00	0. 78405E+00	0. 34811E+00
0. 94697E+00	0. 57693E+00	0. 36155E+00	0. 31910E+00	0. 32535E+00	0. 79542E+00	0. 35470E+00
0. 92426E+00	0. 59810E+00	0. 37245E+00	0. 33176E+00	0. 32665E+00	0. 79117E+00	0. 35235E+00
0. 89969E+00	0. 60695E+00	0. 37701E+00	0. 33773E+00	0. 32814E+00	0. 77933E+00	0. 34499E+00
0. 87370E+00	0. 60565E+00	0. 37784E+00	0. 34029E+00	0. 33110E+00	0. 76902E+00	0. 33618E+00
0. 83251E+00	0. 59664E+00	0. 38059E+00	0. 34237E+00	0. 33389E+00	0. 76441E+00	0. 32089E+00
0. 78798E+00	0. 59360E+00	0. 39472E+00	0. 34351E+00	0. 33018E+00	0. 76894E+00	0. 30170E+00
0. 74173E+00	0. 60114E+00	0. 42151E+00	0. 34261E+00	0. 32407E+00	0. 77586E+00	0. 28239E+00
0. 69570E+00	0. 60855E+00	0. 45254E+00	0. 33520E+00	0. 32067E+00	0. 78077E+00	0. 27087E+00
0. 65031E+00	0. 60630E+00	0. 47870E+00	0. 31485E+00	0. 31931E+00	0. 78031E+00	0. 27489E+00
0. 60528E+00	0. 59148E+00	0. 49664E+00	0. 28165E+00	0. 31902E+00	0. 77067E+00	0. 29571E+00
0. 56248E+00	0. 56555E+00	0. 50627E+00	0. 24536E+00	0. 32072E+00	0. 75036E+00	0. 32345E+00
0. 52270E+00	0. 53617E+00	0. 50829E+00	0. 21506E+00	0. 32427E+00	0. 72211E+00	0. 34610E+00

TS L11'1 L22'1 L33'1 L11'2 L22'2 L33'2

RUN ID: SKH1

0. 10000E+01	0. 40340E+00	0. 29692E+00	0. 24845E+00	0. 29233E+00	0. 70986E+00	0. 30577E+00
0. 97613E+00	0. 40381E+00	0. 29950E+00	0. 25184E+00	0. 29239E+00	0. 71188E+00	0. 30871E+00
0. 95205E+00	0. 40355E+00	0. 30100E+00	0. 25456E+00	0. 29147E+00	0. 71081E+00	0. 31026E+00
0. 92778E+00	0. 40279E+00	0. 30154E+00	0. 25664E+00	0. 28958E+00	0. 70677E+00	0. 31039E+00
0. 90357E+00	0. 40090E+00	0. 30118E+00	0. 25806E+00	0. 28675E+00	0. 69997E+00	0. 30910E+00
0. 87937E+00	0. 47814E+00	0. 30000E+00	0. 25881E+00	0. 28297E+00	0. 69057E+00	0. 30643E+00
0. 85541E+00	0. 47523E+00	0. 29802E+00	0. 25881E+00	0. 27835E+00	0. 67887E+00	0. 30247E+00
0. 83171E+00	0. 47126E+00	0. 29526E+00	0. 25798E+00	0. 27299E+00	0. 66512E+00	0. 29736E+00
0. 80833E+00	0. 46654E+00	0. 29173E+00	0. 25626E+00	0. 26703E+00	0. 64959E+00	0. 29125E+00
0. 78525E+00	0. 46105E+00	0. 28747E+00	0. 25363E+00	0. 26063E+00	0. 63253E+00	0. 28430E+00
0. 76254E+00	0. 45480E+00	0. 28253E+00	0. 25013E+00	0. 25398E+00	0. 61425E+00	0. 27667E+00
0. 74010E+00	0. 44771E+00	0. 27697E+00	0. 24581E+00	0. 24721E+00	0. 59495E+00	0. 26850E+00
0. 71810E+00	0. 43979E+00	0. 27090E+00	0. 24080E+00	0. 24051E+00	0. 57506E+00	0. 25998E+00
0. 69675E+00	0. 43112E+00	0. 26447E+00	0. 23527E+00	0. 23406E+00	0. 55511E+00	0. 25135E+00
0. 67626E+00	0. 42184E+00	0. 25786E+00	0. 22945E+00	0. 22800E+00	0. 53559E+00	0. 24286E+00
0. 65656E+00	0. 41204E+00	0. 25112E+00	0. 22346E+00	0. 22238E+00	0. 51669E+00	0. 23460E+00
0. 63763E+00	0. 40186E+00	0. 24435E+00	0. 21743E+00	0. 21719E+00	0. 49861E+00	0. 22664E+00
0. 61954E+00	0. 39150E+00	0. 23764E+00	0. 21150E+00	0. 21243E+00	0. 48154E+00	0. 21905E+00
0. 60215E+00	0. 38101E+00	0. 23102E+00	0. 20570E+00	0. 20802E+00	0. 46547E+00	0. 21178E+00
0. 58544E+00	0. 37052E+00	0. 22457E+00	0. 20010E+00	0. 20387E+00	0. 45043E+00	0. 20479E+00
0. 56945E+00	0. 36014E+00	0. 21836E+00	0. 19476E+00	0. 19991E+00	0. 43649E+00	0. 19806E+00
0. 55405E+00	0. 34992E+00	0. 21240E+00	0. 18966E+00	0. 19602E+00	0. 42355E+00	0. 19154E+00
0. 53202E+00	0. 33500E+00	0. 20404E+00	0. 18251E+00	0. 19017E+00	0. 40595E+00	0. 18212E+00
0. 51117E+00	0. 32076E+00	0. 19644E+00	0. 17592E+00	0. 18412E+00	0. 39031E+00	0. 17314E+00

TS **L 1 1,3** **L 2 2,3** **L 3 3,3** **Λ 1 1** **Λ 1 2** **Λ 1 3**

RUN ID: SQF
 0. 10000E+01 0. 25240E+00 0. 32863E+00 0. 47015E+00 0. 34442E+00 0. 25605E+00 0. 24336E+00
 0. 77931E+00 0. 17676E+00 0. 25593E+00 0. 36576E+00 0. 26740E+00 0. 19878E+00 0. 18899E+00
 0. 64454E+00 0. 16270E+00 0. 21153E+00 0. 30202E+00 0. 22037E+00 0. 16382E+00 0. 15579E+00
 0. 55173E+00 0. 13930E+00 0. 18096E+00 0. 25812E+00 0. 18798E+00 0. 13973E+00 0. 13293E+00

RUN ID: SQG
 0. 10000E+01 0. 25240E+00 0. 32863E+00 0. 47015E+00 0. 34442E+00 0. 25605E+00 0. 24336E+00
 0. 94257E+00 0. 24222E+00 0. 31468E+00 0. 44705E+00 0. 32889E+00 0. 24487E+00 0. 23266E+00
 0. 89024E+00 0. 20252E+00 0. 30131E+00 0. 42527E+00 0. 31379E+00 0. 23393E+00 0. 22222E+00
 0. 84214E+00 0. 22325E+00 0. 28851E+00 0. 40469E+00 0. 29917E+00 0. 22327E+00 0. 21208E+00
 0. 79816E+00 0. 21448E+00 0. 27438E+00 0. 38541E+00 0. 28522E+00 0. 21305E+00 0. 20237E+00
 0. 75757E+00 0. 20614E+00 0. 26485E+00 0. 36727E+00 0. 27188E+00 0. 20323E+00 0. 19306E+00
 0. 72022E+00 0. 19822E+00 0. 25395E+00 0. 35030E+00 0. 25922E+00 0. 19388E+00 0. 18419E+00
 0. 68585E+00 0. 19073E+00 0. 24367E+00 0. 33445E+00 0. 24727E+00 0. 18501E+00 0. 17579E+00
 0. 65424E+00 0. 18366E+00 0. 23401E+00 0. 31970E+00 0. 23601E+00 0. 17663E+00 0. 16785E+00
 0. 62485E+00 0. 17670E+00 0. 22485E+00 0. 30584E+00 0. 22534E+00 0. 16866E+00 0. 16030E+00

RUN ID: SQI
 0. 10000E+01 0. 25240E+00 0. 32863E+00 0. 47015E+00 0. 34442E+00 0. 25605E+00 0. 24336E+00
 0. 98466E+00 0. 27798E+00 0. 35718E+00 0. 49107E+00 0. 36989E+00 0. 27736E+00 0. 26283E+00
 0. 96703E+00 0. 30257E+00 0. 38535E+00 0. 51352E+00 0. 39669E+00 0. 29917E+00 0. 28240E+00
 0. 94697E+00 0. 32291E+00 0. 41090E+00 0. 53613E+00 0. 42382E+00 0. 32057E+00 0. 30233E+00
 0. 92426E+00 0. 33675E+00 0. 43227E+00 0. 56128E+00 0. 44882E+00 0. 33989E+00 0. 32208E+00
 0. 89969E+00 0. 34145E+00 0. 44768E+00 0. 59499E+00 0. 46884E+00 0. 35489E+00 0. 33894E+00
 0. 87370E+00 0. 33623E+00 0. 45628E+00 0. 63880E+00 0. 48336E+00 0. 36531E+00 0. 35110E+00
 0. 83251E+00 0. 31416E+00 0. 45690E+00 0. 70535E+00 0. 49664E+00 0. 37495E+00 0. 36119E+00
 0. 78798E+00 0. 28496E+00 0. 44558E+00 0. 73995E+00 0. 50319E+00 0. 38087E+00 0. 36414E+00
 0. 74173E+00 0. 26231E+00 0. 42299E+00 0. 72363E+00 0. 50504E+00 0. 38246E+00 0. 36087E+00
 0. 69570E+00 0. 25692E+00 0. 39042E+00 0. 67511E+00 0. 50180E+00 0. 37728E+00 0. 35306E+00
 0. 65031E+00 0. 26897E+00 0. 35374E+00 0. 62096E+00 0. 49266E+00 0. 36447E+00 0. 34297E+00
 0. 60528E+00 0. 20990E+00 0. 31829E+00 0. 57430E+00 0. 47667E+00 0. 34592E+00 0. 33186E+00
 0. 56248E+00 0. 30933E+00 0. 28684E+00 0. 54135E+00 0. 45505E+00 0. 32583E+00 0. 32087E+00
 0. 52270E+00 0. 32093E+00 0. 25871E+00 0. 52088E+00 0. 43108E+00 0. 30634E+00 0. 30989E+00

TS L11'3 L22'3 L33'3 A11 A12 A13

RUN ID: 50H

0. 10000E+00	0. 29240E+00	0. 32863E+00	0. 47015E+00	0. 34442E+00	0. 25605E+00	0. 24336E+00
0. 97613E+00	0. 29564E+00	0. 33139E+00	0. 46755E+00	0. 34569E+00	0. 25778E+00	0. 24481E+00
0. 95205E+00	0. 29839E+00	0. 33335E+00	0. 46422E+00	0. 34600E+00	0. 25870E+00	0. 24550E+00
0. 92770E+00	0. 26054E+00	0. 33456E+00	0. 46029E+00	0. 34548E+00	0. 25892E+00	0. 24548E+00
0. 90357E+00	0. 26198E+00	0. 33502E+00	0. 45586E+00	0. 34424E+00	0. 25848E+00	0. 24484E+00
0. 87937E+00	0. 26265E+00	0. 33471E+00	0. 45091E+00	0. 34234E+00	0. 25743E+00	0. 24362E+00
0. 85541E+00	0. 26249E+00	0. 33363E+00	0. 44550E+00	0. 33983E+00	0. 25581E+00	0. 24191E+00
0. 83171E+00	0. 26152E+00	0. 33180E+00	0. 43962E+00	0. 33675E+00	0. 25366E+00	0. 23976E+00
0. 80833E+00	0. 25974E+00	0. 32923E+00	0. 43331E+00	0. 33311E+00	0. 25098E+00	0. 23722E+00
0. 78525E+00	0. 25719E+00	0. 32594E+00	0. 42662E+00	0. 32891E+00	0. 24781E+00	0. 23434E+00
0. 76254E+00	0. 25394E+00	0. 32200E+00	0. 41966E+00	0. 32418E+00	0. 24418E+00	0. 23114E+00
0. 74010E+00	0. 25000E+00	0. 31743E+00	0. 41256E+00	0. 31891E+00	0. 24010E+00	0. 22764E+00
0. 71810E+00	0. 24546E+00	0. 31232E+00	0. 40557E+00	0. 31317E+00	0. 23563E+00	0. 22387E+00
0. 69675E+00	0. 24040E+00	0. 30678E+00	0. 39897E+00	0. 30709E+00	0. 23086E+00	0. 21986E+00
0. 67626E+00	0. 23493E+00	0. 30095E+00	0. 39303E+00	0. 30078E+00	0. 22588E+00	0. 21567E+00
0. 65656E+00	0. 22908E+00	0. 29488E+00	0. 38786E+00	0. 29432E+00	0. 22075E+00	0. 21129E+00
0. 63763E+00	0. 22292E+00	0. 28864E+00	0. 38350E+00	0. 28776E+00	0. 21551E+00	0. 20676E+00
0. 61954E+00	0. 21653E+00	0. 28229E+00	0. 37992E+00	0. 28116E+00	0. 21024E+00	0. 20210E+00
0. 60215E+00	0. 20992E+00	0. 27584E+00	0. 37697E+00	0. 27454E+00	0. 20494E+00	0. 19733E+00
0. 58544E+00	0. 20317E+00	0. 26933E+00	0. 37446E+00	0. 26791E+00	0. 19965E+00	0. 19246E+00
0. 56945E+00	0. 19634E+00	0. 26280E+00	0. 37219E+00	0. 26132E+00	0. 19441E+00	0. 18756E+00
0. 55405E+00	0. 18947E+00	0. 25626E+00	0. 36994E+00	0. 25476E+00	0. 18922E+00	0. 18264E+00
0. 53202E+00	0. 17917E+00	0. 24648E+00	0. 36617E+00	0. 24499E+00	0. 18153E+00	0. 17526E+00
0. 51117E+00	0. 16899E+00	0. 23682E+00	0. 36150E+00	0. 23537E+00	0. 17401E+00	0. 16796E+00

TS	Λ_{21}	Λ_{22}	Λ_{23}	Λ_{31}	Λ_{32}	Λ_{33}
RUN ID: 50F						
0. 10000E+01	0. 25206E+00	0. 36819E+00	0. 25412E+00	0. 24609E+00	0. 25545E+00	0. 35055E+00
0. 77931E+00	0. 19567E+00	0. 28580E+00	0. 19726E+00	0. 19105E+00	0. 19837E+00	0. 27217E+00
0. 64454E+00	0. 16124E+00	0. 23550E+00	0. 16254E+00	0. 15745E+00	0. 16351E+00	0. 22430E+00
0. 55173E+00	0. 13753E+00	0. 20085E+00	0. 13863E+00	0. 13431E+00	0. 13950E+00	0. 19134E+00
RUN ID: 50G						
0. 10000E+01	0. 75206E+00	0. 36819E+00	0. 25412E+00	0. 24609E+00	0. 25545E+00	0. 35055E+00
0. 94257E+00	0. 24099E+00	0. 35202E+00	0. 24279E+00	0. 23512E+00	0. 24405E+00	0. 33476E+00
0. 89024E+00	0. 22995E+00	0. 33616E+00	0. 23170E+00	0. 22441E+00	0. 23292E+00	0. 31940E+00
0. 84214E+00	0. 21930E+00	0. 32070E+00	0. 22093E+00	0. 21400E+00	0. 22211E+00	0. 30451E+00
0. 79816E+00	0. 20910E+00	0. 30586E+00	0. 21060E+00	0. 20403E+00	0. 21177E+00	0. 29030E+00
0. 75757E+00	0. 19930E+00	0. 29160E+00	0. 20069E+00	0. 19447E+00	0. 20186E+00	0. 27671E+00
0. 72022E+00	0. 18998E+00	0. 27802E+00	0. 19126E+00	0. 18536E+00	0. 19244E+00	0. 26382E+00
0. 68585E+00	0. 18115E+00	0. 26514E+00	0. 18232E+00	0. 17673E+00	0. 18352E+00	0. 25165E+00
0. 65424E+00	0. 17281E+00	0. 25297E+00	0. 17388E+00	0. 16859E+00	0. 17512E+00	0. 24019E+00
0. 62485E+00	0. 16490E+00	0. 24140E+00	0. 16586E+00	0. 16085E+00	0. 16713E+00	0. 22932E+00
RUN ID: 50I						
0. 10000E+01	0. 25206E+00	0. 36819E+00	0. 25412E+00	0. 24609E+00	0. 25545E+00	0. 35055E+00
0. 98466E+00	0. 27154E+00	0. 39760E+00	0. 27323E+00	0. 26480E+00	0. 27437E+00	0. 37620E+00
0. 96703E+00	0. 29101E+00	0. 42577E+00	0. 29181E+00	0. 28350E+00	0. 29302E+00	0. 40214E+00
0. 94697E+00	0. 31083E+00	0. 45120E+00	0. 30991E+00	0. 30227E+00	0. 31085E+00	0. 42724E+00
0. 92426E+00	0. 33072E+00	0. 47311E+00	0. 32713E+00	0. 32028E+00	0. 32587E+00	0. 44960E+00
0. 89969E+00	0. 34853E+00	0. 49126E+00	0. 34240E+00	0. 33540E+00	0. 33680E+00	0. 46781E+00
0. 87370E+00	0. 36302E+00	0. 50605E+00	0. 35557E+00	0. 34656E+00	0. 34451E+00	0. 48201E+00
0. 83251E+00	0. 37701E+00	0. 52166E+00	0. 37112E+00	0. 35590E+00	0. 35202E+00	0. 49602E+00
0. 78798E+00	0. 38259E+00	0. 53042E+00	0. 38018E+00	0. 35760E+00	0. 35572E+00	0. 50268E+00
0. 74173E+00	0. 38150E+00	0. 52310E+00	0. 38055E+00	0. 35343E+00	0. 35415E+00	0. 50294E+00
0. 69570E+00	0. 37594E+00	0. 52891E+00	0. 37301E+00	0. 34631E+00	0. 34676E+00	0. 49667E+00
0. 65031E+00	0. 36768E+00	0. 51713E+00	0. 35940E+00	0. 33777E+00	0. 33617E+00	0. 48415E+00
0. 60528E+00	0. 35725E+00	0. 49716E+00	0. 34066E+00	0. 32712E+00	0. 32434E+00	0. 46509E+00
0. 56248E+00	0. 34411E+00	0. 47092E+00	0. 31863E+00	0. 31324E+00	0. 31167E+00	0. 44077E+00
0. 52270E+00	0. 32810E+00	0. 44256E+00	0. 29523E+00	0. 29669E+00	0. 29780E+00	0. 41412E+00

TS	Λ_{21}	Λ_{22}	Λ_{23}	Λ_{31}	Λ_{32}	Λ_{33}
RUN ID: SQH						
0. 10000E+01	0. 25206E+00	0. 36819E+00	0. 25412E+00	0. 24609E+00	0. 25545E+00	0. 35055E+00
0. 97613E+00	0. 25337E+00	0. 37044E+00	0. 25530E+00	0. 24725E+00	0. 25657E+00	0. 35185E+00
0. 95205E+00	0. 25383E+00	0. 37139E+00	0. 25561E+00	0. 24761E+00	0. 25682E+00	0. 35210E+00
0. 92778E+00	0. 25354E+00	0. 37119E+00	0. 25515E+00	0. 24726E+00	0. 25631E+00	0. 35143E+00
0. 90357E+00	0. 25260E+00	0. 36992E+00	0. 25399E+00	0. 24627E+00	0. 25516E+00	0. 34996E+00
0. 87937E+00	0. 25109E+00	0. 36766E+00	0. 25221E+00	0. 24471E+00	0. 25345E+00	0. 34777E+00
0. 85541E+00	0. 24911E+00	0. 36448E+00	0. 24990E+00	0. 24264E+00	0. 25125E+00	0. 34493E+00
0. 83171E+00	0. 24670E+00	0. 36044E+00	0. 24711E+00	0. 24014E+00	0. 24860E+00	0. 34147E+00
0. 80833E+00	0. 24393E+00	0. 35563E+00	0. 24389E+00	0. 23726E+00	0. 24553E+00	0. 33743E+00
0. 78525E+00	0. 24084E+00	0. 35011E+00	0. 24029E+00	0. 23404E+00	0. 24204E+00	0. 33282E+00
0. 76254E+00	0. 23747E+00	0. 34399E+00	0. 23633E+00	0. 23051E+00	0. 23815E+00	0. 32770E+00
0. 74010E+00	0. 23381E+00	0. 33733E+00	0. 23204E+00	0. 22668E+00	0. 23385E+00	0. 32207E+00
0. 71810E+00	0. 22990E+00	0. 33026E+00	0. 22745E+00	0. 22259E+00	0. 22921E+00	0. 31602E+00
0. 69675E+00	0. 22579E+00	0. 32293E+00	0. 22267E+00	0. 21832E+00	0. 22430E+00	0. 30966E+00
0. 67626E+00	0. 22154E+00	0. 31553E+00	0. 21778E+00	0. 21393E+00	0. 21924E+00	0. 30313E+00
0. 65656E+00	0. 21715E+00	0. 30809E+00	0. 21282E+00	0. 20944E+00	0. 21407E+00	0. 29647E+00
0. 63763E+00	0. 21263E+00	0. 30066E+00	0. 20784E+00	0. 20489E+00	0. 20885E+00	0. 28972E+00
0. 61954E+00	0. 20804E+00	0. 29333E+00	0. 20291E+00	0. 20032E+00	0. 20365E+00	0. 28297E+00
0. 60215E+00	0. 20336E+00	0. 28604E+00	0. 19802E+00	0. 19572E+00	0. 19848E+00	0. 27620E+00
0. 58544E+00	0. 19863E+00	0. 27883E+00	0. 19321E+00	0. 19111E+00	0. 19335E+00	0. 26944E+00
0. 56945E+00	0. 19388E+00	0. 27171E+00	0. 18851E+00	0. 18651E+00	0. 18830E+00	0. 26273E+00
0. 55405E+00	0. 18913E+00	0. 26466E+00	0. 18391E+00	0. 18193E+00	0. 18332E+00	0. 25606E+00
0. 53202E+00	0. 18203E+00	0. 25422E+00	0. 17720E+00	0. 17508E+00	0. 17599E+00	0. 24614E+00
0. 51117E+00	0. 17501E+00	0. 24398E+00	0. 17071E+00	0. 16831E+00	0. 16883E+00	0. 23639E+00

TS	t	v	S	q ²	ε
RUN ID: EXG					
0. 10000E+01	0. 58789E+00	0. 42990E--02	0. 35870E+02	0. 21980E+00	0. 19311E+00
0. 11081E+01	0. 59075E+00	0. 42990E--02	0. 35870E+02	0. 22165E+00	0. 19868E+00
0. 12482E+01	0. 57407E+00	0. 42990E--02	0. 35870E+02	0. 23161E+00	0. 22169E+00
0. 14149E+01	0. 59756E+00	0. 42990E--02	0. 35870E+02	0. 24959E+00	0. 26217E+00
0. 15960E+01	0. 60092E+00	0. 42990E--02	0. 35870E+02	0. 27281E+00	0. 31475E+00
0. 17647E+01	0. 60372E+00	0. 42990E--02	0. 35870E+02	0. 29618E+00	0. 36743E+00
0. 19188E+01	0. 60605E+00	0. 42990E--02	0. 35870E+02	0. 31830E+00	0. 41571E+00
RUN ID: EXP					
0. 10000E+01	0. 58789E+00	0. 42990E--02	0. 35870E+01	0. 21980E+00	0. 19311E+00
0. 11330E+01	0. 62271E+00	0. 42990E--02	0. 35870E+01	0. 21113E+00	0. 18508E+00
0. 12735E+01	0. 65528E+00	0. 42990E--02	0. 35870E+01	0. 21108E+00	0. 18839E+00
0. 14262E+01	0. 68686E+00	0. 42990E--02	0. 35870E+01	0. 21687E+00	0. 19365E+00
0. 16050E+01	0. 71979E+00	0. 42990E--02	0. 35870E+01	0. 22829E+00	0. 19674E+00
0. 17927E+01	0. 75061E+00	0. 42990E--02	0. 35870E+01	0. 24379E+00	0. 19627E+00
0. 20073E+01	0. 78214E+00	0. 42990E--02	0. 35870E+01	0. 26465E+00	0. 19316E+00
RUN ID: FX0					
0. 10000E+01	0. 58789E+00	0. 42990E--02	0. 35870E+00	0. 21980E+00	0. 19311E+00
0. 11228E+01	0. 91079E+00	0. 42990E--02	0. 35870E+00	0. 13645E+00	0. 91810E-01
0. 12622E+01	0. 12370E+01	0. 42990E--02	0. 35870E+00	0. 99459E-01	0. 51464E-01
0. 14157E+01	0. 15570E+01	0. 42990E--02	0. 35870E+00	0. 83115E-01	0. 33466E-01
0. 15889E+01	0. 18788E+01	0. 42990E--02	0. 35870E+00	0. 76500E-01	0. 24161E-01
0. 17844E+01	0. 22023E+01	0. 42990E--02	0. 35870E+00	0. 75455E-01	0. 19009E-01
0. 20001E+01	0. 25204E+01	0. 42990E--02	0. 35870E+00	0. 78185E-01	0. 16060E-01

TS R₁₁ R₂₂ R₃₃ D_{11/2} D_{22/2} D_{33/2}

RUN ID: EXG
 0. 10000E+01 0. 72339E-01 0. 73439E-01 0. 74018E-01 0. 12824E+00 0. 12919E+00 0. 12881E+00
 0. 11081E+01 0. 84141E-01 0. 68660E-01 0. 68846E-01 0. 13629E+00 0. 13077E+00 0. 13030E+00
 0. 12482E+01 0. 98395E-01 0. 66684E-01 0. 66535E-01 0. 14145E+00 0. 15125E+00 0. 15068E+00
 0. 14149E+01 0. 11397E+00 0. 67925E-01 0. 67693E-01 0. 14182E+00 0. 19160E+00 0. 19093E+00
 0. 15960E+01 0. 12966E+00 0. 71572E-01 0. 71573E-01 0. 13783E+00 0. 24620E+00 0. 24547E+00
 0. 17649E+01 0. 14377E+00 0. 76014E-01 0. 76397E-01 0. 13204E+00 0. 30180E+00 0. 30102E+00
 0. 19188E+01 0. 15657E+00 0. 80495E-01 0. 81244E-01 0. 12604E+00 0. 35311E+00 0. 35227E+00

RUN ID: EXP
 0. 10000E+01 0. 77337E-01 0. 73439E-01 0. 74018E-01 0. 12824E+00 0. 12919E+00 0. 12881E+00
 0. 11330E+01 0. 82512E-01 0. 64271E-01 0. 64351E-01 0. 12680E+00 0. 12194E+00 0. 12141E+00
 0. 12735E+01 0. 92410E-01 0. 59468E-01 0. 59203E-01 0. 12179E+00 0. 12788E+00 0. 12711E+00
 0. 14262E+01 0. 10262E+00 0. 57305E-01 0. 56945E-01 0. 11466E+00 0. 13684E+00 0. 13580E+00
 0. 16050E+01 0. 11423E+00 0. 57105E-01 0. 56959E-01 0. 10612E+00 0. 14435E+00 0. 14301E+00
 0. 17927E+01 0. 12642E+00 0. 58536E-01 0. 58833E-01 0. 97951E-01 0. 14806E+00 0. 14653E+00
 0. 20073E+01 0. 14086E+00 0. 61470E-01 0. 62315E-01 0. 89906E-01 0. 14898E+00 0. 14743E+00

RUN ID: EXD
 0. 10000E+01 0. 72339E-01 0. 73439E-01 0. 74018E-01 0. 12824E+00 0. 12919E+00 0. 12881E+00
 0. 11220E+01 0. 54161E-01 0. 41206E-01 0. 41085E-01 0. 64973E-01 0. 59702E-01 0. 58945E-01
 0. 12622E+01 0. 46506E-01 0. 26701E-01 0. 26252E-01 0. 38887E-01 0. 32263E-01 0. 31778E-01
 0. 14157E+01 0. 43613E-01 0. 20015E-01 0. 19487E-01 0. 26710E-01 0. 20273E-01 0. 19949E-01
 0. 15887E+01 0. 43073E-01 0. 16869E-01 0. 16557E-01 0. 19971E-01 0. 14353E-01 0. 13998E-01
 0. 17844E+01 0. 44294E-01 0. 15531E-01 0. 15631E-01 0. 15854E-01 0. 11268E-01 0. 10896E-01
 0. 20001E+01 0. 47439E-01 0. 15134E-01 0. 15612E-01 0. 13224E-01 0. 95739E-02 0. 93231E-02

TS

	L11'1	L22'1	L33'1	L11'2	L22'2	L33'2
RUN ID: EXG						
0. 10000E+01	0. 72708E+00	0. 12756E+00	0. 14019E+00	0. 13697E+00	0. 24892E+00	0. 13068E+00
0. 11081E+01	0. 73895E+00	0. 90207E-01	0. 99570E-01	0. 14650E+00	0. 23925E+00	0. 17074E+00
0. 12482E+01	0. 75854E+00	0. 57523E-01	0. 63744E-01	0. 16058E+00	0. 21737E+00	0. 22384E+00
0. 14149E+01	0. 78620E+00	0. 34108E-01	0. 37803E-01	0. 17836E+00	0. 18665E+00	0. 28514E+00
0. 15960E+01	0. 31954E+00	0. 19945E-01	0. 22011E-01	0. 19766E+00	0. 15522E+00	0. 34737E+00
0. 17649E+01	0. 35206E+00	0. 12524E-01	0. 13744E-01	0. 21597E+00	0. 13036E+00	0. 40019E+00
0. 19188E+01	0. 38190E+00	0. 84407E-02	0. 92210E-02	0. 23460E+00	0. 11151E+00	0. 44232E+00

RUN ID: EXP

0. 10000E+01	0. 22708E+00	0. 12756E+00	0. 14019E+00	0. 13697E+00	0. 24892E+00	0. 13068E+00
0. 11330E+01	0. 24621E+00	0. 85265E-01	0. 93427E-01	0. 15061E+00	0. 23834E+00	0. 18159E+00
0. 12735E+01	0. 27105E+00	0. 56317E-01	0. 61527E-01	0. 16647E+00	0. 21588E+00	0. 23666E+00
0. 14262E+01	0. 30097E+00	0. 36491E-01	0. 39637E-01	0. 18405E+00	0. 18609E+00	0. 29637E+00
0. 16050E+01	0. 33800E+00	0. 22530E-01	0. 24203E-01	0. 20405E+00	0. 15151E+00	0. 36415E+00
0. 17927E+01	0. 37762E+00	0. 14011E-01	0. 14834E-01	0. 22523E+00	0. 12005E+00	0. 42880E+00
0. 20073E+01	0. 42224E+00	0. 84555E-02	0. 88051E-02	0. 25446E+00	0. 91454E-01	0. 48674E+00

RUN ID: EXO

0. 10000E+01	0. 72708E+00	0. 12756E+00	0. 14019E+00	0. 13697E+00	0. 24892E+00	0. 13068E+00
0. 11228E+01	0. 28569E+00	0. 10554E+00	0. 10937E+00	0. 16535E+00	0. 26050E+00	0. 19476E+00
0. 12622E+01	0. 35262E+00	0. 87026E-01	0. 85742E-01	0. 19339E+00	0. 25135E+00	0. 27801E+00
0. 14157E+01	0. 42079E+00	0. 67485E-01	0. 64343E-01	0. 22156E+00	0. 22247E+00	0. 36050E+00
0. 15889E+01	0. 49471E+00	0. 49272E-01	0. 44803E-01	0. 25742E+00	0. 18749E+00	0. 44148E+00
0. 17844E+01	0. 57236E+00	0. 34762E-01	0. 29676E-01	0. 30630E+00	0. 15754E+00	0. 51884E+00
0. 20001E+01	0. 64396E+00	0. 24569E-01	0. 20095E-01	0. 37447E+00	0. 13427E+00	0. 58258E+00

TS	L11,3	L22,3	L33,3	Λ_{11}	Λ_{12}	Λ_{13}
RUN ID: EXG						
0.10000E+01	0.11944E+00	0.12850E+00	0.26859E+00	0.15558E+00	0.11041E+00	0.10988E+00
0.11081E+01	0.12585E+00	0.16412E+00	0.25955E+00	0.14751E+00	0.11882E+00	0.11818E+00
0.12482E+01	0.13668E+00	0.20864E+00	0.23706E+00	0.14286E+00	0.13049E+00	0.12967E+00
0.14149E+01	0.15210E+00	0.25751E+00	0.20389E+00	0.14263E+00	0.14517E+00	0.14416E+00
0.15940E+01	0.16971E+00	0.30738E+00	0.16910E+00	0.14647E+00	0.16174E+00	0.16054E+00
0.17649E+01	0.18518E+00	0.35416E+00	0.14145E+00	0.15261E+00	0.17764E+00	0.17627E+00
0.19188E+01	0.19649E+00	0.39817E+00	0.12064E+00	0.15971E+00	0.19248E+00	0.19092E+00

RUN ID: EXP						
0.10000E+01	0.11944E+00	0.12850E+00	0.26859E+00	0.15558E+00	0.11041E+00	0.10988E+00
0.11330E+01	0.12949E+00	0.17403E+00	0.25973E+00	0.14930E+00	0.12259E+00	0.12187E+00
0.12735E+01	0.14285E+00	0.22002E+00	0.23777E+00	0.14955E+00	0.13623E+00	0.13523E+00
0.14262E+01	0.15942E+00	0.26756E+00	0.20670E+00	0.15419E+00	0.15154E+00	0.15018E+00
0.16050E+01	0.17956E+00	0.32232E+00	0.16857E+00	0.16261E+00	0.16967E+00	0.16786E+00
0.17927E+01	0.19897E+00	0.38154E+00	0.13242E+00	0.17326E+00	0.18880E+00	0.18650E+00
0.20073E+01	0.21731E+00	0.45063E+00	0.10002E+00	0.18675E+00	0.21099E+00	0.20808E+00

RUN ID: EXD						
0.10000E+01	0.11944E+00	0.12850E+00	0.26859E+00	0.15558E+00	0.11041E+00	0.10988E+00
0.11228E+01	0.14622E+00	0.18734E+00	0.29236E+00	0.17604E+00	0.13701E+00	0.13610E+00
0.12622E+01	0.17665E+00	0.25017E+00	0.28280E+00	0.20603E+00	0.16522E+00	0.16427E+00
0.14157E+01	0.20832E+00	0.32054E+00	0.25360E+00	0.23653E+00	0.19405E+00	0.19317E+00
0.15889E+01	0.24021E+00	0.41068E+00	0.21842E+00	0.26559E+00	0.22496E+00	0.22366E+00
0.17844E+01	0.27096E+00	0.52117E+00	0.17879E+00	0.29478E+00	0.25858E+00	0.25679E+00
0.20001E+01	0.30146E+00	0.59301E+00	0.14652E+00	0.32711E+00	0.29510E+00	0.29372E+00

TS	Λ_{21}	Λ_{22}	Λ_{23}	Λ_{31}	Λ_{32}	Λ_{33}
RUN ID: EXG						
0. 10000E+01	0. 11136E+00	0. 15551E+00	0. 11003E+00	0. 11201E+00	0. 11055E+00	0. 15642E+00
0. 11081E+01	0. 91192E-01	0. 15904E+00	0. 12728E+00	0. 91475E-01	0. 12765E+00	0. 15960E+00
0. 12482E+01	0. 74310E-01	0. 16046E+00	0. 15097E+00	0. 74369E-01	0. 15117E+00	0. 16048E+00
0. 14149E+01	0. 62102E-01	0. 16258E+00	0. 17979E+00	0. 62123E-01	0. 17994E+00	0. 16211E+00
0. 15960E+01	0. 54083E-01	0. 16752E+00	0. 21050E+00	0. 54192E-01	0. 21093E+00	0. 16688E+00
0. 17649E+01	0. 49311E-01	0. 17437E+00	0. 23812E+00	0. 49527E-01	0. 23905E+00	0. 17382E+00
0. 19188E+01	0. 46350E-01	0. 18197E+00	0. 26246E+00	0. 46644E-01	0. 26390E+00	0. 18161E+00
RUN ID: EXP						
0. 10000E+01	0. 11136E+00	0. 15551E+00	0. 11003E+00	0. 11201E+00	0. 11055E+00	0. 15642E+00
0. 11330E+01	0. 89377E-01	0. 16134E+00	0. 13237E+00	0. 89647E-01	0. 13263E+00	0. 16189E+00
0. 12735E+01	0. 76251E-01	0. 16440E+00	0. 15596E+00	0. 76346E-01	0. 15589E+00	0. 16439E+00
0. 14262E+01	0. 68686E-01	0. 16826E+00	0. 18122E+00	0. 68799E-01	0. 18095E+00	0. 16771E+00
0. 16050E+01	0. 64754E-01	0. 17468E+00	0. 00000E+00	0. 65069E-01	0. 20967E+00	0. 73830E-01
0. 17927E+01	0. 63661E-01	0. 18325E+00	0. 23804E+00	0. 64272E-01	0. 23864E+00	0. 18244E+00
0. 20073E+01	0. 64340E-01	0. 19453E+00	0. 26826E+00	0. 65252E-01	0. 26990E+00	0. 19398E+00
RUN ID: EXD						
0. 10000E+01	0. 11136E+00	0. 15551E+00	0. 11003E+00	0. 11201E+00	0. 11055E+00	0. 15642E+00
0. 11228E+01	0. 10701E+00	0. 17931E+00	0. 14131E+00	0. 10791E+00	0. 14077E+00	0. 18099E+00
0. 12622E+01	0. 11135E+00	0. 19800E+00	0. 17058E+00	0. 11159E+00	0. 16831E+00	0. 19928E+00
0. 14157E+01	0. 11836E+00	0. 21496E+00	0. 20089E+00	0. 11789E+00	0. 19778E+00	0. 21541E+00
0. 15889E+01	0. 12653E+00	0. 23318E+00	0. 23501E+00	0. 12726E+00	0. 23364E+00	0. 23402E+00
0. 17844E+01	0. 13441E+00	0. 25363E+00	0. 27231E+00	0. 13773E+00	0. 27596E+00	0. 25626E+00
0. 20001E+01	0. 14144E+00	0. 27564E+00	0. 30967E+00	0. 14617E+00	0. 31861E+00	0. 27948E+00

TS dR_{11}/dt P_{11} $T_{11}^{(1)}$ Φ_{11} ϵ

RUN ID: FXG

0. 10000E+01	-0. 12629E+00	0. 00000E+00	0. 00000E+00	-0. 11385E-01	0. 19311E+01
0. 11081E+01	0. 42109E+01	0. 12073E+02	-0. 77281E+01	-0. 45653E-02	0. 19868E+01
0. 12482E+01	0. 43726E+01	0. 14118E+02	-0. 96092E+01	-0. 39046E-01	0. 22169E+01
0. 14149E+01	0. 45469E+01	0. 16352E+02	-0. 11672E+02	-0. 96544E-01	0. 26217E+01
0. 15960E+01	0. 48375E+01	0. 18604E+02	-0. 13640E+02	-0. 14957E+00	0. 31476E+01
0. 17649E+01	0. 52536E+01	0. 20628E+02	-0. 15255E+02	-0. 18594E+00	0. 36743E+01
0. 19188E+01	0. 57488E+01	0. 22464E+02	-0. 16601E+02	-0. 21062E+00	0. 41571E+01

RUN ID: EXP

0. 10000E+01	-0. 12629E+00	0. 00000E+00	0. 00000E+00	-0. 11385E-01	0. 19311E+01
0. 11330E+01	0. 29670E+00	0. 11839E+01	-0. 76302E+00	-0. 50511E-02	0. 18508E+01
0. 12735E+01	0. 31245E+00	0. 13259E+01	-0. 89653E+00	-0. 35924E-01	0. 18839E+01
0. 14262E+01	0. 33568E+00	0. 14724E+01	-0. 10299E+01	-0. 77462E-01	0. 19365E+01
0. 16050E+01	0. 37181E+00	0. 16390E+01	-0. 11717E+01	-0. 11751E+00	0. 19674E+01
0. 17927E+01	0. 42241E+00	0. 18139E+01	-0. 13062E+01	-0. 14830E+00	0. 19627E+01
0. 20073E+01	0. 49918E+00	0. 20211E+01	-0. 14465E+01	-0. 17571E+00	0. 19316E+01

RUN ID: FXG

0. 10000E+01	-0. 12629E+00	0. 00000E+00	0. 00000E+00	-0. 11385E-01	0. 19311E+01
0. 11228E+01	-0. 35319E-01	0. 77710E-01	-0. 47739E-01	0. 23969E-01	0. 91810E+01
0. 12622E+01	-0. 14414E-01	0. 66726E-01	-0. 40840E-01	0. 71946E-01	0. 51464E+01
0. 14157E+01	-0. 47379E-02	0. 62576E-01	-0. 38830E-01	0. 11874E+00	0. 33466E+01
0. 15889E+01	0. 10925E-02	0. 61801E-01	-0. 39029E-01	0. 15068E+00	0. 24161E+01
0. 17844E+01	0. 65883E-02	0. 63552E-01	-0. 39841E-01	0. 15046E+00	0. 19009E+01
0. 20001E+01	0. 13620E-01	0. 68066E-01	-0. 40463E-01	0. 12558E+00	0. 16060E+01

TS	t	v	S	q ²	ε
RUN ID: 0000					
0. 10000E+01	0. 00000E+00	0. 15000E-01	-0. 81000E+02	0. 89242E+00	0. 15369E+01
0. 84646E+00	0. 18936E-02	0. 13348E-01	-0. 95693E+02	0. 98941E+00	0. 16858E+01
0. 70600E+00	0. 36297E-02	0. 11756E-01	-0. 11473E+03	0. 11204E+01	0. 19187E+01
0. 57166E+00	0. 52802E-02	0. 10141E-01	-0. 14169E+03	0. 13130E+01	0. 23008E+01
0. 50043E+00	0. 61675E-02	0. 92392E-02	-0. 16186E+03	0. 14611E+01	0. 26152E+01
0. 43481E+00	0. 69776E-02	0. 83734E-02	-0. 18629E+03	0. 16438E+01	0. 30214E+01
0. 37429E+00	0. 77248E-02	0. 75394E-02	-0. 21641E+03	0. 18731E+01	0. 35534E+01
0. 32034E+00	0. 83909E-02	0. 67611E-02	-0. 25286E+03	0. 21551E+01	0. 42347E+01
0. 27756E+00	0. 89190E-02	0. 61157E-02	-0. 29183E+03	0. 24604E+01	0. 50006E+01

RUN ID: 0000					
0. 10000E+01	0. 00000E+00	0. 15000E-01	-0. 43000E+01	0. 89242E+00	0. 15369E+01
0. 92854E+00	0. 16620E-01	0. 14241E-01	-0. 46309E+01	0. 88467E+00	0. 14747E+01
0. 85405E+00	0. 33942E-01	0. 13432E-01	-0. 50348E+01	0. 88393E+00	0. 14332E+01
0. 77414E+00	0. 52525E-01	0. 12539E-01	-0. 55545E+01	0. 89249E+00	0. 14134E+01
0. 69472E+00	0. 70994E-01	0. 11624E-01	-0. 61895E+01	0. 91267E+00	0. 14194E+01
0. 61429E+00	0. 89699E-01	0. 10665E-01	-0. 69999E+01	0. 94867E+00	0. 14546E+01
0. 53816E+00	0. 10740E+00	0. 97214E-02	-0. 79902E+01	0. 10029E+01	0. 15207E+01
0. 45126E+00	0. 12762E+00	0. 85938E-02	-0. 95290E+01	0. 11017E+01	0. 16497E+01
0. 37549E+00	0. 14523E+00	0. 75564E-02	-0. 11452E+02	0. 12409E+01	0. 18332E+01
0. 31184E+00	0. 16004E+00	0. 66351E-02	-0. 13789E+02	0. 14253E+01	0. 20724E+01
0. 26084E+00	0. 17190E+00	0. 58554E-02	-0. 16485E+02	0. 16518E+01	0. 23592E+01

TS	t	v	S	q ²	ε
RUN ID: 0000	0. 10000E+01	0. 15000E-01	-0. 86667E+00	0. 89242E+00	0. 15369E+01
	0. 93463E+00	0. 14307E-01	-0. 92728E+00	0. 73055E+00	0. 11074E+01
	0. 86045E+00	0. 13502E-01	-0. 10072E+01	0. 60546E+00	0. 80873E+00
	0. 77707E+00	0. 12572E-01	-0. 11153E+01	0. 51170E+00	0. 60112E+00
	0. 68697E+00	0. 11533E-01	-0. 12616E+01	0. 44728E+00	0. 46175E+00
	0. 58891E+00	0. 10354E-01	-0. 14716E+01	0. 40852E+00	0. 36898E+00
	0. 49354E+00	0. 91499E-02	-0. 17560E+01	0. 39756E+00	0. 31657E+00
	0. 40742E+00	0. 80006E-02	-0. 21272E+01	0. 41270E+00	0. 29344E+00
	0. 33093E+00	0. 69168E-02	-0. 26189E+01	0. 45471E+00	0. 29162E+00
	0. 26816E+00	0. 59699E-02	-0. 32319E+01	0. 52353E+00	0. 30702E+00
	0. 25458E+00	0. 57567E-02	-0. 34043E+01	0. 54488E+00	0. 31313E+00

RUN ID: 0000	0. 10000E+01	0. 15000E-01	-0. 17333E+00	0. 89242E+00	0. 15369E+01
	0. 97163E+00	0. 14701E-01	-0. 17839E+00	0. 55523E+00	0. 73185E+00
	0. 93318E+00	0. 14291E-01	-0. 18574E+00	0. 34507E+00	0. 33634E+00
	0. 88222E+00	0. 13740E-01	-0. 19648E+00	0. 21997E+00	0. 15691E+00
	0. 81386E+00	0. 12986E-01	-0. 21298E+00	0. 14428E+00	0. 75610E-01
	0. 73021E+00	0. 12037E-01	-0. 23738E+00	0. 10135E+00	0. 40077E-01
	0. 63157E+00	0. 10874E-01	-0. 27445E+00	0. 77342E-01	0. 23586E-01
	0. 53214E+00	0. 96452E-02	-0. 32573E+00	0. 66383E-01	0. 16305E-01
	0. 43775E+00	0. 84130E-02	-0. 39596E+00	0. 63404E-01	0. 13045E-01
	0. 35095E+00	0. 72071E-02	-0. 49390E+00	0. 66573E-01	0. 11798E-01
	0. 31079E+00	0. 66174E-02	-0. 55772E+00	0. 70542E-01	0. 11691E-01
	0. 27504E+00	0. 60766E-02	-0. 63022E+00	0. 76037E-01	0. 11870E-01

TS	R ₁₁	R ₂₂	R ₃₃	D _{11/2}	D _{22/2}	D _{33/2}
RUN ID: 01NB						
0. 10000E+01	0. 20011E+00	0. 30759E+00	0. 30472E+00	0. 50378E+00	0. 51872E+00	0. 51436E+00
0. 84646E+00	0. 33998E+00	0. 32645E+00	0. 32297E+00	0. 58120E+00	0. 55489E+00	0. 54967E+00
0. 70600E+00	0. 41857E+00	0. 35306E+00	0. 34874E+00	0. 67491E+00	0. 62513E+00	0. 61870E+00
0. 57166E+00	0. 53113E+00	0. 39369E+00	0. 38819E+00	0. 79598E+00	0. 75655E+00	0. 74822E+00
0. 50043E+00	0. 61593E+00	0. 42575E+00	0. 41938E+00	0. 87870E+00	0. 87321E+00	0. 86330E+00
0. 43481E+00	0. 71910E+00	0. 46605E+00	0. 45867E+00	0. 97116E+00	0. 10311E+01	0. 10192E+01
0. 37429E+00	0. 84673E+00	0. 51747E+00	0. 50895E+00	0. 10752E+01	0. 12463E+01	0. 12319E+01
0. 32034E+00	0. 10014E+01	0. 58166E+00	0. 57194E+00	0. 11888E+01	0. 15318E+01	0. 15141E+01
0. 27756E+00	0. 11569E+01	0. 65214E+00	0. 64138E+00	0. 12980E+01	0. 18620E+01	0. 18406E+01

RUN ID: 01JC						
0. 10000E+01	0. 20011E+00	0. 30759E+00	0. 30472E+00	0. 50378E+00	0. 51872E+00	0. 51436E+00
0. 92854E+00	0. 28977E+00	0. 29891E+00	0. 29600E+00	0. 49515E+00	0. 49198E+00	0. 48757E+00
0. 85405E+00	0. 30316E+00	0. 29188E+00	0. 28890E+00	0. 49078E+00	0. 47343E+00	0. 46903E+00
0. 77414E+00	0. 32223E+00	0. 28669E+00	0. 28357E+00	0. 49124E+00	0. 46332E+00	0. 45886E+00
0. 69472E+00	0. 34753E+00	0. 28424E+00	0. 28090E+00	0. 49727E+00	0. 46337E+00	0. 45878E+00
0. 61427E+00	0. 38203E+00	0. 28513E+00	0. 28150E+00	0. 50985E+00	0. 47470E+00	0. 47005E+00
0. 53816E+00	0. 42558E+00	0. 29018E+00	0. 28616E+00	0. 52921E+00	0. 49818E+00	0. 49329E+00
0. 45126E+00	0. 47932E+00	0. 30350E+00	0. 29886E+00	0. 56330E+00	0. 54583E+00	0. 54061E+00
0. 37549E+00	0. 57411E+00	0. 32606E+00	0. 32072E+00	0. 60834E+00	0. 61528E+00	0. 60957E+00
0. 31184E+00	0. 71292E+00	0. 35918E+00	0. 35325E+00	0. 66321E+00	0. 70768E+00	0. 70148E+00
0. 26084E+00	0. 85279E+00	0. 40258E+00	0. 39643E+00	0. 72448E+00	0. 82073E+00	0. 81401E+00

TS R₁₁ R₂₂ R₃₃ D_{11/2} D_{22/2} D_{33/2}

RUN ID: UDD

0. 10000E+01	0. 28011E+00	0. 30759E+00	0. 30472E+00	0. 50378E+00	0. 51872E+00	0. 51436E+00
0. 93463E+00	0. 23908E+00	0. 24685E+00	0. 24463E+00	0. 36806E+00	0. 37147E+00	0. 36785E+00
0. 86045E+00	0. 20902E+00	0. 19902E+00	0. 19742E+00	0. 27265E+00	0. 26943E+00	0. 26665E+00
0. 77707E+00	0. 18863E+00	0. 16210E+00	0. 16097E+00	0. 20626E+00	0. 19839E+00	0. 19647E+00
0. 68697E+00	0. 17778E+00	0. 13523E+00	0. 13427E+00	0. 16206E+00	0. 15049E+00	0. 14920E+00
0. 58891E+00	0. 17674E+00	0. 11642E+00	0. 11536E+00	0. 13318E+00	0. 11848E+00	0. 11732E+00
0. 49354E+00	0. 18675E+00	0. 10592E+00	0. 10489E+00	0. 11745E+00	0. 10030E+00	0. 98822E-01
0. 40742E+00	0. 20813E+00	0. 10253E+00	0. 10204E+00	0. 11109E+00	0. 91973E-01	0. 90378E-01
0. 33093E+00	0. 24295E+00	0. 10560E+00	0. 10616E+00	0. 11144E+00	0. 90634E-01	0. 89542E-01
0. 26816E+00	0. 29180E+00	0. 11491E+00	0. 11682E+00	0. 11710E+00	0. 95082E-01	0. 94836E-01
0. 25458E+00	0. 30628E+00	0. 11816E+00	0. 12044E+00	0. 11919E+00	0. 96988E-01	0. 96945E-01

RUN ID: UDE

0. 10000E+01	0. 28011E+00	0. 30759E+00	0. 30472E+00	0. 50378E+00	0. 51872E+00	0. 51436E+00
0. 97163E+00	0. 17838E+00	0. 18907E+00	0. 18778E+00	0. 23827E+00	0. 24808E+00	0. 24549E+00
0. 93318E+00	0. 11514E+00	0. 11510E+00	0. 11483E+00	0. 11012E+00	0. 11354E+00	0. 11268E+00
0. 88222E+00	0. 77136E-01	0. 71511E-01	0. 71320E-01	0. 52363E-01	0. 52504E-01	0. 52044E-01
0. 81386E+00	0. 54090E-01	0. 45073E-01	0. 45116E-01	0. 26056E-01	0. 24990E-01	0. 24564E-01
0. 73021E+00	0. 41262E-01	0. 29788E-01	0. 30295E-01	0. 14413E-01	0. 12941E-01	0. 12723E-01
0. 63157E+00	0. 34649E-01	0. 20875E-01	0. 21819E-01	0. 89795E-02	0. 72895E-02	0. 73172E-02
0. 53214E+00	0. 32500E-01	0. 16319E-01	0. 17565E-01	0. 65772E-02	0. 47911E-02	0. 49363E-02
0. 43775E+00	0. 33399E-01	0. 14216E-01	0. 15789E-01	0. 54933E-02	0. 36808E-02	0. 38710E-02
0. 35095E+00	0. 37142E-01	0. 13654E-01	0. 15778E-01	0. 50693E-02	0. 32430E-02	0. 34856E-02
0. 31079E+00	0. 40342E-01	0. 13846E-01	0. 16353E-01	0. 50252E-02	0. 31919E-02	0. 34734E-02
0. 27504E+00	0. 44473E-01	0. 14323E-01	0. 17241E-01	0. 50737E-02	0. 32333E-02	0. 35634E-02

TS	L11,1	L22,1	L33,1	L11,2	L22,2	L33,2
RUN ID: 0DD						
0. 10000E+01	0. 32270E+00	0. 15914E+00	0. 17079E+00	0. 16774E+00	0. 32493E+00	0. 16212E+00
0. 93463E+00	0. 33767E+00	0. 15617E+00	0. 16745E+00	0. 17757E+00	0. 34090E+00	0. 18044E+00
0. 86045E+00	0. 35805E+00	0. 15124E+00	0. 16076E+00	0. 18796E+00	0. 35365E+00	0. 20042E+00
0. 77707E+00	0. 38349E+00	0. 14427E+00	0. 14951E+00	0. 19868E+00	0. 36103E+00	0. 22104E+00
0. 68697E+00	0. 41097E+00	0. 13497E+00	0. 13455E+00	0. 20952E+00	0. 36204E+00	0. 24091E+00
0. 58891E+00	0. 43796E+00	0. 12167E+00	0. 11699E+00	0. 22133E+00	0. 35542E+00	0. 26293E+00
0. 49354E+00	0. 45866E+00	0. 10484E+00	0. 98583E-01	0. 23226E+00	0. 33917E+00	0. 28745E+00
0. 40742E+00	0. 47081E+00	0. 86124E-01	0. 79895E-01	0. 24068E+00	0. 31131E+00	0. 31181E+00
0. 33093E+00	0. 47549E+00	0. 66881E-01	0. 61662E-01	0. 24718E+00	0. 26958E+00	0. 33508E+00
0. 26816E+00	0. 47435E+00	0. 50058E-01	0. 46277E-01	0. 25305E+00	0. 22306E+00	0. 35330E+00
0. 25458E+00	0. 47340E+00	0. 46426E-01	0. 42992E-01	0. 25464E+00	0. 21168E+00	0. 35633E+00
RUN ID: 0DE						
0. 10000E+01	0. 32270E+00	0. 15914E+00	0. 17079E+00	0. 16774E+00	0. 32493E+00	0. 16212E+00
0. 97163E+00	0. 36492E+00	0. 17677E+00	0. 18800E+00	0. 19325E+00	0. 37428E+00	0. 19068E+00
0. 93318E+00	0. 43438E+00	0. 19663E+00	0. 19535E+00	0. 22556E+00	0. 42939E+00	0. 22168E+00
0. 88222E+00	0. 52596E+00	0. 21625E+00	0. 20222E+00	0. 26512E+00	0. 48758E+00	0. 25605E+00
0. 81386E+00	0. 62095E+00	0. 22826E+00	0. 21055E+00	0. 30750E+00	0. 54567E+00	0. 30262E+00
0. 73021E+00	0. 69591E+00	0. 22307E+00	0. 20725E+00	0. 34026E+00	0. 59899E+00	0. 35169E+00
0. 63157E+00	0. 74553E+00	0. 19692E+00	0. 18393E+00	0. 36007E+00	0. 62206E+00	0. 39799E+00
0. 53214E+00	0. 77426E+00	0. 16384E+00	0. 15120E+00	0. 36625E+00	0. 60492E+00	0. 44567E+00
0. 43775E+00	0. 79219E+00	0. 13523E+00	0. 12129E+00	0. 36177E+00	0. 55081E+00	0. 49271E+00
0. 35095E+00	0. 80209E+00	0. 11126E+00	0. 94938E-01	0. 34517E+00	0. 47480E+00	0. 52417E+00
0. 31079E+00	0. 80204E+00	0. 99856E-01	0. 82610E-01	0. 33266E+00	0. 43013E+00	0. 52896E+00
0. 27504E+00	0. 79729E+00	0. 89028E-01	0. 71567E-01	0. 31956E+00	0. 38553E+00	0. 52848E+00

TS	L11,1	L22,1	L33,1	L11,2	L22,2	L33,2
RUN ID: QDB						
0. 10000E+01	0. 32270E+00	0. 15914E+00	0. 17079E+00	0. 16774E+00	0. 32493E+00	0. 16212E+00
0. 84646E+00	0. 31369E+00	0. 12587E+00	0. 13531E+00	0. 16299E+00	0. 30467E+00	0. 17808E+00
0. 70600E+00	0. 30517E+00	0. 96308E-01	0. 10372E+00	0. 15909E+00	0. 28030E+00	0. 19456E+00
0. 57166E+00	0. 29674E+00	0. 69375E-01	0. 74855E-01	0. 15588E+00	0. 24995E+00	0. 21217E+00
0. 50043E+00	0. 29215E+00	0. 55907E-01	0. 60387E-01	0. 15451E+00	0. 23030E+00	0. 22219E+00
0. 43481E+00	0. 28787E+00	0. 44187E-01	0. 47767E-01	0. 15359E+00	0. 20957E+00	0. 23167E+00
0. 37429E+00	0. 28389E+00	0. 34119E-01	0. 36903E-01	0. 15324E+00	0. 18795E+00	0. 24039E+00
0. 32034E+00	0. 28036E+00	0. 25883E-01	0. 27997E-01	0. 15364E+00	0. 16644E+00	0. 24778E+00
0. 27756E+00	0. 27761E+00	0. 19945E-01	0. 21563E-01	0. 15475E+00	0. 14779E+00	0. 25305E+00
RUN ID: QDC						
0. 10000E+01	0. 32270E+00	0. 15914E+00	0. 17079E+00	0. 16774E+00	0. 32493E+00	0. 16212E+00
0. 92854E+00	0. 32237E+00	0. 14598E+00	0. 15677E+00	0. 16800E+00	0. 32126E+00	0. 17176E+00
0. 85405E+00	0. 32213E+00	0. 13224E+00	0. 14203E+00	0. 16816E+00	0. 31542E+00	0. 18200E+00
0. 77414E+00	0. 32187E+00	0. 11749E+00	0. 12613E+00	0. 16825E+00	0. 30658E+00	0. 19335E+00
0. 69472E+00	0. 32153E+00	0. 10285E+00	0. 11026E+00	0. 16826E+00	0. 29477E+00	0. 20510E+00
0. 61429E+00	0. 32094E+00	0. 88063E-01	0. 94180E-01	0. 16820E+00	0. 27926E+00	0. 21759E+00
0. 53816E+00	0. 32000E+00	0. 74151E-01	0. 79029E-01	0. 16808E+00	0. 26062E+00	0. 22995E+00
0. 45126E+00	0. 31824E+00	0. 58441E-01	0. 61919E-01	0. 16807E+00	0. 23373E+00	0. 24415E+00
0. 37549E+00	0. 31595E+00	0. 45021E-01	0. 47338E-01	0. 16863E+00	0. 20462E+00	0. 25530E+00
0. 31184E+00	0. 31342E+00	0. 34114E-01	0. 35528E-01	0. 17028E+00	0. 17573E+00	0. 26211E+00
0. 26084E+00	0. 31100E+00	0. 25789E-01	0. 26563E-01	0. 17326E+00	0. 14983E+00	0. 26474E+00

TS L11'3 L22'3 L33'3 A11 A12 A13

RUN ID: 0000

0. 10000E+01	0. 15337E+00	0. 14468E+00	0. 31762E+00	0. 21464E+00	0. 14249E+00	0. 14294E+00
0. 84646E+00	0. 14800E+00	0. 15981E+00	0. 29824E+00	0. 19590E+00	0. 13981E+00	0. 14023E+00
0. 70600E+00	0. 14328E+00	0. 17536E+00	0. 27483E+00	0. 17878E+00	0. 13725E+00	0. 13764E+00
0. 57166E+00	0. 13702E+00	0. 19173E+00	0. 24551E+00	0. 16242E+00	0. 13474E+00	0. 13510E+00
0. 50043E+00	0. 13604E+00	0. 20101E+00	0. 22644E+00	0. 15373E+00	0. 13340E+00	0. 13375E+00
0. 43481E+00	0. 13400E+00	0. 20997E+00	0. 20623E+00	0. 14570E+00	0. 13218E+00	0. 13252E+00
0. 37429E+00	0. 13279E+00	0. 21863E+00	0. 18506E+00	0. 13827E+00	0. 13107E+00	0. 13141E+00
0. 32034E+00	0. 13078E+00	0. 22665E+00	0. 16389E+00	0. 13159E+00	0. 13012E+00	0. 13045E+00
0. 27756E+00	0. 12900E+00	0. 23312E+00	0. 14546E+00	0. 12624E+00	0. 12939E+00	0. 12974E+00

RUN ID: 0000

0. 10000E+01	0. 15337E+00	0. 14468E+00	0. 31762E+00	0. 21464E+00	0. 14249E+00	0. 14294E+00
0. 92854E+00	0. 15302E+00	0. 15278E+00	0. 31433E+00	0. 20828E+00	0. 14343E+00	0. 14385E+00
0. 85405E+00	0. 15256E+00	0. 16129E+00	0. 30889E+00	0. 20177E+00	0. 14417E+00	0. 14456E+00
0. 77414E+00	0. 15200E+00	0. 17050E+00	0. 30051E+00	0. 19491E+00	0. 14473E+00	0. 14508E+00
0. 69472E+00	0. 15141E+00	0. 17977E+00	0. 28916E+00	0. 18819E+00	0. 14505E+00	0. 14535E+00
0. 61429E+00	0. 15082E+00	0. 18940E+00	0. 27401E+00	0. 18144E+00	0. 14516E+00	0. 14540E+00
0. 53816E+00	0. 15020E+00	0. 19898E+00	0. 25565E+00	0. 17498E+00	0. 14505E+00	0. 14521E+00
0. 45126E+00	0. 14927E+00	0. 21091E+00	0. 22878E+00	0. 16733E+00	0. 14464E+00	0. 14470E+00
0. 37549E+00	0. 14799E+00	0. 22291E+00	0. 19908E+00	0. 16010E+00	0. 14399E+00	0. 14394E+00
0. 31184E+00	0. 14631E+00	0. 23470E+00	0. 16901E+00	0. 15329E+00	0. 14318E+00	0. 14304E+00
0. 26084E+00	0. 14449E+00	0. 24546E+00	0. 14158E+00	0. 14711E+00	0. 14232E+00	0. 14212E+00

RUN ID: ODD	TS	L11'3	L22'3	L33'3	Λ11	Λ12	Λ13
0. 10000E+01	0. 15337E+00	0. 14468E+00	0. 31762E+00	0. 21464E+00	0. 14249E+00	0. 14294E+00	
0. 93463E+00	0. 16144E+00	0. 15720E+00	0. 33342E+00	0. 21816E+00	0. 15179E+00	0. 15216E+00	
0. 86045E+00	0. 17038E+00	0. 17093E+00	0. 34408E+00	0. 22330E+00	0. 16150E+00	0. 16176E+00	
0. 77707E+00	0. 18026E+00	0. 18684E+00	0. 34658E+00	0. 22994E+00	0. 17127E+00	0. 17157E+00	
0. 68697E+00	0. 19035E+00	0. 20521E+00	0. 33894E+00	0. 23712E+00	0. 18043E+00	0. 18097E+00	
0. 58891E+00	0. 20048E+00	0. 22681E+00	0. 32124E+00	0. 24350E+00	0. 18884E+00	0. 18942E+00	
0. 49354E+00	0. 20958E+00	0. 24892E+00	0. 29240E+00	0. 24689E+00	0. 19540E+00	0. 19561E+00	
0. 40742E+00	0. 21777E+00	0. 27287E+00	0. 25690E+00	0. 24644E+00	0. 19959E+00	0. 19942E+00	
0. 33093E+00	0. 22571E+00	0. 30507E+00	0. 22015E+00	0. 24260E+00	0. 20160E+00	0. 20112E+00	
0. 26816E+00	0. 23269E+00	0. 34069E+00	0. 18664E+00	0. 23642E+00	0. 20178E+00	0. 20092E+00	
0. 25458E+00	0. 23426E+00	0. 34838E+00	0. 17884E+00	0. 23463E+00	0. 20162E+00	0. 20065E+00	

RUN ID: ODD	TS	L11'3	L22'3	L33'3	Λ11	Λ12	Λ13
0. 10000E+01	0. 15337E+00	0. 14468E+00	0. 31762E+00	0. 21464E+00	0. 14249E+00	0. 14294E+00	
0. 97163E+00	0. 17574E+00	0. 16242E+00	0. 36377E+00	0. 23685E+00	0. 16531E+00	0. 16565E+00	
0. 93318E+00	0. 20561E+00	0. 18725E+00	0. 40380E+00	0. 26923E+00	0. 19348E+00	0. 19456E+00	
0. 88222E+00	0. 23794E+00	0. 21882E+00	0. 43839E+00	0. 30952E+00	0. 22580E+00	0. 22731E+00	
0. 81386E+00	0. 26848E+00	0. 25434E+00	0. 46538E+00	0. 35673E+00	0. 26140E+00	0. 26170E+00	
0. 73021E+00	0. 29744E+00	0. 30326E+00	0. 48940E+00	0. 40670E+00	0. 29642E+00	0. 29369E+00	
0. 63157E+00	0. 33019E+00	0. 37835E+00	0. 51130E+00	0. 45123E+00	0. 32723E+00	0. 32304E+00	
0. 53214E+00	0. 35859E+00	0. 46245E+00	0. 50458E+00	0. 47618E+00	0. 34911E+00	0. 34571E+00	
0. 43775E+00	0. 37567E+00	0. 53555E+00	0. 45664E+00	0. 48124E+00	0. 36350E+00	0. 36121E+00	
0. 35095E+00	0. 38702E+00	0. 57227E+00	0. 37104E+00	0. 47341E+00	0. 37183E+00	0. 37157E+00	
0. 31079E+00	0. 39592E+00	0. 57757E+00	0. 32556E+00	0. 46722E+00	0. 37400E+00	0. 37561E+00	
0. 27504E+00	0. 40899E+00	0. 57384E+00	0. 28833E+00	0. 46083E+00	0. 37505E+00	0. 37915E+00	

T S	Λ_{21}	Λ_{22}	Λ_{23}	Λ_{31}	Λ_{32}	Λ_{33}
RUN ID: ODH						
0. 10000E+01	0. 14104E+00	0. 20633E+00	0. 14089E+00	0. 16124E+00	0. 14066E+00	0. 20618E+00
0. 84646E+00	0. 13606E+00	0. 19921E+00	0. 14415E+00	0. 13618E+00	0. 14384E+00	0. 19902E+00
0. 70600E+00	0. 11384E+00	0. 18991E+00	0. 14788E+00	0. 11388E+00	0. 14744E+00	0. 18963E+00
0. 57166E+00	0. 93306E-01	0. 17806E+00	0. 15234E+00	0. 93274E-01	0. 15174E+00	0. 17764E+00
0. 50043E+00	0. 82745E-01	0. 17053E+00	0. 15515E+00	0. 82681E-01	0. 15444E+00	0. 17002E+00
0. 43481E+00	0. 73230E-01	0. 16284E+00	0. 15805E+00	0. 73141E-01	0. 15723E+00	0. 16225E+00
0. 37429E+00	0. 64639E-01	0. 15516E+00	0. 16101E+00	0. 64534E-01	0. 16007E+00	0. 15450E+00
0. 32034E+00	0. 57116E-01	0. 14790E+00	0. 16384E+00	0. 57011E-01	0. 16281E+00	0. 14720E+00
0. 27756E+00	0. 51230E-01	0. 14192E+00	0. 16620E+00	0. 51137E-01	0. 16511E+00	0. 14121E+00

RUN ID: ODC						
0. 10000E+01	0. 16104E+00	0. 20633E+00	0. 14089E+00	0. 16124E+00	0. 14066E+00	0. 20618E+00
0. 92854E+00	0. 15073E+00	0. 20605E+00	0. 14433E+00	0. 15082E+00	0. 14417E+00	0. 20588E+00
0. 85405E+00	0. 14012E+00	0. 20450E+00	0. 14758E+00	0. 14011E+00	0. 14748E+00	0. 20432E+00
0. 77414E+00	0. 12891E+00	0. 20140E+00	0. 15066E+00	0. 12882E+00	0. 15062E+00	0. 20117E+00
0. 69472E+00	0. 11795E+00	0. 19684E+00	0. 15330E+00	0. 11781E+00	0. 15328E+00	0. 19654E+00
0. 61429E+00	0. 10706E+00	0. 19072E+00	0. 15550E+00	0. 10685E+00	0. 15546E+00	0. 19033E+00
0. 53816E+00	0. 96946E-01	0. 18355E+00	0. 15710E+00	0. 96715E-01	0. 15699E+00	0. 18305E+00
0. 45126E+00	0. 85668E-01	0. 17379E+00	0. 15831E+00	0. 85409E-01	0. 15802E+00	0. 17315E+00
0. 37549E+00	0. 76056E-01	0. 16398E+00	0. 15878E+00	0. 75802E-01	0. 15823E+00	0. 16320E+00
0. 31184E+00	0. 68107E-01	0. 15489E+00	0. 15874E+00	0. 67881E-01	0. 15791E+00	0. 15401E+00
0. 26084E+00	0. 61765E-01	0. 14711E+00	0. 15845E+00	0. 61598E-01	0. 15740E+00	0. 14623E+00

TS	Λ_{21}	Λ_{22}	Λ_{23}	Λ_{31}	Λ_{32}	Λ_{33}
RUN ID: 0111)						
0. 10000E+01	0. 16104E+00	0. 20633E+00	0. 14089E+00	0. 16124E+00	0. 14066E+00	0. 20618E+00
0. 93463E+00	0. 15705E+00	0. 21667E+00	0. 15190E+00	0. 15696E+00	0. 15216E+00	0. 21655E+00
0. 86045E+00	0. 15284E+00	0. 22544E+00	0. 16270E+00	0. 15261E+00	0. 16339E+00	0. 22564E+00
0. 77707E+00	0. 14837E+00	0. 23217E+00	0. 17312E+00	0. 14812E+00	0. 17386E+00	0. 23300E+00
0. 68697E+00	0. 14351E+00	0. 23609E+00	0. 18259E+00	0. 14328E+00	0. 18285E+00	0. 23751E+00
0. 58891E+00	0. 13755E+00	0. 23634E+00	0. 19058E+00	0. 13751E+00	0. 19000E+00	0. 23817E+00
0. 49354E+00	0. 13042E+00	0. 23250E+00	0. 19535E+00	0. 13092E+00	0. 19464E+00	0. 23423E+00
0. 40742E+00	0. 12252E+00	0. 22517E+00	0. 19696E+00	0. 12350E+00	0. 19726E+00	0. 22680E+00
0. 33093E+00	0. 11421E+00	0. 21539E+00	0. 19659E+00	0. 11515E+00	0. 19843E+00	0. 21753E+00
0. 26816E+00	0. 10625E+00	0. 20507E+00	0. 19518E+00	0. 10692E+00	0. 19840E+00	0. 20808E+00
0. 25458E+00	0. 10435E+00	0. 20253E+00	0. 19471E+00	0. 10497E+00	0. 19825E+00	0. 20576E+00

RUN ID: 011E						
0. 10000E+01	0. 16104E+00	0. 20633E+00	0. 14089E+00	0. 16124E+00	0. 14066E+00	0. 20618E+00
0. 97163E+00	0. 17146E+00	0. 23545E+00	0. 16395E+00	0. 17122E+00	0. 16480E+00	0. 23573E+00
0. 93318E+00	0. 18700E+00	0. 27125E+00	0. 19304E+00	0. 18657E+00	0. 19417E+00	0. 27307E+00
0. 88222E+00	0. 20670E+00	0. 31095E+00	0. 22537E+00	0. 20645E+00	0. 22667E+00	0. 31339E+00
0. 81386E+00	0. 22692E+00	0. 35153E+00	0. 25665E+00	0. 22751E+00	0. 26182E+00	0. 35313E+00
0. 73021E+00	0. 24200E+00	0. 38603E+00	0. 28504E+00	0. 24418E+00	0. 29538E+00	0. 38754E+00
0. 63157E+00	0. 25158E+00	0. 40972E+00	0. 31072E+00	0. 25319E+00	0. 32514E+00	0. 41586E+00
0. 53214E+00	0. 25363E+00	0. 41585E+00	0. 33130E+00	0. 25455E+00	0. 34734E+00	0. 42971E+00
0. 43775E+00	0. 24665E+00	0. 40780E+00	0. 34658E+00	0. 24978E+00	0. 36283E+00	0. 42571E+00
0. 35095E+00	0. 23213E+00	0. 39202E+00	0. 35599E+00	0. 23917E+00	0. 37244E+00	0. 40954E+00
0. 31079E+00	0. 22259E+00	0. 38238E+00	0. 35797E+00	0. 23119E+00	0. 37488E+00	0. 39964E+00
0. 27504E+00	0. 21261E+00	0. 37218E+00	0. 35786E+00	0. 22183E+00	0. 37512E+00	0. 38970E+00

References

- Ahmadi-Befruji, B., Gosman, A.D., Lockwood, F.C., and Watkins, A.P. (1981), "Multidimensional Calculation of Combustion in an Idealized Homogeneous Charge Engine: a Progress Report," SAE Paper No. 810151.
- Arcoumanis, C., Bicen, A.F., and Whitelaw, J.H. (1982), "Measurements in a Motored Four-Stroke Reciprocating Model Engine," ASME Journal of Fluids Engineering, 104: 235-241.
- Arcoumanis, C., Bicen, A.F., and Whitelaw, J.H. (1983), "Squish and Swirl-Squish Interaction in Motored Model Engines," ASME Journal of Fluids Engineering, 105: 105-112.
- Bardina, J., Ferziger, J.H., and Reynolds, W.C. (1983), "Improved Turbulence Models Based on Large Eddy Simulation of Homogeneous, Incompressible, Turbulent Flows," Report TF-19, Thermosciences Div., Dept. of Mech. Engrg., Stanford University, CA.
- Bardina, J., Ferziger, J.H., and Rogallo, R.S. (1985), "Effect of Rotation on Isotropic Turbulence: Computation and Modeling," Submitted to J. Fluid Mech.
- Batchelor, G.K., and Proudman, I. (1954), "The Effect of Rapid Distortion of A Fluid in Turbulent Motion," Quart. Journ. Mech. and Applied Math., 7, Part 1, pp. 83-103.
- Borgnakke, C., Arpacı, V.S., and Tabaczynski, R.J. (1980), "A Model for the Instantaneous Heat Transfer and Turbulence in a Spark Ignition Engine," SAE Paper No. 800287.
- Butler, T.D., Cloutman, L.D., Dukowicz, J.K., and Ramshaw, J.D. (1979), "CONCHAS: An Arbitrary Lagrangian-Eulerian Computer Code for Multi-component Chemically Reactive Fluid Flow at All Speeds," Los Alamos Scientific Laboratory Report LA-8129-MS.
- Clark, R.A., Ferziger, J.H., and Reynolds, W.C. (1979), "Evaluation of Subgrid-Scale Models Using An Accurately Simulated Turbulent Flow," J. Fluid Mech., 91, Part 1, pp. 1-16.
- Comte-Bellot, G., and Corrsin, S. (1971), "Simple Eulerian Time Correlation of Full- and Narrow-Band Velocity Signals in Grid-Generated, 'Isotropic' Turbulence," J. Fluid Mech., 48, Part 2, pp. 273-337.
- Cooley, J.W., and Tukey, J.W. (1965), "An Algorithm for the Machine Calculation of Complex Fourier Series," Mathematics of Computation, 19: 297-301.
- Dang, K.T. (1985), "Evaluation of Simple Subgrid-Scale Models for the Numerical Simulation of Homogeneous Turbulence," AIAA Journal, 23, No. 2, pp. 221-227.

- Dussauge, J.P., Gaviglio, J., and Favre, A. (1978), "Density Changes and Turbulence Production in the Expansion or Compression of A Turbulent Flow at Supersonic Speed," Lecture Notes in Physics (H. Fiedler, ed.), Springer Verlag, Berlin, 76: 385-395.
- El Tahry, S.H. (1983), "k- ϵ Equation for Compressible Reciprocating Engine Flows," Journal of Energy, 7, No. 4, pp. 345-353.
- Feiereisen, W.J., Reynolds, W.C., and Ferziger, J.H. (1981), "Numerical Simulation of a Compressible, Homogeneous, Turbulent Shear Flow," Report TF-13, Thermosciences Div., Dept. of Mech. Engrg., Stanford University, Stanford, CA.
- Gosman, A.D., and Watkins, A.P. (1977), "A Computer Prediction Method for Turbulent Flow and Heat Transfer in Piston/Cylinder Assemblies," Proc. Symposium on Turbulent Shear Flows, Penn. State Univ., pp. 5.23-5.30.
- Gosman, A.D., and Johns, R.J.R. (1978), "Development of a Predictive Tool for In-Cylinder Gas Motion in Engines," SAE Paper No. 780315.
- Gosman, A.D., and Johns, R.J.R. (1980), "Computer Analysis of Fuel-Air Mixing in Direct-Injection Engines," SAE Paper No. 800091.
- Gosman, A.D., Johns, R.J.R., and Watkins, A.P. (1980), "Development of Prediction Methods for In-Cylinder Processes in Reciprocating Engines," Symposium on Combustion Modeling in Reciprocating Engines, Plenum Press, pp. 69-129.
- Gosman, A.D., and Jahanbakhsh, A. (1981), "RPM Code," Comparisons between Measurement and Analysis of Fluid Motion in Internal Combustion Engines," (P.O. Witze, ed.), Sandia National Laboratories Report SAND81-8242.
- Gosman, A.D., and Harvey, P.S. (1982), "Computer Analysis of Fuel-Air Mixing and Combustion in an Axisymmetric D.I. Diesel," SAE Paper No. 820036.
- Grasso, F., and Bracco, F.V. (1983), "Computed and Measured Turbulence in Axisymmetric Reciprocating Engines," AIAA Journal, 21, No.4, pp. 601-607.
- Hanjalic, K., and Launder, B.E. (1972), "A Reynolds Stress Model of Turbulence and Its Application to Thin Shear Flows," J. Fluid Mech., 52, Part 4, pp. 609-638.
- Hanjalic, K., and Launder, B.E. (1976), "Contribution Towards A Reynolds-Stress Closure for Low-Reynolds-Number Turbulence," J. Fluid Mech., 74, Part 4, pp. 593-610.
- Hoult, D.P., and Wong, V.W. (1980), "The Generation of Turbulence in An Internal-Combustion Engine," Symposium on Combustion Modeling in Reciprocating Engines, Plenum Press, pp. 131-160.

- Hunt, J.C.R. (1978), "A Review of the Theory of Rapidly Distorted Turbulent Flows and Its Applications," Fluid Dynamics Transactions, 9: 121-152.
- Jones, W.P., and Launder, B.E. (1972), "The Prediction of Laminarization with a Two-Equation Model of Turbulence," Int. J. Heat Mass Transfer, 15: 301-314.
- Kline, S.J., Cantwell, B.J., and Lilley, G.M. (1981), "1980-1981 AFOSR-HTTM-Stanford Conference on Complex Turbulent Flow," Thermosciences Div., Dept. of Mech Engrg., Stanford University, Stanford, CA.
- Lancaster, D.R. (1976), "Effects of Engine Variables on Turbulence in a Spark-Ignition Engine," SAE Paper 760159.
- Launder, B.E., and Spalding, D.B. (1974), "The Numerical Computation of Turbulent Flows," Computer Methods in Applied Mechanics and Engineering, Vol. 3, pp. 269-289.
- Launder, B.E., Reece, G.J., and Rodi, W. (1975), "Progress in the Development of a Reynolds-Stress Turbulence Closure," J. Fluid Mech., 68, Part 3, pp. 537-566.
- Lee, M.J., and Reynolds, W.C. (1985), "Numerical Experiments on the Structure of Homogeneous Turbulence," Report TF-22, Thermosciences Div., Dept. of Mech. Engrg., Stanford University, Stanford, CA.
- Lumley, J.L., and Newman, G.R. (1977), "The Return to Isotropy of Homogeneous Turbulence," J. Fluid Mech., 82, Part 1, pp. 161-178.
- Lumley, J.L. (1978), "Computational Modeling of Turbulent Flows," Advances in Applied Mechanics, 18: 123-176.
- Lumley, J.L. (1979), "Second Order Modeling of Turbulent Flows," prepared for von Karman Institute lecture series.
- Mansour, N.N. (1982), "Dispersion of Stratified Charges in the Engine-Cylinder During the Compression Stroke," Presented at the ASME Winter Annual Meeting, Phoenix, Arizona.
- Morel, T., and Mansour, N.N. (1982), "Modeling of Turbulence in Internal Combustion Engines," SAE Paper 820040.
- Morse, A.P., Whitelaw, J.H., and Yianneskis, M. (1979), "Turbulent Flow Measurements by Laser-Doppler Anemometry in Motored Piston-Cylinder Assemblies," ASME Journal of Fluids Engineering, 101: 208-216.
- Morse, A., Whitelaw, J.H., and Yianneskis, M. (1980), "The Influence of Swirl on the Flow Characteristics of a Reciprocating Piston-Cylinder Assembly," ASME Journal of Fluids Engineering, 102: 478-480.
- Orszag, S.A., and Patterson, G.S. (1972), "Numerical Simulation of Turbulence," Lecture Notes in Physics, Springer-Verlag, Berlin, 12: 127-147.

- Patterson, G.S., and Orszag, S.A. (1971), "Spectral Calculations of Isotropic Turbulence: Efficient Removal of Aliasing Interactions," Physics of Fluids, 14: 2538-2541.
- Ramos, J.I., Humphery, J.A.C., and Sirignano, W.A. (1979), "Numerical Prediction of Axisymmetric Laminar and Turbulent Flows in Motored, Reciprocating Internal Combustion Engines," SAE Paper No. 790356.
- Reynolds, W.C. (1976), "Computation of Turbulent Flows," Annual Reviews of Fluid Mechanics, 8: 183-208.
- Reynolds, W.C. (1980), "Modeling of Fluid Motions in Engines--An Introductory Overview," Symposium on Combustion Modeling in Reciprocating Engines, Plenum Press, pp. 41-66.
- Reynolds, W.C. (1984), "Physical and Analytical Foundations, Concepts, and New Directions in Turbulence Modeling and Simulation," Proc. Ecole d'Été d'Analyse Numerique-Modelisation Numerique de la Turbulence, in Turbulence Models and Their Applications, Vol. 2, EYROLLES, Paris.
- Richman, R.M., and Reynolds, W.C. (1982), "The Flow Diagnostics Engine: A New System for Piston Engine Research," Report FDE-1, Thermosciences Div., Dept. of Mech. Engrg., Stanford University, Stanford, CA.
- Rogallo, R.S. (1981), "Numerical Experiments in Homogeneous Turbulence," NASA TM-81315.
- Schumann, U., and Herring, J.R. (1976), "Axisymmetric Homogeneous Turbulence: A Comparison of Direct Spectral Simulations with the Direct-Interaction Approximation," J. Fluid Mech., 76, Part 4, pp. 755-782.
- Schumann, U., and Patterson, G.S. (1978), "Numerical Study of Pressure and Velocity Fluctuations in Nearly Isotropic Turbulence," J. Fluid Mech., 88, Part 4, pp. 685-709.
- Schumann, U., and Patterson, G.S. (1978), "Numerical Study of the Return of Axisymmetric Turbulence to Isotropy," J. Fluid Mech., 88, Part 4, pp. 711-735.
- Semenov, E.S. (1958), "Studies of Turbulent Gas Flow in Piston Engines," Otdelenie Tekhnicheskikh Nauk, No. 8 (English Translation: NASA Technical Translation F97, pp. 122-147).
- Shirani, E., Ferziger, J.H., and Reynolds, W.C. (1981), "Mixing of a Passive Scalar in Isotropic and Sheared Homogeneous Turbulence," Report TF-15, Thermosciences Div., Dept. of Mech. Engrg., Stanford University, Stanford, CA.
- Taylor, G.I. (1935), "Turbulence in A Contracting Stream," Zeitschrift für Angewandte Mathematik und Mechanik, 15: 91-96.

- Touloukian, Y.S., Saxena, S.C., and Hestermans, P. (1975), Thermophysical Properties of Matter: Viscosity, IFI/Plenum, 11.
- Townsend, A.A. (1954), "The Uniform Distortion of Homogeneous Turbulence," Quart. Journ. Mech. and Applied Math., 7, Part 1, pp. 104-127.
- Tucker, H.J., and Reynolds, A.J. (1968), "The Distortion of Turbulence by Irrotational Plane Strain," J. Fluid Mech., 32, Part 4, pp. 657-673.
- Watkins, A.P. (1977), "Flow and Heat Transfer in Piston/Cylinder Assemblies," Ph.D. thesis, University of London.
- Winsor, R.E., and Patterson, D.J. (1973), "Mixture Turbulence--A Key to Cyclic Variation," SAE paper No. 730086.
- Witze, P.O. (1977), "Measurements of the Spatial Distribution and Engine Speed Dependence of Turbulent Air Motion in an I.C. Engine," SAE Transactions, 86, Paper No. 770220, pp.1012-1023.
- Witze, P.O. (1980), "A Critical Comparison of Hot-Wire Anemometry and Laser-Doppler Velocimetry for I.C. Engine Applications," SAE Transactions, 89, Paper No. 800132, pp. 711-740.
- Wu, C.T., Ferziger, J.H., Chapman, D.R., and Rogallo, R.S. (1983), "Navier-Stokes Simulation of Homogeneous Turbulence on the CYBER 205," NASA CP-2295, pp. 227-239.